

**GOCE GRADIOMETER MEASUREMENT DISTURBANCES AND THEIR  
MODELLING BY MEANS OF IONOSPHERIC DYNAMICS**

ELMAS SINEM INCE

A DISSERTATION SUBMITTED TO THE FACULTY OF GRADUATE STUDIES  
IN PARTIAL FULFILMENT OF THE REQUIREMENTS  
FOR THE DEGREE OF

**DOCTOR OF PHILOSOPHY**

GRADUATE PROGRAM IN EARTH AND SPACE SCIENCE  
YORK UNIVERSITY  
TORONTO, ONTARIO

October 2016

© Elmas Sinem Ince, 2016

## Abstract

We examine the presence of residual non-gravitational signatures in gravitational gradients measured by GOCE Electrostatic Gravity Gradiometer. These signatures are observed over the geomagnetic poles during geomagnetically active days and contaminate the trace of the Gravitational Gradient Tensor by up to three to five times the expected noise level of the instrument ( $\sim 11 \text{ mE}$ ). We investigate these anomalies in the gradiometer measurements along many satellite tracks and examine possible causes by using external datasets, such as Interplanetary Electric Field observations from the ACE (Advanced Composition Explorer) and WIND spacecraft and Poynting flux (vector) estimated from Equivalent Ionospheric Currents derived from Spherical Elementary Current Systems over North America and Greenland. We show that the variations in the east-west and vertical electrical currents and Poynting flux (vector) components at the satellite position are highly correlated with the disturbances observed in the gradiometer measurements. We identify the relation between the ionospheric dynamics and disturbances and develop a data-driven model to reduce the effects of these disturbances. The results presented in this dissertation discover that the cause of the disturbances are due to intense ionospheric dynamics that are enhanced by increased solar activity which causes a dynamic drag environment. Moreover, using external information about the ionospheric dynamics, we successfully model and remove a high percentage of these disturbances for the first time in GOCE literature and promise improved data for future gravitational field models and studies of the Earth's upper atmosphere.

PEACE AT HOME, PEACE IN THE WORLD.

MUSTAFA KEMAL ATATÜRK

## Acknowledgements

I would like to express my gratitude to my supervisor Professor Dr. Spiros Pagiatakis. Although it is not easy to squeeze all the words here after all these years, I have to mention how working with him has changed my vision. Not only his professional supervision on technical topics but also his principles and passion in research, his understanding and caring and his personality have helped me learn, experience, live and grow. It would therefore literally not been possible to start, continue, nor finish this kind of research without his excellent supervision. There were moments when the research was very slow, and the end was not there yet. He was always there for guidance and always had options to succeed. He was not only patient to all these difficult situations but he also made me a patient researcher. He made me aware of what to concern for and not to escape from challenges but take risks, try and learn. It is a great pleasure having this experience with Dr. Pagiatakis and being part of his team. I have truly felt valued as a person, as a student and as a researcher.

I would like to thank my thesis committee members, Drs. Sunil Bisnath, Anthony Szeto, and Regina Lee for sharing their experiences and knowledge during the last 4 years and help me improve our research. Their support and useful critiques helped to create a more objective research environment and meet the requirements of an original research.

I would like to thank Dr. Rune Floberghagen for sharing his knowledge and experience and supporting me working on this topic from the very beginning. I would like to thank Drs. Christian Siemes and Björn Frommknecht for helping me in the beginning of this research and understanding the data processing. I would like to thank Dr. Anja Schlicht who has been very generous in sharing her ideas and hosting me at the Technical University of Munich. I appreciate her and her team members cooperation. Even though it was only for a short time and end of my research, I am glad I had the chance to work with them. I also appreciate Dr. Roland Pail and his team and other colleagues who also host me at TUM and made the time to discuss about my research and share their knowledge and made me feel at home during my visit in TUM.

I would like to thank Dr. Ebrahim Ghaderpour for discussions on the applications of wavelets and least squares spectrum and Kıvanç Babacan for discussions on transfer functions and system identification.

Funding for my studies was provided by NSERC and GEOIDE NCE grants to my supervisor and awards from the Faculty of Graduate Studies at York University. I am grateful to the thesis examination committee members, Dr. Gordon Shepherd, Dr. Sunil Bisnath, Dr. Regina Lee, Dr. Gary Jarvis from York University and Dr. Thomas Gruber from Technical University of Munich for their time and comments to improve this dissertation.

Finally, I thank my parents Songül and Ilyas and my sister Sibel, who have encouraged and believed in me continuously and unconditionally to pursue my passions. There are no words to acknowledge their support during all those years from miles away. Thank you for everything.

# Contents

<b>Abstract</b>	<b>ii</b>
<b>Dedication</b>	<b>iii</b>
<b>Acknowledgements</b>	<b>iv</b>
<b>Table of Contents</b>	<b>v</b>
<b>List of Tables</b>	<b>ix</b>
<b>List of Figures</b>	<b>x</b>
<b>List of Abbreviations</b>	<b>xx</b>
<b>List of Symbols</b>	<b>xxii</b>
<b>1 Introduction and Background</b>	<b>1</b>
1.1 Background . . . . .	1
1.2 Research Objectives . . . . .	5
1.3 Outline of the Thesis . . . . .	7
<b>2 Satellite Gradiometry</b>	<b>9</b>
2.1 Gravity Missions and GOCE . . . . .	9
2.1.1 GOCE Payload . . . . .	12
2.1.1.1 Electrostatic Gravity Gradiometer . . . . .	13
2.1.1.2 Other Sensors . . . . .	16
2.2 Level 1b Gradiometer Data and In-flight Calibration . . . . .	18

2.2.1	Gradiometer Data . . . . .	18
2.2.2	Calibration of the Gradiometer . . . . .	22
2.2.2.1	Measurement of quadratic factor . . . . .	24
2.2.2.2	Other Gradiometer Calibration Parameters . . . . .	25
2.2.2.3	Determination of the Inverse Calibration Matrices . . . . .	28
2.3	Summary . . . . .	30
<b>3</b>	<b>Gradiometer Data</b>	<b>31</b>
3.1	Data Pre-processing . . . . .	31
3.1.1	Filtering Procedure . . . . .	31
3.1.2	Transformation of the GOCE EGG Measurements . . . . .	36
3.1.2.1	Reference Frames Used in GOCE Measurements and Data Processing . . . . .	36
3.1.2.2	Transformations Among the Reference Frames . . . . .	38
3.2	Calibrated Common-mode and Differential-mode Accelerations . . . . .	39
3.3	Gravitational Gradient Tensor Components in Spatial Domain . . . . .	42
3.4	Identification of Inherent Measurement Problems . . . . .	45
3.4.1	Investigations on the GGT Components . . . . .	45
3.4.2	Investigations on the GGT Trace . . . . .	50
3.4.3	Investigations of the Angular Accelerations . . . . .	53
3.5	Summary . . . . .	58
<b>4</b>	<b>Ionosphere, Geomagnetic Field and Space Weather</b>	<b>59</b>
4.1	Ionosphere . . . . .	59
4.2	Solar Activity and Space Weather Observations . . . . .	61
4.2.0.1	Advanced Composition Explorer (ACE) and WIND Solar Monitoring Satellites . . . . .	64
4.2.0.2	Geomagnetic indices . . . . .	70
4.2.0.3	CARISMA Observations . . . . .	72
4.3	Ionospheric Currents and Poynting Flux . . . . .	74
4.3.1	Spherical Elementary Current Systems . . . . .	74
4.3.2	Equivalent Ionospheric Currents and Spherical Elementary Current Amplitudes . . . . .	78
4.3.3	Electromagnetic Energy Flow . . . . .	84
4.4	Summary . . . . .	86

<b>5</b>	<b>Investigations of GOCE Disturbances using the C-IAM</b>	<b>88</b>
5.1	C-IAM Model Description and Simulations . . . . .	88
5.1.1	Simulations of the Electric Potential . . . . .	89
5.1.2	Simulations of Neutral Winds . . . . .	92
5.1.3	Quiet and Stormy Time Simulations on March 11, 2011 . . . . .	94
5.2	Analysis of C-IAM simulations along track . . . . .	97
5.3	Summary . . . . .	100
<b>6</b>	<b>Analysis of Data in Time-Scale (Frequency) Domain</b>	<b>101</b>
6.1	Analysis in Time-Scale Domain . . . . .	101
6.1.1	Continuous Wavelet Transform . . . . .	102
6.1.2	Cross Wavelet Analysis . . . . .	109
6.1.3	Cross Coherence Analysis . . . . .	109
6.2	Summary . . . . .	112
<b>7</b>	<b>Impulse-Response Analysis and Model Development</b>	<b>113</b>
7.1	Dynamic Systems . . . . .	113
7.2	Data-driven Modelling . . . . .	114
7.2.1	Identification of the System . . . . .	118
7.2.2	Determination of the Model Structure . . . . .	120
7.3	Development of the Model . . . . .	121
7.3.1	Basics of Transfer Function . . . . .	121
7.3.2	Model Structure Selection . . . . .	122
7.4	Model estimation . . . . .	124
7.5	Summary . . . . .	131
<b>8</b>	<b>Modelling the Measurement Errors</b>	<b>132</b>
8.1	Characteristics of the disturbances . . . . .	132
8.2	Characteristics of CM accelerations and GGT components . . . . .	134
8.3	Investigations of other tracks . . . . .	136
8.4	Modelling the disturbances . . . . .	140
8.5	Summary . . . . .	146

**9 Conclusions and Recommendations for Future Research** **148**

9.1 Conclusions . . . . . 148

9.2 Recommendations for Future Research . . . . . 150

**References** **153**

# List of Tables

2.1	Specifications of the three gravity missions. . . . .	10
2.2	Ultra- and less-sensitive axes of the GOCE Gradiometer. . . . .	15
2.3	Measurements included in Level 1 Block. Note that the ones used in this research are indicated as bold. . . . .	18
7.1	List of transfer functions and numerical values for the coefficients that are used in the simulations.	126
7.2	List of arx models and numerical values for the coefficients that are used in the simulations. .	126
8.1	Statistics of 954 ascending tracks before and after corrections based on arx625 transfer function. See the values in parenthesis for the statistics of corrected series. The values are given in miliEotvos unit. . . . .	146
8.2	Statistics of the 5 ascending tracks before and after corrections based on arx625 transfer function. See the values in parenthesis for the statistics of corrected series. The values are given in miliEotvos unit. . . . .	146

# List of Figures

1.1	Artistic image of GOCE, image credit: ESA. . . . .	3
2.1	GOCE top view, image credit: ESA. Electrostatic Gravity Gradiometer is mounted precisely near the centre of the mass of the spacecraft. . . . .	11
2.2	GOCE Electrostatic Gravity Gradiometer, image credit: TAS/ONERA. See the accelerometer pairs mounted in X,Y, and Z directions orthogonally. . . . .	13
2.3	Gradiometer Reference Frame, image credit: TUM. The $X_{\text{GRF}}$ refers to along the satellite track direction, whereas $Y_{\text{GRF}}$ and $Z_{\text{GRF}}$ correspond to cross-track and radial direction, respectively. $O_{\text{GRF}}$ stands for the origin of the GRF. The ultra-sensitive axes are displayed by bold lines, whereas the less-sensitive axes are displayed by dashed lines. . . . .	15
2.4	Accelerometer Electrode System Reference Frame and location/nomenclature of the 8 electrode pairs, image credit: TAS/ONERA. . . . .	16
3.1	Square root of the power spectral densities of original diagonal components. The vertical black dashed lines represent the GOCE EGG measurement bandwidth, whereas the vertical red dashed lines represent the orbital ( $1.86 \cdot 10^{-04}$ Hz) and semi-orbital periodicities ( $3.71 \cdot 10^{-04}$ Hz). Diagonal original GGT components show increasing noise level for the lower frequencies of the MBW and the frequencies outside of the MBW. . . . .	34
3.2	Square root of the power spectral densities of filtered diagonal components. The black dashed lines represent the GOCE EGG measurement bandwidth, whereas the red dashed lines represent the orbital ( $1.86 \cdot 10^{-04}$ Hz) and semi-orbital periodicities ( $3.71 \cdot 10^{-04}$ Hz). Note the reduction of the power outside of the MBW and as well as within the MBW. . . . .	35
3.3	Reference Frames used for GOCE products, image credit: TUM. . . . .	37

3.4	CM accelerations from A1 and A4 pair in the along-track direction are filtered into the Gradiometer MBW. Notice the larger drag effects in the polar regions. . . . .	41
3.5	CM accelerations from A2 and A5 pair cross the track direction are filtered into the Gradiometer MBW. Notice the larger drag effects at higher latitudes. Moreover, ascending tracks are exposed to larger drag conditions over magnetic poles. . . . .	41
3.6	CM accelerations from A3 and A6 pair radial direction are filtered into the Gradiometer MBW. Notice the larger drag conditions over magnetic poles similar to cross-track CM accelerations. . . . .	41
3.7	$V_{xx}$ filtered into the Gradiometer MBW during March-April, 2011 for ascending and descending tracks. See the geophysical features along the track and the different resolution due to the different orientation of the X-axis in ascending and descending tracks. . . . .	43
3.8	$V_{yy}$ filtered into the Gradiometer MBW during March-April, 2011 for ascending and descending tracks. See geophysical features and the different resolution due to the different orientation of the Y-axis in ascending and descending tracks. . . . .	43
3.9	$V_{zz}$ filtered into the Gradiometer MBW during March-April, 2011 for ascending and descending tracks. Since the orientation does not change for the Z-direction as opposed to the other diagonal components, the structure of the features does not change between the ascending and descending tracks. . . . .	43
3.10	$V_{xz}$ filtered into the Gradiometer MBW during March-April, 2011 for ascending and descending tracks. $V_{xz}$ is the only ultra-sensitive off-diagonal GGT component. Note the effect of the rotational acceleration over Equator which leaks into the gravitational gradient due to the shortcomings of the calibration procedure that should be removed. . . . .	44
3.11	$V_{xy}$ filtered into the Gradiometer MBW during March-April, 2011 for ascending and descending tracks. $V_{xy}$ is derived from less-sensitive measurements. Note the signature over Equator and high noise level that obliterates any useful information. . . . .	44
3.12	$V_{yz}$ filtered into the Gradiometer MBW during March-April, 2011 for ascending and descending tracks. $V_{yz}$ is derived from less-sensitive measurements. Note the high noise level that obliterates any useful information. . . . .	44
3.13	$V_{yy}$ filtered into the Gradiometer MBW (0.1-0.005 Hz) during March-April, 2011 for ascending tracks. Note the small bumps over polar areas indicated by the yellow arrows. . . . .	45

3.14 The differences between the EGG measured  $V_{xx}$  and the ITSG-Grace2014k model computed  $V_{xx}$  are shown for the EGG MBW (10-200s) during March-April, 2011. The differences along the ascending tracks are shown in left panel, whereas the differences along the descending tracks are shown in right panel. There are no considerable differences appear in  $V_{xx}$ . . . . . 48

3.15 The differences between the EGG measured  $V_{yy}$  and the ITSG-Grace2014k model computed  $V_{yy}$  are shown for the EGG MBW (10-200s) during March-April, 2011 in the left and right panels of the figure for ascending and descending tracks, respectively. Note the very distinctive differences over geomagnetic poles which hints the error coming from EGG retrieved  $V_{yy}$ . . . 48

3.16 The differences between the EGG measured  $V_{zz}$  and the ITSG-Grace2014k model computed  $V_{zz}$  are shown for the EGG MBW (10-200s) during March-April, 2011 in the left and right panels of the figure for ascending and descending tracks, respectively. No considerable differences appear in the polar regions. . . . . 48

3.17 The differences between the EGG measured  $V_{xx}$  and the ITSG-Grace2014k model computed  $V_{xx}$  are shown for the bandwidth of [180-300]s during March-April, 2011. The differences along the ascending tracks are shown in left panel, whereas the differences along the descending tracks are shown in right panel. There are no considerable differences appear in  $V_{xx}$ . . . . . 49

3.18 The differences between the EGG measured  $V_{yy}$  and the ITSG-Grace2014k model computed  $V_{yy}$  are shown for the bandwidth of [180-300]s during March-April, 2011 in the left and right panels of the figure for ascending and descending tracks, respectively. Note the very distinctive differences over geomagnetic poles which hints the error coming from EGG retrieved  $V_{yy}$ . Also note the differences wrt Figure 3.15. . . . . 49

3.19 The differences between the EGG measured  $V_{zz}$  and the ITSG-Grace2014k model computed  $V_{zz}$  are shown for the bandwidth of [180-300]s during March-April, 2011 in the left and right panels of the figure for ascending and descending tracks, respectively. Some signatures appear over the Equator. . . . . 49

3.20 Trace along the ascending tracks filtered into the Gradiometer MBW and geolocated over the Polar regions during March-April, 2011. Note the disturbances visible around the geomagnetic poles and larger scale variations in the North Pole. . . . . 51

3.21 Trace along the descending tracks filtered into the Gradiometer MBW and geolocated over the Polar regions during March-April, 2011. Note the reduced disturbances around the geomagnetic poles in the North compared to the ascending tracks. Disturbances over the South Pole almost vanish. . . . . 51

3.22	Trace filtered into the Gradiometer MBW (10-200 s). The 954 tracks are plotted wrt latitude along the tracks. Note the disturbances visible around the high latitudes where there are more variabilities in the ascending tracks (upper panel). . . . .	52
3.23	Trace filtered into 180-300 s interval where the variations show their characteristics the most. The 953 tracks are plotted wrt latitude along the tracks. One track is detected as outlier. Note the higher level of variations in the ascending tracks (upper panel). Note the different characteristics of the trace along ascending and descending tracks. . . . .	53
3.24	Yaw angle between the LORF and GRF along ascending and descending tracks filtered into the GOCE MBW. Note that the larger attitude control corresponds to the regions over the magnetic poles which has an effect on the computation of $V_{yy}$ . . . . .	57
3.25	Pitch angle between the LORF and GRF along ascending and descending tracks filtered into the GOCE MBW. Note the larger variations over the Equator. . . . .	57
3.26	Roll angle between the LORF and GRF along ascending and descending tracks filtered into the GOCE MBW. Note the larger variations over the Equator. . . . .	57
4.1	Typical profiles of neutral atmospheric temperature and ionospheric plasma density for the various layers of the atmosphere, image credit: Kelley [2009]. . . . .	60
4.2	A sketch of the magnetosphere retrieved from <a href="http://geomag.org/info/magnetosphere.html">http://geomag.org/info/magnetosphere.html</a> based on Kivelson and Russell [1995]. . . . .	62
4.3	ACE payload consists of nine science instruments and positioned at about 1.5 million kilometres from the Earth, image credit: Caltech. . . . .	64
4.4	L1 Lagrange Point and other Lagrange Points. $B_x$ , $B_y$ , and $B_z$ shows the Interplanetary Magnetic Field Component directions in the GSE Coordinate System (adopted from wikipedia). . . . .	65
4.5	Trace and IEF are filtered into [120-300]s interval for 2-month period (March-April, 2011). Note the agreement of burst groups in both time series. Refer to Figure 4.8 for original IEF. . . . .	66
4.6	IMF components in GSE for 2-month period (March-April, 2011). . . . .	69
4.7	IMF components in GRF for 2-month period (March-April, 2011). . . . .	69
4.8	Magnetic indices are used to understand the cause of the disturbances. $Kp$ and PCN indices are derived from terrestrial measurements, whereas IEF, $B_z$ -GSE and $V_y$ are observed by ACE and WIND spacecraft. Note the storm periods cause higher variations as indicated in the red rectangles. . . . .	71
4.9	CARISMA array is shown by black colour, whereas the stations selected for our investigations are shown by red squares. . . . .	73

4.10	East-west components of the magnetic field measured at the four CARISMA stations along the Churchill line. . . . .	74
4.11	Sketch of spherical elementary current systems (SECS). The equivalent currents are developed based on divergence free elementary system that is depicted on the right-hand side (taken from Amm et al. [2002]). . . . .	76
4.12	Magnetometers used in the development of EICS and SECS (left panel) and Grid EICS and SECS (right panel) that the EICS computations are performed at as given in Weygand et al. [2011]. Big dots indicate where the SECS amplitudes are calculated, whereas the smaller dots show the location where the EICS are calculated. . . . .	79
4.13	Derivatives of EICS and SECS series along GOCE ascending tracks similar to 3.23. . . . .	81
4.14	Equivalent Ionospheric Currents and Spherical Elementary Current Amplitudes for one ground track (see also Figure 4.15) on March 11th, 2011. Note that this is an extreme case that GOCE experienced. . . . .	82
4.15	Equivalent Ionospheric Currents at 00:24:00 on March 11th, 2011. Note that this is an extreme case that GOCE experienced. Note the strong east-west equivalent current at satellite's position. . . . .	82
4.16	Spherical Elementary Current Amplitudes at 00:24:00 on March 11th, 2011. Note that this is an extreme case that GOCE experienced. Note the significant negative to positive variation at the satellite's position. . . . .	83
4.17	Another example of Equivalent Ionospheric Currents and Spherical Elementary Current Amplitudes that are measured at 22:55:30 on March 10th, 2011. Strong east-west horizontal and downward and upward vertical currents affect the satellite measurements along its orbit. . . . .	84
4.18	Time series of CM and DM accelerations, and Trace and Poynting vector along the satellite track scaled to Trace. a) The measurements of 22:49:00-22:59:00 UTC on March 10th. b) The measurements of 22:39:00-22:50:00 UTC on April 2nd, 2011. Note the simultaneous behaviour of the series with some delay. . . . .	86
5.1	Electric potential for quiet (left panel) and stormy (right panel) time for March 10th, 23:00:00 UTC, 2011 are displayed. Notice the enhancement over Northern Canada and Southern Greenland during storm period. The ascending and descending tracks are displayed by black and magenta coloured lines and correspond to approximately 6:00 pm and 6:00 am local time, respectively. The satellite crosses over a negative electric potential during evening time and a positive electric potential region during morning time. . . . .	91

5.2	Electric potential for quiet (left panel) and stormy (right panel) time for March 11th, 18:20:00 UTC, 2011. Notice the enhancement over Arctic and Greenland during storm period (right panel). The ascending and descending tracks are displayed by black and magenta colours and correspond to approximately 6:00 pm and 6:00 am local time, respectively. . . . .	91
5.3	Neutral winds for quiet (left panel) and stormy (right panel) time for March 10th, 23:00:00 UTC, 2011 are displayed. Neutral winds during stormy period show circular movements over the magnetic pole and some enhancements and direction changes are observed in other regions (e.g. over Alaska). . . . .	93
5.4	Neutral winds for quiet (left panel) and stormy (right panel) time for March 11th, 18:20:00 UTC, 2011 are displayed. Neutral wind components are enhanced and change directions and move from east to west. . . . .	93
5.5	Electric potential and neutral winds at 06:20:00 UTC, $Kp = 4$ . . . . .	95
5.6	Electric potential and neutral winds at 08:00:00 UTC, $Kp = 4$ . . . . .	95
5.7	Electric potential and neutral winds at 11:09:00 UTC, $Kp = 2$ . . . . .	95
5.8	Electric potential and neutral winds at 19:40:00 UTC, $Kp = 6$ . . . . .	96
5.9	Electric potential and neutral winds at 21:20:00 UTC, $Kp = 6$ . . . . .	96
5.10	Electric potential and neutral winds at 22:40:00 UTC, $Kp = 6$ . . . . .	96
5.11	Cross-track neutral wind at GRF, differentiated electric potential are compared with Trace and cross track CM accelerations along the satellite ascending tracks at 09:20:00 and 23:00 on March 11th. . . . .	99
5.12	Cross-track neutral wind at GRF, differentiated electric potential are compared with Trace and cross track CM accelerations along the satellite descending track at 09:20:00 and 23:00 on March 11th. . . . .	99
6.1	The time-frequency boxes of wavelet basis define a tiling of the time-frequency plane (taken from Mallat [1998]). . . . .	104
6.2	The 8th derivative of a Gauss Wavelet is represented. Note the real part and the imaginary parts complement each other. . . . .	106
6.3	The two commonly observed disturbance signatures in trace. The signature is not unique for all the cases and shows variations depending on the non-gravitational forces present in the satellite environment. . . . .	106

6.4	Case 1: CWT analyses of trace and cross-track Poynting vector component from 22:49:00 to 22:59:00 UTC on March 10th. Note that this example represents a case when intense ionospheric dynamics occur and the signal variation in both series is highly coherent with slight differences in the frequency content. . . . .	107
6.5	Case 2: CWT analyses of trace and cross-track Poynting vector component from 22:39:00 to 22:50:00 UTC on April 2nd, 2011. Note that the similarities of the peaks and differences measured in the frequency content between the trace and Poynting vector series. . . . .	108
6.6	Coherency analyses of the trace and cross-track Poynting vector component measured from 22:49:00 to 22:59:00 UTC on March 10th, 2011. The arrows superimposed indicate the phase angle between the two time series. Note the phase angle about $22^\circ$ within the scales of 8-16 indicated by the rectangle. . . . .	110
6.7	Coherency analyses of the trace and cross-track Poynting vector component measured from 22:39:00 to 22:50:00 UTC on April 2nd, 2011. The arrows superimposed indicate the phase angle between the two time series. Note the phase delay is between $45^\circ$ and $90^\circ$ which means that the Poynting vector leads the trace by $45^\circ$ - $90^\circ$ in almost all the scales. . . . .	111
7.1	Representation of a dynamic system. The input (impulse) of the system is represented by $u(t)$ , whereas the output (response) of the system is represented by $y(t)$ . . . . .	114
7.2	Dynamic System identification via the box-concept. The black-box concept is used when there is no prior knowledge available on the dynamic system. If there is any prior knowledge (physical properties) available, the grey-box concept, which takes into account these parameters, can be used. . . . .	115
7.3	Input-output dynamic system representation for black-box model determination. Estimation data are used to estimate model parameters based on different model structures. Each model structure trial is validated by the validation data. Autocorrelation and cross correlation test applied to residuals. If the test results are within the confidence level, then the model can be accepted. If the results are not within the confidence level, the model needs to be revised by adjusting its parameters. (adopted from Lennart [1999]). . . . .	117
7.4	Input-output dynamic system representation. Input signal consists of different sources, such as ionospheric dynamics and errors due to calibration and instruments, as well as data processing. Output of the dynamic system is the trace and CM acceleration. . . . .	119

7.5	Input-output modified dynamic system representation that assumes the ionospheric dynamics as the only source for the disturbances observed in trace. The other error sources are assumed as not measured. The original $v(t)$ concept is adopted from Lennart [1999]. . . . .	119
7.6	ARX Model Structure. The basic input, output, and error configuration is depicted. B and A are polynomials in the delay operator. The white noise is represented by e. . . . .	123
7.7	Example of input and output series along an ascending track. The black colour shows all the measurements along the track, whereas the red colour represents the segment that is used in the model development due to high signal to noise ratio. The extraction of the segment is performed manually. . . . .	125
7.8	Step response of the transfer functions. The left panel shows the transfer functions computed based on continuous input and output signal assumption. The right panel shows the transfer functions that are computed based on ARX model structure. . . . .	128
7.9	Frequency response of the transfer functions. The left panel shows the frequency response of the system based on continuous input and output signal assumption. The right panel shows the frequency response of the transfer functions that are computed based on ARX model structure.	128
7.10	Trace measured along an ascending track over North America and simulated output values computed based on the continuous transfer functions ( $tf_{21}, tf_{31}, tf_{32}$ ). The cyan colour depicts the original signal, whereas the black line shows the simulated output via $tf_{21}$ , and green line and red line shows the estimated outputs of $tf_{31}$ and $tf_{32}$ , respectively. . . . .	129
7.11	Trace measured along an ascending track over North America and simulated output values computed based on the ARX polynomial functions (arx221, arx321, arx625). The cyan colour depicts the original signal, whereas the black line shows the simulated output via arx221, and green line and red line shows the estimated outputs of arx625 and arx321, respectively. . . . .	129
7.12	Autocorrelation of the residuals are displayed in the upper panel. Higher values exceeding the confidence intervals are observed over the samples close to zero which indicates that the model is not good enough for this application and estimation of the noise components is not adequate. Cross-correlation results between the input and the residuals which are within the confidence interval are shown in the lower panel. The green colour represents $tf_{31}$ , whereas the red and black colours represent $tf_{32}$ and $tf_{21}$ , respectively. . . . .	130

7.13	Autocorrelation of the residuals are displayed in the upper panel. Higher values exceeding the confidence intervals are observed over the samples close to zero for lower polynomial models, whereas they are reduced in a higher order model arx625. Cross-correlation results between the input and the residuals which are within the confidence interval are shown in the lower panel. The green colour represents the arx625, whereas the black and red colour represent the arx221 and arx321, respectively. . . . .	130
8.1	Original trace and trace obtained from filtered series are displayed for the period of March 9-11, 2011. The original trace is the summation of the calibrated diagonal gravity gradients whereas the filtered trace is the summation of the filtered diagonal gravity gradients measured by GOCE EGG. The original trace shows a linear trend which is related to the instrumental drift. . . . .	133
8.2	CM accelerations filtered into the frequency band of [180-300]s. The cross-track CM acceleration shows larger variations compared to the other two directions. Moreover, CM measurements in the radial direction show considerable variation which may enhance the effect of the external sources on the EGG measurements. . . . .	135
8.3	Filtered GGT components and trace. The $V_{yy}$ component and trace are shown in red and black solid lines, respectively, whereas $V_{xx}$ and $V_{zz}$ components are shown by blue and green dashed lines. Note that the larger variations in trace coincide with the larger variations of $V_{yy}$ . . . . .	135
8.4	The scaled cross-track CM accelerations and Poynting vector component, scaled radial CM accelerations, trace and cross-track gradient are shown. Note the time interval when the Poynting vector component varies from positive to negative, and the trace shows higher noise level. . . . .	136
8.5	Five subsequent tracks investigated are shown. Note that the corrections will be effective over the grid area only. . . . .	137
8.6	The five tracks investigated: The blue track that passes over Greenland shows a signature of the disturbance starting from latitude 60° North. The following tracks are 15 degrees apart to the West from the previous track and experience similar signatures over similar regions with slight phase differences. . . . .	138
8.7	A closer look at the five tracks. Note the similar characteristics of the signatures shifting with the shifting tracks in space domain. . . . .	138

8.8	The blue track crosses over Greenland; therefore, it is only available for a short period of time since the SEC grid extension does not reach to the North Atlantic Ocean and it is limited over Greenland. The subsequent tracks correspond to observations of electromagnetic energy flow over Canada and show remarkable variations over latitudes between 50° and 70° North. . . .	139
8.9	A closer look at the five tracks. Note the positive-to-negative variations between the latitudes 56° and 66° North. . . . .	139
8.10	The graphical representation of the arx625 model. Note the 50 seconds of delay between the red full circles filled in the input and output signals which indicates the delay ( $\delta = nk$ ) of the system response. . . . .	141
8.11	A closer look at the five subsequent tracks over a geomagnetically active period. Now the trace is corrected (except the blue track) and within the noise level of the instrument. . . . .	142
8.12	Trace obtained from filtered diagonal gravitational gradients is downsampled in 10 second interval during March-April, 2011. Note the strong signatures over high latitudes and auroral oval. . . . .	143
8.13	Corrected trace obtained by using model arx625 during March-April, 2011 . Note the improvement over Canada and western Greenland. . . . .	144

## List of Abbreviations

ACE	Advanced Composition Explorer
ARF	Accelerometer Reference Frame
ARX	Auto-regressive Exogeneous
CARISMA	Canadian Array for Realtime Investigations of Magnetic Activity
CHAMP	CHALLENGING Minisatellite Payload
C-IAM	Canadian Ionosphere and Atmosphere Model
CM	Common-mode
COM	Centre of Mass
COP	Centre of Pressure
CWT	Continuous Wavelet Transform
DFAC	Drag Free Attitude Control
DM	Differential-mode
GGT	Gravity Gradient Tensor
GOCE	Gravity-field and steady-state Ocean Circulation Explorer
GPS	Global Positioning System
GRACE	Gravity Recovery and Climate Experiment
GRF	Gradiometer Reference Frame
GSE	Geocentric Solar Ecliptic
EFRF	Earth-Fixed Reference Frame
EGG	Electrostatic Gravity Gradiometer
EGM2008	Earth Geopotential Model of 2008
EICS	Equivalent Ionospheric Currents
EOQ	Earth Orientation Quaternions
ESA	European Space Agency
ESOC	European Space Operations Centre
ESRIN	ESA Centre for Earth Observation
IAQ	Inertial Attitude Quaternions
ICM	Inverse Calibration Matrices
IEF	Interplanetary Electric Field
IMF	Interplanetary Magnetic Field
IPA	Ion Propulsion Assembly
IRF	Inertial Reference Frame

ITRF	International Terrestrial Reference Frame	
LEO	Low Earth Orbiter	
LORF	Local Orbital Reference Frame	
LRR	Laser Retro Reflector	
MBW	Gradiometer Measurement Bandwidth	
MTQ	Magnetorquer	
MTR	Magnetometer	ll
OAGRF	Origin of Accelerometer Reference Frame	
SECS	Spherical Elementary Current System	
SLR	Satellite Laser Ranging	
SSTI	Satellite-to-Satellite Tracking	
STR	Star tracker	
TUM	Technical University of Munich	

## List of Symbols

$a_{c,nm,i}$	Common-mode acceleration retrieved from nm accelerometer pair in the $i$ direction
$a_{d,nm,i}$	Differential-mode acceleration retrieved from nm accelerometer pair in the $i$ direction
$\mathbf{a}_i$	Acceleration measured by any of the six accelerometers
$A(q)$	Polynomial in the shift operator
$\mathbf{b}_i$	Measurement bias vector
$B_x(GSE)$	Interplanetary Magnetic Field component in GSE towards the Sun
$B_y(GSE)$	Interplanetary Magnetic Field component in GSE towards dusk
$B_z(GSE)$	Interplanetary Magnetic Field $z$ component in GSE parallel to the Earth's spin direction
$\mathbf{d}$	Non-gravitational acceleration
$\delta$	Impulse-response system delay
$\delta\mathbf{B}$	Vector of geomagnetic field wrt the main geomagnetic field
$e'_\psi, e'_\theta$	Unit base vectors in the spherical coordinate system
$[e'_s, e'_T, e'_w]$	Unit base vectors in LORF' wrt IRF
$\mathbf{E}$	Electric field vector
$g(\tau)$	Impulse-response function
$g(x)$	Gaussian function in time domain
$G(f)$	Gaussian function in frequency domain
$I$	Scaling factors
$I_{o,df}$	Divergence-free elementary current amplitude
$I_{o,cf}$	Curl-free elementary current amplitude
$J_{df}$	Divergence-free current system
$J_{cf}$	Curl-free current system
$\mathbf{K}^2$	Quadratic factor
$\mathbf{K}_i$	Accelerometer scale factor matrix
$Kp$	Standardized K index (Geomagnetic storm index)
$M^{-ij}$	Inverse calibration matrix
$\mathbf{n}$	Accelerometer measurement noise
$\mathbf{n}_i$	Measurement noise vector
$\omega$	Angular rate
$\dot{\omega}$	Angular acceleration
$P$	Numerator polynomial
$q$	Quaternion

ii

$q^{-1}$	Shift operator
$Q$	Denominator polynomial
$r_i$	Distance between the centre of the mass of the satellite and the centre of the accelerometer $i$
$R_{3 \times 3}$	3 by 3 rotation matrix
$\mathbf{R}_i$	Accelerometer misalignment matrix
$\sigma_x$	Standard deviation in time domain
$\sigma_f$	Standard deviation in frequency domain
$\mathbf{S}$	Poynting vector
$\mathbf{S}_i$	Accelerometer axes coupling matrix
$T$	The magnetic field effect of a unit SECS each SECS grid at each terrestrial station
$tf_{nm}$	Transfer function ( $n = \text{number of poles}, m = \text{number of zeros}$ )
$V$	Gravity potential
$\dot{\mathbf{\Omega}}$	Angular acceleration tensor
$\mathbf{\Omega}^2$	Angular velocity tensor
$V_y$	Plasma flow velocity
$V_{xx}$	Gravity gradient measured along the satellite track
$V_{yy}$	Gravity gradient measured cross satellite track
$V_{zz}$	Gravity gradient measured in radial direction
$V_{xy}$	Gravity gradient measured via transversal acceleration
$V_{xz}$	Gravity gradient measured via transversal acceleration
$V_{yz}$	Gravity gradient measured via transversal acceleration
$X(f)$	Input signal in frequency domain
$x(t)$	Input signal in time domain
$y(t)$	Output signal
$Z$	Measurement at different terrestrial magnetometer stations
$\mu_0$	Permeability

11



# Introduction and Background

## 1.1 Background

---

The Gravity field and steady-state Ocean Circulation Explorer (GOCE) which was the first mission to employ the concept of “gradiometry” in space completed its mission in November 2013. GOCE was specifically designed to achieve the determination of the Earth’s static gravity field with an accuracy of one centimetre in geoid height and 1 mGal in gravity anomalies both to 100 km spatial resolution [Rummel et al., 2004, Drinkwater et al., 2006].

Since the launch of GOCE mission in March, 2009, there have been very interesting and promising research topics addressed under the mission applications. GOCE has provided an enormous amount of useful information for geodesy, solid Earth, and oceanography [Bouman et al., 2015, Floberghagen et al., 2011, Fuchs et al., 2013, Knudsen et al., 2011]. Moreover, literature reveals that the GOCE measurements and data products can be used to retrieve/evaluate thermospheric air density and wind models [Bruinsma et al., 2014, Doornbos et al., 2013], whereas more useful information on space weather can be obtained when combined with other measurements and models (e.g., ESA’s Cluster II measurements, NCAR’s TIE-GCM). Therefore, GOCE mission has exceeded its design goals and expanded the application areas of accelerometer measurements in space.

Based on the gradiometer principle, one can retrieve variations of linear as well as angular accelerations of the satellite from the linear and transversal accelerations, respectively, measured between the on-board accelerometer pairs. No doubt, the GOCE gradiometer is one of the most sensitive instruments used in measuring accelerations in space [Drinkwater et al., 2006, Knudsen et al., 2011, Rummel et al., 2011, Stummer

et al., 2012]; however, the mission (see Figure 1.1) was the very first of its kind because of highly accurate gradiometer measurements and it is still under investigation as to how best process the GOCE measurements.

During the 5th GOCE International User Workshop [Benveniste and Floberghagen, 2015], the main results of the mission, discussions, and recommendations were summarized by scientists from different disciplines worldwide. It has been confirmed that the mission was very successful. Moreover, it is claimed that there is still great potential to improve the gradiometer data analysis and the calibration of the cross-track component of the Gravitational Gradient Tensor (GGT) so that the gradient (cross-track) can be improved near the geomagnetic poles, a subject that is directly related to this research.

From our analysis of the gradients and GGT trace as well as from literature review, we understand that the GOCE gradiometer measurements were affected by some unknown non-gravitational accelerations around the geomagnetic poles [Siemes et al., 2012, Stummer et al., 2012]. These effects appear as disturbances of high to low frequency (e.g., signal that lasts 1-5 minutes) over the geomagnetic poles, leaking into the lower frequencies of the gradiometer measurement bandwidth (e.g., 0.016-0.005 Hz) and into the gravitational gradients.

There might be several reasons behind these signatures, such as thermospheric neutral cross-wind effects over the polar regions [Lühr et al., 2007, Doornbos et al., 2013], instrumental imperfections, shortcomings of the attitude control based on magnetic torquers only, and inadequacy of the data processing methods, such as the calibration of the gradiometer measurements [Bouman et al., 2011, Peterseim et al., 2011, Stummer et al., 2011, Siemes et al., 2012, Siemes, 2012].

Since the attitude control was performed by magnetic torquers, it was coupled with the magnetic field of the Earth and possibly with other external magnetic field sources. The magnetic torquers are only able to control the attitude about the perpendicular direction to the magnetic field lines and cannot act in the parallel direction to them. Therefore, there is little or no control about the  $Z$ -axis (yaw angle) around the geomagnetic poles where the magnetic field lines are vertical to the Earth's surface and almost parallel to the  $Z$ -axis of the satellite body frame [Sechi et al., 2006, Siemes, 2012]. Moreover, the response of the magnetic torquers may be subject to a delay.

The attitude of the satellite was measured by the star trackers and the gradiometer in terms of orientation angles and angular accelerations, respectively, and it was subtracted from the differential-mode accelerations. Therefore, the effect of the residual orientation angle should not have been propagated further into the GGT if computed correctly. In this research, we assume that the coupling of the torquers with the geomagnetic field is not the cause of the disturbances observed over the geomagnetic poles. Also, we understand that the

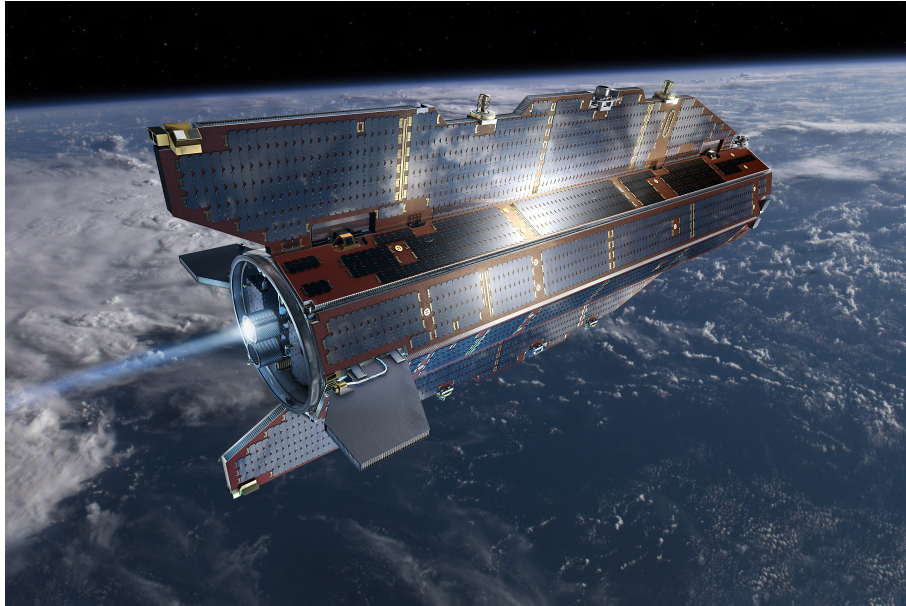


Figure 1.1: Artistic image of GOCE, image credit: ESA.

mission payload was magnetically shielded (Floberghagen R. and Frommkecht B., pers. comm., 2014) against any other external magnetic field effects. Therefore, neither magnetic field coupling with the instruments nor coupling between the Electrostatic Gravity Gradiometer (EGG) measurements and the space environment is expected.

The GOCE data processing methodology has been improved and upgraded since the pre-launch period when only simulated data were used [Stummer et al., 2011]. However, even the improved data still exhibit the effects of unknown phenomena. Causes of these disturbances are not very well understood but speculated to be due to the cross-wind over the geomagnetic poles [Stummer et al., 2011, Siemes et al., 2012]. By examining other Level 1b data<sup>1</sup>, we demonstrate (Section 3.4.3, Figures 3.24, 3.25, and 3.26) that the GOCE attitude angles show similar deviations when filtered into appropriate bandwidth (e.g., Gradiometer Measurement Band). Also, GPS L2 signals experienced data loss due to scintillation over the same regions [Van den IJssel et al., 2011]. Even though the source behind these disturbances observed in the gravitational gradients and GPS signal loss could be different, it indicates the complexity of the problem over the high latitudes and geomagnetic poles on the satellite measurements. Therefore, other Level 1b data (internal data) were affected

---

<sup>1</sup>Level 1b data: The Level 1b processing is carried out by the Instrument Processing Facility (IPF). L1b products include gravity gradients, frame transformation matrices, linear accelerations and angular rates and accelerations, satellite-to-satellite measurements and derived positions and reconstructed satellite orbits in Earth-Fixed Reference Frame, attitude and orbit data (position, velocity and time) [ESA, 2006].

from the ionospheric dynamics (space environment) and we can safely say that neither the magnetic shielding nor the data processing methods nor any erratic behaviour of the accelerometers were the causes of these disturbances. We can conclude that the spacecraft itself was affected by intense ionospheric dynamics [Ince and Pagiatakis, 2016]. Consequently, we are motivated to use external datasets to understand the satellite environment and its effect on the GOCE measurements.

In summary, the causes of these disturbances need to be investigated in terms of:

- (a) Extreme geomagnetic field disturbance events and dynamics of the satellite environment over the geomagnetic poles.
- (b) Instrumental imperfections, inadequacy and shortcomings of the data processing methods and/or the in-flight calibration of the gradiometer.

In this research, we investigate the first cause listed above by examining the satellite environment, effects of the space weather and ionospheric dynamics on the GOCE measurements by using data external to GOCE. These datasets are interplanetary magnetic field components, interplanetary electric field, plasma velocity, equivalent ionospheric currents that are derived from terrestrial magnetometer measurements, and finally electric potential, neutral wind, neutral density and temperature profile simulations. We perform our investigations along many satellite tracks and examine the correlations between the disturbances measured by GOCE EGG and external datasets. We aim to eliminate/reduce the disturbances observed over the geomagnetic poles based on input-output response analysis.

The second possible cause of the disturbances (b) has been investigated by Stummer et al. [2012] and Siemes et al. [2012] which supports the hypothesis that the disturbances are due to the cross wind effect over polar regions and imperfect calibration and details can be found as referenced. We expand our investigation on the first cause and the outcomes of this research are products of cross-cutting disciplines which are not only useful for geodesy but also for ionosphere-magnetosphere coupling studies, space physics and space weather research. This research demonstrates the importance of accelerometer measurements not only in gravity field modelling but also for future use of them in understanding ionospheric dynamics and modelling. In many cases, the reader will find connections between two different disciplines and ideas for bridging them via different measurements and data processing techniques presented in this thesis.

## 1.2 Research Objectives

---

The recent advancements in space geodetic observing systems require significant improvements in the data processing algorithms and methodologies to meet the needs of applications. Pre-launch simulations of GOCE mission showed that the accelerometers would have the ability to improve the global gravity field models (e.g., geoid) in the medium wavelength (100-400 km). However, the simulations did not take into account possible variations of the conditions that the satellite would be exposed to in the real flight environment. Accordingly, the data processing methodologies were upgraded/revisited based on real measurements.

GOCE data processing was upgraded in 2011 by improving the derivation of the angular accelerations from the star trackers and gradiometer measurements [Stummer et al., 2011]. The advancement came from the combination of the star tracker and gradiometer measurements in the frequency domain based on an optimum cut-off frequency. Moreover, measurements from the three star trackers mounted on-board were also combined together in order to take advantage of the measurements of each star tracker when such measurements are available simultaneously [Stummer et al., 2011].

The gravity field models computed by using the datasets derived from the upgraded measurement processing techniques showed that GOCE had exceeded its designed goals. However, there are still some disturbances present in the cross-track gravitational gradient measurements. These disturbances appear over the geomagnetic poles<sup>2</sup> in form of spurious signals along the satellite tracks. It is known from the literature [Peterseim et al., 2011, Stummer et al., 2011, Siemes, 2012] and shown in Chapter 3 that the cross-track gravitational gradient  $V_{yy}$  component shows higher noise level and unknown abrupt signal variations over the geomagnetic poles than the cross-track gravitational gradient at the satellite altitude computed from ITSG-Grace2014k [Mayer-Gürr et al., 2014] and EGM2008 [Pavlis et al., 2012] gravitational field models. Therefore, the literature also confirms that there are still inherent problems within the GOCE data processing methodologies.

In this research, we investigate these disturbances over the geomagnetic poles to further understand their causes. We investigate the relationship between the ionospheric dynamics and the disturbances observed in GOCE gradiometer measurements using response analysis. The response analysis is simply used to establish the response between the source of the disturbance and the effect.

---

<sup>2</sup>The intersections of the Earth's surface and the axis of a bar magnet that is hypothetically placed at the centre of the Earth by which we approximate geomagnetic field are called the geomagnetic poles (dipole poles). Each hemisphere has such a pole and these poles are called as "the geomagnetic north pole" and "the geomagnetic south pole. On the other hand, the magnetic poles are the points at which magnetic needles become vertical" (<http://wdc.kugi.kyoto-u.ac.jp/poles/polesexp.html>). Throughout this thesis we use these two terms interchangeably.

*Questions leading to this research can be summarized as follows:*

1. What are the causes of these disturbances and when do they occur?
2. What is the temporal and spatial resolution of the disturbances observed in EGG measurements?
3. How does the solar wind contribute to the ionospheric dynamics from medium to large scale thermospheric variations?
4. What is the impact of the flow of the electromagnetic energy (Poynting flux) on the cross winds and GOCE EGG measurements?
5. Is it possible to model these disturbances and improve the quality of the GOCE gravitational gradients?

*Answers to the above questions that constitute original and significant contributions of this dissertation are briefly as follows:*

1. Intense ionospheric dynamics driven by the Poynting flux increase the satellite drag environment and cause disturbances to the EGG measurements. The disturbances appear over the geomagnetic poles during geomagnetically active days.
2. The signatures of the disturbances do not have a specific periodicity. The disturbances last for few minutes over high latitude regions.
3. Solar wind driven interplanetary magnetic field components interact with the Earth's magnetic field over the polar regions, which create unstable and highly variable environment.
4. The effect of the Poynting flux on the EGG measurements is not linear. In certain circumstances, the Poynting flux in the form of thermospheric heating or bulk flow introduces different effects on the EGG measurements.
5. It is possible to model these disturbances by using datasets external to the satellite system. We performed the modelling using the Autoregressive Exogenous Model approach in developing the relationship between the Poynting flux and EGG disturbances.

## 1.3 Outline of the Thesis

---

This dissertation is dedicated to understanding the causes of the disturbances measured by GOCE accelerometers. It was the first time in the history of space missions that a gradiometer was used to measure gravitational gradients from the space. Therefore, understanding the various measurements and appropriate data processing methodologies tailored to the quality of the data are of importance. We therefore perform trans-disciplinary research to further improve the quality of the data by reducing the systematic errors that appear over the geomagnetic poles. The contribution of external datasets in the modelling of systematic errors is examined in spatial and frequency domains and treated in detail throughout this dissertation.

We introduce the GOCE mission and payload in Chapter 2. The GOCE mission had many different instruments and sensors on-board that performed a number of heterogeneous measurements. In this chapter, we introduce the instruments and explain which measurements are used throughout this research. The gravitational gradients that are derived from the differential-mode accelerations are given and the in-flight calibration procedure is summarized.

In Chapter 3, besides providing an extensive literature review, we focus on the raw gradiometer measurements and describe the preprocessing step. The transformations of the various measurements from their reference frame to a common one (usually the Gradiometer Reference Frame) are given in this chapter. Thus, further investigations on the common-mode accelerations, gravitational gradients, and angular accelerations are given in detail. Moreover, we introduce the inherent problems that are present within Level 1b data and explain the main objective of this research.

In Chapter 4, we explain the basics of ionospheric dynamics, along with the relevant space weather and geomagnetic field measurements. We introduce the external datasets used in this study and the preparation of required time series and examples that provide comparisons of the disturbances measured in EGG gradients to the external measurements representing the satellite environment. It is the first time in GOCE literature that such disturbances are examined rigorously using external datasets.

In Chapter 5, we describe another external dataset used in our comparisons that is simulated by the Canadian Ionosphere and Atmosphere Model. The simulations are used to understand the disturbances over the Northern hemisphere, not only over North America, and also to understand variations of the ionosphere during quiet and stormy periods.

In Chapter 6, we perform data analyses and present correlation analyses by using the Continuous Wavelet Transform and wavelet coherency analysis. Chapter 6 expands the investigations presented in Chapters 3 and

4 and depicts the results in the time and frequency (scale) domains. Our contribution includes the correlation analyses of the space weather proxies and GOCE gradiometer measurements. Moreover, in this chapter, we refer to the causes of these disturbances.

In Chapter 7, we include the response analysis which aims to reduce the effect of these disturbances by using external datasets and develop empirical models over Canada. We describe the fundamentals of different models that are found to be helpful in explaining the relationship between the disturbances observed in GOCE gradients and the ionospheric variations. The correction of the disturbances at the geomagnetic poles is presented in this chapter.

Finally, we present our results and show the improved trace of GGT in Chapter 8 and propose various approaches to improve the quality of the gravitational gradients globally. The discussion and plans for future work are summarized in Chapter 9, which also concludes this dissertation.

# 2

## Satellite Gradiometry

### 2.1 Gravity Missions and GOCE

---

The Gravity field and steady-state Ocean Circulation Explorer (GOCE) mission was launched on March 17th, 2009. GOCE was the first Earth Explorer Core Mission of ESA's Living Planet Programme [Drinkwater et al., 2006, ESA, 2006]. The development and launch of GOCE took about a decade and it has been supporting with the latest advancements in solid Earth, oceanography, ice mass, sea level, and many geodetic applications.

GOCE mission objectives were complementary to those of GRACE (Gravity Recovery and Climate Experiment) [Tapley et al., 2004] and CHAMP (CHALLENGING Minisatellite Payload) [Reigber et al., 2002] missions. Compared to CHAMP and GRACE, GOCE had an Electrostatic Gravity Gradiometer (EGG) on-board which made very sensitive acceleration measurements possible from space. Touboul et al. [2012] indicated that the GOCE accelerometer "sensitivity" was improved by  $10^{-2}$  compared to the GRACE accelerometer. GOCE collected medium to short wavelength gravitational field information with an unprecedented accuracy at an altitude of about 250 km, much lower than CHAMP and GRACE. GOCE was on a sun-synchronous<sup>1</sup> and nearly circular orbit with an inclination angle of  $96.7^\circ$ . Its orbital period was about 90 minutes and covered the entire Earth in about 2 months (979 orbits/61 days) [ESA, 2006]. A summary of the three missions is listed in Table 2.1.

At such low altitude, the non-gravitational forces acting on the satellite increase and development of the on-board instruments and data processing become even more challenging and require novel technologies and methodologies. As given in Floberghagen et al. [2011], these technologies include drag-free-control

---

<sup>1</sup>Sun-synchronous orbit is a geocentric orbit which uses altitude and inclination information such a way to develop an orbit that the satellite would pass over any given point at the same local solar time. By this, the satellite would be exposed to the sunlight constantly which can be useful for different applications ([https://en.wikipedia.org/wiki/Sun-synchronous\\_orbit](https://en.wikipedia.org/wiki/Sun-synchronous_orbit)).

along track, electric propulsion, electrostatic gravity gradiometry, triple-junction GalliumArsenide (GaAs) solar cells and three-dimensional carbon-carbon honeycomb structures with no moving parts, and minimum weights providing extreme mechanical stability for the gradiometer.

Table 2.1: Specifications of the three gravity missions.

Mission	GOCE	GRACE	CHAMP
Launch date	17.03.2009	17.03.2002	15.07.2000
Status	End of mission 10.11.2013	Still in service	End of mission 19.09.2010
Orbit	Sun sync., 96.7°	Near circular, 89°	Near circular, 87°
Altitude	Initial altitude 270 km	485 km	454 km
Objectives	Determination of the static gravity field and geoid with an accuracy of 1mGal and 1cm, respectively both with a spatial resolution better than 100 km wavelength	Gravity field and its temporal variation with a 400 km spatial and monthly temporal resolution	Measurement of gravity and magnetic fields Atmospheric Limb and Ionosphere Sounding
Instrumentation	Six 3-axis accelerometers the gradiometer, GPS/ GLONASS and SLR	3-axis accelerometers GPS and SLR K-band inter-satellite ranging	3-axis accelerometer GPS and SLR
Sensitivity	$10^{-12} m/s^2$	$10^{-10} m/s^2$	$10^{-9} m/s^2$

There are complex steps and procedures involved in GOCE data collection and processing which are performed by different institutes, research centres, and universities. GOCE mission was operated and controlled by the Flight Operations Segment at ESA’s European Space Operations Centre (ESOC) in Darmstadt, Germany. Therefore, the condition, health and control of the mission were the responsibility of this institute. Raw observations were retrieved by the ground stations in Kiruna, northern Sweden and Svalbard. The observations were sent to the Flight Operations Segment and then to the Payload Data Ground Segment which is located at ESA’s European Space Research Institute (ESRIN), in Frascati, Italy.

The Level 1b data products which are used in this study were created by ESRIN, where the last step, the development of Level 2 from Level 1b data, is performed in the High-Level Processing Facility by many different international institutes [Rummel et al., 2004]. More detail on the different level data sets namely, Level 0, Level 1b, and Level 2 can be found in ESA [2006] and Rummel et al. [2010]. The on-board instruments and the corresponding measurements are described in the following section.

GOCE was designed to achieve drag-free conditions at very low altitude. The length of the satellite was 5.26 m and had a launch mass of 1077 kg with a full symmetric configuration about XY-plane. There were many different platforms on-board the mission as the nature of the satellite required the integration of different sensors that are shown in Figure 2.1.

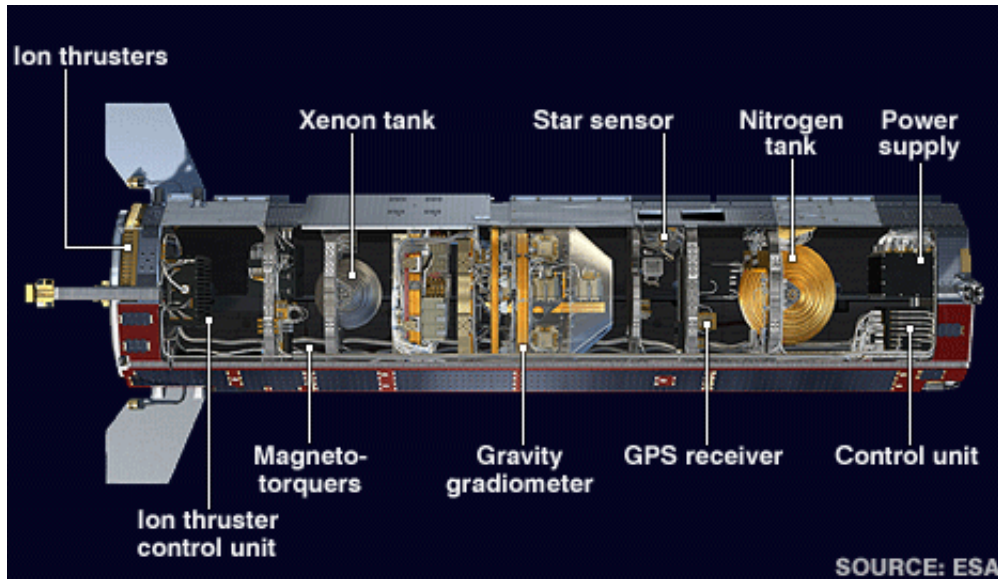


Figure 2.1: GOCE top view, image credit: ESA. Electrostatic Gravity Gradiometer is mounted precisely near the centre of the mass of the spacecraft.

The Drag-Free and Attitude Control (DFAC) System made GOCE mission challenging and unique. GOCE was and still is the first European drag-free satellite at an altitude of 240-280 km. Moreover, it was also the first medium sized Low Earth Orbit (LEO) mission which had a pure magnetically actuated Attitude and Orbit Control System (AOCS) implemented [Sechi et al., 2006, Floberghagen et al., 2011, Stummer et al., 2011].

Having GOCE at a very low Earth orbit required a complex orbit maintenance system that continuously compensated for the air drag along the satellite track and a challenging aerodynamic shape to minimize the drag force. Due to very high accuracy acceleration measurement requirements, no moving parts were implemented on-board and an ultra-high, thermoelastic stability was required to provide a very quiet environment. As detailed in Floberghagen et al. [2011], the following components were designed and implemented.

- Aerodynamic shape of the satellite that minimized the drag along flight direction,
- Fully symmetric configuration about the horizontal centre of the satellite (along the centre of XY plane) in order to adapt the launch date<sup>2</sup>,

---

<sup>2</sup>The symmetric configuration needed so that the satellite can be launched in either prograde or retrograde orbit depending on the launch time.

- The Centre of Pressure (COP) was positioned behind the Centre of Mass (COM) of the satellite to provide passive aerodynamic stability,
- The gradiometer was mounted precisely near the COM of the spacecraft.

### 2.1.1 GOCE Payload

Data processing and development of global gravity field models are as important as the development of the mission, its launch and monitoring. Comprehensive investigations were needed both on the instruments used on-board and ground, communication between the two as well as the methodologies applied in the data processing. In order to measure the Earth's static gravitational field solely, the influence of all other gravitational and non-gravitational sources should be eliminated or measured and compensated. Some of these gravitational and non-gravitational effects include but are not limited to the Earth and ocean tides, relativity effect of other planets, solar radiation pressure, air-drag and albedo [Seeber, 2003].

The measurement of these effects is generally possible by using accelerometers on-board. For CHAMP and GRACE, the accelerometers were mounted at the centre of mass (COM) of the satellite to effectively eliminate rotational accelerations. Due to the free-fall motion of the satellite, the accelerometer which was rigidly mounted at the COM would only measure the non-gravitational accelerations [Hofmann-Wellenhof and Moritz, 2006]. Then, these measurements are used together with orbit perturbation information of the satellite to extract information on the gravitational forces.

In addition to the concept of the previous missions CHAMP and GRACE, the key instrument that made GOCE unique was the Electrostatic Gravity Gradiometer (EGG) which is displayed in Figure 2.1 and detailed in Figure 2.2. The EGG was mounted almost perfectly at the centre of the mass of the satellite and had 3 accelerometer pairs which were placed on three mutually orthogonal axes. These axes defined the Gradiometer Reference Frame (GRF), whose origin was located at the centre of the gradiometer. The three axes were designated as X-axis pointing approximately along-track, Z-axis along the local gravity vector in downward direction and Y-axis perpendicular to the instantaneous orbital plane completing a right-handed coordinate system as shown in Figure 2.3. The distance between the accelerometer couples was about 50 cm and the distance between the centre of mass of the gradiometer and the centre of each individual accelerometer was about 25 cm. This distance between the centre of gradiometer and centre of each accelerometer caused the accelerometers to be influenced by the gravitational forces differently from each other since they were offset from the COM. Moreover, they also experienced rotational accelerations [Frommknecht et al., 2011,

Rummel et al., 2011]. Therefore, the differences of the accelerations retrieved from each accelerometer pair mounted on the same axis were recorded and used in the derivation of the gravitational gradients.

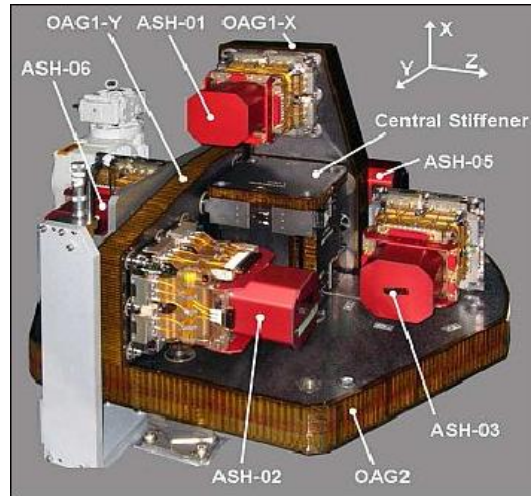


Figure 2.2: GOCE Electrostatic Gravity Gradiometer, image credit: TAS/ONERA. See the accelerometer pairs mounted in X,Y, and Z directions orthogonally.

Apart from the EGG, GOCE had the satellite-to-satellite tracking instrument (SSTI), which consisted of advanced dual-frequency, 12 channel GPS receiver and L-band antenna, 3 star trackers (STR) and a laser retro reflector (LRR) in order to provide a complete dataset with necessary information on the position and orientation of the satellite. A top-down view of GOCE with the instruments installed on-board is presented in Figure 2.1 on page 11.

### 2.1.1.1 Electrostatic Gravity Gradiometer

The Electrostatic Gravity Gradiometer (EGG) was the core instrument of GOCE mission. In order to achieve very high accuracy measurements, a very quiet environment was desired. As mentioned in the previous section, keeping the satellite internally very quiet required the absence of moving parts and an ultra-high thermoelastic stability. Thus, the gradiometer had a separate specially designed thermal control, which was decoupled from the satellite thermal control [Floborghagen et al., 2011].

The EGG consisted of three orthogonal accelerometer pairs that were mounted on an ultra-stable support structure (see Figure 2.2). Each accelerometer had a proof mass that was electrostatically kept levitated in

the centre of the cage (e.g., X1, X2,...,Z2 shown in Figure 2.4). So-called control voltages were applied by eight electrode pairs embedded in the cage. These voltages were proportional to the accelerations sensed by the proof mass and constituted the first input to the data processing chain. The accelerometers were designed to collect reliable and accurate information within the frequency range of 5 – 100 mHz and the accelerations measured were as sensitive as  $10^{-13}$  of the gravity at the Earth surface. Therefore, GOCE accelerometers were specifically designed to be about 100 times more sensitive than the ones mounted on GRACE satellites (see Table 2.1).

The accelerometer pairs were mounted along the three orthogonal axes of the gradiometer frame. The pairs mounted along the X-direction are named as A1 and A4, whereas the pairs mounted along Y- and Z-directions are named as A2 and A5, and A3 and A6, respectively. The distance between a pair (50 cm) could only vary by 1% over a time interval of three minutes which can only be accomplished by using enhanced design technologies [Fehring et al., 2008].

The sensitivity of the accelerometers were not completely verified on the ground due to the complexity of the design. Accordingly, simulation tools were used for high-fidelity performance modelling. Due to the geometry of the proof mass, lower sensitivity was accomplished in the direction of gravity. Therefore, the accelerometers had two ultra-sensitive axes and one less sensitive axis as indicated by solid and dashed lines, respectively in Figure 2.3.

The two proof masses of dimension  $4 \times 4 \times 1$  cm were made of a bulk platinum-rhodium alloy. The proof masses of any pair of accelerometers experienced the influence of the Earth's gravitational field and its spatial variation along the satellite path. The differences between the behaviour of the two proof masses of the same gradiometer axis can be defined as the differential acceleration between the pair. Therefore, this differential observation technique is used in this research to retrieve gravitational gradients along the satellite track.

Accelerations measured along any in-line direction between each pair are the most important measurements; therefore, measured by the ultra-sensitive axes. The ultra-sensitive axes and the instrument design were modified to maximize the sensitivity of the determination of the in-line and angular accelerations about the cross-track direction of the satellite [Floberghagen et al., 2011]. The ultra and less sensitive axes of each accelerometer pair and their sensitivity are summarized in Table 2.2.

According to this configuration, accelerations in along-track direction (X-axis) can be retrieved from any of the three of the accelerometer pairs, whereas accelerations along Y- and Z-axes can only be retrieved from the A25 and A36 accelerometer pairs, respectively, since the ultra-sensitive axes are configured this way.

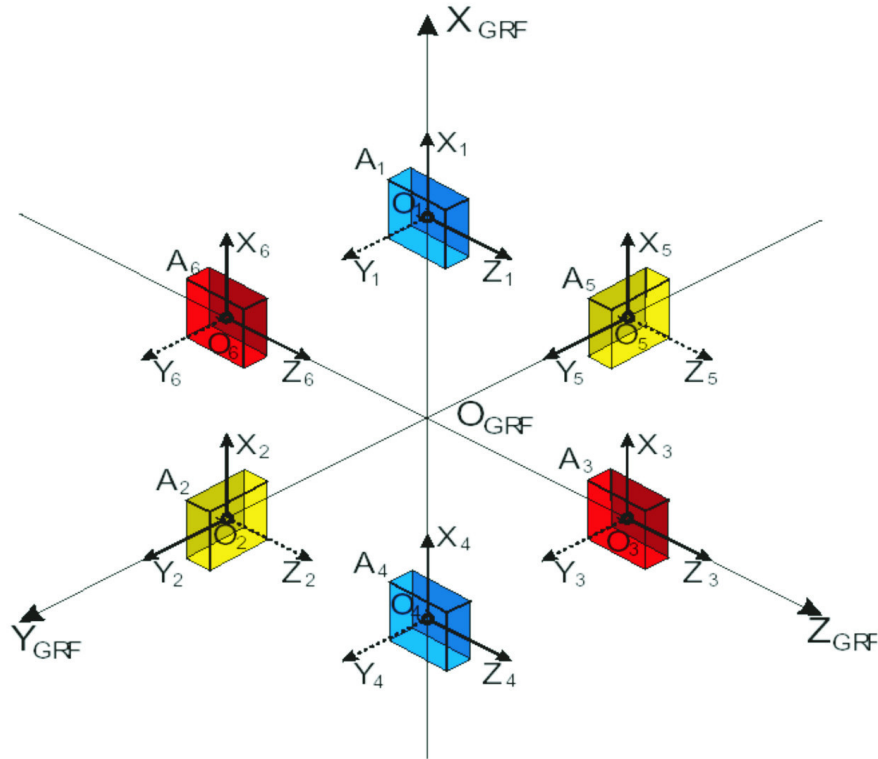


Figure 2.3: Gradiometer Reference Frame, image credit: TUM. The  $X_{GRF}$  refers to along the satellite track direction, whereas  $Y_{GRF}$  and  $Z_{GRF}$  correspond to cross-track and radial direction, respectively.  $O_{GRF}$  stands for the origin of the GRF. The ultra-sensitive axes are displayed by bold lines, whereas the less-sensitive axes are displayed by dashed lines.

Table 2.2: Ultra- and less-sensitive axes of the GOCE Gradiometer.

Accelerometer Pair	Ultra Sensitive	Less Sensitive
A14	X, Y	Y
A25	X, Y	Z
A36	X, Z	Y
Sensitivity	$2 \cdot 10^{-12} \text{ m/s}^2/\sqrt{\text{Hz}}$	$2 \cdot 10^{-10} \text{ m/s}^2/\sqrt{\text{Hz}}$

The differential mode technique is based on the differences between the measurements of the two accelerometers of the same gradiometer arm that cancel out the noise and disturbing forces that are common to both measurements. This process is called “common-mode rejection”. The remaining part represents the differences in the acceleration that are due to the Earth’s gravitation measured at two different locations separated by 50 cm, which is the basic scientific product of the gradiometer [Floberghagen et al., 2011].

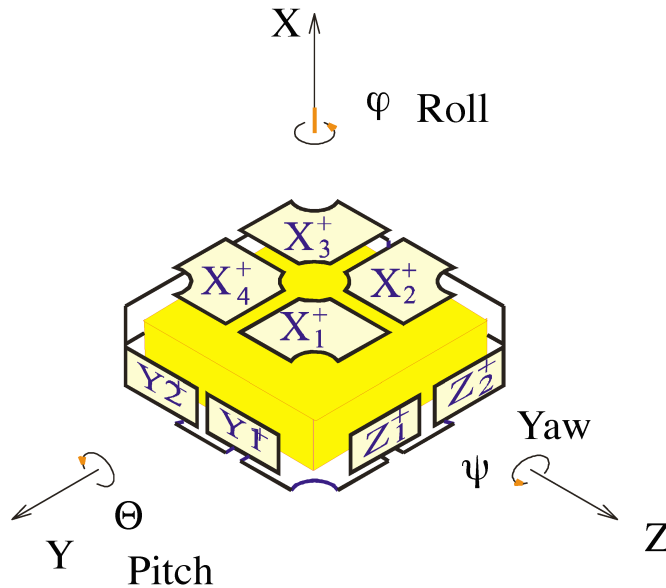


Figure 2.4: Accelerometer Electrode System Reference Frame and location/nomenclature of the 8 electrode pairs, image credit: TAS/ONERA.

In addition to the differential measurements, the common measurements are also considered in GOCE data processing. The common measurements which are the average measurements in one arm represent external non-gravitational forces acting on the spacecraft. This information was used to continuously compensate the air-drag and keep the satellite drag-free along the flight direction. The ion engine thruster responded to the increasing and decreasing common accelerations to maintain the satellite in near free-fall conditions. Accordingly, the satellite was kept in its orbital altitude and the noise in differential measurements were reduced. Consequently, very sensitive measurements of linear and angular accelerations of the spacecraft and four of the six components of the gravitational gradient tensor are derived [Floborghagen et al., 2011].

### 2.1.1.2 Other Sensors

**Satellite-to-Satellite Tracking Instrument (SSTI):** The GPS receiver on-board GOCE was used to determine the position and velocity vectors of the satellite. Moreover, the position of the satellite includes the orbital perturbations which can be used to retrieve the long wavelength components of the gravitational field. The highly accurate gradiometer measurements were not designed to map the gravitational field of the Earth at all scales with the same precision. Satellite-to-satellite tracking (SSTI) measurements complement

the gradiometer data that represent the medium to short wavelength components of the gravitational field [Frommknecht et al., 2011] and provide highly precise orbit information at the cm-level in each of the three orthogonal directions.

The SSTI system simultaneously tracked 12 GPS satellites at L1/L2 frequencies. By using the two signal frequencies, the error caused by the ionosphere between GOCE and GPS orbits were eliminated from the measurements [Floberghagen et al., 2011].

**Star Trackers (STR):** GOCE had three star trackers which were used to retrieve the attitude of the satellite with respect to the known stellar constellations from a star catalogue [Frommknecht et al., 2011]. GOCE star trackers had different orientations which helped improve the accuracy of the spacecraft attitude. The upgraded method presented in Stummer et al. [2012] combined the observations of the three star trackers and optimized the derivation of angular rates.

**Magnetometer (MGM):** The 3-axis magnetometer was used for magnetic torquer control. It is mentioned that the magnetometer data were not scientific data but only helped to monitor the satellite's condition (Siemes., personal comms, 2012). Therefore, the magnetometer data are not available except from the last phase of GOCE when the satellite altitude was lowered.

**Magnetic torquers (MTR):** The three magnetic torquers (MTR) were used to control the attitude of the satellite. More precisely, the torquers were the only sensors that were used in GOCE attitude control. This method has advantages and disadvantages. The sensors were lightweight and inexpensive, and required low power. However, since the torquers act in response to the Earth's magnetic field, there were regions where the control torque could not be created along the Earth magnetic field lines but only perpendicular to them. Therefore, there were instability issues in the roll and yaw angles over the Equator and polar regions, respectively.

**Ion Propulsion Assembly (IPA):** The IPA system was designed to provide a real-time drag force compensation along the satellite orbit. The thrusters helped to compensate the drag in X-direction based on the common-mode accelerations measured by the pair mounted along the satellite track.

**Laser Retro Reflector (LRR):** The LRR used was a corner-cube array that reflected laser pulses back along the incident light path. The reflector was a passive device of 2.5 kg total mass that enabled tracking the satellite by Satellite Laser Ranging Service. The LRR measurements provide a supplementary set of data for precise orbit determination in post-processing.

## 2.2 Level 1b Gradiometer Data and In-flight Calibration

---

### 2.2.1 Gradiometer Data

GOCE Level 1b EGG data consist of many different components which are listed in Table 2.3. The data used in this research are listed as the calibrated common-mode (CM) and differential-mode (DM) accelerations (EGG\_CCD\_1i), the diagonal and off-diagonal components of the GGT (EGG\_GGT\_1i), Gradiometer Inertial Attitude Quaternions<sup>3</sup> (EGG\_IAG\_1i) and transformation matrices from GRF to (quasi) Inertial Reference Frame (IRF) (EGG\_GIM\_1i) [ESA, 2006], which are highlighted in bold in the table.

The measurements sampled at 1 Hz are collected from Earth Observation data platform of ESA, EOLISA. For the purpose of this study, all the EGG derived accelerations and GGT components are kept in the GRF in order to prevent the propagation of less-sensitive measurements into the ultra-sensitive ones via the transformation matrices. For the position information of the satellite, satellite-to-satellite tracking data provided under Level 2 products (SST\_PSO\_2) are included. These data are represented in an Earth-Fixed Reference Frame (EFRF), such as ITRF.

Table 2.3: Measurements included in Level 1 Block. Note that the ones used in this research are indicated as bold.

Measurement Dataset	Description of contents
EGG_CTR_1i	EGG control Voltages
EGG_POL_1i	EGG polarisation Voltages
EGG_NLA_1i	Nominal linear and angular accelerations
EGG_NCD_1i	Nominal common and differential accelerations
EGG_NGA_1i	Nominal gradiometer angular accelerations
EGG_CCV_1i	Corrected Control Voltages
<b>EGG_CCD_1i</b>	<b>Calibrated common and differential accelerations</b>
EGG_CGA_1i	Calibrated angular accelerations
EGG_GAR_1i	Gradiometer angular rates
<b>EGG_IAG_1i</b>	<b>Gradiometer inertial attitude quaternions</b>
<b>EGG_GGT_1i</b>	<b>Gravity gradient tensor GRF system</b>
<b>EGG_GIM_1i</b>	<b>Transformation matrix from GRF to IRF</b>

---

<sup>3</sup>Quaternions: Quaternions are representations of orientations and rotations of objects in three dimensions. Compared to rotation matrices, they are numerically more stable. Therefore, in this research the quaternions are used when interpolation of the rotation matrices is necessary.

It is found that Level 1b kinematic orbit solution<sup>4</sup> has gaps over the polar regions. Accordingly, we use reduced-dynamic precise science orbits (PSO)<sup>5</sup> along with the rotation matrices between the IRF and EFRF that are provided under GOCE Level 2 data at 10 second interval. GPS time is used for time tag information and the position is interpolated into the EGG time tag (1s interval) in order to estimate the position of the satellite corresponding to the EGG measurements. Inertial Attitude Quaternions (IAQs) used in the transformation of external datasets from IRF to GRF are given in more detail in the following sections.

The main diagonal GGT components can be derived from the calibrated in-line measurements along the accelerometer couples. The common-mode (CM) rejection is applied in order to retrieve the differential-mode (DM) accelerations along with the rotational accelerations of the satellite about the GRF. What follows are the fundamental equations that describe the various accelerations and their derivatives and are taken from Rummel et al. [2010], Frommknecht et al. [2011], and Stummer et al. [2011].

The CM and DM accelerations are expressed as follows:

$$\begin{aligned} a_{c,nm,i} &= \frac{1}{2}(a_{n,i} + a_{m,i}), \\ a_{d,nm,i} &= \frac{1}{2}(a_{n,i} - a_{m,i}), \end{aligned} \tag{2.1}$$

where  $n$  and  $m$  are the ID numbers of the accelerometers (e.g., 14, 25, and 36) and  $i$  represents the measurement direction,  $x$ ,  $y$  and  $z$ , and  $c$  and  $d$  correspond to the CM and DM accelerations, respectively.

The gravitational gradient tensor elements cannot be measured directly, but in combination with the centrifugal and angular accelerations, since the measurements are performed in a moving frame that is fixed to the satellite. The acceleration measured by any of the accelerometers is

$$\mathbf{a}_i = -(\mathbf{V} - \mathbf{\Omega}^2 - \dot{\mathbf{\Omega}})\mathbf{r}_i + \mathbf{d} + \mathbf{n}, \tag{2.2}$$

where  $\mathbf{V}$  is the GGT,  $\mathbf{r}_i$  represents the distance between the centre of mass of the satellite and the centre of the accelerometer,  $\mathbf{\Omega}$  and  $\dot{\mathbf{\Omega}}$  represent the angular velocity and angular acceleration tensors, respectively,  $\mathbf{d}$  represents the non-gravitational accelerations and  $\mathbf{n}$  is the measurement noise.

---

<sup>4</sup>Kinematic orbit determination: The three components of the satellite position and the receiver clock error are estimated from the GPS observations for every epoch (every single second) [http : //www.iapg.bgu.tum.de/46738 - bD11bg - iapg\\_forschung\\_goce\\_orbit\\_determination.html](http://www.iapg.bgu.tum.de/46738-bD11bg-iapg_forschung_goce_orbit_determination.html).

<sup>5</sup>Reduced-dynamic orbit determination: The initial Keplerian elements and additional disturbing accelerations are estimated in a least-squares-adjustment to estimate the orbit for a period of 30 hours. Also, for every epoch (every 10 seconds) a receiver clock error has to be determined [http : //www.iapg.bgu.tum.de/46738 - bD11bg - iapg\\_forschung\\_goce\\_orbit\\_determination.html](http://www.iapg.bgu.tum.de/46738-bD11bg-iapg_forschung_goce_orbit_determination.html).

The angular velocity and accelerations tensor,

$$\boldsymbol{\Omega} = \begin{pmatrix} 0 & -\omega_z & \omega_y \\ \omega_z & 0 & -\omega_x \\ -\omega_y & \omega_x & 0 \end{pmatrix}, \quad (2.3)$$

and

$$\dot{\boldsymbol{\Omega}} = \begin{pmatrix} 0 & -\dot{\omega}_z & \dot{\omega}_y \\ \dot{\omega}_z & 0 & -\dot{\omega}_x \\ -\dot{\omega}_y & \dot{\omega}_x & 0 \end{pmatrix}, \quad (2.4)$$

therefore;

$$\boldsymbol{\Omega}^2 = \begin{pmatrix} -\omega_y^2 - \omega_z^2 & \omega_x\omega_y & \omega_x\omega_z \\ \omega_x\omega_y & -\omega_x^2 - \omega_z^2 & \omega_y\omega_z \\ \omega_x\omega_z & \omega_y\omega_z & -\omega_x^2 - \omega_y^2 \end{pmatrix}. \quad (2.5)$$

The Gravitational Gradient Tensor is defined as follows:

$$\mathbf{V} = \begin{bmatrix} V_{xx} & V_{xy} & V_{xz} \\ V_{yx} & V_{yy} & V_{yz} \\ V_{zx} & V_{zy} & V_{zz} \end{bmatrix}, \quad (2.6)$$

where the diagonal elements of gravitational gradient tensor are derived from the in-line DM accelerations  $a_{d,14,x}$ ,  $a_{d,25,y}$ , and  $a_{d,36,z}$ :

$$\begin{aligned} V_{xx} &= -\frac{2a_{d,14,x}}{L_x} - \omega_y^2 - \tilde{\omega}_z^2, \\ V_{yy} &= -\frac{2a_{d,25,y}}{L_y} - \tilde{\omega}_x^2 - \tilde{\omega}_z^2, \\ V_{zz} &= -\frac{2a_{d,36,z}}{L_z} - \tilde{\omega}_x^2 - \omega_y^2. \end{aligned} \quad (2.7)$$

The off-diagonal elements of the GGT are computed by using the transversal<sup>6</sup> DM accelerations of different combination of accelerometer pairs as follows:

$$\begin{aligned}
\tilde{V}_{xy} &= -\frac{2\tilde{a}_{d,14,y}}{L_x} - \frac{2a_{d,25,x}}{L_y} + \tilde{\omega}_x\omega_y, \\
V_{xz} &= -\frac{2a_{d,14,z}}{L_x} - \frac{2a_{d,36,x}}{L_z} + \tilde{\omega}_z\tilde{\omega}_x, \\
\tilde{V}_{yz} &= -\frac{2\tilde{a}_{d,25,z}}{L_y} - \frac{2\tilde{a}_{d,36,y}}{L_z} + \omega_y\tilde{\omega}_z.
\end{aligned} \tag{2.8}$$

As mentioned in the previous section, the configuration of the accelerometers was designed to achieve most accurate measurements possible. The diagonal gradients and  $V_{xz}$  are derived from the ultra-sensitive DM accelerations, whereas two of the off-diagonal components,  $V_{xy}$  and  $V_{yz}$  are retrieved from the less-sensitive DM accelerations. The tilde represents the less sensitive measurements,  $a_d$  and  $a_c$  represent differential- and common-mode accelerations, respectively, between the accelerometer pairs 14, 25 and 36, where  $L_x$ ,  $L_y$ , and  $L_z$  represent the distances between the accelerometer pairs 14, 25 and 36, respectively, which were measured by the manufacturer before the satellite was launched.

The angular accelerations can be derived from the EGG measurements and are represented as follows:

$$\begin{aligned}
\tilde{\omega}_x &= -\frac{a_{d,36,y}}{L_z} + \frac{\tilde{a}_{d,25,z}}{L_y}, \\
\omega_y &= -\frac{a_{d,14,z}}{L_x} + \frac{a_{d,36,x}}{L_z}, \\
\tilde{\omega}_z &= -\frac{a_{d,14,y}}{L_x} + \frac{\tilde{a}_{d,25,x}}{L_y},
\end{aligned} \tag{2.9}$$

where  $\omega_x$  is the angular acceleration about the  $x$ -axis, and  $\omega_y$  and  $\omega_z$  are the angular accelerations about the  $y$ - and  $z$ -axes, respectively. The  $\omega_y$  is the only angular acceleration that is computed from the ultra-sensitive DM measurements. Angular rates are computed by combining angular accelerations (Equation 2.9) and observations of the star trackers. In order to combine the two, angular accelerations need to be integrated and first derivatives of star tracker directions need to be computed before they are combined.

The less sensitive angular accelerations indicated by the tilde, are influenced by the less-sensitive DM measurements. The angular acceleration about the  $Y$ -axis is the most important of the three since the satellite rotates once per orbital period and  $\omega_y$  is the largest component [Stummer et al., 2012]. The configuration of the accelerometers and the ultra- and less- sensitive axes were designed to retrieve the highest accuracy

---

<sup>6</sup>Transversal accelerations are collected along the transversal axes to the gradiometer arm such as  $V_{xy}$  is measured along the gradiometer arm of accelerometer pair 14 (x-axis) in y-direction which is transversal to the baseline 14.

level of this component. Moreover, these components are used to calculate the angular accelerations which are used in the derivation of the gradients as shown above.

Cesare [2002] mentioned that the following errors affect the measurements of the gravitational gradients.

- Instrument errors which depend only on the gradiometer elements.
- Instrument satellite coupling errors which depend on the interaction of the gradiometer and the satellite and mission environment.
- Satellite errors which depend on the satellite performance excluding the gradiometer.
- Processing errors which include the transformation of Level 0 to Level 1b products.

Accelerometer noise is the dominant part of the instrumental errors. Moreover, the largest part of the instrument satellite coupling errors is due to the coupling of non-gravitational linear accelerations acting on the satellite's COM with the in-line differential mode accelerations [Cesare, 2002]. It is worth noting that the in-line differential-mode accelerations contain the diagonal gravity gradient signal. Moreover, errors due to the imperfect instrumentation need to be taken into account. The calibration procedure that minimizes the errors due to the imperfect instrumentation is given in the next section.

### 2.2.2 Calibration of the Gradiometer

Calibration is one of the main tasks to be performed very cautiously in GOCE Level 1 processing. It is very often that the literature covers the calibration as “internal” and “external” [Bouman et al., 2004, Koop et al., 2002, Stummer et al., 2011] depending on the datasets used in the calibration procedure. Internal calibration uses datasets obtained by the GOCE sensors, such as gradiometer and star sensor measurements, whereas external calibration is performed based on external information provided by other sources (geopotential models derived from other missions and/or terrestrial gravity observations) [Rispen and Bouman, 2009, Siemes et al., 2012, Visser, 2008].

Geodetic or geophysical instruments require calibration due to instrument drift and imperfections. With an uncalibrated gradiometer, the measurement of gravitational gradients is not accurate and not to be trusted. Even though there are some calibration activities performed on-ground, not all calibration parameters can be derived because of the 1 g environment [Cesare and Catastini, 2005]. Accordingly, the calibration needs to be performed in-flight since the gradiometer is manufactured to operate under micro-g conditions [Siemes et al., 2012].

In this section, we summarize the in-flight calibration procedure of the GOCE gradiometer. This procedure can be investigated in two steps. The first step is the determination of the quadratic factors that take into account the non-linearities of the accelerometer transfer function, whereas the second step is to reduce the gradiometer imperfections, such as scale factor errors, misalignments, and non-orthogonalities. In other words, to achieve the required accuracy in retrieving the diagonal components of the gravitational gradient tensor, the differences between the principles of an ideal gradiometer and a real gradiometer need to be investigated and corrected.

As given in Cesare [2002], for an ideal gradiometer the following assumptions are made. Following the assumptions the conditions for a real gradiometer are given.

- The internal dynamics and the read-out process of each accelerometer do not show any effect on the input acceleration, whereas they affect the input acceleration.
- The ultra-sensitive axes of an accelerometer are perfectly aligned with respect to the axes of the corresponding accelerometer reference frame (ARF). In fact the ultra-sensitive axes of ARF's are not perfectly aligned to the corresponding axes of the one axis gradiometer reference frame (OAGRF).
- All six accelerometers occupy their nominal positions and the axes of the accelerometer reference frames are in perfect alignment with the corresponding axes of the OAGRF. However, for a real gradiometer the six accelerometers do not occupy their nominal positions and the accelerometers' sensitive axes are not mutually orthogonal (Each accelerometer has its own frame and more detail can be found in Stummer [2012] and Cesare [2002]).
- The origins of the three OAGRF coincide and their corresponding axes are in perfect alignment with each other, whereas the origins of the three OAGRF do not coincide and their corresponding axes are not perfectly aligned.
- The position/alignment of the six accelerometers with respect to the OAGRF and the position/alignment of the OAGRF with respect to the GRF do not change in time, whereas the position/alignment of the six accelerometers in the respective OAGRF and the position/alignment of the OAGRF in the GRF are not constant in time.

Therefore, the in-flight calibration is of importance in terms of reducing instrumental errors and improving the accuracy and quality of the GOCE gradiometer measurements.

### 2.2.2.1 Measurement of quadratic factor

As introduced in the previous section, the GOCE working principle is based on the levitation of a proof mass that is maintained at the same position in the accelerometer reference frame. This is achieved by applying counteracting voltages produced by electrostatic actuators. The voltages are applied by the control loops involved in the feedback system that retrieves the outputs. These outputs are related to the accelerations experienced by the proof mass in a linear manner [Frommknecht et al., 2011, Stummer, 2012] as follows:

$$\begin{aligned} a_{i,X_e} &= \frac{1}{4G_{read}}(G_{el-X_1}V_{i,X_1} + G_{el-X_2}V_{i,X_2} + G_{el-X_3}V_{i,X_3} + G_{el-X_4}V_{i,X_4}), \\ a_{i,Y_e} &= \frac{1}{2G_{read}}(G_{el-Y_1}V_{i,Y_1} + G_{el-Y_2}V_{i,Y_2}), \\ a_{i,Z_e} &= \frac{1}{2G_{read}}(G_{el-Z_1}V_{i,Z_1} + G_{el-Z_2}V_{i,Z_2}), \end{aligned} \quad (2.10)$$

where  $G_{el-X_1}$ ,  $G_{el-X_2}$ ,  $G_{el-X_3}$ ,  $G_{el-X_4}$ ,  $G_{el-Y_1}$ ,  $G_{el-Y_2}$ ,  $G_{el-Z_1}$ , and  $G_{el-Z_2}$  are the electrostatic gains of the accelerometer and  $G_{read}$  is the read-out gain.

EGG measures the position of the proof masses in terms of voltages. Accordingly, any movement of the proof mass inside the accelerometer is measured by the amount of voltages and is kept in levitation electrostatically. These voltages need to be transformed into accelerations. However, this transformation is not linear. Quadratic factors take care of the non-linearities in the accelerometer transfer functions. Therefore, second degree corrections need to be applied which are taken care of by the quadratic factors [Cesare, 2002]. For details, the reader is referred to Cesare [2002], Lamarre [2007], Frommknecht et al. [2011], Siemes [2012], and Stummer [2012].

A measured acceleration  $a'_{i,k}$  of accelerometer  $i$  in the  $k$  direction can be written as:

$$a'_{i,k} = K2_{i,k} \cdot a_{i,k}^2, \quad (2.11)$$

where  $a_{i,k}$  are the real accelerations and the quadratic factor matrix is

$$\underline{K2}_i = \begin{pmatrix} K2_{i,x} & 0 & 0 \\ 0 & K2_{i,y} & 0 \\ 0 & 0 & K2_{i,z} \end{pmatrix}, \quad (2.12)$$

where  $K2_{i,x}$ ,  $K2_{i,y}$ , and  $K2_{i,z}$  are the quadratic factors of the different directions.

### 2.2.2.2 Other Gradiometer Calibration Parameters

Gradiometer imperfections, such as accelerometer scale factor errors, misalignments of the accelerometers, and non-orthogonalities of the accelerometer axes are taken care of via the in-flight “satellite shaking”. The imperfections are given in Cesare and Catastini [2005], and summarized in Frommknecht et al. [2011], Stummer et al. [2012]. The visual representation of these deviations are presented in Stummer [2012] and not repeated here. The gradiometer imperfections are listed as follows:

**Scale factors:** The scale factor of the six accelerometers on-board GOCE mission is not perfectly equal to 1, but deviates by a small amount. A measured acceleration is expressed by:

$$a'_{i,k} = (1 + K_{i,k} \cdot a_{i,k}), \quad (2.13)$$

where  $i$  is the accelerometer ID and  $k$  is its direction and the scale factor matrix for the three directions can be written as

$$\underline{K}_i = \begin{pmatrix} 1 + K_{i,x} & 0 & 0 \\ 0 & 1 + K_{i,y} & 0 \\ 0 & 0 & 1 + K_{i,z} \end{pmatrix}, \quad (2.14)$$

and

$$\underline{K}_i = \underline{I}_3 + \begin{pmatrix} K_{i,x} & 0 & 0 \\ 0 & K_{i,y} & 0 \\ 0 & 0 & K_{i,z} \end{pmatrix} = \underline{I}_3 + \underline{dK}_i, \quad (2.15)$$

where  $\underline{I}_3$  is the  $3 \times 3$  identity matrix.

**Misalignment:** The accelerometer  $A_i$  may have a rotational deviation from its nominal orientation. This small deviation can be expressed as:

$$\underline{R}_i = \begin{pmatrix} 1 & \psi_i & -\theta_i \\ -\psi_i & 1 & \varphi_i \\ \theta_i & -\varphi_i & 1 \end{pmatrix} = \underline{I}_3 + \begin{pmatrix} 0 & \psi_i & -\theta_i \\ -\psi_i & 0 & \varphi_i \\ \theta_i & -\varphi_i & 0 \end{pmatrix} = \underline{I}_3 + \underline{dR}_i, \quad (2.16)$$

where  $\theta_i$ ,  $\psi_i$ , and  $\varphi_i$  are the small misalignments about the  $x$ ,  $y$ , and  $z$  axes, respectively.

**Coupling:** The axes of accelerometer  $A_i$  may not be perfectly perpendicular to each other. This would cause the measurements in different directions to be coupled. These small deviations from orthogonality,  $\varepsilon_i$ ,  $\eta_i$ , and  $\varsigma_i$  are the couplings between the  $x$  and  $y$ ,  $x$  and  $z$  and  $y$  and  $z$  axes, respectively, and is expressed as follows:

$$\underline{S}_i = \begin{pmatrix} 1 & \varepsilon_i & \eta_i \\ \varepsilon_i & 1 & \varsigma_i \\ \eta_i & \varsigma_i & 1 \end{pmatrix} = \underline{I}_3 + \begin{pmatrix} 0 & \varepsilon_i & \eta_i \\ \varepsilon_i & 0 & \varsigma_i \\ \eta_i & \varsigma_i & 0 \end{pmatrix} = \underline{I}_3 + \underline{dS}_i. \quad (2.17)$$

**Accelerometer bias:** Each accelerometer axis measures an unknown bias. This unknown biased measured by accelerometer  $A_i$  is expressed as:

$$\bar{b}_i = \begin{pmatrix} b_{i,x} \\ b_{i,y} \\ b_{i,z} \end{pmatrix}, \quad (2.18)$$

where  $b_{i,x}$  is the bias in  $x$ -axis and  $b_{i,y}$  and  $b_{i,z}$  are the biases in  $y$  and  $z$  axes, respectively.

**Accelerometer noise:** Similar to the accelerometer bias, each accelerometer axis measures coloured noise. The noise vector for accelerometer  $A_i$  can be written as:

$$\bar{n}_i = \begin{pmatrix} n_{i,x} \\ n_{i,y} \\ n_{i,z} \end{pmatrix}, \quad (2.19)$$

where  $n_{i,x}$  is the noise in  $x$ -axis and  $n_{i,y}$  and  $n_{i,z}$  are the noises in  $y$  and  $z$  axes, respectively.

A measured acceleration, including all deviations listed above, is written as follows:

$$\bar{a}_i' = (\underline{I}_3 + \underline{dK}_i) \cdot (\underline{I}_3 + \underline{dR}_i) \cdot (\underline{I}_3 + \underline{dS}_i) \cdot \bar{a}_i + \underline{K2}_i \cdot \bar{a}_i^2 + \bar{b}_i + \bar{n}_i, \quad (2.20)$$

which approximates to

$$\bar{a}_i' \approx (\underline{I}_3 + \underline{dK}_i + \underline{dR}_i + \underline{dS}_i) \cdot \bar{a}_i + \underline{K2}_i \cdot \bar{a}_i^2 + \bar{b}_i + \bar{n}_i, \quad (2.21)$$

and

$$\bar{a}_i = (\underline{K}_i + \underline{dR}_i + \underline{dS}_i) \cdot \bar{a}_i + \underline{K2}_i \cdot \bar{a}_i^2 + \underline{b}_i + \underline{n}_i. \quad (2.22)$$

Containing the above mentioned gradiometer imperfections, the basic measurement equation can be written as follows:

$$\begin{pmatrix} \bar{a}'_{c,i,j} \\ \bar{a}'_{d,i,j} \end{pmatrix} = \bar{M}_{i,j} + \begin{pmatrix} \bar{a}_{c,i,j} \\ \bar{a}_{d,i,j} \end{pmatrix} + \frac{1}{2} \underline{K2}_{ij} \begin{pmatrix} (\bar{a}_{c,i,j} + \bar{a}_{d,i,j})^2 \\ (\bar{a}_{d,i,j} - \bar{a}_{c,i,j})^2 \end{pmatrix} + \begin{pmatrix} \bar{b}_{c,i,j} \\ \bar{b}_{d,i,j} \end{pmatrix} + \begin{pmatrix} \bar{n}_{c,i,j} \\ \bar{n}_{d,i,j} \end{pmatrix}, \quad (2.23)$$

where the calibration matrix is written as :

$$\bar{M}_{i,j} = \begin{pmatrix} 1 + K_{c,ij,X} & \psi_{c,ij} + \epsilon_{c,ij} & -\theta_{c,ij} + \eta_{c,ij} & K_{d,ij,X} & \psi_{d,ij} + \epsilon_{d,ij} & -\theta_{d,ij} + \eta_{d,ij} \\ -\psi_{c,ij} + \epsilon_{c,ij} & 1 + K_{c,ij,Y} & \phi_{c,ij} + \zeta_{c,ij} & -\psi_{d,ij} + \epsilon_{d,ij} & K_{d,ij,Y} & \phi_{d,ij} + \zeta_{d,ij} \\ \theta_{c,ij} + \eta_{c,ij} & -\phi_{c,ij} + \zeta_{c,ij} & 1 + K_{c,ij,Z} & \theta_{d,ij} + \eta_{d,ij} & -\phi_{d,ij} + \zeta_{d,ij} & K_{d,ij,Z} \\ K_{d,ij,X} & \psi_{d,ij} + \epsilon_{d,ij} & -\theta_{d,ij} + \eta_{d,ij} & 1 + K_{c,ij,X} & \psi_{c,ij} + \epsilon_{c,ij} & -\theta_{c,ij} + \eta_{c,ij} \\ -\psi_{d,ij} + \epsilon_{d,ij} & K_{d,ij,Y} & \phi_{d,ij} + \zeta_{d,ij} & -\theta_{c,ij} + \eta_{c,ij} & 1 + K_{c,ij,Y} & \phi_{c,ij} + \zeta_{c,ij} \\ \theta_{d,ij} + \eta_{d,ij} & -\phi_{d,ij} + \zeta_{d,ij} & K_{d,ij,Z} & \theta_{c,ij} + \eta_{c,ij} & -\phi_{c,ij} + \zeta_{c,ij} & 1 + K_{c,ij,Z} \end{pmatrix}, \quad (2.24)$$

and

$$\begin{pmatrix} (\bar{a}_{c,i,j} + \bar{a}_{d,i,j})^2 \\ (\bar{a}_{d,i,j} - \bar{a}_{c,i,j})^2 \end{pmatrix} = \begin{pmatrix} (a_{c,i,j,X} + a_{d,i,j,X})^2 \\ (a_{c,i,j,Y} + a_{d,i,j,Y})^2 \\ (a_{c,i,j,Z} + a_{d,i,j,Z})^2 \\ (a_{c,i,j,X} - a_{d,i,j,X})^2 \\ (a_{c,i,j,Y} - a_{d,i,j,Y})^2 \\ (a_{c,i,j,Z} - a_{d,i,j,Z})^2 \end{pmatrix}, \quad (2.25)$$

then

$$\frac{1}{2}K2_{ij} \begin{pmatrix} (\bar{a}_{c,i,j} + \bar{a}_{d,i,j})^2 + \\ (\bar{a}_{d,i,j} - \bar{a}_{d,i,j})^2 + \end{pmatrix} = \begin{pmatrix} K2_{c,ij,X}(a_{c,i,j,X}^2 + a_{d,i,j,X}^2) + 2K2_{d,ij,X}a_{c,i,j,X}a_{d,i,j,X} \\ K2_{c,ij,Y}(a_{c,i,j,Y}^2 + a_{d,i,j,Y}^2) + 2K2_{d,ij,Y}a_{c,i,j,Y}a_{d,i,j,Y} \\ K2_{c,ij,Z}(a_{c,i,j,Z}^2 + a_{d,i,j,Z}^2) + 2K2_{d,ij,Z}a_{c,i,j,Z}a_{d,i,j,Z} \\ K2_{c,ij,X}(a_{c,i,j,X}^2 - a_{d,i,j,X}^2) + 2K2_{d,ij,X}a_{c,i,j,X}a_{d,i,j,X} \\ K2_{c,ij,Y}(a_{c,i,j,Y}^2 - a_{d,i,j,Y}^2) + 2K2_{d,ij,Y}a_{c,i,j,Y}a_{d,i,j,Y} \\ K2_{c,ij,Z}(a_{c,i,j,Z}^2 - a_{d,i,j,Z}^2) + 2K2_{d,ij,Z}a_{c,i,j,Z}a_{d,i,j,Z} \end{pmatrix}. \quad (2.26)$$

Neglecting the noise and bias, and assuming that the quadratic term is determined and taken care of, the inversion of Equation 2.23 can be used to retrieve the true common- and differential-mode accelerations can be retrieved as follows:

$$\begin{pmatrix} \bar{a}_{c,i,j} \\ \bar{a}_{d,i,j} \end{pmatrix} = \bar{M}_{i,j}^{-1} \begin{pmatrix} \bar{a}'_{c,i,j} \\ \bar{a}'_{d,i,j} \end{pmatrix}, \quad (2.27)$$

where  $\bar{a}_{c,i,j}$  and  $\bar{a}'_{d,i,j}$  are the measured CM and DM accelerations and  $\bar{a}_{c,i,j}$  and  $\bar{a}_{d,i,j}$  are the calibrated CM and DM accelerations, respectively where  $\bar{M}_{i,j}^{-1}$  is the inverse of the calibration matrix. It is worth reminding that the gravitational gradients are derived from the calibrated (true) differential-mode accelerations,  $\bar{a}_{d,i,j}$ .

### 2.2.2.3 Determination of the Inverse Calibration Matrices

The current calibration method applied in the GOCE data processing is called the ESA-L method which is also known as the baseline method. Details are given in Stummer et al. [2011] and Siemes [2012] and we will not repeat here but summarize the solution only. In ESA-L method, deviations of the real accelerometers from ideal ones are taken into account. These deviations can be in the scale factor, and direction and position of each accelerometer. The parameters derived based on the assumption of imperfect instrument can be listed as the following 12 parameters for each accelerometer.

- 3 scale factors representing the responses along the accelerometer axes
- $3 \times 2$  angles representing the directions of the accelerometer axes
- 3 coordinates representing the position of each accelerometer

Since the gradiometer consists of six accelerometers, the calibration will be based on 72 parameters in total. The ESA-L calibration procedure is based on the spacecraft shaking during which strong linear and

angular accelerations are artificially introduced. These accelerations are much stronger than the gravitational gradient signal. It is important that the satellite shaking be performed in a way to create only small correlations between the 3 angular and 3 linear accelerations measured. Therefore, each of the 6 created accelerations will have a unique signature which is used to identify the gradiometer measurements. In order to identify the unique signatures, the deviations of the real signal from the theoretical signal of an ideal gradiometer are used. At this point, it is assumed that the gradiometer output signal is dominated by the accelerations induced by the satellite shaking; therefore, the centrifugal accelerations and gravitational gradients can be neglected.

This step includes the determination of the relative parameters which can be used to remove any trace of applied accelerations from the gravitational gradient measurements. The scale factor determined based on relative parameters then needs to be refined by using some external absolute information. According to Lamarre [2007], first, the relative parameters between the accelerometer pairs are determined. Then, the absolute scale factor is determined by the help of star sensor measurements. Therefore, a comparison between the gradiometer and star sensor derived attitude is performed. Within the TAS (Thales Alenia Space) method the comparisons are performed at the level of angular accelerations, whereas within the ESA-L they are performed at the level of angular rates. Comparison of angular rates at low and high frequencies cannot be performed because it would cause a poor signal to noise ratio. ESA decided to angularly shake the spacecraft near 1.3 mHz so that an intermediate bandwidth is found where both instruments provide sufficiently accurate estimates. Following the determination of the absolute scale factor, the determination of the Inverse Calibration Matrices of the gradiometer parameters are performed.

It is worth noting that the calibration process is one of the challenging tasks for improving GOCE data products. According to the literature and personal communications (R., Floberghagen, B., Frommknecht, and C., Siemes), the calibration needs further improvement, especially for the cross-track accelerometer measurements. Even though the concept of calibration procedure is covered in this chapter, any improvement concerning the calibration is not the scope of this research. The interested reader can refer to Siemes [2012] for detailed investigations.

## 2.3 Summary

---

In this chapter, we described GOCE mission and payload, and the gradiometry technique that was used to measure the gravitational gradients in space. The different instruments and sensors used on-board GOCE were described and the Level 1b data used in this research were given. What was provided in this chapter were already given in the literature, including ESA reports, PhD dissertation and journal papers and the aim of this chapter was to prepare the reader for the following chapters by giving the necessary background.

It is worth reminding that we used Level 1b gradiometer and Level 2 SST data in this research. One needs to recall that there are certain differences between Level 1b and Level 2 gravitational gradients (e.g., the tidal corrections). Moreover, there are also instrumental imperfections affecting the gradiometer measurements which were also given in this chapter. We described the differences between an ideal and a real gradiometer and summarized the calibration procedure. According to the literature and personal communications, the calibration procedure needs further improvement but this is not the scope of our research. We mentioned that the measurements that were not calibrated cannot be used for high-accuracy geoid computations and other geodetic or geophysical applications since they are not accurate. In summary, we presented the basics of the mission and introduced the measurements that were used in this study.

# 3

## Gradiometer Data

### 3.1 Data Pre-processing

---

GOCE was the first satellite to measure gravitational gradients in space. The measured gravitational gradients represent the second spatial derivatives of the Earth's gravitational potential. As presented in the previous chapter, the goal of GOCE was to determine the Earth's static gravitational field with high accuracy at spatial resolutions down to 100 km [Rummel et al., 2010, Bouman et al., 2011]. The gravitational gradients used in this research are given in the Gradiometer Reference Frame (GRF) and are in-flight calibrated using the satellite shaking and star sensor measurements. Additional pre-processing must be applied to the gradients in order to retrieve the gravitational field models. For example, temporal gravity field information, such as tides should be removed from the gradients [Bouman et al., 2009]. Moreover, the gradients should be filtered into the gradiometer measurement bandwidth (MBW) to minimize the error arising from sources of frequencies outside of the designed bandwidth. Based on Bouman et al. [2009], the error of the tidal corrections is below the gravitational gradient error; therefore, it is not considered in the analyses presented in this thesis. We only apply band-pass filtering to filter the measurements into the MBW.

#### 3.1.1 Filtering Procedure

As indicated in the previous chapters, the GOCE gradiometer was designed to provide the highest accuracy within 5-100 mHz measurement bandwidth. Therefore, a bandpass filter needs to be applied to the acceleration measurements to prevent the noise of low- and high-frequency components leaking into the MBW. The measurement bandwidth of the GOCE EGG corresponds to 10-200 seconds and approximately to 80-1600 km long orbit arcs; and therefore to spherical harmonic degree 250-13 (half-wavelength).

In our analyses, the Gaussian filter is used as a low pass filter for several reasons. The Gaussian window in the time domain that is designed as a low-pass filter has a Gaussian form in the frequency domain. This prevents the Gibbs phenomena [Gottlieb and Shu, 1997] from occurring at the edges due to absence of side lobes. The Gaussian function and its Fourier transform are given as follows, respectively.

$$g(x) = \frac{1}{\sigma_x \sqrt{2\pi}} e^{-(x)^2/2\sigma_x^2}, \quad (3.1)$$

and

$$G(f) = e^{-(f)^2/2\sigma_f^2}, \quad (3.2)$$

where  $\sigma_x$  and  $\sigma_f$  are standard deviations in time and frequency domain, respectively, and  $x$  represents the distance from the origin. Since we are interested in a particular bandwidth interval, we design two low pass Gaussian filters with different cut-off frequencies and use them together as a band-pass filter. The cut-off frequencies are defined by the EGG MBW (0.1-0.005 Hz). Moreover, the size of the Gaussian windows are computed based on -3 dB or half power point principle. The Gaussian window full width in the time domain is represented by  $7\sigma_x$  where

$$\sigma_x = \frac{\sqrt{2 \ln \frac{1}{\sqrt{2}}}}{2\pi f_c}, \quad (3.3)$$

and  $f_c$  is the cut-off frequency.

The Gaussian filter can be applied in different ways to band-pass filter the data and has the same effect as other filters commonly used, such as the Butterworth band-pass filter. There are two ways of developing a band-pass Gaussian filter. The first way is to calculate the high-pass filter coefficients by subtracting the low-pass Gaussian filter coefficients from 1. Therefore, a low-pass filter and a high-pass filter can be applied to the data successively in order to filter the original acceleration measurements and gradients into the MBW. The second way, which we perform here, is that two low-pass Gaussian filters each with cut-off frequency defined by the EGG MBW can be applied to the accelerations and gradients separately and the difference between the filtered series can be calculated. The filtered series represent the observations within the MBW to avoid any shortcomings of other filters and phase shifts.

We need to mention here that the GOCE measurements have many short and long gaps due to the reasons related to the instruments on-board and satellite environment. For the filtering process, it is assumed that the observations are continuous and uninterrupted and small gaps are maintained. Moreover, the Gaussian filter is restarted after long gaps, such as after calibration processes, each lasting about one day.

The influence of the filtering is investigated via spectral techniques. The square root of the power spectral densities of the original diagonal GGT components measured on March 21, 2011 are shown in Figure 3.1. The noise shows an increasing behaviour over lower frequency components. Within the MBW, the original diagonal components show similar behaviour with increasing noise level from higher to lower frequencies. Outside the EGG bandwidth, there is a  $1/f$  noise dominating the signal. The black vertical dashed lines show the EGG MBW, whereas the red dashed lines indicate the orbital ( $\sim 90$  min) and semi-orbital ( $\sim 45$  min) periods that are the dominant periodicities in the original measurements. The trace within the MBW shows a flat error behaviour, whereas it has increasing error outside the MBW. It is also shown that the  $V_{zz}$  component has a higher noise level (twice that of  $V_{xx}$  and  $V_{yy}$ ) within and outside the MBW which is attributed to instrumental errors (Schlicht, A. pers. comm., 2016); however, this link has not been proven by any researcher or institution yet.

For the same time period, the same measurements are filtered into the MBW and displayed in Figure 3.2. The square root of the PSDs of the filtered series show reduction in power outside the MBW which also indicate that the filtering applied reduces the effect of the noise outside the MBW on the components of MBW. The trace displays similar reduction of the noise within the MBW as well as outside the MBW. It is worth mentioning that the Gaussian filter is applied in the time domain, which is similar to the moving average technique and we do not expect to see zero PSD outside of the MBW but much lower power compared to the PSDs of the original series.

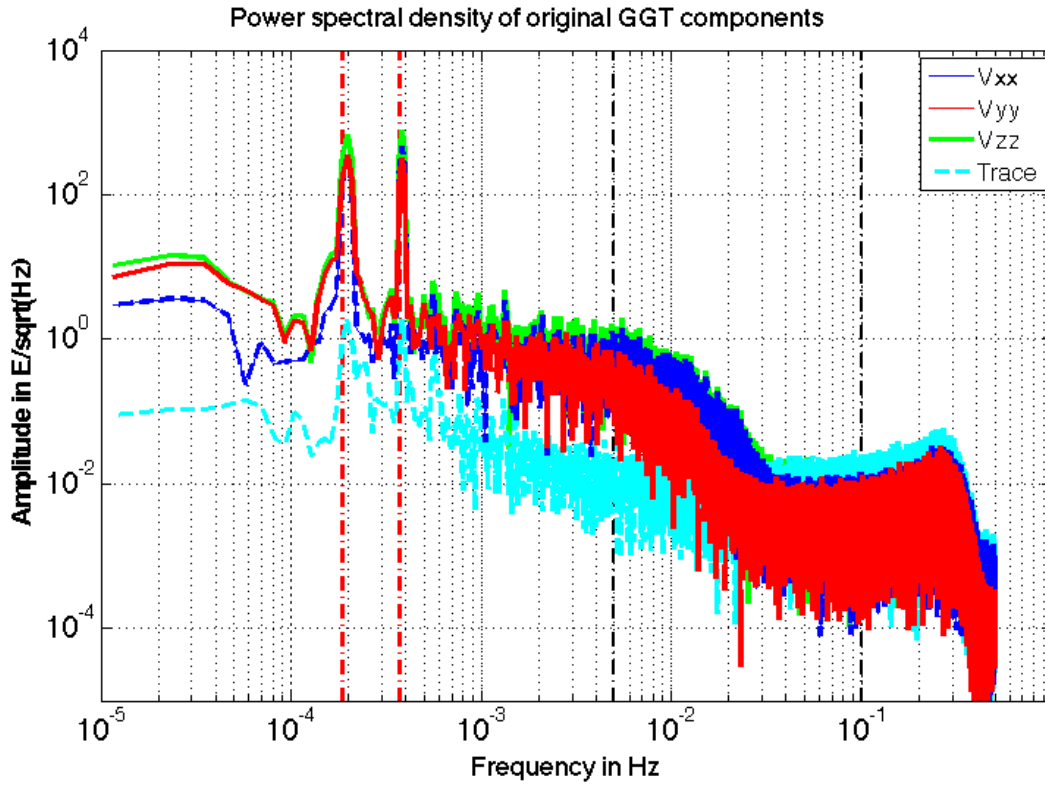


Figure 3.1: Square root of the power spectral densities of original diagonal components. The vertical black dashed lines represent the GOCE EGG measurement bandwidth, whereas the vertical red dashed lines represent the orbital ( $1.86 \cdot 10^{-04}$  Hz) and semi-orbital periodicities ( $3.71 \cdot 10^{-04}$  Hz). Diagonal original GGT components show increasing noise level for the lower frequencies of the MBW and the frequencies outside of the MBW.

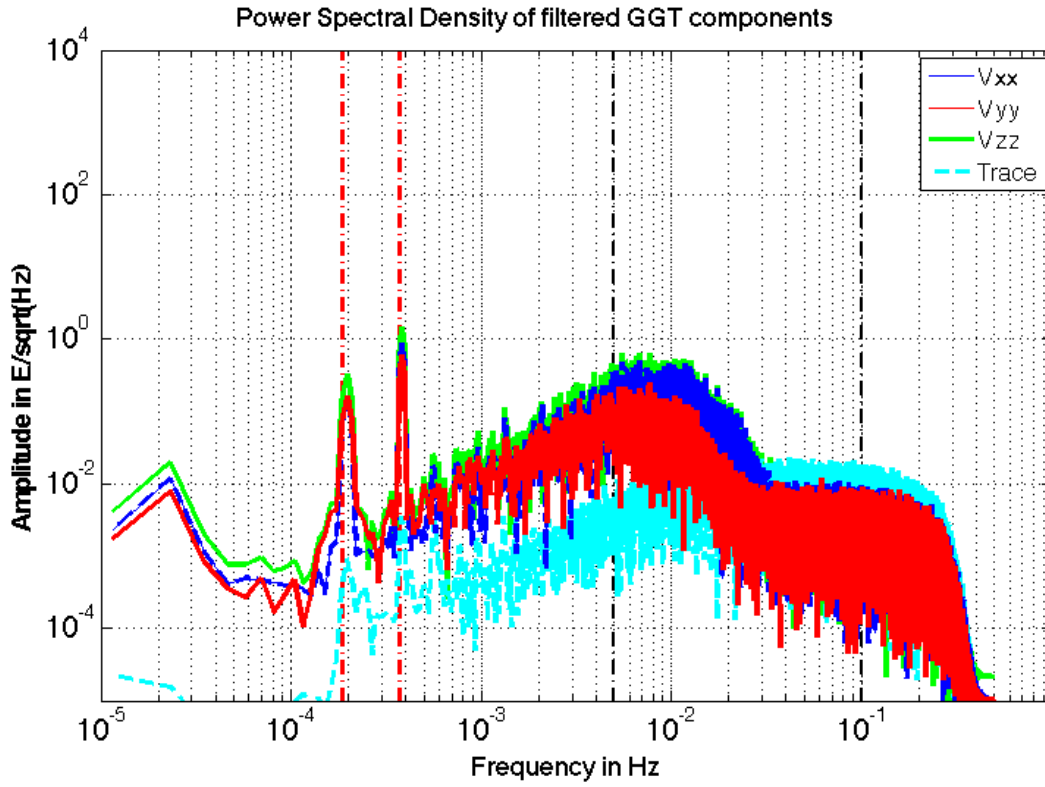


Figure 3.2: Square root of the power spectral densities of filtered diagonal components. The black dashed lines represent the GOCE EGG measurement bandwidth, whereas the red dashed lines represent the orbital ( $1.86 \times 10^{-4}$  Hz) and semi-orbital periodicities ( $3.71 \times 10^{-4}$  Hz). Note the reduction of the power outside of the MBW and as well as within the MBW.

### 3.1.2 Transformation of the GOCE EGG Measurements

There were different instruments on-board GOCE. Moreover, GOCE EGG measurements are referred to different reference frames in different applications. The CM and DM accelerations and GGT elements are provided in the GRF. The GRF with respect to (quasi) Inertial Reference Frame (IRF) and Earth-Fixed Reference Frame (EFRF) are shown in Figure 3.3. The definition of each system and transformation between them are given in this section.

#### 3.1.2.1 Reference Frames Used in GOCE Measurements and Data Processing

The reference frames that are used in GOCE data processing and analyses are given in [ESA, 2006] and summarized here as follows:

**GRF:** The Gradiometer Reference Frame (GRF) is the coordinate system that the GOCE gradiometer measurements are referred to. The GRF represents the three-axis gradiometer common reference frame for the three one-axis gradiometers and is also used for the positioning and orientation of the entire instrument with respect to the external reference frames. The origins of all one-axis gradiometer reference frames are common with the origin of the GRF [ESA, 2006]. The three axes have been designed as follows: X-axis aligns approximately with the along track direction, Z-axis is along the local gravity in downward direction and Y-axis is perpendicular to the orbital plane and completes a right-handed system as shown in Figures 2.3 and 3.3.

**LORF:** The origin of the Local Orbital Reference Frame (LORF) is located at the actual satellite centre of mass. The LORF is defined as follows: X-axis is along the satellite velocity vector; the Z-axis is approximately upwards from the Earth centre opposite to gravitational vector; and the Y-axis is in the direction of the angular momentum vector of the orbit that completes a right-handed system. It is worth noting that the GRF does not fully coincide with the LORF [ESA, 2006].

**ITRF:** The International Terrestrial Reference Frame (ITRF) consists of a set of points with their 3-dimensional Cartesian coordinates that are used in the realization of an ideal reference system, the International Terrestrial Reference System (ITRS) [McCarthy and Petit, 2004].

**IRF:** The inertial reference frame (IRF) is a spatial reference frame that is fixed in space. Its origin is positioned at the centre of the mass of the Earth (geocentre). The Z-axis is the direction of the celestial pole, the X-axis is fixed in the equatorial plane pointing the vernal equinox and Y-axis completes a right-handed system [ESA, 2006]. It is worth mentioning that this system is a quasi-inertial system.

**EFRF:** The Earth-Fixed Reference Frame (EFRF) is a spatial reference system that co-rotates with the Earth in its diurnal motion in space. Its origin is positioned at the centre of the mass of the Earth (geocentre), Z-axis points to the north pole (along the spin axis of the Earth), X-axis is fixed on the equatorial plane pointing to the Greenwich meridian and Y-axis completes a right-handed system. The angle between the X-axis of the IRF and X-axis of EFRF is called as Greenwich Apparent Sidereal Time (GAST) [ESA, 2006].

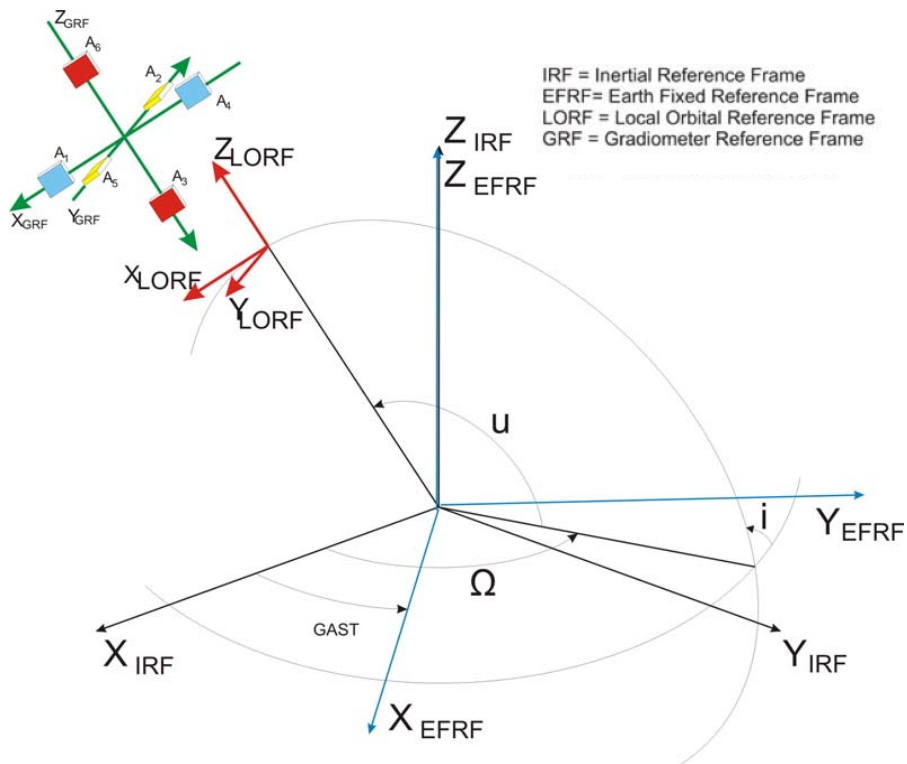


Figure 3.3: Reference Frames used for GOCE products, image credit: TUM.

The transformation from the GRF to any other frame causes less-sensitive measurements propagate into the ultra-sensitive measurements. Therefore, all other measurements (e.g., terrestrial) are transformed into the GRF for the analyses included in this thesis.

### 3.1.2.2 Transformations Among the Reference Frames

Transformation from the EFRF (e.g., ITRF) into the GRF can be performed using the Inertial Attitude Quaternions (IAQs) that are provided under Level 1b data block and Earth Orientation Quaternions (EOQs) which are computed based on IERS conventions [McCarthy and Petit, 2004] and provided under Level 2 SST (Satellite-to-Satellite Tracking) block. The two transformations from ITRF to a quasi-inertial frame and from quasi-inertial frame to GRF can be represented as:

$$\begin{pmatrix} X \\ Y \\ Z \end{pmatrix}_{GRF} = R_{IRF}^{GRF} R_{ITRF}^{IRF} \begin{pmatrix} X \\ Y \\ Z \end{pmatrix}_{ITRF}, \quad (3.4)$$

where  $R_{ITRF}^{IRF}$  is the  $3 \times 3$  rotation matrix from ITRF to IRF and  $R_{IRF}^{GRF}$  is the  $3 \times 3$  rotation matrix from inertial frame to GRF and X, Y, and Z represent the vector components of the measurements in the  $x, y$ , and  $z$  directions, respectively. This transformation will be used in the following sections to transform equivalent ionospheric currents and model derived electric field and neutral wind components into GRF.

The rotation matrix for transforming measurements from one reference frame into another reference frame via the use of quaternions can be expressed as follows:

$$R_{3 \times 3} = \begin{bmatrix} q_1^2 - q_2^2 - q_3^2 + q_4^2 & 2(q_1 q_2 + q_3 q_4) & 2(q_1 q_3 - q_2 q_4) \\ 2(q_1 q_2 - q_3 q_4) & -q_1^2 + q_2^2 - q_3^2 + q_4^2 & 2(q_2 q_3 + q_1 q_4) \\ 2(q_1 q_3 + q_2 q_4) & 2(q_2 q_3 - q_1 q_4) & -q_1^2 - q_2^2 + q_3^2 + q_4^2 \end{bmatrix}, \quad (3.5)$$

where a quaternion is expressed as

$$q = q_4 + \mathbf{i}q_1 + \mathbf{j}q_2 + \mathbf{k}q_3, \quad (3.6)$$

where  $q$  has one real part ( $q_4$ ) and three complex parts  $\mathbf{i}q_1$ ,  $\mathbf{j}q_2$ , and  $\mathbf{k}q_3$ .

## 3.2 Calibrated Common-mode and Differential-mode Accelerations

---

The definition of the common-mode and differential-mode accelerations, CM- and DM accelerations, respectively, were given in the previous chapter. In this section, we investigate the filtered calibrated common-mode and differential-mode accelerations in detail and provide here our results.

Common-mode (CM, cf., Section 2.2.1) accelerations provide information on the non-gravitational accelerations of the satellite COM, whereas differential-mode (DM) accelerations represent the GGT components mixed with the centrifugal and angular accelerations of the satellite about its COM. Since the cause of the disturbances are non-gravitational forces, CM accelerations are investigated further here. Most of the results presented in this section are original and have been published in Ince and Pagiatakis [2016].

Calibrated CM accelerations are filtered (cf., section 3.1.1) into the GOCE gradiometer MBW. The CM accelerations in the along-track, cross-track, and radial directions are presented in Figures 3.4, 3.5 and 3.6, respectively. Since the ascending and descending tracks show different properties, they are examined separately. The measurements along satellite ascending tracks are given in the left panel, whereas the measurements along satellite descending tracks are given in the right panels of the figures.

The CM accelerations along the satellite track are collected by the accelerometer pair mounted along the  $X$ -axis of the GRF (A1-4). It is expected that these accelerations be very small, since there is a continuous air-drag compensation along the satellite track. Indeed, compared to the cross-track and radial directions, the filtered CM accelerations along the satellite track are very small and between  $\pm 5 \text{ nm/s}^2$ , as displayed in Figure 3.4. Even though the variability is very small, it is visible that the drag effect increases as the satellite approaches the polar regions.

The orientations of the satellite in the ascending and descending tracks are different; therefore, different features are observed in Figure 3.4. Moreover, we notice that there is a transition in the drag conditions around  $40^\circ$  south as the satellite altitude increases from north to south. The satellite altitude reaches the highest altitude over the South Pole, whereas it has the lowest altitude over the Equator; thus, it is exposed to different drag environment.

The CM accelerations in the cross-track direction of the satellite are shown in Figure 3.5. Compared to Figure 3.4, we see much larger variations representing the cross-track drag conditions over polar regions. One may notice positive and negative CM accelerations (blue and red colours over auroral regions) along both ascending and descending tracks, which correspond to the changes in the drift direction (e.g., eastern and western). The drag effects on the ascending tracks are larger in magnitude and spread over a larger

region compared to the descending tracks which correspond to 6 pm and 6 am local time, respectively. The cross-track CM accelerations are important in understanding the disturbances observed over the polar regions and it will be examined deeper in the following chapters.

Lastly, CM accelerations obtained in the radial direction from the accelerometer pair A3 and A6 are displayed in Figure 3.6. We see similar disturbances as the CM accelerations in cross-track direction with smaller magnitude ( $\pm 30 \text{ nm/s}^2$ ) over the polar regions. This indicates that there are forces dragging the satellite in the vertical direction (e.g., lift effect) both along ascending and descending tracks, which are similar to the ones seen in the cross-track direction. This may also indicate that the changes in the accelerations of the cross-track direction are related to the changes in the downward and upward radial drag changes and this effect may be projected onto other directions and needs to be considered in the following investigations.

It is worth mentioning that the CM accelerations show different signatures depending on the season and solar activity. The time period displayed in Figures 3.4, 3.5, and 3.6 (March-April, 2011) corresponds to medium to high level solar activity and drag conditions. In general, smaller variations are visible over the equatorial region. Siemes [2012], Stummer [2012], and Peterseim et al. [2011] mentioned that these signatures are due to cross wind over polar regions, but no specific description on the problem has been provided in the literature.

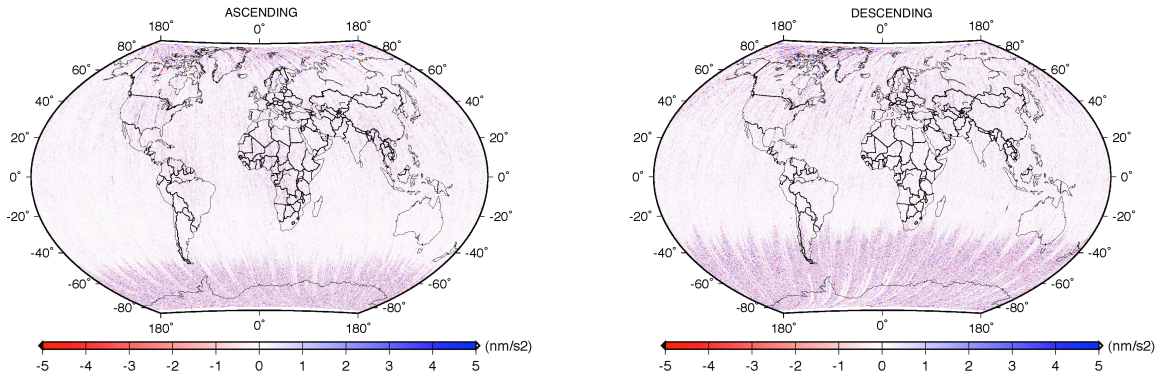


Figure 3.4: CM accelerations from A1 and A4 pair in the along-track direction are filtered into the Gradiometer MBW. Notice the larger drag effects in the polar regions.

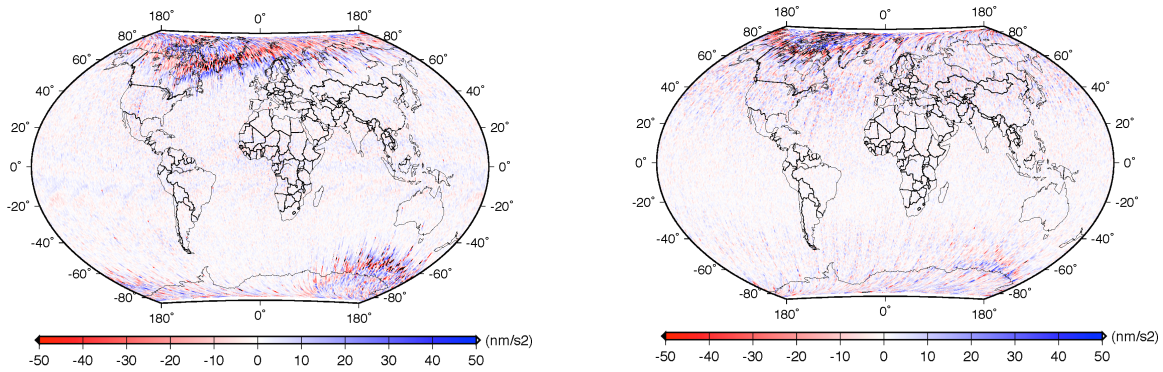


Figure 3.5: CM accelerations from A2 and A5 pair cross the track direction are filtered into the Gradiometer MBW. Notice the larger drag effects at higher latitudes. Moreover, ascending tracks are exposed to larger drag conditions over magnetic poles.

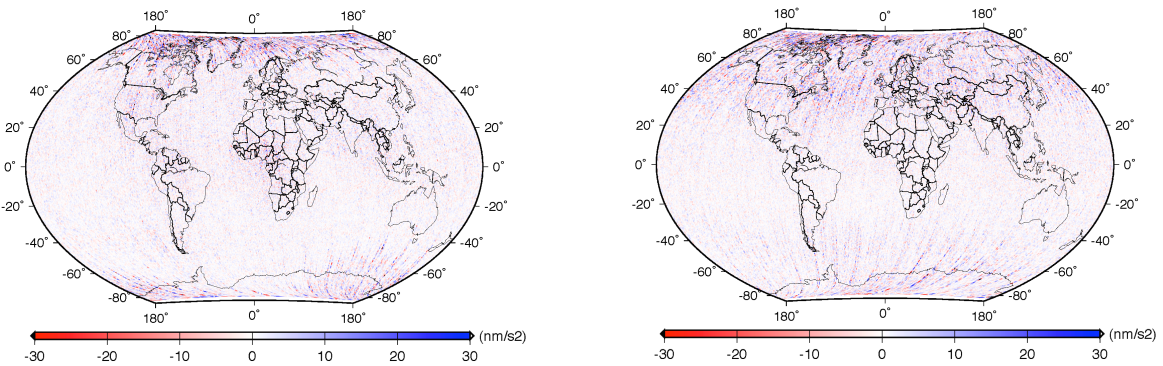


Figure 3.6: CM accelerations from A3 and A6 pair radial direction are filtered into the Gradiometer MBW. Notice the larger drag conditions over magnetic poles similar to cross-track CM accelerations.

### 3.3 Gravitational Gradient Tensor Components in Spatial Domain

---

The gravitational gradients that are filtered into the EGG MBW along the satellite tracks are geolocated and shown in Figures 3.7 to 3.12. The filtering process minimizes the effect of the noise outside of the MBW and reduces its effect in the measurement components of the MBW. Similar to the CM accelerations displayed above, the left panels of Figures 3.7 to 3.12 show the gradients along the satellite ascending tracks, whereas the right panels show the ones along the descending tracks.

One can recognize from the figures tectonic features, plate boundaries, mountainous regions and topography. For the first time in the gravity missions history, GOCE has provided gravitational gradients that contribute to the improvement of the global geoid model. Moreover, GOCE measurements contribute to the improvement of regional geoid models where high precision terrestrial gravity measurements are not available.

As mentioned in CM acceleration analyses, the orientation and altitude of the satellite differ between the ascending and descending tracks. Accordingly,  $V_{xx}$  and  $V_{yy}$  components displayed in the left and right panels of Figures 3.7 and 3.8 show differences in orientation and spectral resolution of the features. Since the orientation of the gravity vector, which also corresponds to the Z-axis of the GRF, does not differ between the ascending and descending tracks  $V_{zz}$  displayed in Figure 3.9 does not show any appreciable difference between the ascending and descending tracks.

The  $V_{xz}$  component is the only off-diagonal component that is measured by the ultra-sensitive axes; therefore, with higher accuracy, whereas the  $V_{xy}$  and  $V_{yz}$  components are less accurate and have a higher noise level globally. With further filtering, it may be possible to extract some useful information from the  $V_{xy}$  and  $V_{yz}$  gradients but this is not of concern in this research. Yi et al. [2013] states that the  $V_{xz}$  component contributes to the global geopotential models and should be included in the model computations. However, as displayed in Figure 3.10, this component is erroneous and shows the effect of the rotational acceleration over the Equator in both the ascending and descending tracks. Since it is a gravitational gradient, rotational accelerations should be removed entirely. Therefore, our analyses confirm that there are also significant errors involved in the high accuracy off-diagonal component  $V_{xz}$  and a revision in the data processing is indispensable for the improved gravitational gradients.

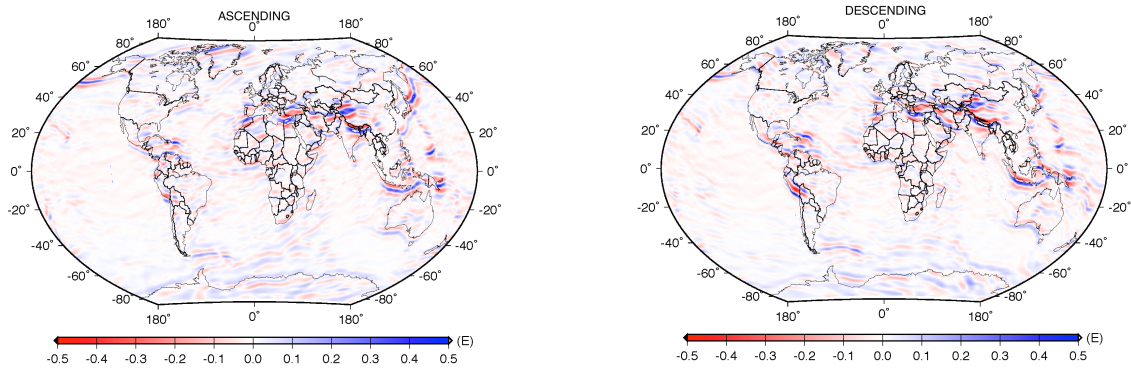


Figure 3.7:  $V_{xx}$  filtered into the Gradiometer MBW during March-April, 2011 for ascending and descending tracks. See the geophysical features along the track and the different resolution due to the different orientation of the X-axis in ascending and descending tracks.

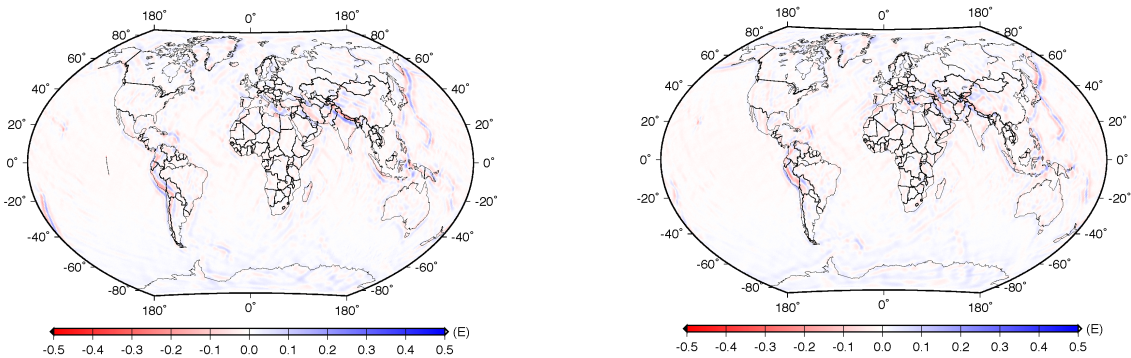


Figure 3.8:  $V_{yy}$  filtered into the Gradiometer MBW during March-April, 2011 for ascending and descending tracks. See geophysical features and the different resolution due to the different orientation of the Y-axis in ascending and descending tracks.

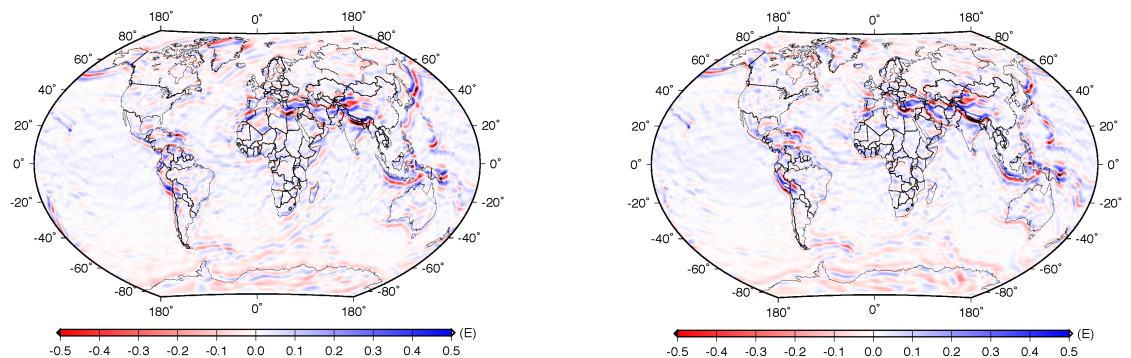


Figure 3.9:  $V_{zz}$  filtered into the Gradiometer MBW during March-April, 2011 for ascending and descending tracks. Since the orientation does not change for the Z-direction as opposed to the other diagonal components, the structure of the features does not change between the ascending and descending tracks.

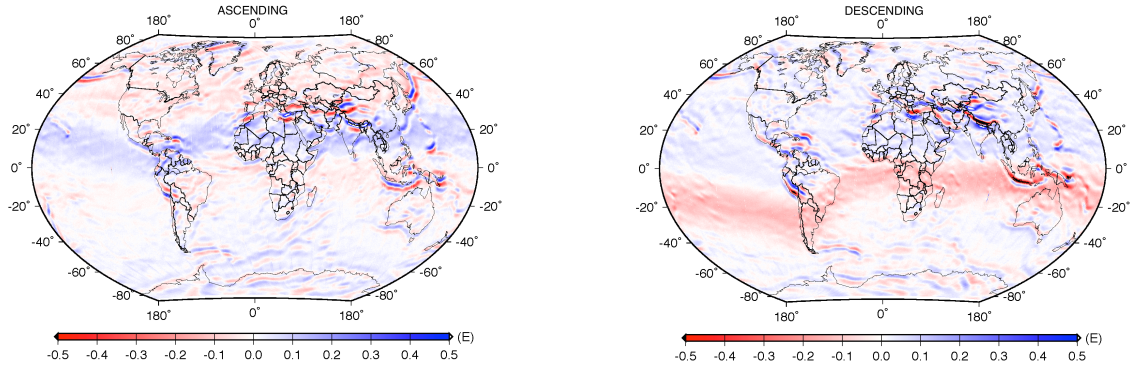


Figure 3.10:  $V_{xz}$  filtered into the Gradiometer MBW during March-April, 2011 for ascending and descending tracks.  $V_{xz}$  is the only ultra-sensitive off-diagonal GGT component. Note the effect of the rotational acceleration over Equator which leaks into the gravitational gradient due to the shortcomings of the calibration procedure that should be removed.

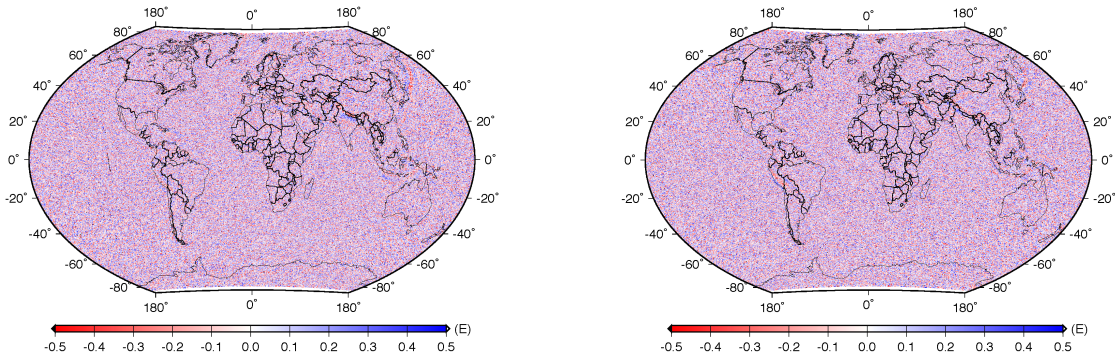


Figure 3.11:  $V_{xy}$  filtered into the Gradiometer MBW during March-April, 2011 for ascending and descending tracks.  $V_{xy}$  is derived from less-sensitive measurements. Note the signature over Equator and high noise level that obliterates any useful information.

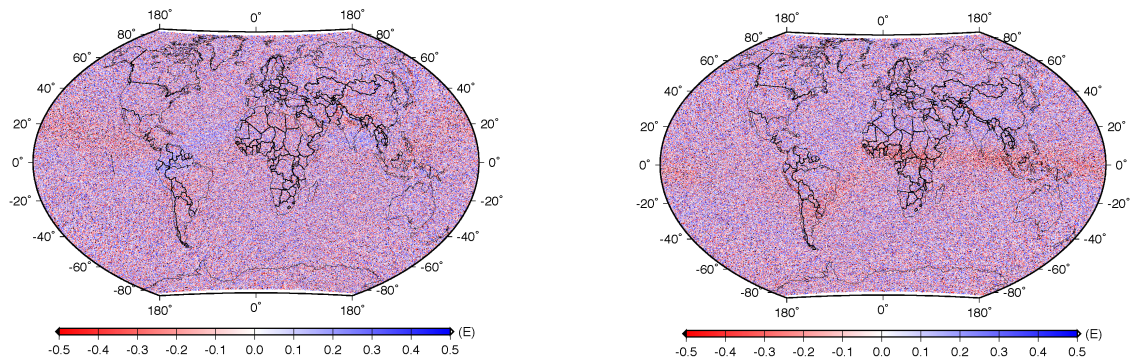


Figure 3.12:  $V_{yz}$  filtered into the Gradiometer MBW during March-April, 2011 for ascending and descending tracks.  $V_{yz}$  is derived from less-sensitive measurements. Note the high noise level that obliterates any useful information.

## 3.4 Identification of Inherent Measurement Problems

---

Our investigations and literature show that there are inherent problems in the currently applied processing scheme and analyses of data. This also means that there is still potential for the improvement of the GOCE data products as also indicated in Benveniste and Floberghagen [2015]. We look at the individual components as well as the trace of the GGT as given in this section.

### 3.4.1 Investigations on the GGT Components

Since the  $V_{yy}$  diagonal component is blamed for being the cause of these disturbances, a closer look at the ascending tracks is presented in Figure 3.13. These signals that are of non-gravitational origin appear over the high latitudes in the Northern hemisphere, over the Hudson Bay area and western Greenland, whereas they appear over the ocean in the Southern Hemisphere. Even though they show small variations in this representation, it is still visible that they cause short discontinuities in the filtered gradients in both hemispheres.

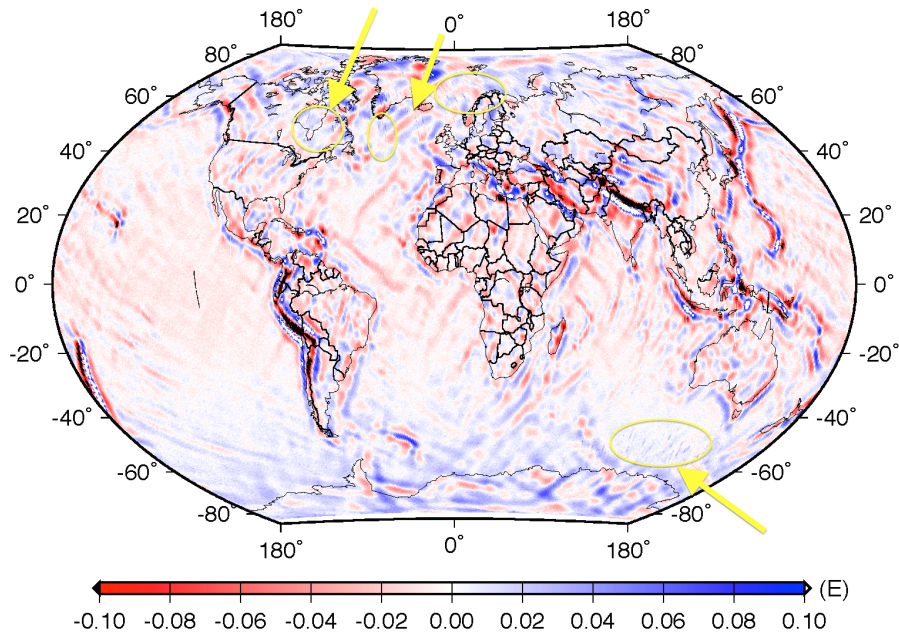


Figure 3.13:  $V_{yy}$  filtered into the Gradiometer MBW (0.1-0.005 Hz) during March-April, 2011 for ascending tracks. Note the small bumps over polar areas indicated by the yellow arrows.

The individual gradients that are measured by the gradiometer are investigated in the previous section. Figures 3.7 to 3.10 show the gradients that are filtered into the EGG MBW. In this section, we present comparisons of the gradients measured by the EGG and calculated based on one of the latest GRACE satellite-only models, ITSG-Grace2014k [Mayer-Gürr et al., 2014]. First, model-based gradients are calculated at the satellite altitude by using spherical harmonic coefficients expanded up to degree and order 200 using the routines provided by the team in Technical University of Munich. Then, each gravitational gradient calculated in EFRF is transformed into the GRF and band-pass filtered into the EGG MBW (10-200 s). The filtered EGG-measured gravitational gradients are compared with these ITSG-Grace2014k-based filtered series and geographically presented in the left and right panels of the Figures 3.14 to 3.16 for ascending and descending tracks, respectively. The left panels show the differences for ascending tracks, whereas the right panels show the differences for descending tracks.

The differences computed for  $V_{xx}$  are shown in Figure 3.14. It is seen that the differences are within the noise level of the instrument for both the ascending and descending tracks and they are homogeneously distributed over the globe. Therefore, we do not expect to have any significant shortcomings of the data processing due to the  $V_{xx}$  measurements. The differences for  $V_{yy}$  are shown in Figure 3.15. Strong spurious signals appear over the geomagnetic poles and larger spatial scale signatures exist over the North magnetic pole along ascending tracks. This proves that there are considerable differences between the EGG measurements and model computed  $V_{yy}$  and it is an indication of the errors coming from the  $V_{yy}$  measurements. Finally, the differences for  $V_{zz}$  are displayed in Figure 3.16 which show similar characteristics to  $V_{xx}$ . However, higher noise level is seen in the  $V_{zz}$  comparisons due to the higher noise level of EGG  $V_{zz}$  measurement itself. Therefore, we confirm that there are considerable differences between the  $V_{yy}$  gradients and the predicted ones based on ITSG-Grace2014k model and the other two diagonal components,  $V_{xx}$  and  $V_{zz}$  can be assumed as errorless. This outcome hints that the GOCE gradients computed from cross-track measurements include larger errors compared to the other two diagonal GGT elements and need to be eliminated for final products of GOCE EGG.

As mentioned in the previous sections, these disturbances appear in the lower frequency interval of the MBW and outside of it. Therefore, the same gravitational gradients computed based on ITSG-Grace2014k are this time filtered into a different frequency interval (180-300 s). The comparisons are performed once again for this interval and differences along the ascending and descending tracks are presented in left and right panels of Figures 3.17 to 3.19, respectively.

Comparisons performed for this frequency band in the spatial domain show that the differences are much larger in the  $V_{yy}$  component and mimic the areas of auroral ovals. Differences observed in  $V_{xx}$  and  $V_{zz}$  do not exceed a few percent of the errors observed in  $V_{yy}$ . Therefore, the measured  $V_{yy}$  component is again the one to blame. However, it is worth noting that there are also some differences due to the angular accelerations, such as the ones observed in the equatorial regions of the  $V_{zz}$  ascending and descending tracks. These visualizations help us understand how the differences in various bandwidths look like in the three diagonal GGT components in the spatial domain and have not been mentioned in the literature and they complement the spectral analyses performed in this research.

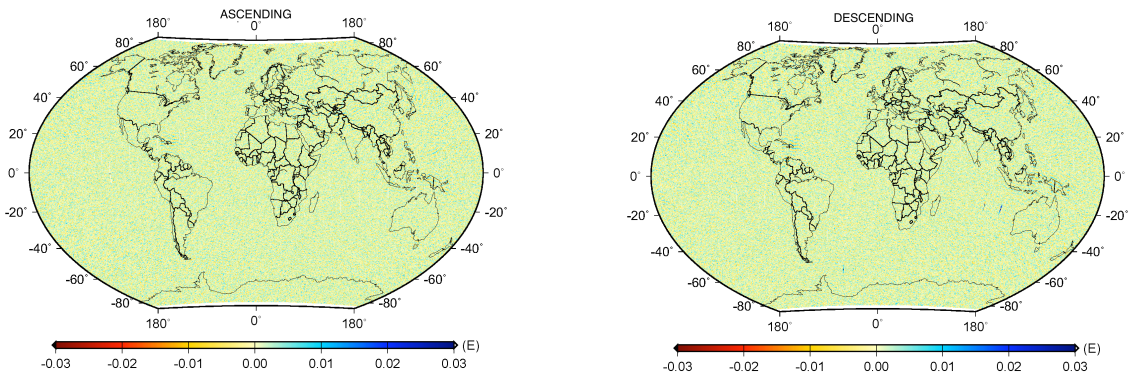


Figure 3.14: The differences between the EGG measured  $V_{xx}$  and the ITSG-Grace2014k model computed  $V_{xx}$  are shown for the EGG MBW (10-200s) during March-April, 2011. The differences along the ascending tracks are shown in left panel, whereas the differences along the descending tracks are shown in right panel. There are no considerable differences appear in  $V_{xx}$ .

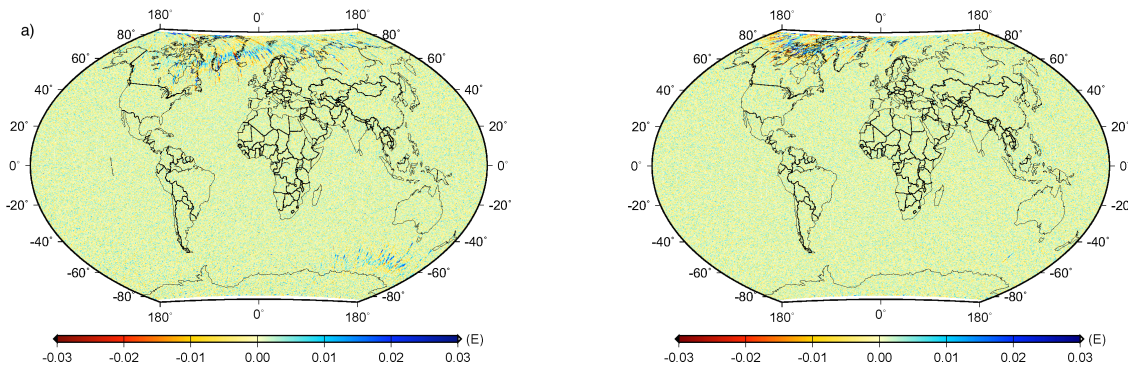


Figure 3.15: The differences between the EGG measured  $V_{yy}$  and the ITSG-Grace2014k model computed  $V_{yy}$  are shown for the EGG MBW (10-200s) during March-April, 2011 in the left and right panels of the figure for ascending and descending tracks, respectively. Note the very distinctive differences over geomagnetic poles which hints the error coming from EGG retrieved  $V_{yy}$ .

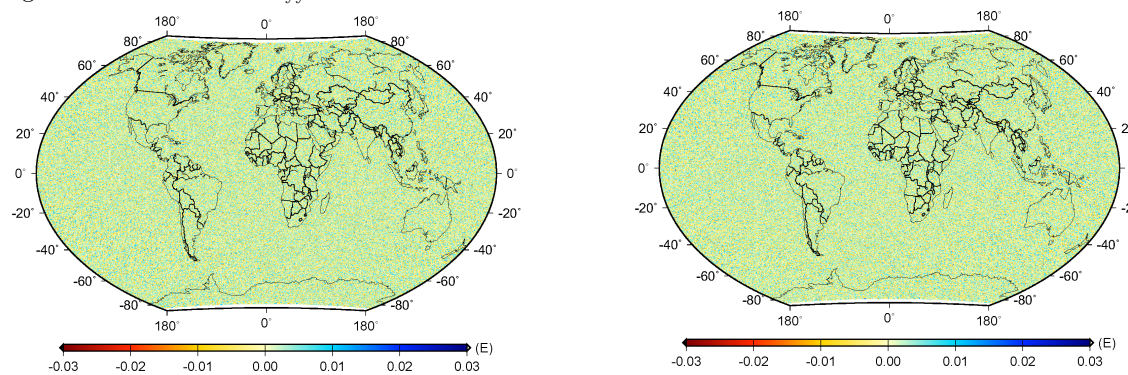


Figure 3.16: The differences between the EGG measured  $V_{zz}$  and the ITSG-Grace2014k model computed  $V_{zz}$  are shown for the EGG MBW (10-200s) during March-April, 2011 in the left and right panels of the figure for ascending and descending tracks, respectively. No considerable differences appear in the polar regions.

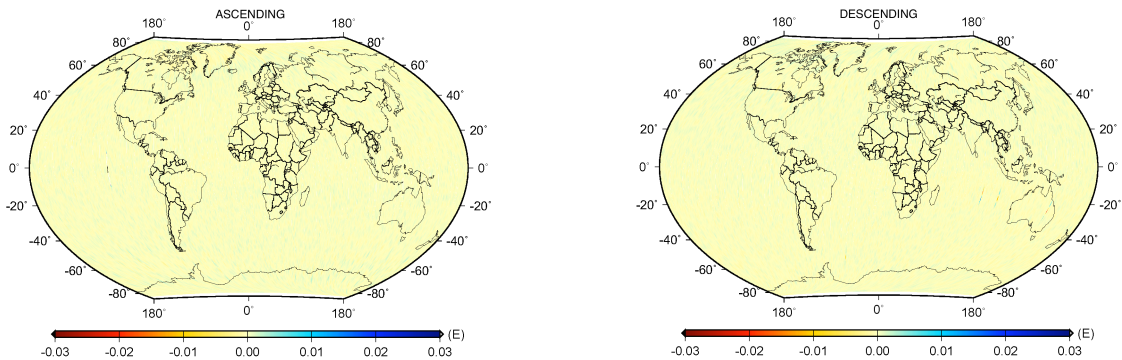


Figure 3.17: The differences between the EGG measured  $V_{xx}$  and the ITSG-Grace2014k model computed  $V_{xx}$  are shown for the bandwidth of [180-300]s during March-April, 2011. The differences along the ascending tracks are shown in left panel, whereas the differences along the descending tracks are shown in right panel. There are no considerable differences appear in  $V_{xx}$ .

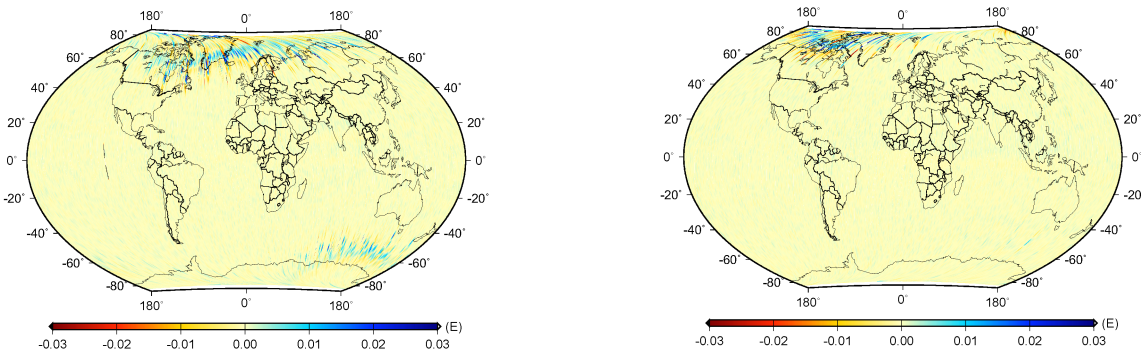


Figure 3.18: The differences between the EGG measured  $V_{yy}$  and the ITSG-Grace2014k model computed  $V_{yy}$  are shown for the bandwidth of [180-300]s during March-April, 2011 in the left and right panels of the figure for ascending and descending tracks, respectively. Note the very distinctive differences over geomagnetic poles which hints the error coming from EGG retrieved  $V_{yy}$ . Also note the differences wrt Figure 3.15.

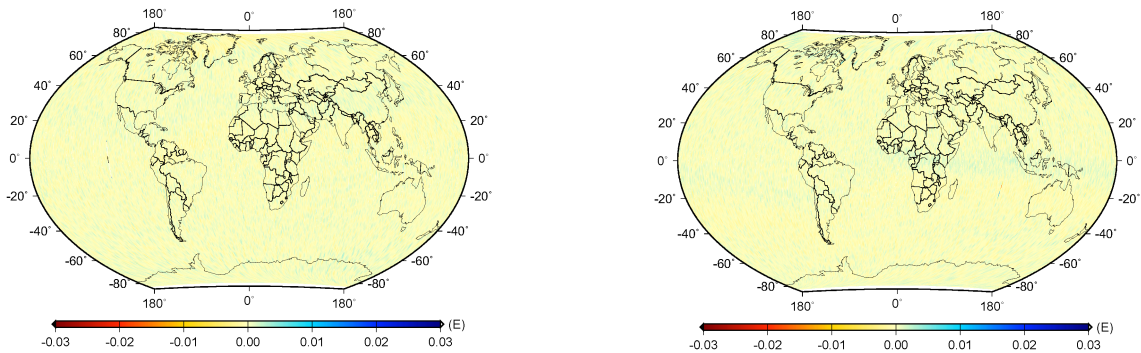


Figure 3.19: The differences between the EGG measured  $V_{zz}$  and the ITSG-Grace2014k model computed  $V_{zz}$  are shown for the bandwidth of [180-300]s during March-April, 2011 in the left and right panels of the figure for ascending and descending tracks, respectively. Some signatures appear over the Equator.

### 3.4.2 Investigations on the GGT Trace

The GGT trace is a very good indicator of the quality of the gradiometer measurements. According to Laplace equation, the GGT trace is expected to be zero within the noise level of the instrument ( $\sim 11 \text{ mE}$ ) and within the MBW. Therefore, looking into the trace in time, space, and frequency domains helps researchers identify any inherent problems present in the GGT diagonal components. The trace of the GGT along the ascending and descending tracks of March-April, 2011 over the geomagnetic poles are shown in Figures 3.20 and 3.21, respectively.

The trace along the ascending tracks demonstrates that there exist signals of significant magnitude, about five times of the noise level of the instrument, over the magnetic poles as shown in Figure 3.20. These spurious signals do not represent any gravitational field-related signal, but show residual non-gravitational signals projected onto the diagonal gradients. It is shown that these signals are residuals of larger scale spatial variations of ionospheric dynamics and spread over a larger area of the North Pole ascending tracks and centred over a much smaller area in the South Pole along ascending tracks.

GOCE was a dusk-dawn satellite, therefore the ascending tracks correspond to 6 pm local time, whereas the descending tracks correspond to 6 am local time. Accordingly, there are differences in the satellite environment. It is seen that the spurious signals are smaller in descending tracks in the North Pole and almost vanish in the South as shown in Figure 3.21.

In this research, we focus on the larger disturbances along ascending tracks over the North Pole and aim to reduce their effect of non-gravitational accelerations leaking into the gradients by using external datasets, such as proxies of ionospheric dynamics which help us understand the satellite environment and the extreme conditions it is exposed to.

The non-gravitational accelerations leaking into the gradients are possibly caused by the increased ionospheric dynamics in the east-west and radial directions over the polar regions [Ince and Pagiatakis, 2016]. The diagonal gravitational gradients of the tensor are filtered into the gradiometer MBW (10-200s) and plotted as a stack of trace observations with respect to latitude. Figure 3.22 displays the 954 ascending and descending tracks of March-April, 2011 with respect to latitude along the satellite tracks in the upper and lower panels, respectively. As expected, the largest variations occur over high latitudes, over the auroral oval<sup>1</sup> which can reach up to 100 mE in the ascending tracks. The descending tracks show smaller disturbances in general and located at latitudes above 65° North.

---

<sup>1</sup>Auroral oval is where the aurora borealis (in the North) or the aurora australis (in the South) occurs. Energetic particles that precipitate from the magnetosphere into the upper atmosphere produce the visible emissions as “aurora” [Cravens, 2004].

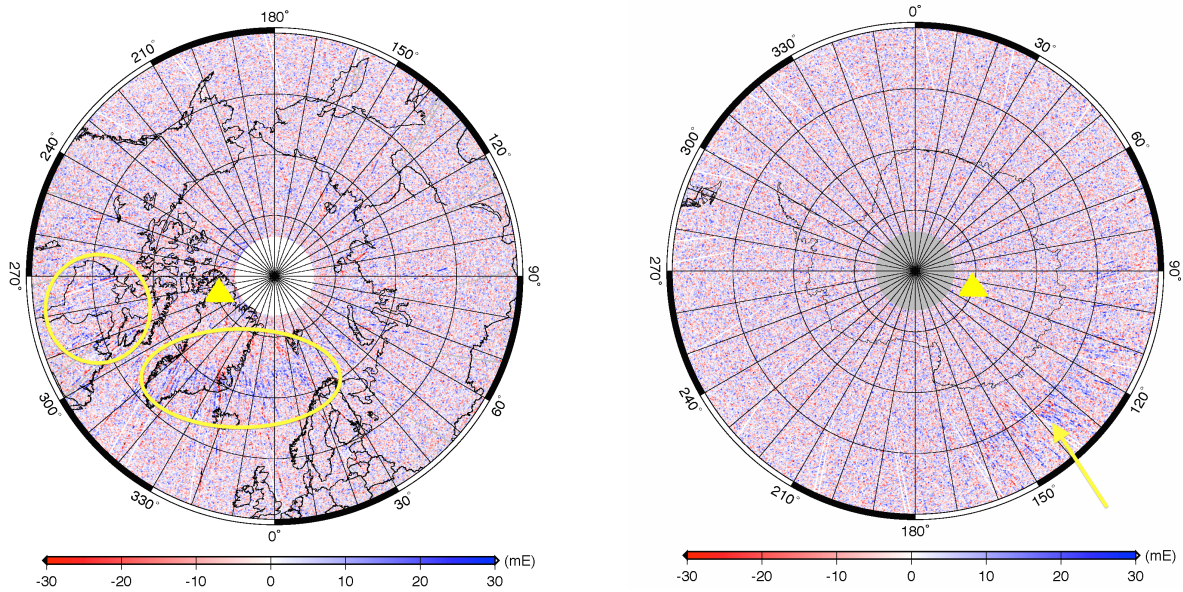


Figure 3.20: Trace along the ascending tracks filtered into the Gradiometer MBW and geolocated over the Polar regions during March-April, 2011. Note the disturbances visible around the geomagnetic poles and larger scale variations in the North Pole.

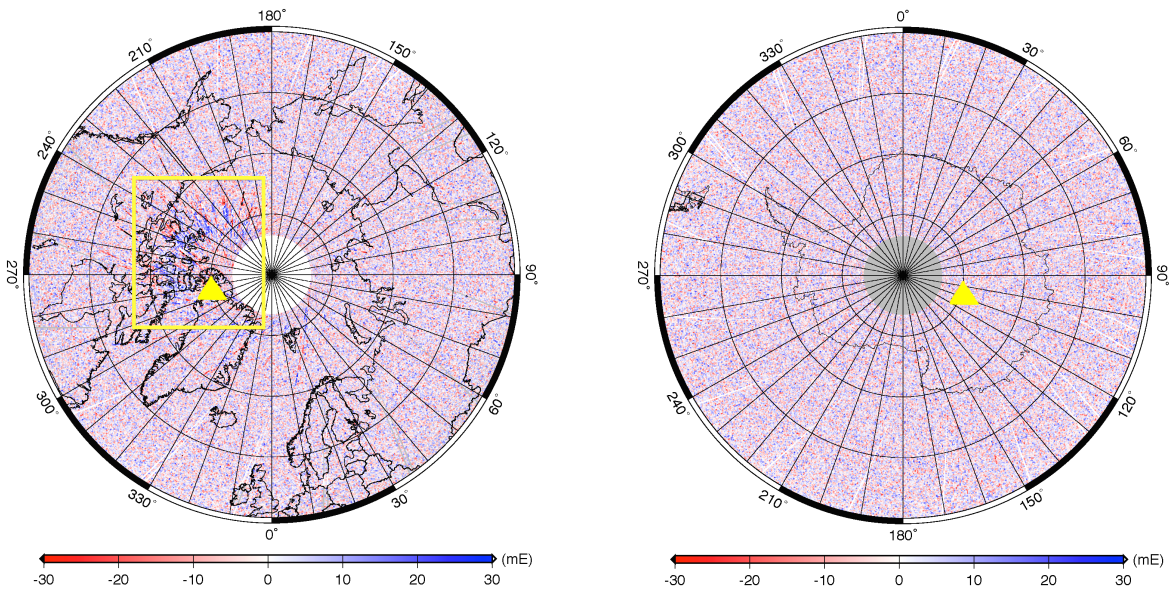


Figure 3.21: Trace along the descending tracks filtered into the Gradiometer MBW and geolocated over the Polar regions during March-April, 2011. Note the reduced disturbances around the geomagnetic poles in the North compared to the ascending tracks. Disturbances over the South Pole almost vanish.

It is clearly seen in the left panel of Figure 3.20 that the spurious signals along the ascending tracks over the North Pole mimic the regions of auroral oval including Northern Canada and Greenland. There are extensive research studies on this topic to understand the complex interaction of the ionosphere with the magnetosphere [Atkinson, 1970, Cowley, 2000, Lühr et al., 2007, Doornbos et al., 2013, Lu et al., 2014] and its effects on ionosphere. In the following chapter, we show our analyses performed on the products of other research topics.

The diagonal gravitational gradients are filtered into a bandwidth where we observe the strongest effects (180-300 s) and displayed in terms of the GGT trace for many tracks in Figure 3.23 similar to Figure 3.22. The ascending tracks are exposed to ionospheric variations above 50°N, where the larger disturbances are located between latitudes 50°N and 70°N. Descending tracks show different properties and are exposed to large variations around the areas above 70°N and show variable signal strength. In the next chapter, we investigate two different cases that are shown by red and green lines along the ascending tracks and compare them with the dynamics of the ionosphere [Ince and Pagiatakis, 2016].

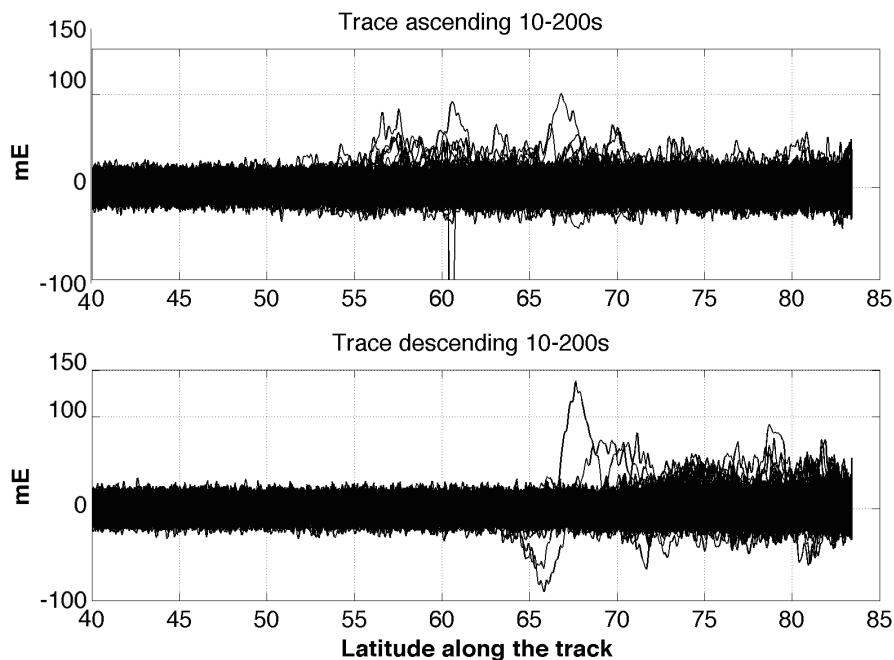


Figure 3.22: Trace filtered into the Gradiometer MBW (10-200 s). The 954 tracks are plotted wrt latitude along the tracks. Note the disturbances visible around the high latitudes where there are more variabilities in the ascending tracks (upper panel).

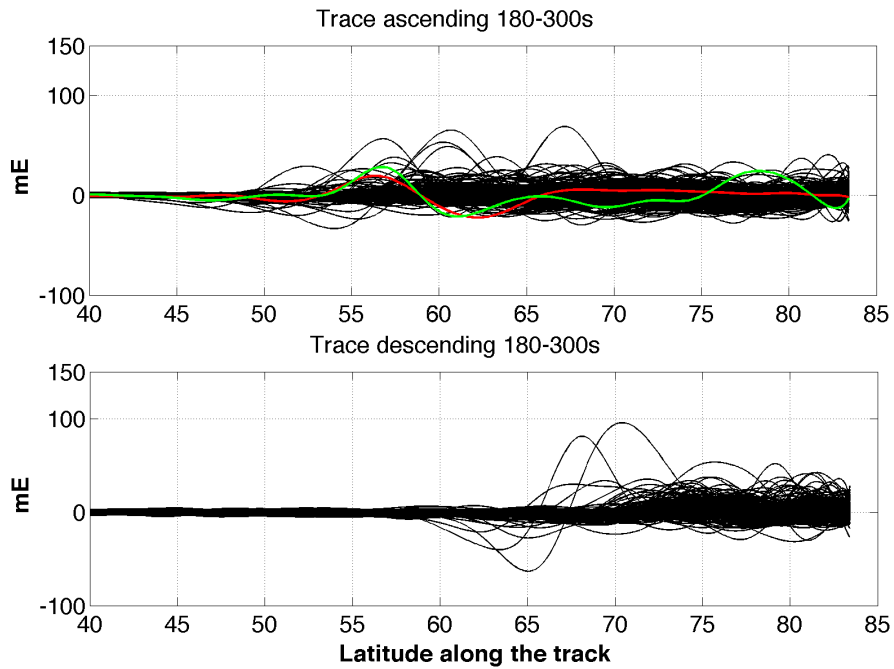


Figure 3.23: Trace filtered into 180-300 s interval where the variations show their characteristics the most. The 953 tracks are plotted wrt latitude along the tracks. One track is detected as outlier. Note the higher level of variations in the ascending tracks (upper panel). Note the different characteristics of the trace along ascending and descending tracks.

### 3.4.3 Investigations of the Angular Accelerations

The GOCE mission comprises many different instruments and sensors. In this section, we investigate the angular accelerations derived from the combination of the star trackers and acceleration measurements in transversal directions. We investigate the angular accelerations of the GRF with respect to the Local Orbital Reference Frame (LORF) (see Figure 3.3). It is worth remembering that the Z-axis of GRF approximately points downwards to the geocentre; whereas the Y-direction is in the opposite direction of angular momentum vector. LORF differs from the GRF in the directions of the Y- and Z-axes by  $180^\circ$ . Accordingly, Yi [2011] defines a new system LORF', with its X-axis the same as that of LORF, but the Y- and Z-axes are defined to point in the opposite direction of those of LORF.

The unit base vectors in LORF' are given in the inertial frame (IRF) as follows:

$$\begin{aligned} \mathbf{e}'_S &= \frac{\mathbf{v}}{|\mathbf{v}|}, \\ \mathbf{e}'_T &= \frac{\mathbf{r} \times \mathbf{v}}{|\mathbf{r} \times \mathbf{v}|}, \\ \mathbf{e}'_W &= -\mathbf{e}'_S \times \mathbf{e}'_T, \end{aligned} \tag{3.7}$$

where  $\mathbf{r}$  and  $\mathbf{v}$  are the position and velocity vectors, respectively. The transformation (rotation) matrix from LORF' to IRF is expressed as:

$$R_{LORF'}^{IRF} = \begin{bmatrix} \mathbf{e}'_S \\ \mathbf{e}'_T \\ \mathbf{e}'_W \end{bmatrix}. \tag{3.8}$$

Therefore, the transformation between the LORF' and GRF is

$$R_{LORF'}^{IRF} = R_3(\psi)R_2(\theta)R_1(\varphi), \tag{3.9}$$

which is

$$R_{LORF'}^{IRF} = \begin{bmatrix} \cos\theta\cos\psi & \cos\varphi\sin\psi + \sin\psi\sin\theta\cos\psi & \sin\varphi\sin\psi - \cos\varphi\sin\theta\cos\psi \\ -\cos\theta\sin\psi & \cos\varphi\cos\psi - \sin\varphi\sin\theta\sin\psi & \sin\varphi\cos\psi + \cos\varphi\sin\theta\sin\psi \\ \sin\theta & -\sin\varphi\cos\theta & \cos\varphi\cos\theta \end{bmatrix}, \tag{3.10}$$

where  $\theta$ ,  $\varphi$ , and  $\psi$  are the pitch, roll, and yaw angles about the Y', X', and Z' axes, respectively.

The transformation from GRF to LORF' is provided by Equation 3.4 as,

$$R_{GRF}^{LORF'} = R_{IRF}^{LORF'} R_{GRF}^{IRF}.$$

The three rotation angles can be computed as follows:

$$\begin{aligned}
\varphi &= \arctan \left( -\frac{R_{GRF}^{LORF'}(3, 2)}{R_{GRF}^{LORF'}(3, 3)} \right), \\
\theta &= \arctan \left( -\frac{R_{GRF}^{LORF'}(3, 1)}{\text{sqrt}R_{GRF}^{LORF'}(3, 2)^2 + R_{GRF}^{LORF'}(3, 3)^2} \right), \\
\psi &= \arctan \left( -\frac{R_{GRF}^{LORF'}(2, 1)}{R_{GRF}^{LORF'}(1, 1)} \right),
\end{aligned} \tag{3.11}$$

where  $R_{nm}$  is the rotation matrix and  $n$  and  $m$  represent the row and column number of the matrix. For example,  $R_{IRF}^{LORF'}$  represents the  $3 \times 3$  rotation matrix from IRF to LORF'.

The pitch angle shows strong correlation with the magnetic field over the Equator and experiences large oscillations over these areas. This correlation is due to the attitude control system driven by magnetic torquers [Yi, 2011]. We furthermore filter these angles into the GOCE MBW in order to see whether there are common features (larger variations over polar regions) in the angular accelerations that are similar to the ones observed in trace and  $V_{yy}$  component. These analyses also indicate how well the GOCE GRF follows the LORF. It is shown in Figure 3.24 that the GOCE attitude angle about the Z-direction (yaw) is also exposed to larger variations over the magnetic poles and the Equator [Ince and Pagiatakis, 2016].

As mentioned previously, the satellite attitude is controlled by the magnetic torquers only. This technique comes with pros and cons. It is a very useful technique since it does not require large energy consumption. However, magnetic torquers can only apply a torque perpendicular to the magnetic field lines and are not able to control the attitude about the direction of the magnetic field lines. Accordingly, the magnetic torquers are not able to control the roll angle about the X-axis around the equatorial region and the yaw angle about the Z-axis over the polar regions. Therefore, there is little or no control about the Z-axis around the magnetic poles since the magnetic field lines are nearly vertical [Siemes, 2012].

The pitch and roll angles between the LORF and GRF are also presented in Figures 3.25 and 3.26, respectively. Both figures show larger variations over the Equator, but do not show any hints related to the spurious signals similar to the ones observed in Trace and  $V_{yy}$  differences.

It is also worth discussing that the response of the magnetic torquers may not be applied as precisely and without delay since the magnetic torquers provide a smooth directional change and not instantaneous correction. This may also create problematic attitude control when the ionospheric variations are extreme and abrupt. However, the attitude of the satellite is measured by the three star trackers and gradiometer

observations. The combination of these instruments provide high accuracy in both lower and high frequency bands, since the star trackers provide accurate information in the low frequency band, whereas the transversal accelerations are used to obtain high frequency attitude angles. The combination is performed based on the noise level of the instruments as given in Stummer et al. [2011]. The rotational angle is removed from the differential-mode accelerations. Accordingly, this effect should not propagate into GGT if computed correctly.

In this research, based on the literature and personal communications, we assume that the coupling of the torquers with the magnetic field are eliminated from being the cause of these disturbances. We also assume that any problems in the computation of attitude angle cannot give such a rise to the gradiometer disturbances. Therefore, we proceed to investigate external sources causing these disturbances over the polar regions and develop an empirical correction model in order to eliminate/reduce these disturbances.

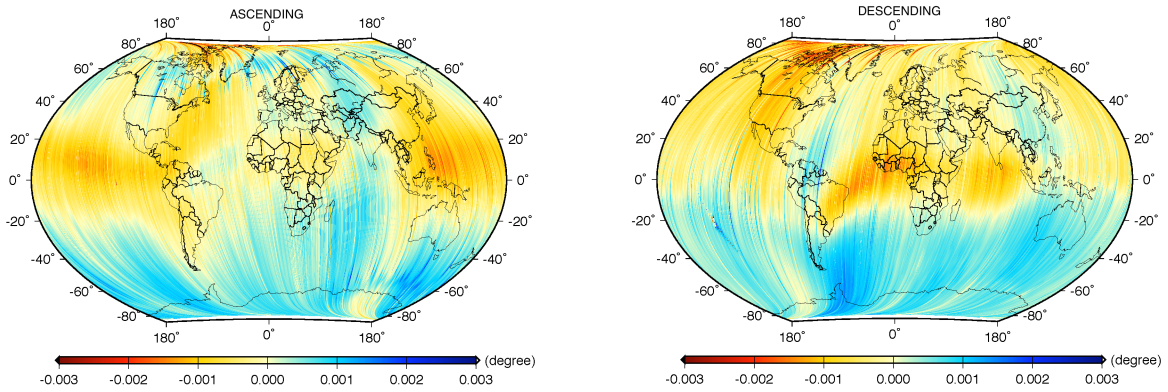


Figure 3.24: Yaw angle between the LORF and GRF along ascending and descending tracks filtered into the GOCE MBW. Note that the larger attitude control corresponds to the regions over the magnetic poles which has an effect on the computation of  $V_{yy}$ .

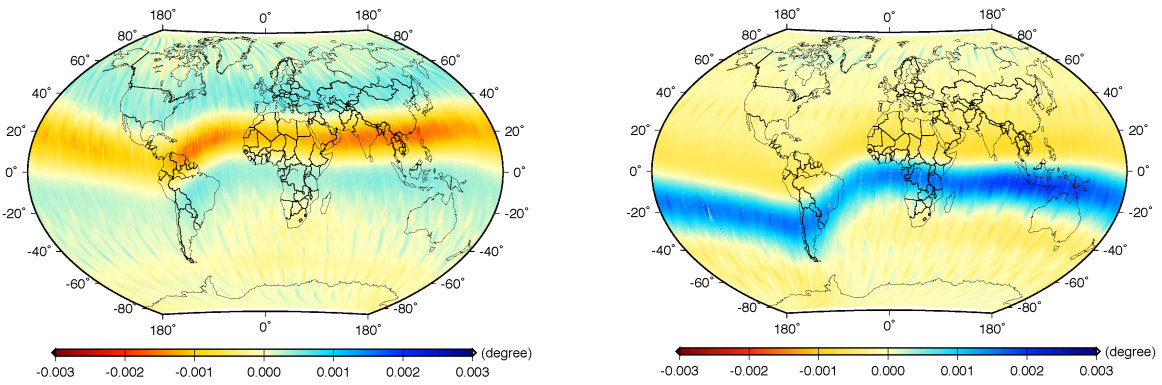


Figure 3.25: Pitch angle between the LORF and GRF along ascending and descending tracks filtered into the GOCE MBW. Note the larger variations over the Equator.

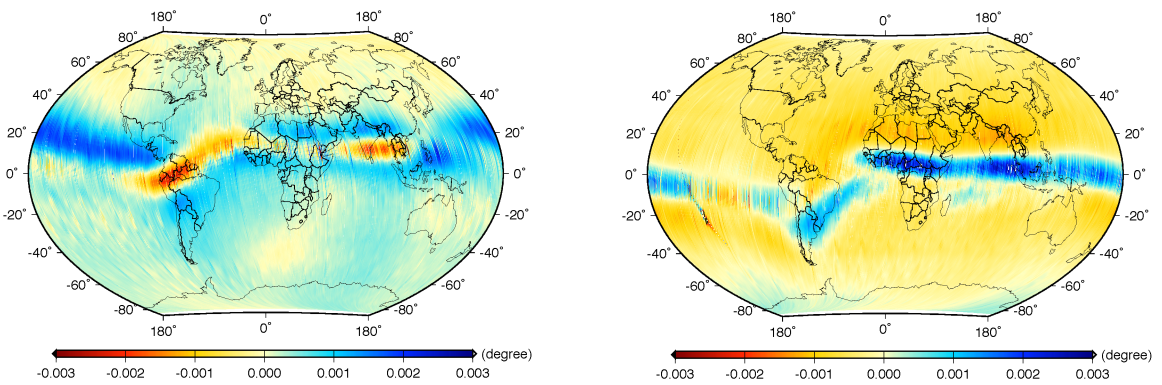


Figure 3.26: Roll angle between the LORF and GRF along ascending and descending tracks filtered into the GOCE MBW. Note the larger variations over the Equator.

## 3.5 Summary

---

In this chapter, we described the gradiometer data and their properties in detail. The gradiometer design required applying a band-pass filter to the gradiometer data to reduce the measurement noise outside of the gradiometer measurement bandwidth. Consequently, a filtering procedure was designed and applied. We have shown the power spectral densities of the original diagonal gravitational gradients and filtered gravitational gradients in order to emphasize the importance of the filtering procedure. We mentioned that we applied a different filter, namely the Gaussian filter than the commonly used Butterworth filter to evaluate the EGG data.

We summarized the reference frames associated with the gradiometer orbit, ITRF, and IRF and presented all necessary transformations among the coordinate systems. We presented calibrated common-mode accelerations and gradients that were filtered into the gradiometer measurement bandwidth and geolocated and we investigated them in detail. We discovered problems observed in the gradients by comparing them with satellite-based reference gradients and emphasized the larger errors in the  $V_{yy}$  component. Finally, we introduced the gravitational gradiometer tensor trace, which is commonly used to check the quality of the gradiometer measurements and investigated in spatial domain and along the satellite ascending and descending tracks. We discovered that the trace can reach up to 5 times the expected noise level of the instrument in particular regions at particular epochs. We confirmed that the trace is affected at higher latitudes. Moreover, we saw that the ascending tracks show higher level of variations and noise level, distributed into a larger area and show larger spatial variations compared to the descending tracks. Finally, we investigated attitude angles and found that the deviations of the Gradiometer Reference Frame from the Local Orbital Reference Frame are larger over the polar regions for yaw angle and larger over the Equator for pitch and roll angles. The investigations on the attitude angles are original and most of them are presented here for the first time. We confirmed that the attitude control of the satellite was also affected in these regions particularly, which also supported the relationship between the disturbances observed in the gradients with the satellite environment.

This chapter summarized how the disturbances were discovered and what the preliminary investigations were in understanding their causes. This chapter will help understand the following chapters clearly and develop a relationship between the GOCE data and external datasets that are going to be introduced in the next chapter.

# 4

## Ionosphere, Geomagnetic Field and Space Weather

### 4.1 Ionosphere

---

The Earth's ionosphere (at an altitude range of approximately 60-2000 km) consists of a partially ionized gas which surrounds the Earth and creates an interface between the neutral atmosphere and space. The ionized gas cannot be fully described by using the equations of neutral fluid dynamics. Both atmospheric dynamics and deep space plasma physics need to be considered to understand how the ionosphere is formed [Kamide and Chian, 2007, Kelley, 2009].

Historically, knowledge of ionospheric physics is desired to understand the origin and effects of the ionized upper atmosphere on radio wave propagation. The various ionospheric layers and their variability with local time, latitude, and season are of particular interest. For this purpose, ionosondes<sup>1</sup> which help to derive electron density profiles were used as the primary research tool [Kelley, 2009].

The ionosphere coexists with the upper portion of the neutral atmosphere<sup>2</sup>. It receives considerable energy and momentum from the lower atmosphere (below the ionosphere) as well as from the magnetosphere. Particles, electromagnetic fields, and atmospheric waves carry energy and momentum fluxes [Kelley, 2009].

A representative temperature profile can be used to understand the structure of the atmosphere, while the number density of plasma<sup>3</sup> is used for the ionosphere. Typical mid-latitude profiles of temperature and plasma density are shown in Figure 4.1. The atmospheric temperature initially decreases with increasing

---

<sup>1</sup>The ionosonde technique is used to determine the density profile of the ionosphere. The technique is based on the reflection of a radio wave at a critical layer of the ionosphere due to wave cut-off [Kamide and Chian, 2007].

<sup>2</sup>Neutral Atmosphere: A neutral atmosphere is an atmosphere that consists of neutral gas, in contrast with the ionosphere [Selsis, 2011].

<sup>3</sup>Plasma: The stream of charged particles of both signs in equal number [Kivelson and Russell, 1995].

altitude from the surface, where the rate of the change is about 7 K/km in the troposphere. This temperature gradient reverses at about 10 km altitude (at the tropopause), where the stratosphere begins. The increase is mostly due to the absorption of the ultraviolet portion of the solar radiation by ozone. The temperature gradient once again reverses at the stratopause (at 50 km). At about 90 km, radiation cooling creates a very distinctive temperature decrease to its minimum at 130–190 K. Then, the temperature increases sharply from the mesopause upwards due to very high energy solar photons. Therefore, this region is called thermosphere [Kelley, 2009] where GOCE was orbiting.

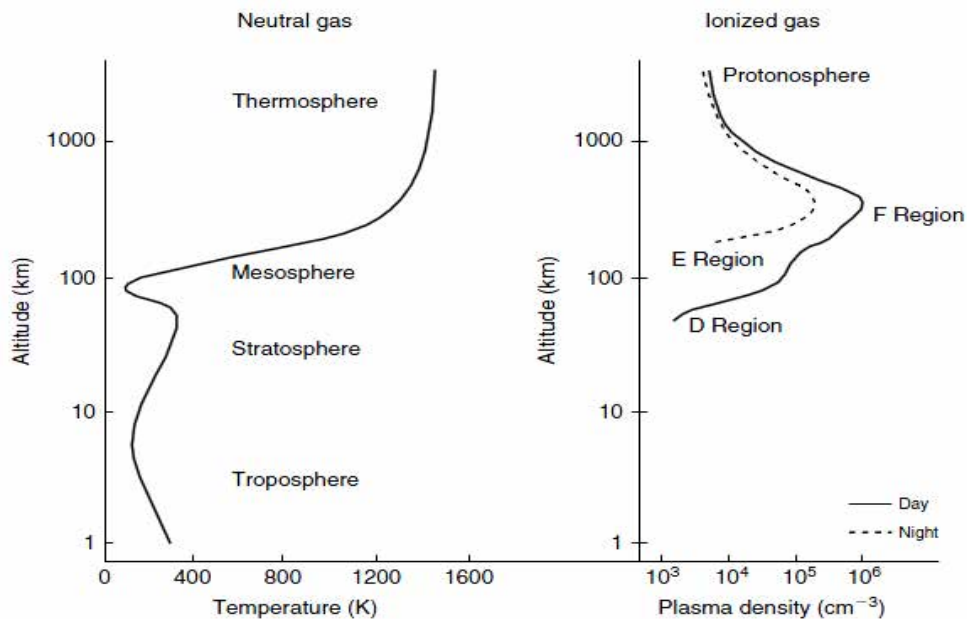


Figure 4.1: Typical profiles of neutral atmospheric temperature and ionospheric plasma density for the various layers of the atmosphere, image credit: Kelley [2009].

The absorption of UV and EUV (Extreme ultraviolet) radiation from the Sun causes temperature increase in the thermosphere. These solar photons have sufficient energy to ionize the neutral atmosphere. Therefore, the EUV radiation is also responsible for the production of plasma in the sunlit hemisphere.

The Earth’s ionosphere is divided in different regions, such as D, E, and F (Figure 4.1), where F is subdivided into F1 and F2 regions. In the F region, electric-field driven currents are formed in the direction of the electric field, whereas in the E region, electric field-driven currents are formed in the direction of the

electric field near the peak in the Pedersen Conductivity<sup>4</sup> and in the opposite direction of the  $\mathbf{E} \times \mathbf{B}$  vector near the peak in the Hall Conductivity<sup>5</sup> where  $\mathbf{B}$  is the magnetic field strength [Kelley, 2009].

F region currents are weakly dependent on time. Very small differences occur between the night and daytime, where slightly smaller currents occur during the night time. However, E region currents are strongly dependent on time and they are the largest during daytime. Electric currents in the E region occur in the auroral regions during daytime, where the conductivity is enhanced by particle precipitation. At high latitude, the electric potential created by the field-aligned currents drives E-region currents in the direction of  $\mathbf{E} \times \mathbf{B}$  that are referred to as the auroral electrojets and in the direction of  $\mathbf{E}$ , which have a strong impact on the ionospheric dynamics; therefore our analyses of GOCE gradient disturbances.

## 4.2 Solar Activity and Space Weather Observations

---

Space weather is described as “conditions on the Sun, in the solar wind, and within the Earth’s magnetosphere, ionosphere and thermosphere that can influence the performance and reliability of space-borne and ground-based technological systems” [Wright Jr et al., 1995], and most importantly measurements in our case. Coupling of magnetosphere and ionosphere is one of the most important phenomena affecting ionospheric dynamics. Especially in the polar regions, the coupling of the magnetosphere<sup>6</sup> and ionosphere causes ion convection (ion winds) which are greatly perturbed during geomagnetic storms. Moreover, due to ion-neutral momentum transfer and thermospheric heating, neutral winds at all thermospheric latitudes becomes larger.

Interaction of the solar wind that is a fully ionized plasma with the Earth’s magnetic field is very crucial in predicting space weather variations. In Kelley [2009], the solar wind is described as steadily streaming outflow of material that escapes from the gravitational attraction of the Sun due to its high temperature. These charged particles released from the upper atmosphere of the sun create a plasma flow that interacts with the geomagnetic field around the geomagnetic poles where the magnetosheath plasma has direct access to the ionosphere [Russell, 2000].

---

<sup>4</sup>Pedersen Conductivity: The conductivity parallel to an electric field  $\mathbf{E}$ . Joule heating develops due to Pedersen currents flow.

<sup>5</sup>Hall Conductivity: The conductivity orthogonal to  $\mathbf{E}$  and the main internal geomagnetic field  $\mathbf{B}$ .

<sup>6</sup>Magnetosphere: The magnetosphere is the region of space that surrounds the Earth where the dominant magnetic field is the magnetic field of the Earth, rather than the magnetic field of interplanetary space. The magnetosphere is formed by the interaction of the solar wind with the Earth’s magnetic field (<http://www.swpc.noaa.gov/phenomena/earths-magnetosphere>).

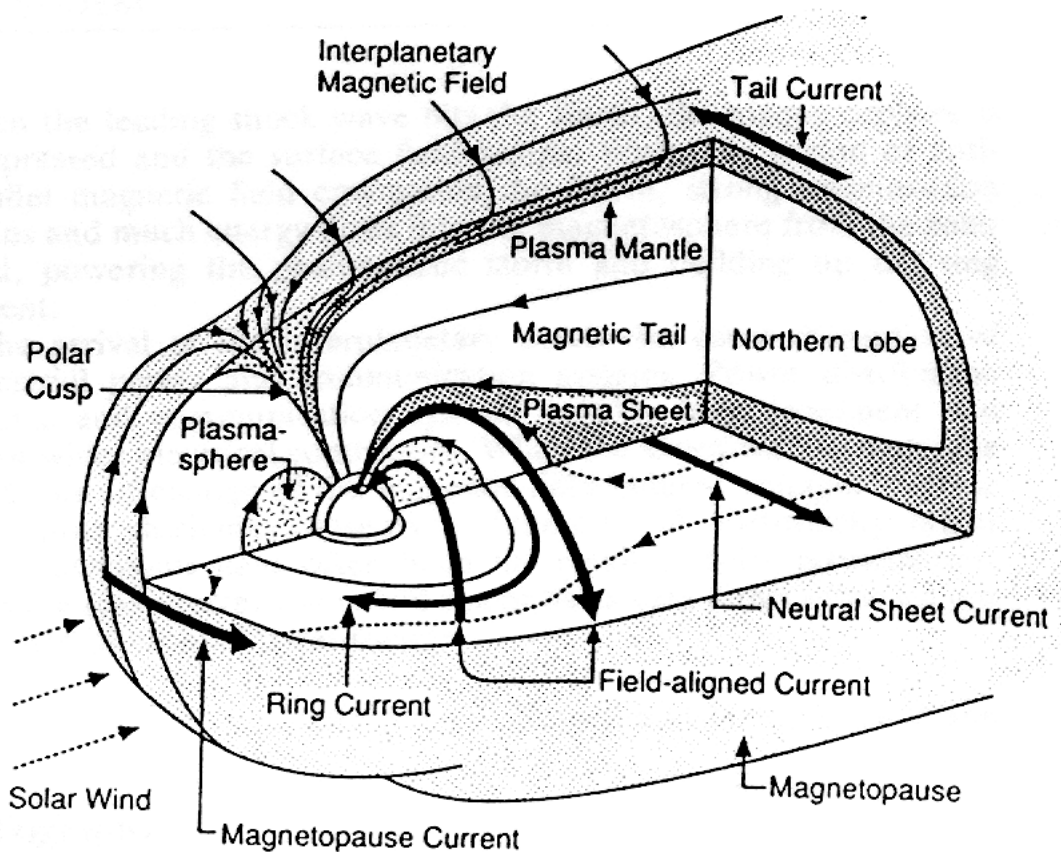


Figure 4.2: A sketch of the magnetosphere retrieved from <http://geomag.org/info/magnetosphere.html> based on Kivelson and Russell [1995].

The components of this dynamic system are displayed in Figure 4.2 [Kivelson and Russell, 1995] and their descriptions can be found in the footnotes<sup>7,8,9</sup>.

<sup>7</sup>Magnetosheath: The magnetosheath is the region of space between the magnetopause and the bow shock of a planet's magnetosphere. The regularly organized magnetic field generated by the planet becomes weak and irregular in the magnetosheath due to interaction with the incoming solar wind, and is incapable of fully deflecting the highly charged particles (<https://en.wikipedia.org/wiki/Magnetosheath>).

<sup>8</sup>Polar cusp: The polar cusp is a region in which the magnetosheath plasma has direct access to the ionosphere. It exists in both conditions when the interplanetary magnetic field is northward or southward. The location of the cusp depends on the shape of the magnetopause in a non-reconnecting magnetosphere but the location of the cusp is altered when the magnetosphere reconnects with either southward or northward interplanetary magnetic field (<http://www-ssc.igpp.ucla.edu/personnel/russell/papers/polarcusp/>).

<sup>9</sup>A field aligned current (Birkeland current) is a set of currents which flow along geomagnetic field lines connecting the Earth's magnetosphere to the Earth's high latitude ionosphere. In the Earth's magnetosphere, the currents are driven by the solar wind and interplanetary magnetic field and by bulk motions of plasma through the magnetosphere. The strength of the field-aligned currents changes with activity in the magnetosphere and small scale variations in the downward flowing electrons accelerate magnetospheric electrons which, when they reach the upper atmosphere, create the Auroras Borealis and Australis ([https://en.wikipedia.org/wiki/Birkeland\\_current](https://en.wikipedia.org/wiki/Birkeland_current)).

Solar wind can be result of different kinds of solar activity. Variations in space weather can be associated with four forms of solar activity, namely: solar flares, coronal mass ejections, high-speed solar wind, and solar energetic particles as given in NASA's mission pages:

[https://www.nasa.gov/mission\\_pages/sunearth/spaceweather/index.html](https://www.nasa.gov/mission_pages/sunearth/spaceweather/index.html).

**Solar flares:** Solar flares are the largest explosion events of our solar system and they are produced by the release of magnetic energy associated with sunspots in the shape of intense burst of radiation. They can last from minutes to hours and are observable as bright areas on the Sun. Flares are made of photons that travel out directly from the flare site and monitored by x-rays and optical light.

**Coronal Mass Ejections (CMEs):** Coronal mass ejections are sudden and violent releases of bubbles of gas in the shape of large clouds of plasma. These plasma clouds can erupt in any direction and the solar material that streams out can impact the planets and spacecraft in its orbit during the explosion, considering that a large CME can consist of a billion tons of matter accelerating to several million kilometres per hour.

**High-speed solar wind:** High-speed solar wind streams come from the areas in the Sun known as coronal holes which can be formed anywhere on the Sun. They impact the Earth by help of the winds only when they occur closer to the solar Equator.

**Solar energetic particles:** Solar energetic particles are high-energy charged particles. Primarily, they are thought to be released by shocks formed at the front of CMEs and solar flares. For instance, these high velocity solar energetic particles can be produced when a CME cloud moves through the solar wind. Moreover, since these particles are charged, they follow the magnetic field lines which penetrate into the space between the Sun and Earth. Therefore, only the charged particles that follow magnetic field lines intersecting the Earth will impact.

In this research, we use satellite and terrestrial magnetometer measurements in order to understand the effects of space weather variations on ionospheric dynamics; therefore, to understand the satellite environment. We mostly refer to geomagnetic storms in our analyses<sup>10</sup>.

We investigate space weather measurements from different platforms [Lu et al., 1998], solar monitoring satellites that are positioned at about the L1 Lagrange point (cf., 4.4) , such as ACE and WIND [King and Papitashvili, 2005], and terrestrial magnetometers over North America and Greenland [Mann et al., 2008, Weygand et al., 2011] and their relation to the disturbances observed in GOCE EGG measurements.

---

<sup>10</sup>Based on earlier observations, magnetic storms and sub-storms were identified in 1970s [McPherron et al., 1973]. Sub-storms are one of the main mechanisms that transports energy from the magnetotail into the ionosphere. Moreover, it also dissipates the storm energy. However, the relationship between the storms and sub-storms is still not very well-known [Partamies et al., 2011]. The duration of a sub-storm varies from 2 to 4 hours including the phases of growth, expansion and recovery [Tanskanen, 2009, Gjerloev et al., 2007].

As mentioned above, there are many different ways of observing the activity in the Sun. In the following sections, we describe the observations that are used in this study.

#### 4.2.0.1 Advanced Composition Explorer (ACE) and WIND Solar Monitoring Satellites

The Advanced Composition Explorer (ACE) was launched in August, 1997 [Stone et al., 1998] and designed to observe energetic particles coming from the Sun and other sources. ACE data have been used to improve solar storm forecasting and warning. Communication with ACE satellite which is located at about 1.5 million km away from the Earth is performed via microwave (S-band). Its location is about 148.5 million km from the Sun.

As shown in Figure 4.3, nine science instruments are mounted on-board ACE. In this research, we use interplanetary magnetic and electric fields as well as plasma flow velocity that are retrieved from different measurements measured by different sensors on-board ACE.

WIND helps further understanding of the static and dynamic properties of solar wind and the effect of its embedded magnetic field on the Earth's magnetosphere [Lepping et al., 1995]. WIND was launched on November 1, 1994 and is still in operation. The mission aims to contribute to the International Solar Terrestrial Program.

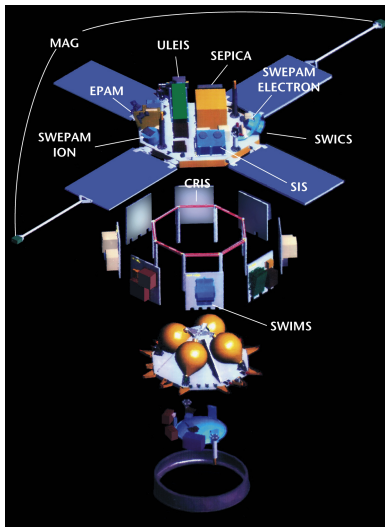


Figure 4.3: ACE payload consists of nine science instruments and positioned at about 1.5 million kilometres from the Earth, image credit: Caltech.

The solar wind observations are reduced to bow-shock<sup>11</sup> nose point. To check whether this process has been done properly, the ACE data are shifted to WIND measurement point and compared with the WIND's observations. The ACE and WIND observed datasets at the L1 Lagrange point and reduced to the bow-shock nose are represented in the Geocentric Solar Ecliptic Coordinate System (GSE) [Hapgood, 1992] as shown in Figure 4.4. The GSE Coordinate System is widely used in space physics applications and defined as follows: The X-axis points towards the Sun from the centre of the Earth, Z-axis is parallel to the Earth's spin axis (to the north) and perpendicular to the ecliptic plane, and Y-axis completes a right handed system (chosen to be in ecliptic plane pointing towards dusk).

For comparison purposes with GOCE EGG measurement disturbances, the ACE and WIND measurements need to be transformed into the geographical coordinate system. It is worth mentioning that we are more interested in the features and variations of the signals (e.g., electric field, plasma flow velocity) rather than their exact magnitude at the satellite positions. Accordingly, we do not need to worry about the distance and attenuation of the signal from the measured point (or the bowshock nose) to the Earth's surface, which is a very complex transformation process.

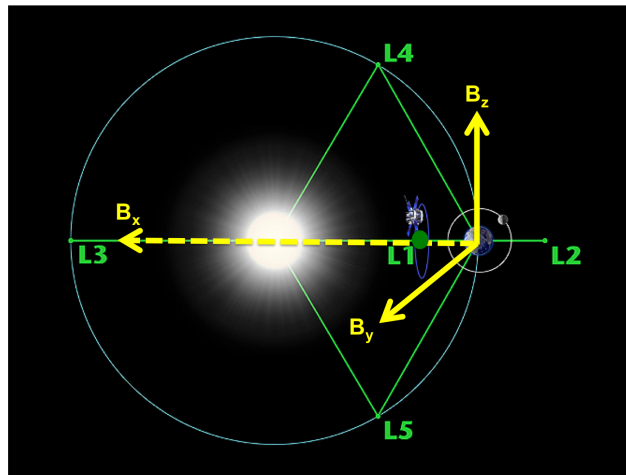


Figure 4.4: L1 Lagrange Point and other Lagrange Points.  $B_x$ ,  $B_y$ , and  $B_z$  shows the Interplanetary Magnetic Field Component directions in the GSE Coordinate System (adopted from wikipedia).

<sup>11</sup>Bow shock: “The bow shock is a shock wave formed at a distance of 3-4 Earth radii or so in front of the nose of the magnetopause by the encounter of the supersonic solar wind with the “obstacle” to its flow presented by the Earth’s magnetic field” ([http://pluto.space.swri.edu/image/glossary/bow\\_shock.html](http://pluto.space.swri.edu/image/glossary/bow_shock.html)).

The interplanetary electric field observed from ACE and WIND satellites can be used in our investigation as a proxy for the solar activity. The electric field reduced to the bow-shock nose point is furthermore filtered into the frequency band of our interest (3-8 mHz), where we observe the GOCE disturbances most. Figure 4.5 shows the time series of GOCE disturbances and Interplanetary Electric Field (IEF) measurements that are filtered into the same bandwidth for March-April, 2011.

The disturbances observed in the trace in GRF correspond to the burst groups of the  $\mathbf{E}$  field in GSE, which can be used as an indicator for understanding the cause of the disturbances. It shows that the increasing solar activity causes the trace to become noisier and degrades the quality of the measurements and final products of GOCE EGG measurements. This discovery is very important since it leads to understanding the disturbances present in GOCE measurements and help improve the final products. This study is the first to discover these effects and perform such kind of comparisons.

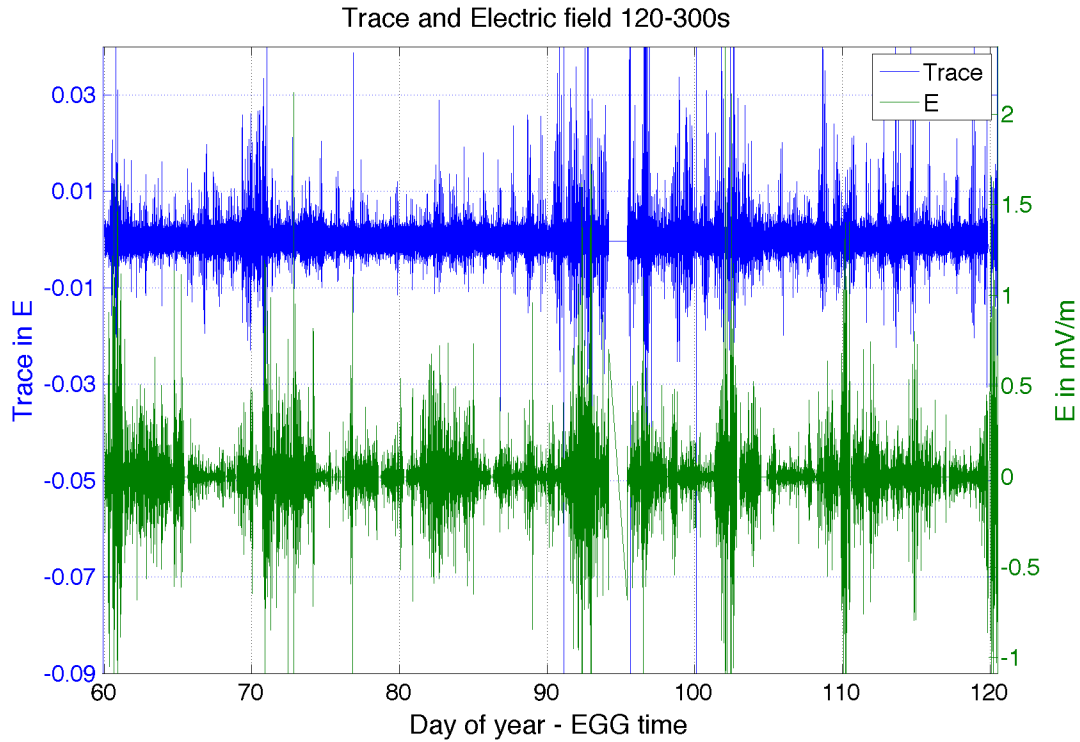


Figure 4.5: Trace and IEF are filtered into [120-300]s interval for 2-month period (March-April, 2011). Note the agreement of burst groups in both time series. Refer to Figure 4.8 for original IEF.

We complement our analyses above with the investigations on the Interplanetary Magnetic Field (IMF) components. As mentioned in the previous chapter, for comparison purposes, measurements obtained from other platforms and reference frames are transformed into the GRF. Therefore, without dealing with the distance of the bow-shock nose to the satellite orbit, we take care of the orientation differences of the two datasets and apply coordinate transformations from the GSE to GRF. This transformation consists of two steps.

First, the measurements in the GSE are transformed into EFRF. Once the measurements are represented with respect to an Earth-fixed reference frame then they are transformed into the GRF. The transformation of the IMF components into the GRF and their comparisons with GOCE disturbances is again one particular example, which is applied for the first time in this study and gives a very good example of combining two different disciplines, geodesy and space physics. The transformation steps are given in the following section:

**Transformation from Geocentric Solar Ecliptic (GSE) to Earth Fixed Reference Frame (EFRF)**

There are two transformations involved between the GSE and EFRF (e.g., International Terrestrial Reference Frame). It is worth mentioning that the International Terrestrial Reference Frame (ITRF) is commonly mentioned as Earth Fixed Reference Frame in the recent publications.

The first rotation is in the plane of the Earth’s geographic equator from the first point of Aries (Vernal Equinox) to Greenwich. The second one is the rotation from the Earth’s Equator to the plane of the ecliptic and rotation in the plane of the ecliptic from vernal equinox to the Earth-Sun direction [Hapgood, 1992]. The transformation steps can be described as follows:

$$\begin{aligned} T_1 &= R_3(\theta), \\ T_2 &= R_3(\lambda_s)R_1(\epsilon), \end{aligned} \tag{4.1}$$

where  $R_3$  and  $R_1$  are the transformation matrices about Z- and X-axes, respectively and

$$\begin{aligned} \theta &= 100.461^\circ + 36000.770^\circ T_o + 15.04107^\circ UT, \\ \lambda_s &= \lambda + (1.915 - 0.0048T_o) \sin(M) + 0.020 \sin(2M), \\ \lambda &= 280.460^\circ + 36000.772T_o + 0.04107UT, \end{aligned} \tag{4.2}$$

and

$$\begin{aligned}
M &= 357.52^\circ + 35999.050T_o + 0.04107UT, \\
\epsilon &= 23.439^\circ - 0.013 T_o, \\
T_o &= \frac{(MJD - 51544.5)}{36525},
\end{aligned} \tag{4.3}$$

and UT is the Universal time.

Therefore, the transformation from GSE to EFRF is

$$\begin{pmatrix} X \\ Y \\ Z \end{pmatrix}_{EFRF} = T_1 T_2 \begin{pmatrix} X \\ Y \\ Z \end{pmatrix}_{GSE}. \tag{4.4}$$

The IMF components that are given in the GSE system are shown in Figure 4.6. The  $B_z$  is the most important component because it influences the coupling of the ionosphere and magnetosphere. It is known that southward (negative)  $B_z$  component causes very dynamic changes in the  $\mathbf{E} \times \mathbf{B}$  drift which causes changes in the drift direction at higher latitudes [Lu et al., 2014]. The IMF observations given in the GSE are transformed into the GRF as indicated above and the three IMF components in the GRF are displayed in Figures 4.6 and 4.7.

Strong variabilities are seen in both IMF components in the GSE and GRF. Distinctive increases and decreases in the strength of the signal are observed without a particular periodicity. It is seen that all components show similar behaviour, therefore we can safely say that the influence is effective in the three directions.

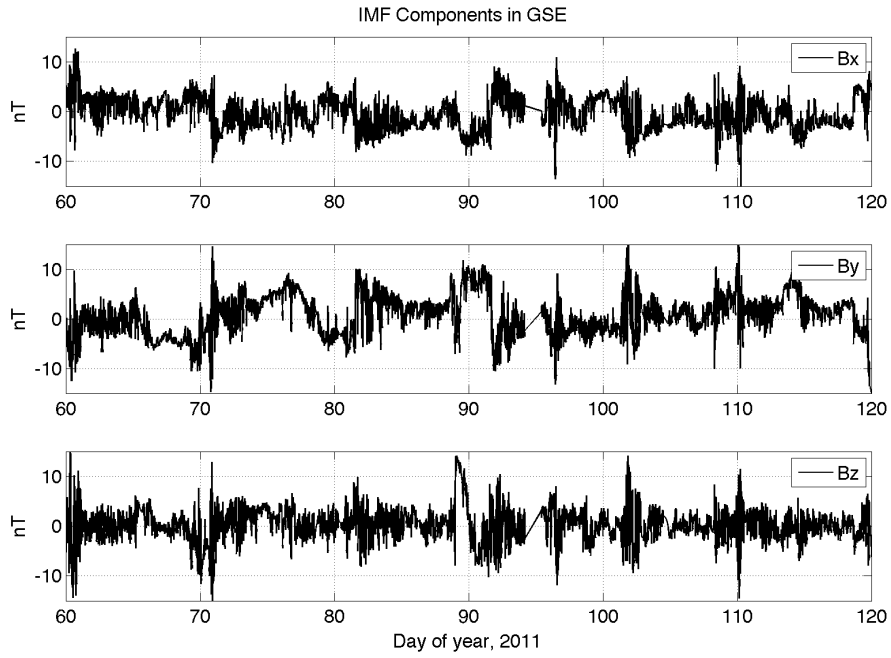


Figure 4.6: IMF components in GSE for 2-month period (March-April, 2011).

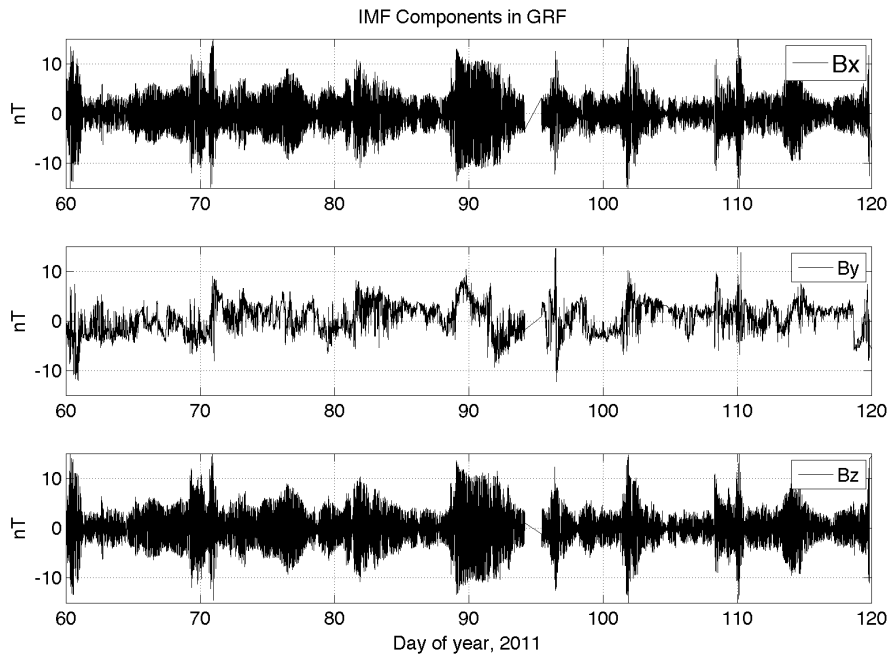


Figure 4.7: IMF components in GRF for 2-month period (March-April, 2011).

#### 4.2.0.2 Geomagnetic indices

Our initial investigations include time series correlation analyses with different geomagnetic indices. These indices are used as proxies for the solar activity and its effect on the Earth's ionosphere and magnetosphere. Calculation of these indices is based on the terrestrial observatories selected. Therefore, the outcomes of our analyses are useful in understanding the regional and global effects of these activities on the Earth's surface. The indices used in this research are described below followed by our analyses.

**Kp:** The  $Kp$  index [Rostoker, 1972] was introduced in 1949 and is derived from the standardized K index (Ks) from 13 terrestrial magnetic observatories.  $Kp$  index is designed to measure solar particle radiation by its magnetic effects.  $Kp$  index between 1 and 3 represents quiet magnetic field, between 4 and 5 represents active magnetic field, and between 5 and 8, represents storm, whereas 9 indicates extreme storm cases.

**PC:** PC indices [Troshichev et al., 2006] are ground-based indices.  $Kp$  could be derived directly from the PC index with time shifts of around 5-10 min. PC indices are derived from polar magnetic variations that are scaled to align the merging electric field (in mV/m) in the solar wind. They are indicators of the conditions that dominate the interaction of the solar wind with the magnetosphere. PCN index smaller than 2 indicates no substorm, between 2-5 indicates substorm onset after a delay of 5-60 minutes, over 5 indicates imminent substorm (delay 0-10 minutes) and finally PCN=10 means violent substorm activity that may create risk for power grids (<http://swe.ssa.esa.int/DOCS/SWWT/m31/PCindexSSWTStauning.pdf>).

We look at the  $Kp$  index, the original unfiltered IEF, the polarity of the IMF  $B_z$  component, the dawn-dusk plasma flow velocity ( $V_y$ ), and the PCN index during the 2-month period of March-April 2011. The  $Kp$  and PCN indices are computed based on terrestrial measurements, whereas,  $B_z$  and  $V_y$  are measured on-board ACE satellite.  $Kp$  index has a 3-hour averaged sampling rate, whereas the other four proxies are sampled at 1 minute interval. The two cases we investigate in the following sections are within the time intervals indicated by red rectangles in Figure 4.8. Larger variations are observed around March 10th and April 2nd corresponding the 69th and 92nd days of year 2011. The large variations observed in the time series of geomagnetic indices give an insight to the problem we look at and justify why the disturbances degrading the GGT components occur on specific days. To our best knowledge, the use of geomagnetic indices to understand the characteristics of GOCE disturbances have not been studied and published before.

The five indices representing the solar activity and its interaction with the geomagnetic field are used in our investigations. It is seen that the indices agree among themselves in terms of indicating the external effect. For example, for the 70th day of the year, all of the series show increased variations with high amplitudes

which can also be used as an indicator of the propagation of increasing effect of the solar activity over the magnetosphere and ionosphere and Earth's surface.

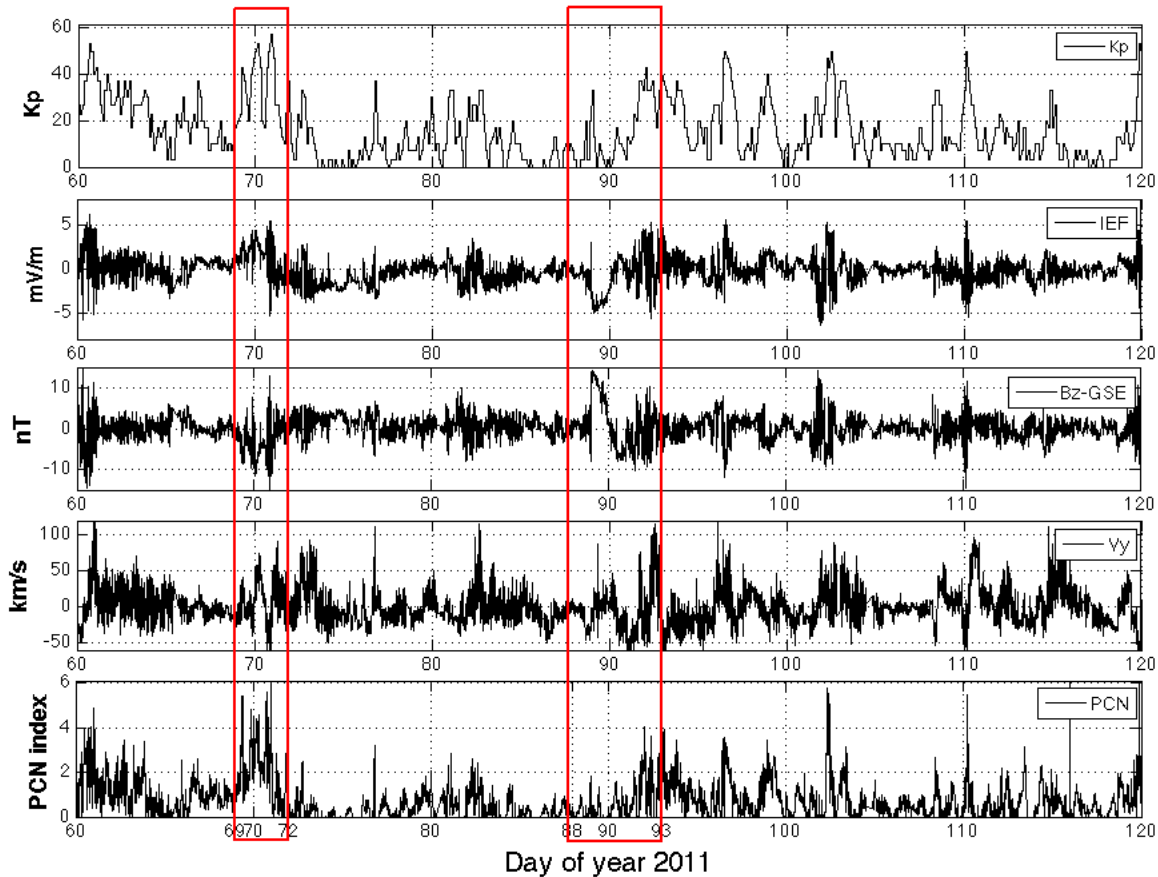


Figure 4.8: Magnetic indices are used to understand the cause of the disturbances.  $Kp$  and PCN indices are derived from terrestrial measurements, whereas IEF, Bz-GSE and  $V_y$  are observed by ACE and WIND spacecraft. Note the storm periods cause higher variations as indicated in the red rectangles.

There are limitations in using the proxies since they only represent global and regional changes and are lacking spatial detail that is required to understand the effect to the satellite measurements along its track. Therefore, these measurements need to be supported by other datasets collected by other geostationary satellites (e.g., NASA's IMAGE satellite) or terrestrial magnetometers (e.g., Canadian Array for Realtime Investigations of Magnetic Activity) since they are not adequate to model or eliminate these disturbances alone.

Nevertheless, ACE and WIND data undoubtedly prove for the first time that increased solar activity enhances the ionospheric dynamics, propagates into the GOCE measurements and degrades the quality of the products. To the best of our knowledge, this is the first time such visible correlation between the high resolution IEF (or IMF) and GGT trace is discovered and examined. The outcomes lead to detailed analyses of these measurements in space (time) and frequency domain, given in Chapter 6.

#### 4.2.0.3 CARISMA Observations

The Canadian Array for Realtime InvestigationS of Magnetic Activity (CARISMA) magnetometer array is a network that consists of ground magnetometers across North America. The CARISMA magnetometers monitor the magnetic field and its variations in 3D. Therefore, CARISMA is capable of monitoring the magnetic field perturbations due to the solar wind-magnetosphere coupling [Mann et al., 2008]. Moreover, the sensitive instruments used in the array can capture the global, meso-scale and local magnetic effects from electrical current systems and waves. CARISMA is operated by the University of Alberta and funded by the Canadian Space Agency (CSA). The goal of CARISMA array is to understand the transport of plasma and energy across different scales in the solar-terrestrial system. CARISMA measurements can be obtained at 1 s sampling resolution from raw measurements sampled at 8 Hz.

It is mentioned in Mann et al. [2008] that more stations will be added at strategic locations to increase the capability of the array for scientific applications. In this research, we use CARISMA measurements as proxies for the space weather variations and its influence on the ionospheric dynamics. Moreover, we investigate time series of the CARISMA measurements and disturbances observed in GOCE EGG measurements to understand the possible influence of the geomagnetic disturbances on GOCE environment and EGG measurements.

We perform our investigations on selected stations from north to south to take into consideration the propagation of the dynamics along the satellite track as well as the spatio-temporal ambiguities. The CARISMA stations are shown in Figure 4.9 by black squares, whereas the stations we used are shown by red squares.

CARISMA observations at four stations, namely TALO, RANK, GILL, and PINA along the Churchill line are investigated. The observations of the east-west component of the magnetic field disturbances are shown in Figure 4.10 from the northern most stations to the south. One can notice that the perturbations are reduced from northern stations to the southern ones due to the reduced ionospheric dynamics at lower latitudes. The storm periods of our interest around the 70th and 92nd days of the year indicate larger

magnetic perturbations at the Earth's surface. We can safely use the CARISMA measurements to evaluate our comparison results given in the next section.

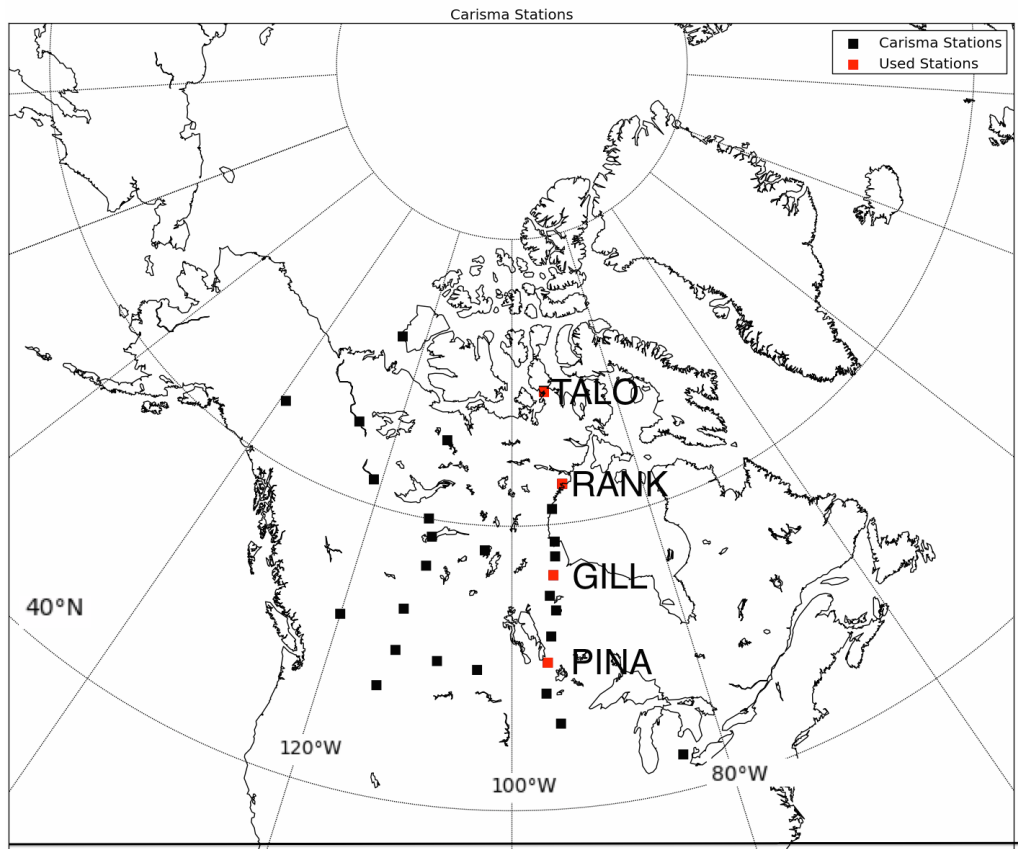


Figure 4.9: CARISMA array is shown by black colour, whereas the stations selected for our investigations are shown by red squares.

Our analyses in this section confirm that the auroral oval is affected from the solar activity the most. As a consequence, the disturbances observed in GOCE EGG gradients over these regions are due to increasing dynamics. We do not use these observations any further, but consider their products, namely the equivalent ionospheric currents, which are given in the next section retrieved from a larger terrestrial observatory network.

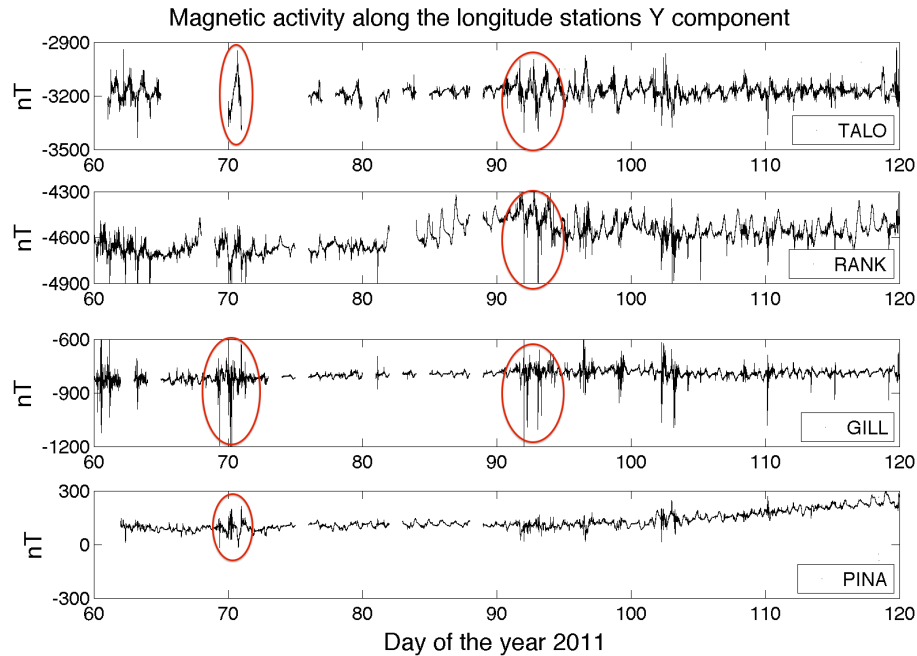


Figure 4.10: East-west components of the magnetic field measured at the four CARISMA stations along the Churchill line.

## 4.3 Ionospheric Currents and Poynting Flux

---

In this section, we present our investigations on the ionospheric dynamics by means of ionospheric currents. The main currents in the ionosphere can be approximated by using the terrestrial magnetic field disturbance records. We explain the methodology below and give examples of the use of this information in our research.

### 4.3.1 Spherical Elementary Current Systems

Complex electrical current systems can be represented as simple set of equivalent currents at a specific height in the ionosphere by using the Spherical Elementary Current Systems (SECS) method [Amm, 1997]. Terrestrial geomagnetic field measurements are used as input data. These measurements taken on the Earth's surface represent temporally and spatially varying components as follows:

1. The main geomagnetic field generated in the Earth's outer core,
2. The main geomagnetic field generated in the Earth's crust,
3. The field produced by the interaction of the solar and geomagnetic fields (external effect).

Disturbances of the magnetic field that last short period of time (e.g., seconds to days) are caused by the external sources, such as solar wind, magnetosphere and ionosphere/upper atmosphere interaction [Campbell, 2003]. The effects of the external magnetic field measured at the Earth's surface can be modelled in terms of ionospheric equivalent currents. This approach is based on the representation of the 3-D complex current systems as simple spherical sheets of currents, which represent the magnetic field of the ionospheric currents on the Earth's surface [Vanhamäki et al., 2003]. Moreover, telluric currents<sup>12</sup> induced in the subsurface can induce disturbances which can reach up to 40% of the total observed change during sub-storm onset [Tanskanen et al., 2001].

Ionospheric currents and corresponding geomagnetic observations measured by radar and terrestrial magnetometers, respectively, are compared which helps to identify the local time dependence of the electric field and current pattern around the auroral latitudes during disturbance times. They showed (ibid, 2001) that the evening sector<sup>13</sup> experiences an eastward electrojet, while the morning sector is exposed to the westward electrojet. The transition between the two is called the Harang discontinuity which GOCE was possibly exposed to many times.

Spherical elementary current systems are introduced in Amm and Viljanen [1999]. Magnetic field disturbances due to external sources measured at the Earth's surface are upward continued to the ionosphere in order to understand the magnetosphere-ionosphere interaction. The traditional spherical harmonic analysis that is used in gravity field modelling is also very commonly used in magnetic field studies. However, this technique can only be used in global studies and performs poorly in regional and local scales. Therefore, a few other different methodologies are developed to overcome this problem. Amm and Viljanen [1999] introduced the Spherical Elementary Current Systems which expand the ground measurements into a sum of magnetic field effect of spherical elementary current systems placed in the ionosphere. The centres of these spherical elementary current systems can be positioned freely but the best choices would be the regions of high density of observatories.

Amm and Viljanen [1999] defined two types of spherical elementary (sheet) current systems, namely divergence-free  $\vec{J}_{df,el}$  and curl-free systems  $\vec{J}_{cf,el}$  as represented in Figure 4.11. In a spherical coordinate system  $(r', \theta', \lambda')$  with unit vectors  $(\underline{e}_{r'}, \underline{e}_{\theta'}, \underline{e}_{\lambda'})$ <sup>14</sup>, where the northern pole (or the pole) is in the centre of the elementary system, the definitions can be given as follows:

---

<sup>12</sup>Telluric current: An electric current which moves underground or through the sea that results from both natural causes and human activity.

<sup>13</sup>Evening sector: Magnetic Local Time (MLT) sector.

<sup>14</sup>Please note that [Amm, 1997] used the  $\varphi$  and *vartheata* in the original manuscript.

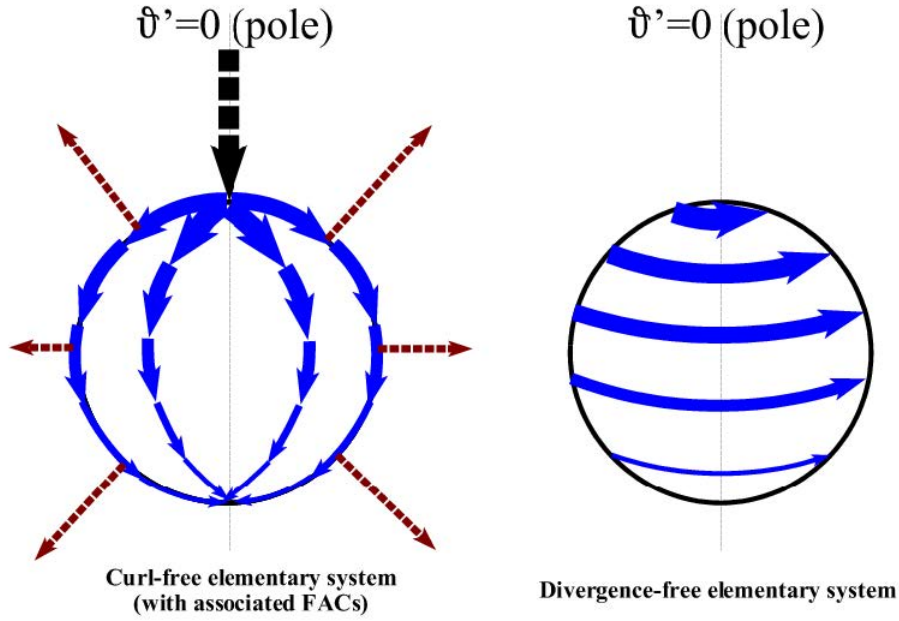


Figure 4.11: Sketch of spherical elementary current systems (SECS). The equivalent currents are developed based on divergence free elementary system that is depicted on the right-hand side (taken from Amm et al. [2002]).

$$\vec{J}_{df,el}(\vec{r}') = \frac{I_{0,df}}{4\pi R_I} \cot(\theta'/2) \underline{e}_{\lambda'}, \quad (4.5)$$

and

$$\vec{J}_{cf,el}(\vec{r}') = \frac{I_{0,cf}}{4\pi R_I} \cot(\theta'/2) \underline{e}_{\theta'}, \quad (4.6)$$

where  $R_I$  is the radius of the ionosphere that is assumed to be an infinitely thin layer at 100 km above the Earth's surface. Weygand et al. [2011] assumed this height to be 110 km.  $I_{0,df}$  and  $I_{0,cf}$  are the scaling factors of the elementary systems. The curl-free elementary current system is associated with a field aligned current of magnitude  $I_{0,cf}$  at its pole. However, its magnitude is opposite to the field aligned currents (FACs) of magnitude  $-\frac{I_{0,cf}}{4\pi R_I^2}$ . This would cause the net FACs over the whole ionosphere to become zero. This curl-free elementary current system is attributed to Pedersen currents in a uniformly conducting ionosphere that is given in Fukushima [1976].

Based on Helmholtz's theorem, any ionospheric current density can be uniquely constructed by using the superposition of the divergence-free and curl-free components, placing poles of elementary current systems all over the ionosphere [Amm, 1997]. It is also noted that the total or actual current density cannot be reconstructed but the equivalent currents, in other words horizontal currents that flow in the ionosphere which produce the same magnetic effect below the ionosphere as the true currents (3 dimensional currents including both horizontal and field aligned currents) [Untiedt and Baumjohann, 1993]. Equivalent currents,  $\vec{J}_{eq, Ion}$ , are divergence-free, because the curl-free part of the actual current system does not produce any magnetic field below the ionosphere. Therefore, only the divergence-free elements are needed in the process of upward continuation of the magnetic field to the ionosphere.

The magnetic field disturbances are measured at terrestrial stations that are irregularly spaced and the centres of Spherical Elementary Current Systems. As mentioned above, the poles can be but do not have to be located regularly. The problem is reduced to solving the Spherical Elementary Current Systems scaling factor which represents the relation between the observations and real currents in the ionosphere at a specific altitude on a spherical surface by taking into account the geometry of the stations included in the computations.

The scaling factors of the elementary current system that fit best to the ground magnetic field measurement can be obtained by solving

$$\bar{T}\bar{I} = \bar{Z}, \quad (4.7)$$

where

$$\bar{Z} = \left( Z_{1,\vartheta} \quad Z_{1,\varphi} \quad Z_{2,\vartheta} \quad Z_{2,\varphi} \quad \cdot \quad \cdot \quad Z_{n_{obs},\vartheta} \quad Z_{n_{obs},\varphi} \right)^T, \quad (4.8)$$

is the vector of observations,

$$\bar{I} = \left( I_{0,df,1} \quad I_{0,df,2} \quad \cdot \quad \cdot \quad I_{0,df,n_{el}} \right)^T, \quad (4.9)$$

is the vector of scaling vectors of the elementary current systems, and

$$\bar{T} = \begin{pmatrix} T_{11,\vartheta} & T_{12,\vartheta} & \cdot & \cdot & \cdot & T_{1n_{el},\vartheta} \\ T_{11,\varphi} & T_{12,\varphi} & \cdot & \cdot & \cdot & T_{1n_{el},\varphi} \\ T_{21,\vartheta} & T_{22,\vartheta} & \cdot & \cdot & \cdot & T_{2n_{el},\vartheta} \\ T_{21,\varphi} & T_{22,\varphi} & \cdot & \cdot & \cdot & T_{2n_{el},\varphi} \\ \cdot & \cdot & \cdot & \cdot & \cdot & \cdot \\ T_{n_{obs}1,\vartheta} & T_{n_{obs}2,\vartheta} & \cdot & \cdot & \cdot & T_{n_{obs}n_{el},\vartheta} \\ T_{n_{obs}1,\varphi} & T_{n_{obs}2,\varphi} & \cdot & \cdot & \cdot & T_{n_{obs}n_{el},\varphi} \end{pmatrix}, \quad (4.10)$$

where  $\bar{Z}$  represents the measurements at different stations,  $\bar{T}$  represents the “the magnetic field effect of a unit SECS placed at each of the positions of the SECS grid evaluated at each of the stations” and  $\bar{I}$  is the scaling factors that we need to retrieve in order to derive the EICS. The solution is obtained via Singular Value Decomposition. It is worth mentioning that the geometry of the stations is of importance in this computation and impacts the results [Amm and Viljanen, 1999, Weygand et al., 2011].

### 4.3.2 Equivalent Ionospheric Currents and Spherical Elementary Current Amplitudes

We use Equivalent Ionospheric Currents (EICS) that are developed based on the observations and techniques provided in Amm [1997], Amm and Viljanen [1999], and Weygand et al. [2011], as given in the previous section. The technique and its outcomes are proven to be very useful in understanding the characteristics of the electrical currents in the ionosphere. Geomagnetic disturbances measured at terrestrial observatories over North America and Greenland, namely CANMOS (Canadian Magnetic Observatory System), CARISMA (Canadian Array for Real-time Investigations of Magnetic Activity and Global Geomagnetic Indices), Geophysical Institute Magnetometer Array, Greenland, THEMIS (Time History of Events and Macroscale Interactions during Substorms), and Magnetometer Array for Cusp and Cleft Studies that are shown in Figure 4.12 are included in the network [Weygand et al., 2011].

Spherical Elementary Current Systems developed by Amm [1997] are used to calculate the EICS and SECS over North American auroral region. The datasets are downloaded from:

*http : //www.igpp.ucla.edu/jweygand/htmls/EICS\_NA-Greenland.html*. This system is based on the upward continuation to the ionosphere in spherical geometry of the anomalous magnetic field measured on the ground (terrestrial) that is caused by ionospheric currents. Computed current values are provided on a

grid (Figure 4.12) at 10 second temporal resolution; whereas, the stations have  $\sim 350$  km spatial resolution in densest regions in Alaska.

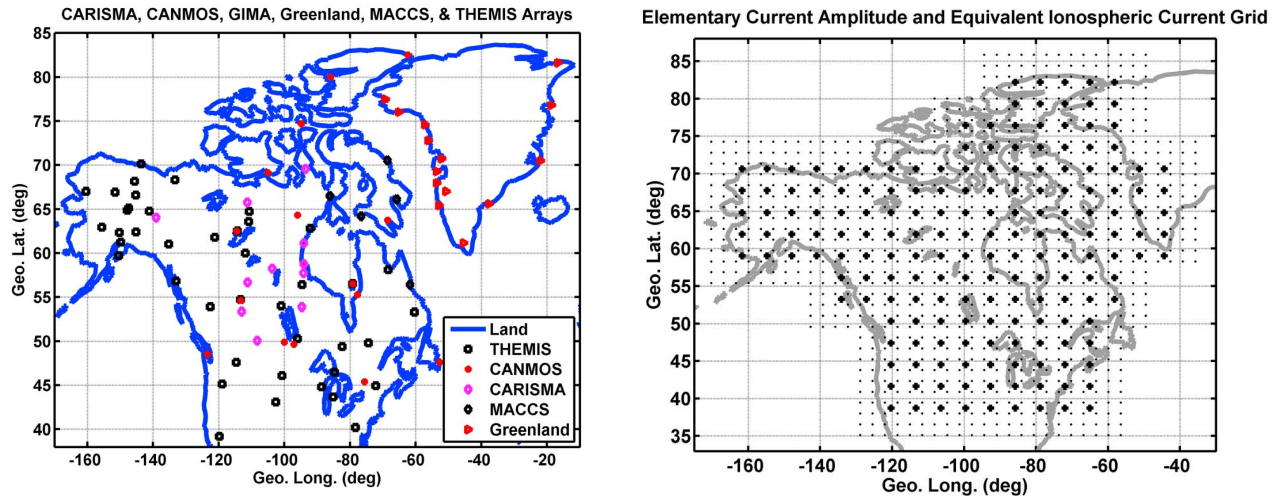


Figure 4.12: Magnetometers used in the development of EICS and SECS (left panel) and Grid EICS and SECS (right panel) that the EICS computations are performed at as given in Weygand et al. [2011]. Big dots indicate where the SECS amplitudes are calculated, whereas the smaller dots show the location where the EICS are calculated.

EICS, in the north-south and east-west directions are given in  $mA/m$ , and SECS, currents in *Amperes* in upward and downward directions in a left-handed local coordinate system, but do not share the same grid area and resolution. We apply the collocation method (kriging) to interpolate the grid values into the satellite ground track position for correlation analysis. It is validated by Amm and Viljanen [1999], Pulkkinen et al. [2003] that the error in the grid values is  $\sim 1\%$  in the vicinity of each magnetometer but can reach up to  $15\%$  when the grid point is farther away from them. Accordingly, we limit our along-track comparisons within the gridded region and we give examples of tracks crossing areas of denser spatial magnetometer distribution.

The EICS vector components and SECS values that are interpolated into the GOCE positions and their derivatives (their variations) are examined track by track with respect to the latitude along the satellite ground track. Similar to Figure 3.22, the variations of SECS and EICS with latitude are shown in Figure 4.13 for many ascending tracks in March-April, 2011. Simple visual observations indicate that there are abrupt changes in the EICS and SECS amplitudes along the track between latitudes  $50^\circ N$  and  $70^\circ N$ . This heuristic analysis confirms that the terrestrial observations of magnetic field disturbances represent the higher dynamics in higher latitude (between 50 and 70 degrees) and can be used for further rigorous analysis of the disturbances observed in GOCE EGG measurements.

The combined analyses of the EGG trace and ionospheric currents are limited within the grid area of the SECS and EICS values [Weygand et al., 2011]. One of the tracks is presented here for visual comparison purposes only. The four time series, EICS vector components, SECS amplitude and trace, along a complete satellite pass (around 15 minutes period) over North America are shown in Figure 4.14. The ew and ns correspond to East-West and North-South horizontal currents, respectively, whereas r corresponds to the vertical currents. The ew, ns, and r currents are scaled by 1/10, 1/10 and 1/1000, respectively. EICS positive directions are represented in geographic north and east directions. It is obvious that the four series have variations in common locations namely between the latitude 50°N and 65°N. This is an indication that the ionospheric currents have a direct or an indirect effect on the GOCE EGG measurements.

The EICS in east-west, SECS and trace show common variations occurring within the same time interval as demonstrated. We argue that GOCE was exposed to extreme ionospheric current direction changes and this effect furthermore propagated into the EGG measurements as displayed in trace (high positive to high negative change at latitude around 59°N).

The EIC vectors and SECS at 00:24:00 UTC on March 11th, 2011 are shown in Figures 4.15 and 4.16, respectively. This example is one of the extreme cases that GOCE was exposed to. The green circles indicate the satellite's position at this epoch while the red arrow in Figure 4.15 corresponds to the interpolated EICS vector. The satellite at this particular epoch experienced the influence of an east-west horizontal current while the following sections of the same track experienced a south-north current trend. This indicates a distinctive change in the direction of the horizontal currents. Moreover, vertical currents (SECS) displayed in Figure 4.16 panel also show a distinctive negative to positive (downward to upward) current variation along the satellite ground track [Ince and Pagiatakis, 2016].

From Figures 4.15 and 4.16, one can see that the influence of the currents on GOCE can extend as far as 45° N. Moreover, the SEC amplitude also mimics Region 1 and 2 currents, which represent the energy input to the ionosphere and drifting from the ionosphere. Track by track analysis presented in this study includes ascending tracks only. It is known that satellite ascending and descending tracks differ not only in terms of satellite altitude but also in orientation. Moreover, the ascending and descending passes correspond approximately to 6 pm and 6 am local time, respectively, which causes different space environments. However, analysis of the descending tracks will be performed in the next chapter since the coverage of the EICS and SECS grids do not let us perform complete analyses over descending tracks (e.g., over Alaska where we observe disturbances along descending tracks).

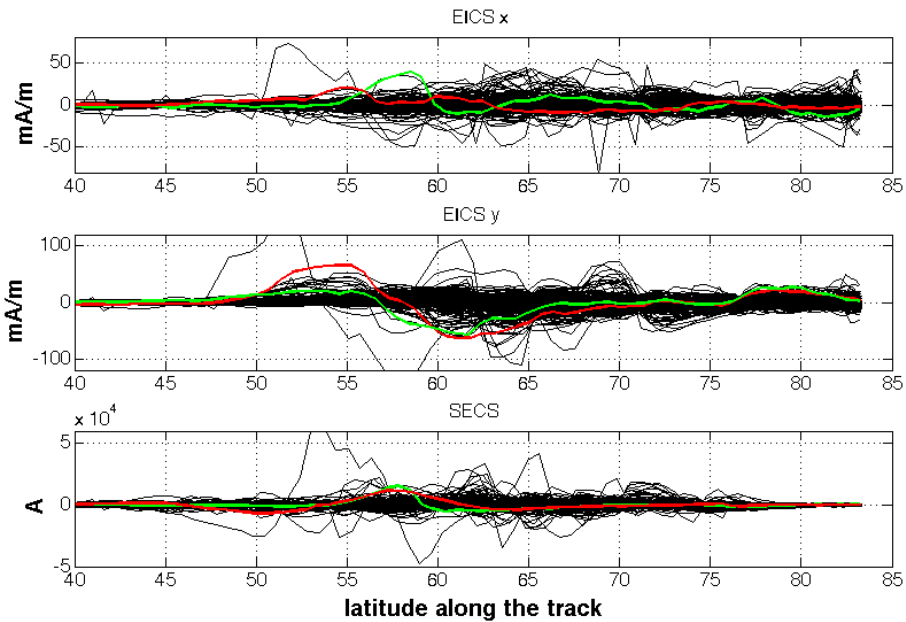


Figure 4.13: Derivatives of EICS and SECS series along GOCE ascending tracks similar to 3.23.

A randomly chosen second example of EICS and SECS is shown in Figure 4.17. This example also indicates an east-west horizontal current flow corresponding to an upward to downward current transition. It is expected that these steep variations cause the satellite's orbit be disturbed.

It is worth mentioning here that the reason that these currents are called “equivalent” is because they are not equal to true horizontal ionospheric currents, but are equivalent to them in spatial and temporal scales of the basic processes in the ionosphere [Pulkkinen et al., 2003]. Also, EICS and SECS presented in Weygand et al. [2011] are computed and provided at the altitude of 110 km where the main ionospheric currents exist and therefore not at the GOCE altitude. Kamide and Brekke [1993] mentioned that the ionospheric current varies considerably with height. In particular, even though the height-integrated ionospheric current shows a well-known pattern of the eastward-westward electrojets in the evening and morning sectors, respectively, current vectors at different heights are at times directed in the opposite direction [Kamide et al., 1981]. This indicates that the equivalent currents at GOCE altitude represent similar variations in similar directions

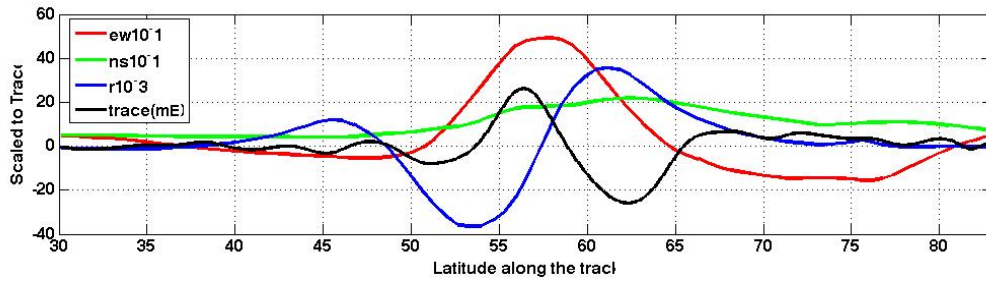


Figure 4.14: Equivalent Ionospheric Currents and Spherical Elementary Current Amplitudes for one ground track (see also Figure 4.15) on March 11th, 2011. Note that this is an extreme case that GOCE experienced.

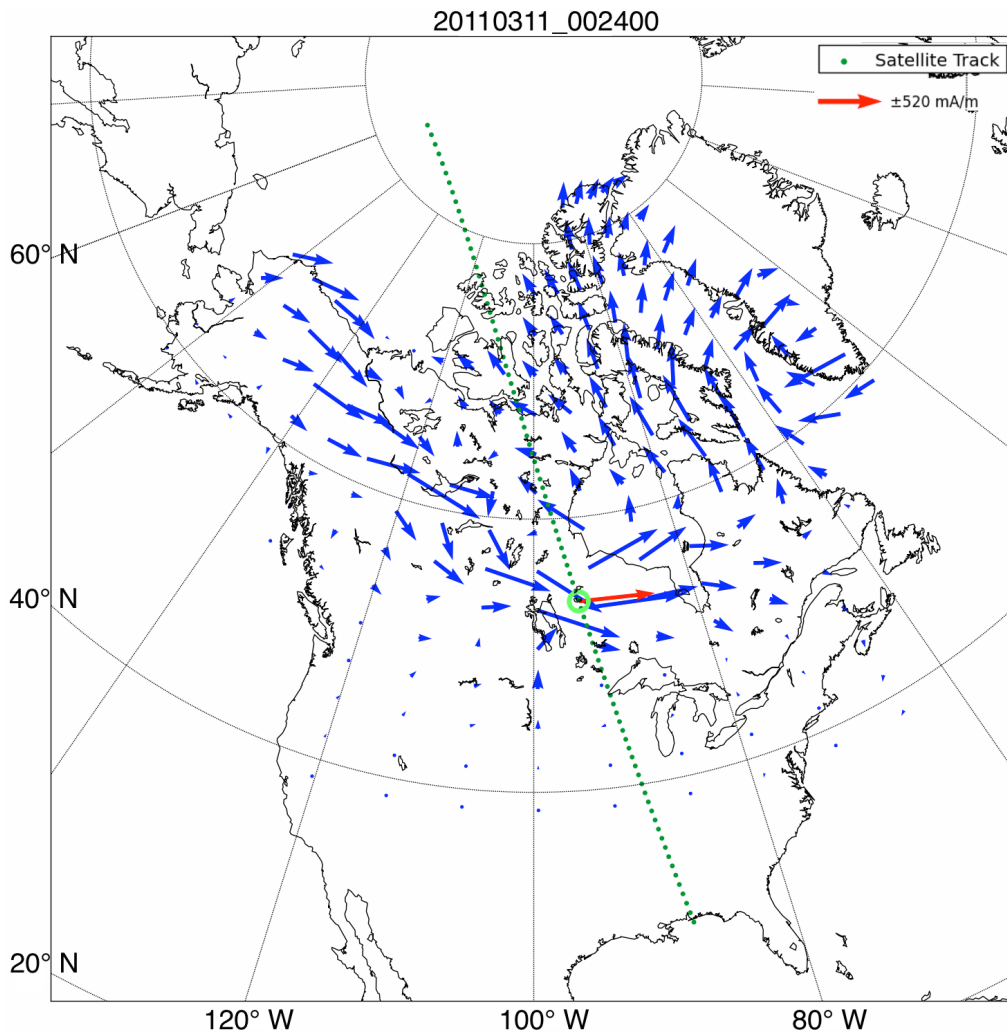


Figure 4.15: Equivalent Ionospheric Currents at 00:24:00 on March 11th, 2011. Note that this is an extreme case that GOCE experienced. Note the strong east-west equivalent current at satellite's position.

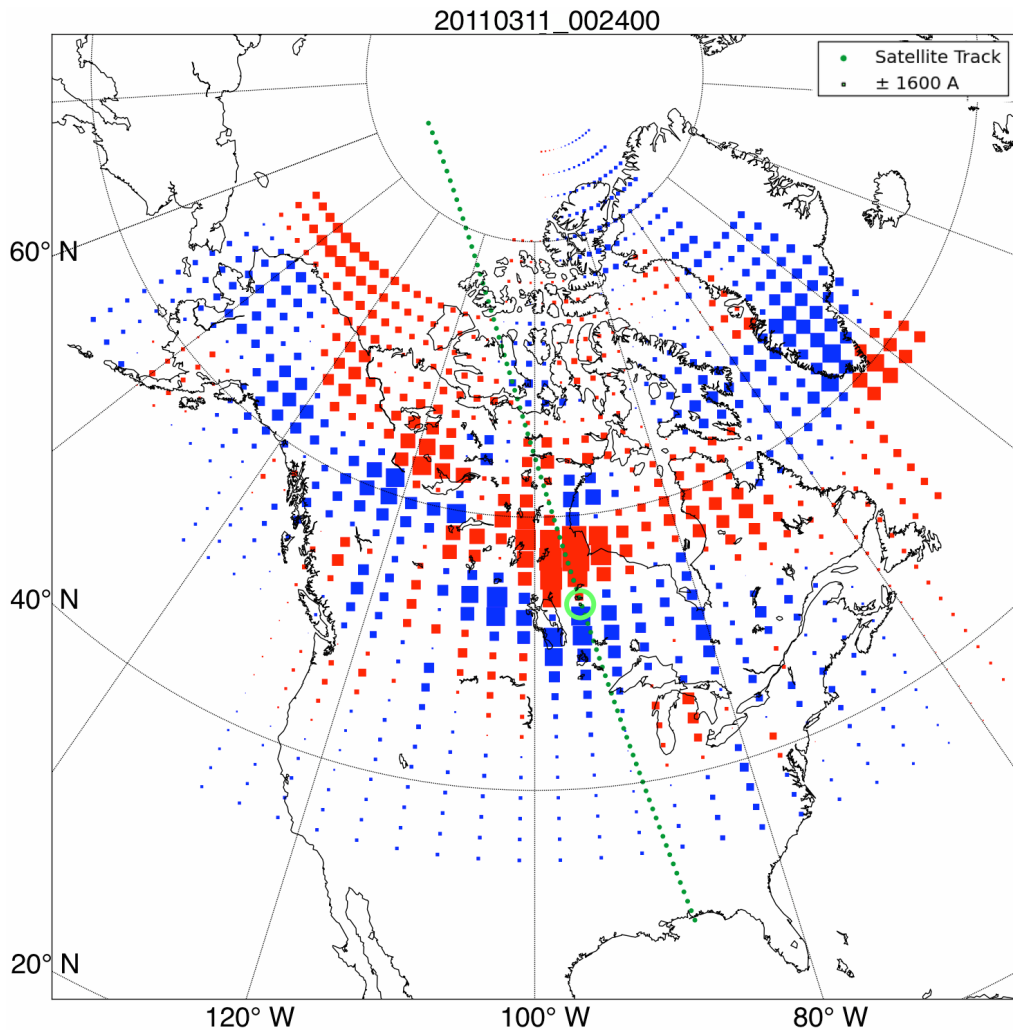


Figure 4.16: Spherical Elementary Current Amplitudes at 00:24:00 on March 11th, 2011. Note that this is an extreme case that GOCE experienced. Note the significant negative to positive variation at the satellite's position.

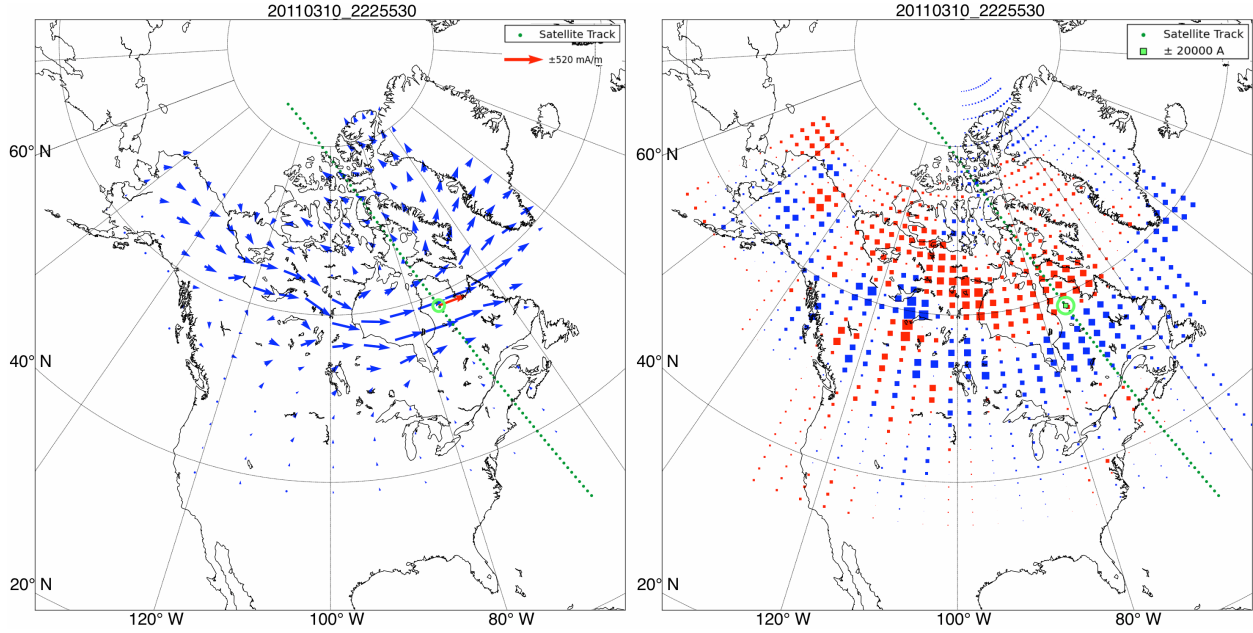


Figure 4.17: Another example of Equivalent Ionospheric Currents and Spherical Elementary Current Amplitudes that are measured at 22:55:30 on March 10th, 2011. Strong east-west horizontal and downward and upward vertical currents affect the satellite measurements along its orbit.

### 4.3.3 Electromagnetic Energy Flow

In this study, we proceed a step further and estimate the electromagnetic energy density flow (energy flux) using EICS and SECS amplitudes that are calculated on a spherical geographic grid. EICS ( $mA/m$ ) represent horizontal magnetic field components, whereas the SECS amplitudes (*Amperes*) are normalized by the area of the grid cells and represent the electric field current intensity per unit area  $A/m^2$  in upward (positive) and downward (negative) directions in local coordinate system. The electromagnetic energy flow is represented by the Poynting vector.

The Poynting vector can be represented as:

$$\mathbf{S} = \mathbf{E} \times \frac{\delta \mathbf{B}}{\mu_0}, \quad (4.11)$$

which is the cross product of the convection electric field,  $\mathbf{E}$ , with the perturbation vector of the geomagnetic field  $\delta \mathbf{B}$  with respect to the main geomagnetic field  $\mathbf{B}_0$ , and  $\mu_0$  is permeability [Kelley, 2009] and it is represented in units of  $J/sm^2$  or  $W/m^2$ . In general, the direction of the Poynting vector ( $\mathbf{S}$  vector) indicates

the direction of the propagation or flow of electromagnetic energy that drives the ionospheric currents. We anticipate that the direction and amplitude changes of the Poynting vector correlate with the drag in the satellite orbit and explain the causes of the disturbances observed in the EGG measurements [Ince and Pagiatakis, 2016].

Although our analyses presented in Chapter 3 and literature suggest that cross winds affect the measurements of cross-track accelerometer pair and  $V_{yy}$  diagonal component when compared with the geopotential model computed  $V_{yy}$ , it is difficult to understand which accelerometer pair is affected from the current changes and in which direction by using the trace only. Accordingly, all CM and DM accelerations measured in different directions need to be included in our investigations. In order to avoid such a tedious process, we are motivated to compute the Poynting vector instead, which has a physical meaning and indicates the direction of the flow of electromagnetic energy and therefore the energy input to the satellite environment. It is worth noting that, for the sake of the correctness of our analyses, the Poynting vector computed from the EICS and normalized SECS is furthermore transformed into the GRF by using the azimuth angle of the satellite ground track with respect to the geographical north about the Z-axis of the gradiometer.

Here, we show the two examples examined above by means of Poynting vector components. The left panel of Figure 4.18 shows the time series of the trace (green) and Poynting vector component,  $S_y$  (magenta) in the cross track direction, CM and DM accelerations scaled by 0.5 and 1000 along the complete satellite track over Canada that correspond to the time period from 22:49:00 to 22:59:00 UTC on March 10th. The right panel displays the same four time series from 22:39:00 to 22:50:00 UTC on April 2nd, 2011. Both examples are taken from a period when we observe a  $Kp$  index  $> 3$ . Both cases accentuate a distinctive variation in the flow direction between the latitudes about  $52^\circ$  N and  $66^\circ$  N that correspond to the high variation in the trace in time domain. The behaviour of the CM accelerations and Poynting vector point out the correlation between the two. Moreover, the DM accelerations show distinctive variation at the epochs when the Poynting vector varies abruptly. This is an indication that the CM accelerations are not completely eliminated but leak into the DM accelerations. Most importantly, the agreement between the trace and the Poynting vector is striking and also hints that the relationship between the two exist but may not be linear. The correlation between the trace and the Poynting vector components are further analyzed in time-frequency (scale) domain in the following chapters.

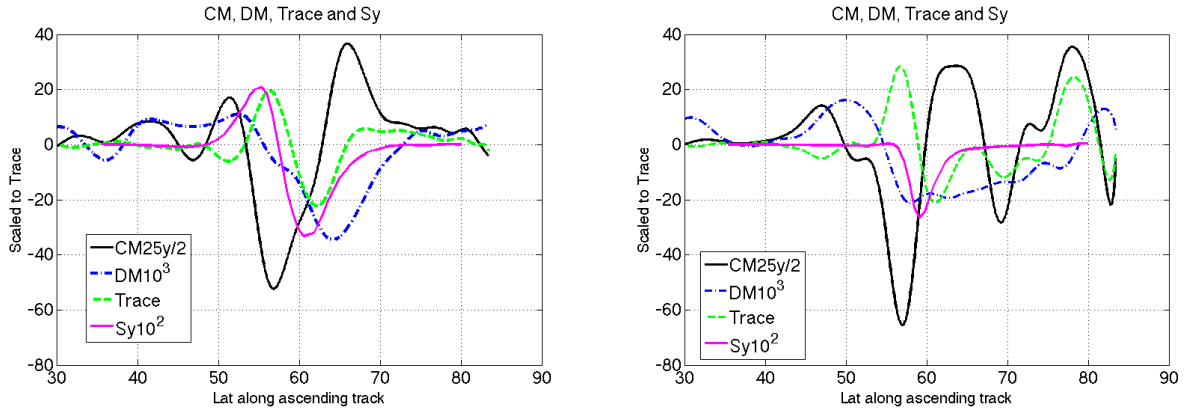


Figure 4.18: Time series of CM and DM accelerations, and Trace and Poynting vector along the satellite track scaled to Trace. a) The measurements of 22:49:00-22:59:00 UTC on March 10th. b) The measurements of 22:39:00-22:50:00 UTC on April 2nd, 2011. Note the simultaneous behaviour of the series with some delay.

## 4.4 Summary

---

In this chapter, we investigated independent observations external to GOCE to understand the cause(s) of the disturbances measured by GOCE EGG. We described the fundamentals of ionosphere, geomagnetic field, and space weather observations for the readers to follow the analyses performed with the presented data in this chapter as well as the analyses in the following chapters. This chapter is critical since it introduces different material to the geodesists. Therefore, there are footnotes which reader may refer to throughout the thesis.

We performed correlation analyses between the EGG disturbances and ACE and WIND observations, geomagnetic indices, terrestrial magnetic disturbance observations and finally equivalent ionospheric currents. We showed that the increasing solar activity measured by different sensors on-board ACE and WIND and propagating into the ionosphere, reaches the Earth surface and causes excitation in the ionospheric dynamics. These dynamics indeed caused a less quiet satellite environment and influenced the EGG measurements. We showed that these sort of extreme ionospheric dynamics were measured by GOCE gradiometer as common-mode accelerations and leaked into the differential-mode accelerations.

One of the most critical points introduced in this chapter was the equivalent ionospheric currents which lead the final results of this thesis later. Equivalent ionospheric currents and spherical elementary currents were summarized and their importance in understanding ionospheric dynamics as a whole was pointed out.

We expanded our analysis and investigated 954 tracks and examined two random examples in detail. We showed that the ionospheric dynamics are highly correlated with the GGT trace. It is the first time such a thorough and rigorous investigation has been performed on the EGG disturbances and solid explanations have been provided. These results constitute an original and significant discovery that sheds light into LEO satellites orbit perturbations. The results of this chapter have been published in Ince and Pagiatakis [2016] and further investigations on these data and the corrections applied to trace are presented in Chapters 7 and 8.

# 5

## Investigations of GOCE Disturbances using the C-IAM

### 5.1 C-IAM Model Description and Simulations

---

In this chapter, we present comparisons between the disturbances observed in the GGT gradients and simulated ionospheric parameters during quiet and stormy periods. The simulations are performed using the Canadian Ionosphere and Atmosphere Model (C-IAM) [Martynenko et al., 2014] that is developed at York University which models the variations and possible enhancement of the electric field, neutral wind, temperature, and density in the ionospheric dynamics during stormy periods. The simulations based on the C-IAM complement the findings of the previous chapter by providing yet additional evidence on the source of perturbation in GOCE measurements.

The ionospheric and thermospheric (IT) dynamics are developed directly by external (solar) driving forces. Moreover, since the density of the charged particles characterize the ionosphere and thermospheric (IT) system, the role of electromagnetic forcing is important. Compared to the lower atmosphere, the neutral density is much lower in the IT. Literature reveals that these two systems, IT and lower atmosphere (troposphere) influence each other and should be considered as a single system. Therefore, the model development covers the entire region from the Earth's surface up to the exosphere (see Figure 4.1). Understanding the entire system is important since it contributes to the determination of the atmosphere's response to solar and magnetic variability [Martynenko et al., 2014].

The Canadian Ionosphere and Atmosphere Model (C-IAM) has been developed to represent the whole atmosphere modelling capability in Canada. The two existing models, Canadian Middle Atmosphere Model (CMAM) [Fomichev et al., 2002] and Murmansk Upper Atmosphere Model (UAM) [Namgaladze et al., 2000], have been used in the development of the first version of C-IAM [Martynenko et al., 2014]. In this research,

C-IAM is used to simulate the electric potential and neutral wind components during magnetic storm and quiet time periods and compare them to the EGG disturbances. Investigations are also expanded on neutral density and temperature simulations.

The C-IAM model is a global model and has been run globally via global proxies as input parameters; therefore, there is no specific input included to tune it for the simulations over Canada. The simulations are performed by means of proxy and boundary conditions and provided by Oleg Martynenko, York University (personal communication, 2015). In this research, the proxy parameters used in the simulations are  $Kp$  and F10.7 indices, which are taken from the Kyoto World Data centre (2011). The F10.7 is used to define the varying solar EUV (Extreme Ultra-Violet) spectrum, whereas  $Kp$  index is used to calculate the polar cap boundary position and cross-polar cap electric field potential drop. Moreover,  $Kp$  index is also used for the spatial and energetic distribution of the auroral precipitation. The use of realistic day-to-day variations of solar and geomagnetic activity help simulate the corresponding variability of the ionospheric emission better [Martynenko et al., 2014].

For the quiet period simulations,  $Kp$  index is set to 2, whereas the real time  $Kp$  index is used for stormy period simulations. The simulations are performed in a spherical geomagnetic grid where the latitude grid interval varies from  $2^\circ$  in auroral area to  $5^\circ$  at the Equator and the longitudinal interval is  $7.5^\circ$  and constant. The simulations used in this study have a 20-minute temporal resolution.

Neutral wind components in zonal and meridional directions ( $m/s$ ), electric potential ( $kV$ ), electric field strength (E-field) components in east-west and north-south directions ( $mV/m$ ), temperature of the neutrals ( $K$ ), and density of the neutrals ( $kg/m^3$ ) are simulated globally and comparisons are performed along satellite tracks near the North Pole. Electric field strength components and potential are computed at an altitude of 175 km, since higher altitudes have constant properties as given at this particular altitude. The rest of the parameters are computed at the approximate satellite altitude, of 250 km.

### 5.1.1 Simulations of the Electric Potential

The electric potential for two different quiet and stormy periods that are simulated based on input proxies are shown in Figures 5.1 and 5.2. The left panel of Figure 5.1 displays the quiet time electric potential at 23:00:00 UTC on March 10th 2011; whereas the right panel of the same figure displays the stormy time electric potential at the same epoch. The ascending and descending tracks corresponding to approximately 6:00 pm and 6:00 am local time are displayed as black and magenta coloured lines, respectively. Since the model produces global values, we do not need to limit our investigations over Canada and Greenland in this

particular example. Therefore, we include a second example when the satellite crosses over east Greenland. The left panel of Figure 5.2 displays quiet time simulations at 18:20:00 UTC on March 11th, 2011; whereas the right panel represents the stormy time simulations at the same epoch.

The enhancement in the electric potential in both cases is very distinguishable around the geomagnetic pole. In the first example, GOCE crosses over a region that has a high negative electric potential accumulated over Northern Canada and Southern Greenland (see the right panel of Figure 5.1). Moreover, continuation of the same track experiences positive electric potential along the descending track.

Both examples show that the simulated electric potential for  $Kp = 2$  (left panels of Figures 5.1 and 5.2) show small positive and negative variability over the day-time (descending) and evening-time (ascending) regions, whereas these values are much more enhanced when the real  $Kp$  index value is used as an input to the simulations (see right panels of Figures 5.1 and 5.2). The potential drop increases distinctively in the stormy time representation. Moreover, the affected regions are expanded in both cases to the east and west. It is expected that the increase in the electric potential affects the ionospheric dynamics and particularly causes changes in zonal wind directions, which is given in the next section.

Convective electric fields are always present over polar regions expanding broadly at ionospheric altitudes. Moreover, the convection follows a standard pattern, such that it follows anti-solar flow in the central polar cap region and east-west flow back toward the sun in both the adjacent evening and morning hours. The basics of the convective electric field are given in `Ionospheric_convection`. The location of the low latitude limit of the high latitude convection is related to the 3-hour magnetic disturbance  $Kp$  index [Heppner, 1973]. The exact position of the maximum and minimum electric potential also depends on  $Kp$  index. The location of these maxima and minima of the electric potential move away from the pole with the  $Kp$  index increasing; therefore, they expand to the south, east, and west. However, in general, the position of these extrema can be identified at near 6:00 am and 6:00 pm local time and around 70 degree latitude as indicated in both examples.

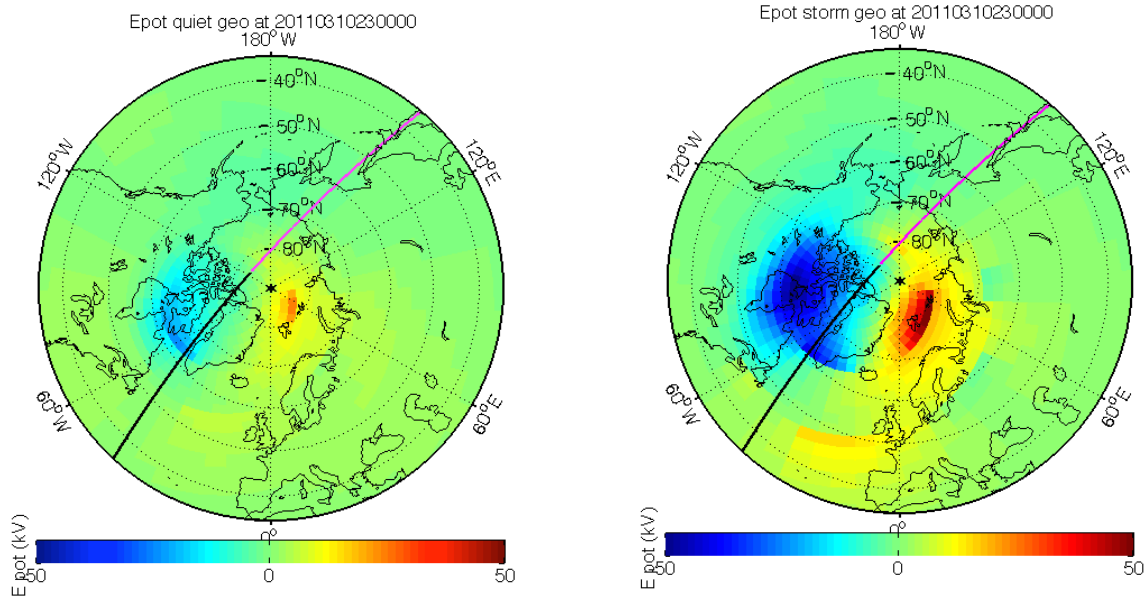


Figure 5.1: Electric potential for quiet (left panel) and stormy (right panel) time for March 10th, 23:00:00 UTC, 2011 are displayed. Notice the enhancement over Northern Canada and Southern Greenland during storm period. The ascending and descending tracks are displayed by black and magenta coloured lines and correspond to approximately 6:00 pm and 6:00 am local time, respectively. The satellite crosses over a negative electric potential during evening time and a positive electric potential region during morning time.

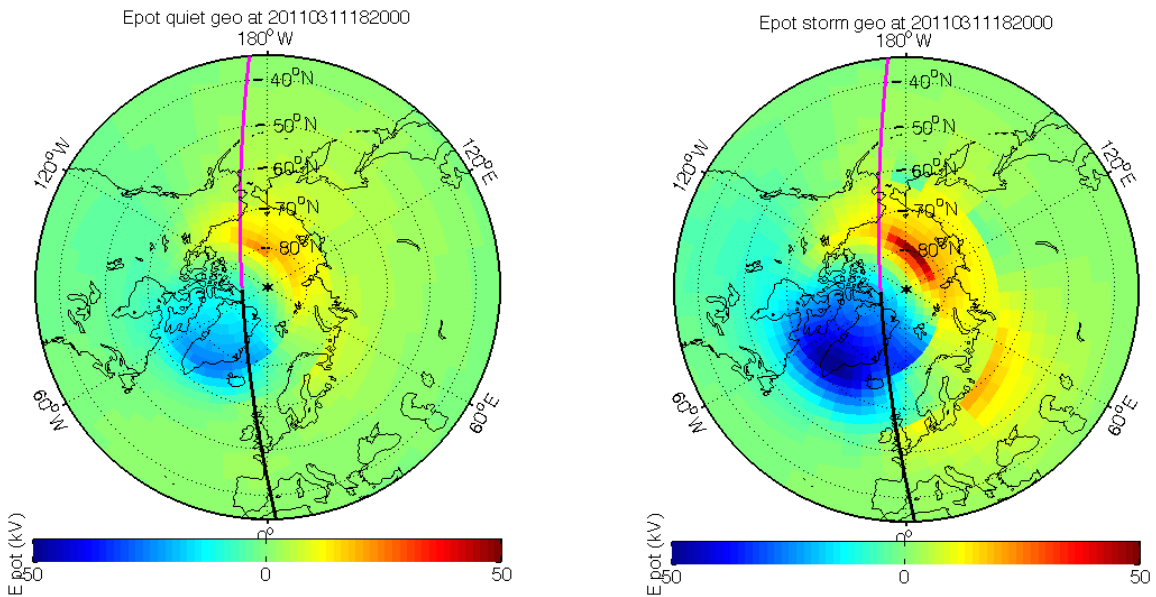


Figure 5.2: Electric potential for quiet (left panel) and stormy (right panel) time for March 11th, 18:20:00 UTC, 2011. Notice the enhancement over Arctic and Greenland during storm period (right panel). The ascending and descending tracks are displayed by black and magenta colours and correspond to approximately 6:00 pm and 6:00 am local time, respectively.

### 5.1.2 Simulations of Neutral Winds

Neutral wind components in the east-west and north-south directions simulated in the spherical geomagnetic coordinate system are transformed into the geographical coordinate system. The transformed series for the same quiet and stormy periods, at 23:00:00 UTC, March 10th and 18:20:00 UTC, March 11th 2011 are presented in Figures 5.3 and 5.4. The left panel of Figure 5.3 shows the quiet period neutral winds in the Northern Hemisphere; whereas the right panel shows the stormy periods wind information. Neutral winds during stormy period are enhanced and show circular movements over the magnetic pole. Also, some direction changes are observed in other regions (e.g., over Alaska). The left panel of Figure 5.4 shows the quiet period neutral winds of the second example; whereas the right panel displays the stormy period neutral winds. It is also visible in this example that the neutral wind components are enhanced and change directions and move from east to west different than the first example.

The enhancement of the neutral winds can be due to the temperature and density variations (increase) as well as to the enhancement of the electric field (E-field). The rotational patterns in the neutral winds are expected to show changes due to the ion motion. It is worth noting that the rotations in neutral winds can sometimes be dominating the usual behaviour of the neutral winds.

One can notice that the electric field discrepancies do not expand to the western Canada, whereas the neutral winds can still show strong variations expanding toward western and southern Canada around local evening time. It is worth noting that the electric field effect is not a local effect and expanding widely. Accordingly, direct comparisons of neutral winds and electric field at the satellite position would not be possible. Therefore, satellite tracks in particular regions should be used in understanding the causality of neutral winds and electric field and their possible effects on the GOCE disturbances. Moreover, not all the tracks can explain the relation between the disturbances observed in gravity gradients and ionospheric dynamics.

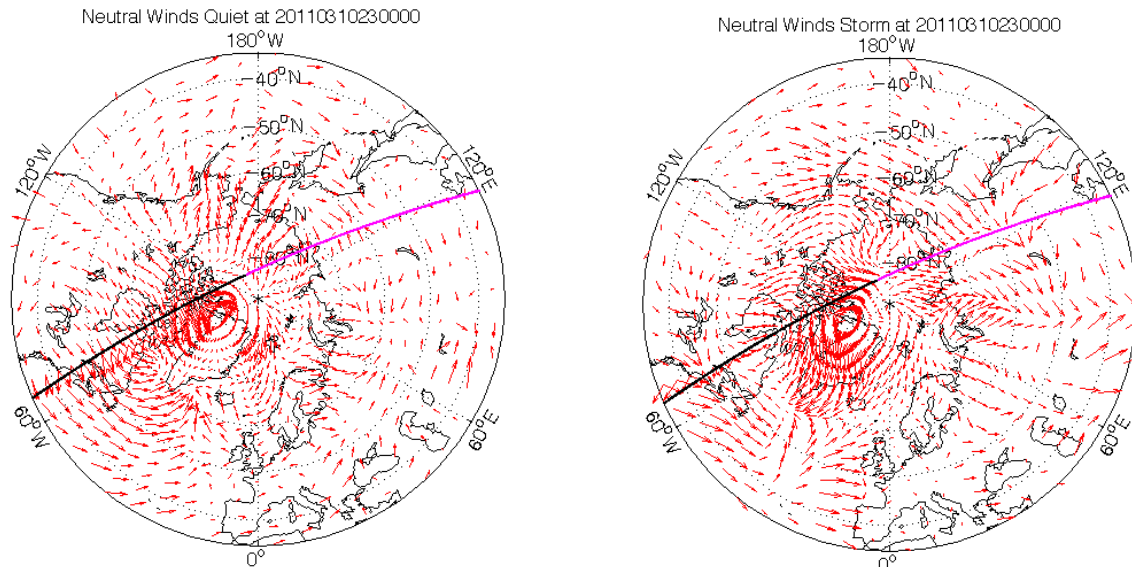


Figure 5.3: Neutral winds for quiet (left panel) and stormy (right panel) time for March 10th, 23:00:00 UTC, 2011 are displayed. Neutral winds during stormy period show circular movements over the magnetic pole and some enhancements and direction changes are observed in other regions (e.g. over Alaska).

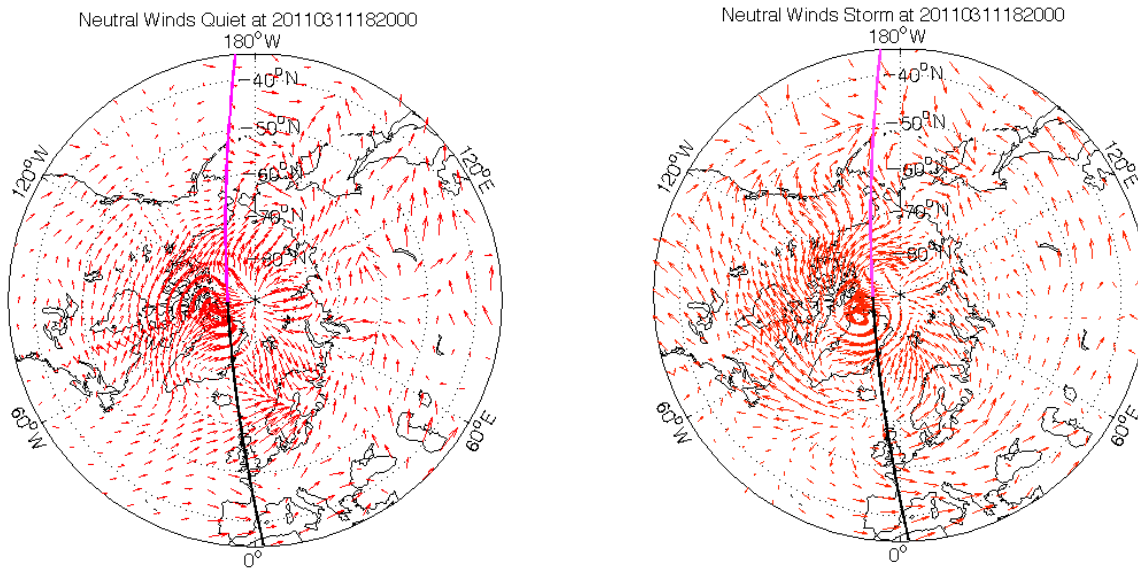


Figure 5.4: Neutral winds for quiet (left panel) and stormy (right panel) time for March 11th, 18:20:00 UTC, 2011 are displayed. Neutral wind components are enhanced and change directions and move from east to west.

### 5.1.3 Quiet and Stormy Time Simulations on March 11, 2011

The electric potential and neutral wind components simulated for 3 morning and 3 evening epochs, precisely at 06:20, 08:00, 09:20 and 19:40, 21:20, and 22:40 UTC time on March 11, 2011, are shown in Figures 5.5 to 5.10 with the corresponding  $Kp$  index as 4,4,2,6,6, and 6, respectively. These six examples show how the electric potential and neutral winds evolve during the day and what kind of extreme conditions are developed due to the increasing solar activity and geomagnetic storms.

Figures from 5.5 to 5.10 depict the evolution of the electric field and neutral winds over North Pole during stormy period where the real  $Kp$  index is used as input. It is seen that there are some large variations present in the morning time, 06:20:00 UTC where the  $Kp = 4$  indicates some magnetic activity as depicted in Figure 5.5. The electric field variations in terms of potential drop are much smaller at 12:00 pm UTC time and the neutral winds also show smaller variations in a limited region at noon as depicted in Figure 5.7.

We further investigate the simulations during a geomagnetic storm where the  $Kp$  index is calculated as 6. We present simulations in Figures 5.8 to 5.10. The electric field simulations indicate much higher potential drop (the difference between the negative and positive peaks of the electric potential) between the morning and evening sectors in the stormy time simulations. Moreover, the ascending satellite track shown by black line in Figures 5.5 to 5.10 crosses through a region where we observe strong negative electric field accumulation. The variation of the electric field along the satellite path is expected to influence the satellite environment and non-gravitational acceleration measurements. The neutral winds are centred over the geomagnetic poles and we could not assess the effect of them on the satellite environment.

Based on the stormy time simulations, we do not expect to have identical behaviour of electric potential and neutral winds in identical areas. Figures 5.5 to 5.10 presented here show that the winds are always centred over the geomagnetic poles, whereas the enhancements in the electric potential show their influences at morning and evening sectors. We also see that the neutral winds are expanded over a larger region and to the east-west and south in the evening sector and show smaller magnitude in the morning sector. A direct relationship between the two is not considered, but it is expected that the orientation of the neutral winds be dependent on the electric field.

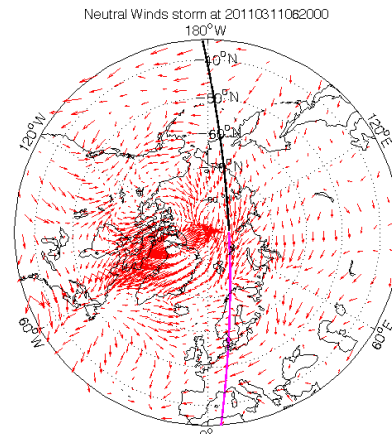
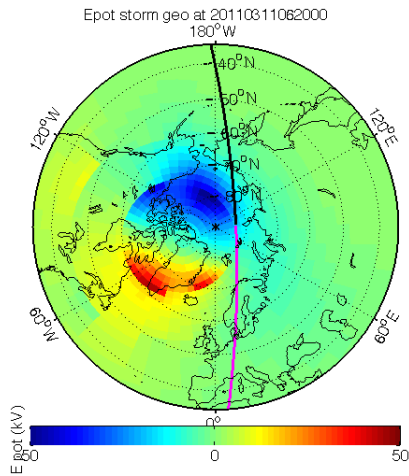


Figure 5.5: Electric potential and neutral winds at 06:20:00 UTC,  $Kp = 4$ .

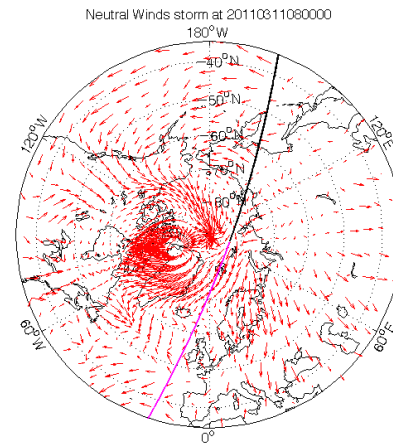
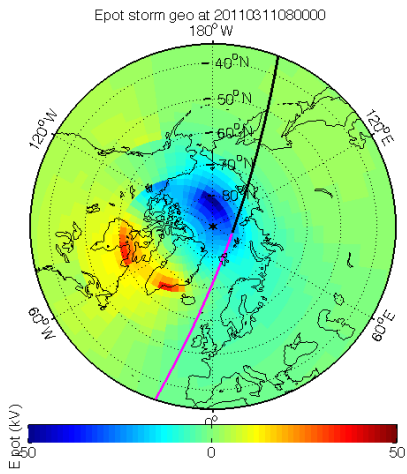


Figure 5.6: Electric potential and neutral winds at 08:00:00 UTC,  $Kp = 4$ .

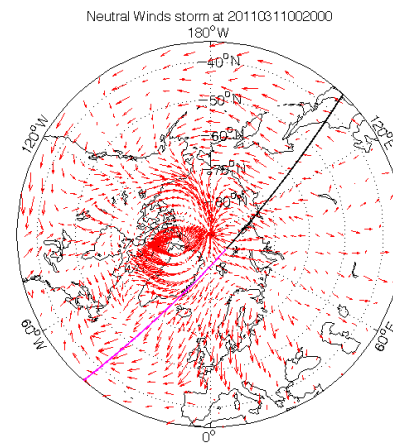
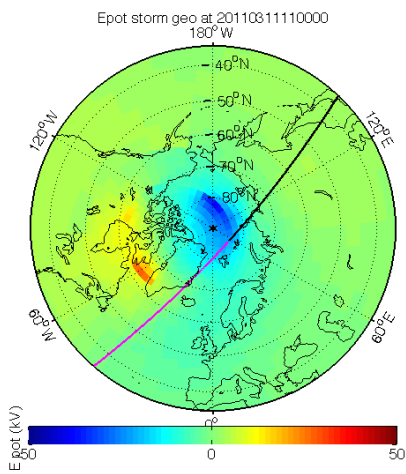


Figure 5.7: Electric potential and neutral winds at 11:09:00 UTC,  $Kp = 2$ .

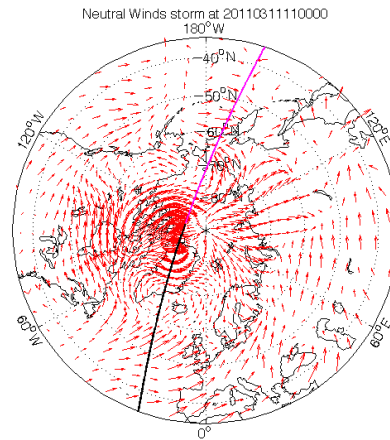
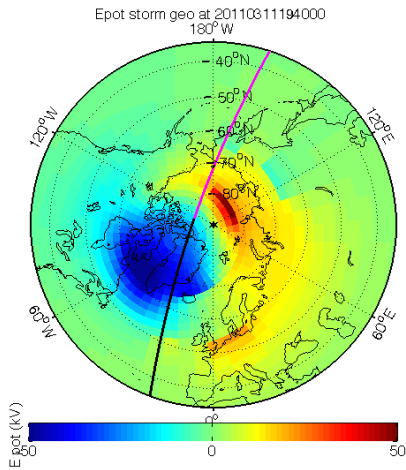


Figure 5.8: Electric potential and neutral winds at 19:40:00 UTC,  $Kp = 6$ .

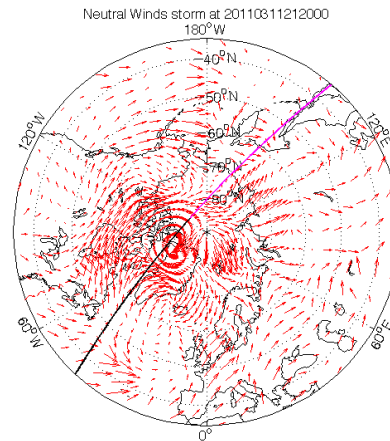
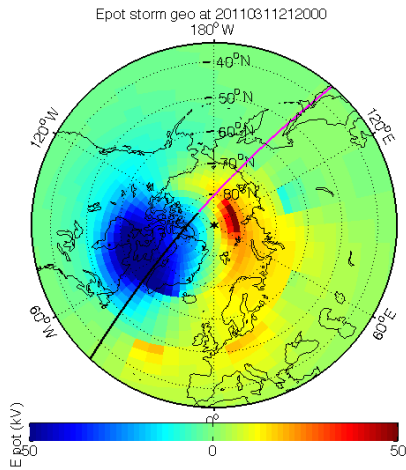


Figure 5.9: Electric potential and neutral winds at 21:20:00 UTC,  $Kp = 6$ .

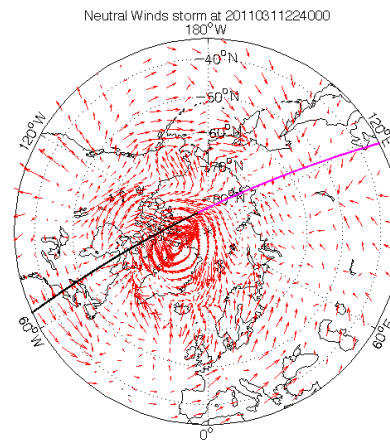
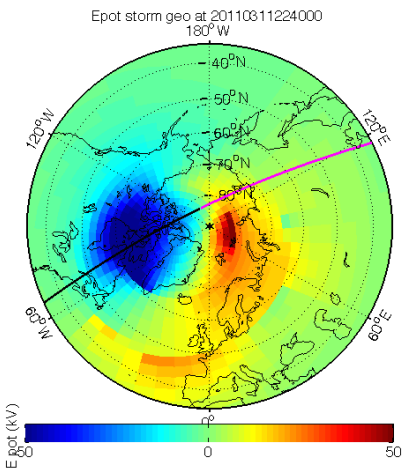


Figure 5.10: Electric potential and neutral winds at 22:40:00 UTC,  $Kp = 6$ .

## 5.2 Analysis of C-IAM simulations along track

---

In this section, we present comparisons of the disturbances measured by GOCE accelerometers and C-IAM simulations that are interpolated to GOCE positions. These comparisons are parallel to those presented in Chapter 4 and complementary in particular to the comparisons with energy flux along the satellite track. Moreover, by this approach it is possible to look into the GOCE measurements and their response to the ionospheric dynamics along both ascending and descending tracks (evening and morning sectors).

In this section, the neutral winds and electric potential are compared with the common-mode accelerations and trace of GGT along the satellite track at 09:20:00 and 22:40:00 UTC, March 11 2011. Figures 5.11 and 5.12 show the neutral winds, the derivative of electric potential, GGT trace and CM accelerations along the ascending and descending satellite tracks, respectively. Our investigations show that the large electric potential variations at latitudes above  $75^\circ$  North are not reliable for our comparison purposes, especially for descending track analyses. Even though there are very dynamic changes over these regions, they do not represent any variations that are observed in the trace or CM accelerations. Accordingly, the investigations need to be limited for the regions of consistent variations (e.g.,  $40^\circ$  to  $75^\circ$  North).

It is speculated [Peterseim et al., 2011, Siemes, 2012, Stummer et al., 2011, Schack et al., 2014] that the disturbances observed in GOCE  $V_{yy}$  gradients are due to cross winds. Martynenko et al. [2014] indicates that the winds affect the structure of the ionosphere based on two mechanisms. One is via the ionospheric dynamo. Charge separation that occurs through the differential motions of the ions and electrons generate the electric fields. Ions are transported by the neutral winds across magnetic field lines in the day time E region. Magnetized electrons are not transported. The  $\mathbf{E} \times \mathbf{B}$  drift of ionospheric plasma tubes are produced by the resulting electric field. The  $\mathbf{E} \times \mathbf{B}$  drift causes vertical movements in the plasma where the tube inclination is small enough (e.g. at low and middle latitudes). As a result of the vertical drift, ions move to heights with different atmosphere density therefore with a different recombination rate<sup>1</sup>.

The second mechanism is due to direct neutral-ion momentum transfer in the F2 layer. The neutral-ion collision frequency in the ionospheric F2 layer is too low to overcome the Lorentz force<sup>2</sup>. Therefore, the wind cannot push ions across the magnetic field. However, as a result of collisions with neutral particles, the ions can still be pushed upward or downward along the magnetic field lines. This is observed in the ionospheric layer F2 in the low and middle latitudes where the neutral wind has a large field aligned component [Knyazeva

---

<sup>1</sup>Recombination: In physics, the union of free electrons and holes in a semiconductor.

<sup>2</sup>Lorentz force: The force which is exerted by a magnetic field on a moving electric charge.

et al., 2012]. Therefore, this principle explains why we do not expect to have instantaneous and direct effect on the GOCE accelerometers coming from the neutral winds.

In our examples presented previously, it is observed that the neutral wind speed can reach up to 250  $m/s$  in mid- to high-latitudes along the ascending tracks, whereas the speed seems to be much smaller along the descending tracks. Direct relation between the neutral winds and electric potential or neutral winds or CM accelerations is not observed and a linear relation between any of these phenomena cannot be developed.

Based on our investigations, the derivative of the simulated electric potential shown along the satellite tracks need to be investigated closer. The right panel of figure 5.11 indicates a high coherency between the electric potential variations and CM and Trace. Within similar latitude interval one can observe similar dynamics in accelerometer observations. This can indicate that long-lasting (at least few minutes) accumulation of the electric potential can influence the gradiometer measurements.

It is expected that the accumulation of the electric potential along the satellite track can create an impulse effect on the gradiometer measurements that can leak into the gradients. However, the investigations should be limited between the latitudes of around  $40^\circ$  and  $75^\circ$  North, since the lower and higher latitudes show very different dynamics. Therefore, we cannot rely on the linearly interpolated potential values along the satellite track to be used in our impulse response system but other interpolation techniques should be considered. Moreover, it is also anticipated that the other interpolation techniques may also not be useful due to the coarse time and spatial resolution of the C-IAM.

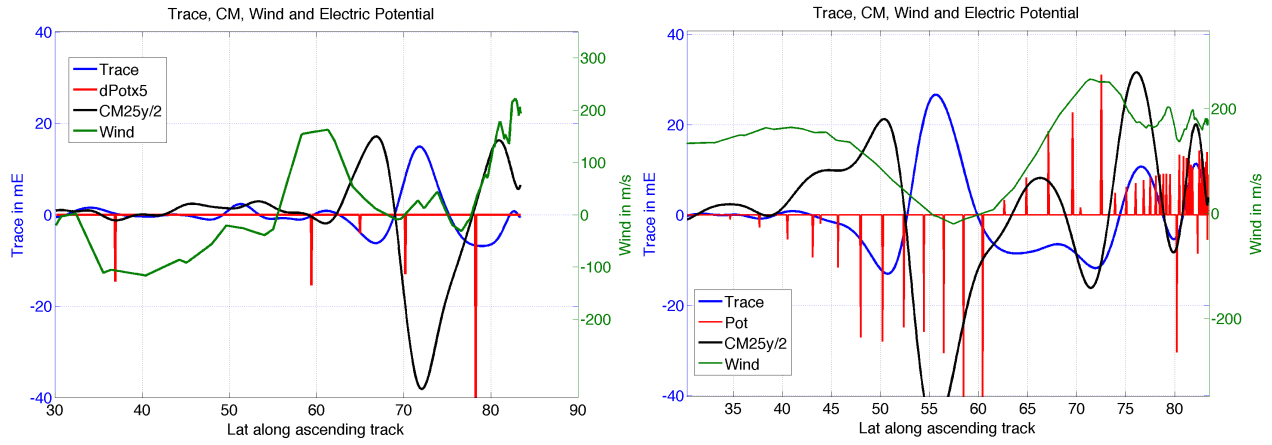


Figure 5.11: Cross-track neutral wind at GRF, differentiated electric potential are compared with Trace and cross track CM accelerations along the satellite ascending tracks at 09:20:00 and 23:00 on March 11th.

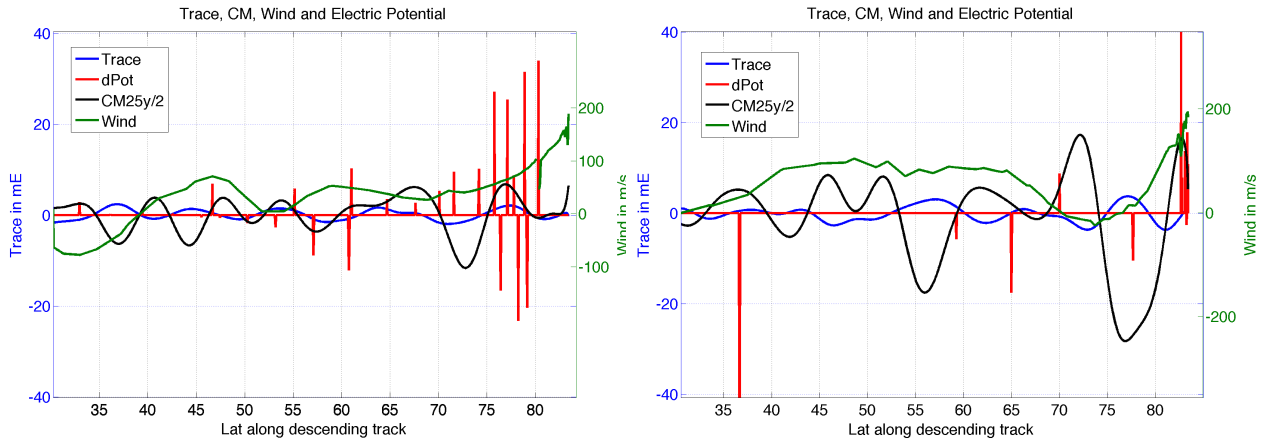


Figure 5.12: Cross-track neutral wind at GRF, differentiated electric potential are compared with Trace and cross track CM accelerations along the satellite descending track at 09:20:00 and 23:00 on March 11th.

## 5.3 Summary

---

In this chapter, we introduced the Canadian Ionosphere and Atmosphere Model (C-IAM) and presented electric field and neutral wind simulations that were used to investigate different conditions of the ionosphere, e.g., intense ionospheric dynamics during geomagnetic storms. This study was necessary and unique since it complemented our analysis presented in Chapter 4. In addition, we discussed the possibility of the neutral winds to influence the satellite dynamics since it was mentioned in the literature that cross winds over polar regions were the cause of these disturbances.

We presented electric field and neutral wind simulations for quiet time and stormy time and identified differences for the North Pole. We showed that there are substantial differences between a quiet and stormy period conditions in the ionosphere which influence the satellite environment. Moreover, the model simulations are produced at the satellite positions along the satellite track and transformed into the gradiometer reference frame for more rigorous analyses. These values are compared with the EGG disturbances along the satellite track which also revealed that a higher resolution model outputs are needed for proper comparisons and a direct comparison was not possible with the simulation results we retrieved.

The analyses presented in this chapter are original and complement independently our investigations using the Poynting energy flux. It is worth reminding that this study may give an insight to mission scientists for using external high resolution model in understanding GOCE gradiometer measurements response to the external spacecraft environment.

# 6

## Analysis of Data in Time-Scale (Frequency) Domain

### 6.1 Analysis in Time-Scale Domain

---

In this chapter, we cover the analyses of the GOCE gravitational gradients along with solar activity and geomagnetic storm proxies in time and scale (frequency) domains by using the Continuous Wavelet Transform, and Cross Wavelet Phase and Wavelet Coherence Analysis. We understand that GOCE gravitational gradients and proxies used in this research are time-variant series and traditional methods, such as Fourier Transform provide little information in frequency domain and have shortcomings. Accordingly, the wavelet transform which gives detail both in time and scale (frequency) domains is used in our analyses. The analyses are performed by using scale instead of frequency since the wavelet transform is based on scale and not on frequency. Moreover, conversion between the two may not be straightforward depending on the complexity of the wavelet function used in the analyses.

Track by track analyses are performed in order to explore the gravitational gradients in detail in order to detect large magnitude variations common in both the gradiometer measurements and ionospheric dynamics. As mentioned in previous chapters, the orientation of the ascending and descending tracks is different and causes different satellite perturbations. We focus on the ascending satellite tracks over the geomagnetic poles since the observed perturbations identified over these regions are larger than in the descending tracks. Accordingly, we need to investigate the two separately. Moreover, we extract the Poynting vector components and GGT trace starting from latitude 40 up to degree 85 for comparison purposes.

In previous chapters, EIC vectors and SECS amplitudes were used to compute the Poynting vector over North America and Greenland. The limitation in the area is due to the limited number of magnetometer stations used in the development of modelled EICS values (see Figure 4.12). We investigate 954 satellite

tracks during March and April, 2011. Over 400 of them have Poynting vector components in spatial domain corresponding to the area of the magnetometer stations. Therefore, the satellite tracks we investigate have 5 to 15 minutes of gradiometer measurements over North America and Greenland.

Wavelet analysis is commonly used in the analysis of geophysical time series that contain non-stationary power at many different frequencies. This method has its advantages and drawbacks compared to the traditional signal processing methods. Traditional mathematical methods implicitly assume that the time series examined are stationary in time, which is not the case in most of the real signals. Geophysical signals are often generated by complex systems and investigations on the trend and periodicities of such signals are of great interest.

Wavelet transform expands a time series into scale (frequency) and time domain and provides localized information on its power. There are two classes of wavelet transforms, namely Continuous and Discrete Wavelet Transforms (CWT and DWT, respectively). According to Grinsted et al. [2004] the Discrete Wavelet Transform (DWT) helps in data compression and reduction of noise. On the other hand, the Continuous Wavelet Transform (CWT) is particularly more useful in feature extraction. In this research, we are interested in extracting features in the trace and Poynting vector components that correspond to magnetically active periods. The CWT helps localize the disturbances, provides information on the scale (frequency content) and allows extraction of useful information. Accordingly, we are motivated to use the CWT analysis in our investigations. The extracted features in CWT analysis are further investigated by Cross Wavelet Phase and Wavelet Coherence Analysis.

### 6.1.1 Continuous Wavelet Transform

The Continuous Wavelet Transform (CWT) is defined as the integral of the signal multiplied by a scaled and shifted wavelet function over the entire time domain. The results of this transform are the wavelet coefficients which are functions of scale and position [Misiti et al., 1996, Kumar and Foufoula-Georgiou, 1997].

The CWT of a time series  $f(t)$  is represented by the convolution integral

$$W_\psi f(a, k) = \frac{1}{\sqrt{|a|}} \int_{-\infty}^{\infty} \bar{\psi} \left( \frac{t-k}{a} \right) f(t) dt, \quad (6.1)$$

where  $a$  is scale,  $k$  is the translation value, and  $t$  time, whereas  $\psi$  is a continuous function in both time and frequency and is called mother wavelet and  $\bar{\psi}$  means the dual function of  $\psi$ .

Scaling of the wavelet function can be understood as stretching or compressing the function. The smaller the scale factor, the more compressed the wavelet function, whereas shifting  $k$  means delaying the signal in time domain, such that the position of the wavelet would be  $f(t - k)$ . More examples can be seen in Misiti et al. [1996]. As a result of wavelet transform, the data in time domain are transformed into 2D domain, time and scale by using this transform.

The first step in the wavelet analysis is to make a decision on which wavelet to use. Even though wavelet analyses have only been used in geophysical applications recently and grew from Jean Morlet's research on seismic signals in the 1980s; there is a vast number of examples based on the Morlet Wavelet [Kumar and Foufoula-Georgiou, 1997, Grinsted et al., 2004, Jevrejeva et al., 2006, Moore et al., 2006]. According to Grinsted et al. [2004], the Morlet wavelet provides a good balance between time and frequency localization when using wavelets for feature extraction purposes.

We start with the Morlet wavelet and test various wavelets by comparing the wavelet function to a segment of our signal. This experimental approach applies to cross correlation of the mother wavelet with the average shape of the waveform we want to detect. The correlations are measured along the entire signal by shifting the wavelet function. Once the mother wavelet is chosen, the next step is to scale the wavelet function so that the correlations can be performed for all small to large scale variations. The range of the scale can be chosen based on the frequency bandwidth of the signal characteristics. The shifting process is repeated by using a scaled wavelet.

This process estimates the wavelet coefficients at different scales of different sections of the signal. Then, these computed coefficients can be displayed on a 2D figure where the  $x$ -axis represents time and the  $y$ -axis represents scale (or frequency) with a colour code representing the magnitude of the wavelet coefficient. The time-frequency representation is commonly called spectrogram and larger coefficients mean larger amount of resemblance between the original signal and the wavelet function chosen. High scale values are derived by using the stretched wavelet that represents the low frequency part of the signal (see Figure 6.1), whereas the low scale values refer to the compressed wavelet and show rapidly changing signal components, in other words, high frequency information [Misiti et al., 1996]. Therefore, we can say that there holds a general inverse relationship between scale and frequency for signals.

Figure 6.1 represents the principle of wavelet analysis, which is based on a windowing technique with variable size windows. As mentioned above, high scale values represent the low frequency components of the signal that are derived from the stretched wavelet function, whereas low scale values represent the high frequency components. In Figure 6.1, we show that the height and width of the "boxes" varies from low to high scale values. For example, the first box displayed by the black rectangle on the left side shows a

range where we have wider range in scale (frequency domain) and a narrower range in time domain, whereas the second example shows narrower range in scale but larger range in time domain. This indicates that the localization of the low frequency components in time domain can be done more precisely than the high frequency components. On the contrary, the location of the high frequency components in the frequency domain can be performed more precisely than the low frequency components. In other words, the wavelet analysis allows the use of long time intervals when more precise low-frequency information is required, and shorter time intervals when high-frequency information is required.

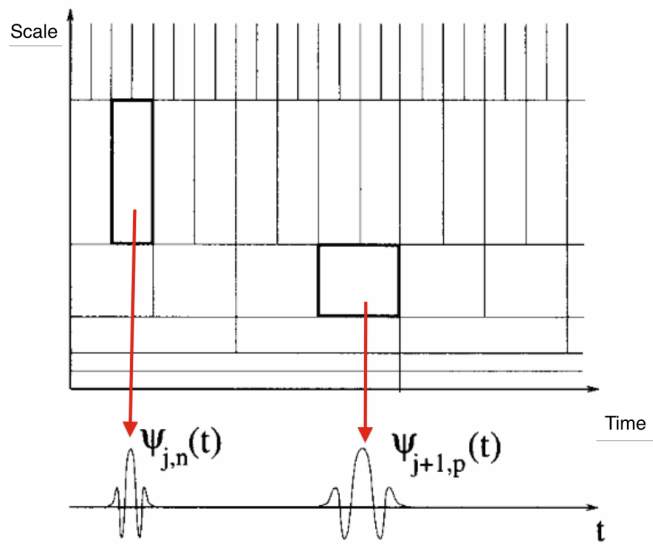


Figure 6.1: The time-frequency boxes of wavelet basis define a tiling of the time-frequency plane (taken from Mallat [1998]).

The CWT is a convolution process of the time series with the wavelet function or in other words the local basis functions. These basis functions can be scaled (stretched) and translated in both frequency and time domain. Thus, a time series can be decomposed in time and scale (frequency) by using wavelet analysis. It is worth mentioning that Matlab's CWT operates on discrete time series. Different from the DWT, CWT can operate to every scale and is continuous when shifting the wavelet function smoothly during the operation [Misiti et al., 1996].

As mentioned above, the Morlet wavelet is one of the most commonly used local basis in investigating geophysical time series. In our study, after testing different wavelet functions, we found that the complex Gauss Wavelet of eighth order extracts more useful information. Therefore, the 8th order Gaussian wavelet which is shown in Figure 6.2 is applied in our analyses.

The complex Gauss wavelet function of the 8th order consists of a real and an imaginary part and it is expressed as:

$$\overline{\psi(t)} = C_p e^{-it} e^{-t^2}, \quad (6.2)$$

by taking the  $p^{th}$  derivative of mother wavelet where  $C_p$  is the normalization constant.

The two common types of the signature observed in the filtered trace are displayed in Figure 6.3. These two types are observed in most tracks. However, the signatures are not limited to these two kinds and many different signatures have been observed. Therefore, further investigations are needed to model them. Moreover, the length of the signature in time domain and its constituents also show variations depending on the satellite environment.

The two cases that we looked at in Chapter 4 (see Figures 4.16 and 4.17) are examined in this chapter by using CWT. These two cases are found in two stormy periods in which we observe high correlation between the trace disturbances and the Poynting vector components in the cross-track direction. The time series along the satellite ascending track are shown in the upper panels of Figures 6.4 and 6.5 corresponding to Case 1 and Case 2, respectively. The corresponding CWT analyses are shown in the lower panels of the same figures. It is worth remembering that the Poynting vector signal is computed from EICS vectors and SECS amplitudes with no filtering applied. Moreover, the trace is retrieved from the diagonal components of the GGT that are filtered into 180-300 s bandwidth interval.

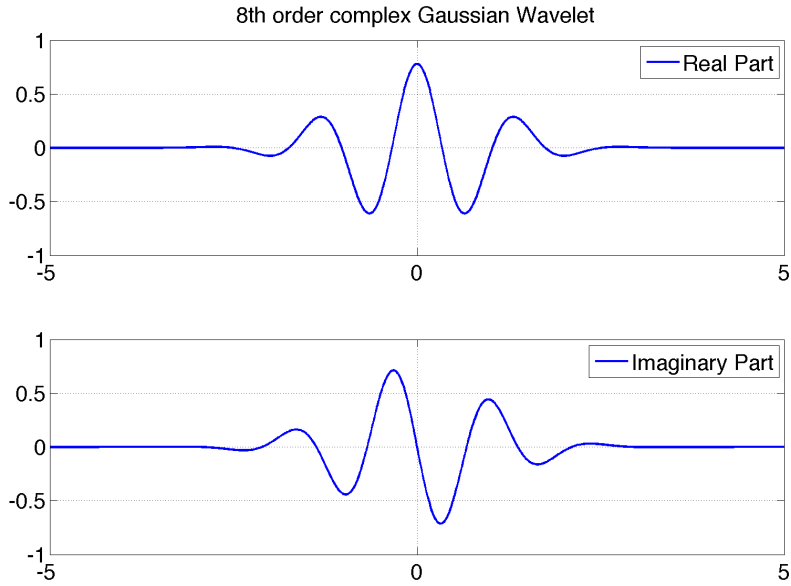


Figure 6.2: The 8th derivative of a Gauss Wavelet is represented. Note the real part and the imaginary parts complement each other.

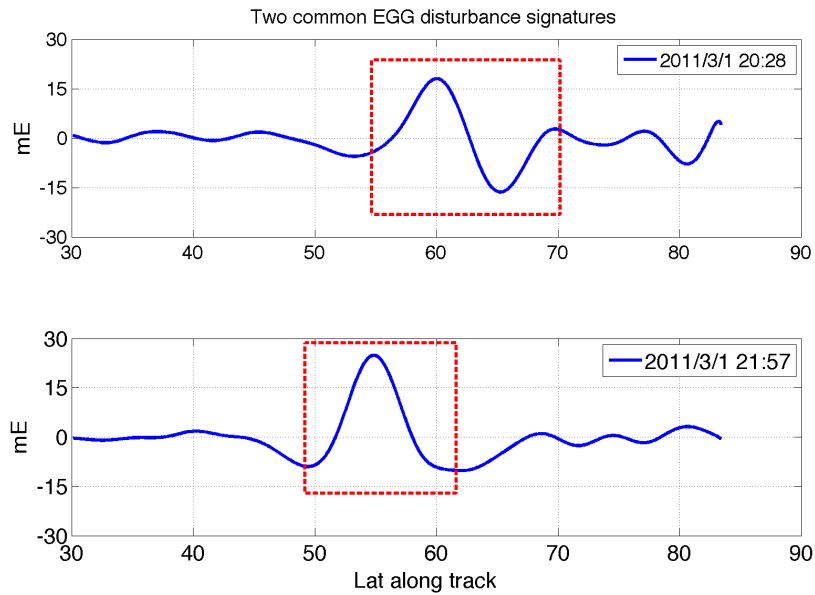


Figure 6.3: The two commonly observed disturbance signatures in trace. The signature is not unique for all the cases and shows variations depending on the non-gravitational forces present in the satellite environment.

Case 1 CWT analyses show that a strong peak exists in both series corresponding to time interval localized around 350 to 400 seconds. One needs to note that the sampling interval and start time should be the same for both series. In our investigations, start time is  $t_0=0$  when the satellite starts crossing over  $40^\circ\text{N}$  latitude. Therefore, the length of the series varies from a few minutes up to 15 minutes. Case 1 is a particular case in which we observe very similar signatures in both signals measured from 22:49:00 to 22:59:00 UTC on March 10th with slightly different scales (frequency) components. We assume that the satellite was exposed to intense ionospheric dynamics. The similarity between the two signal signatures (cf., Figure 6.3) hints the direct or indirect relation between the variations in the cross-track Poynting vector component  $S_y$ , and accelerometer measurements. Moreover, the measured effects leak into the gradients and are observed in the trace which proves the high level sensitivity of the GOCE accelerometers.

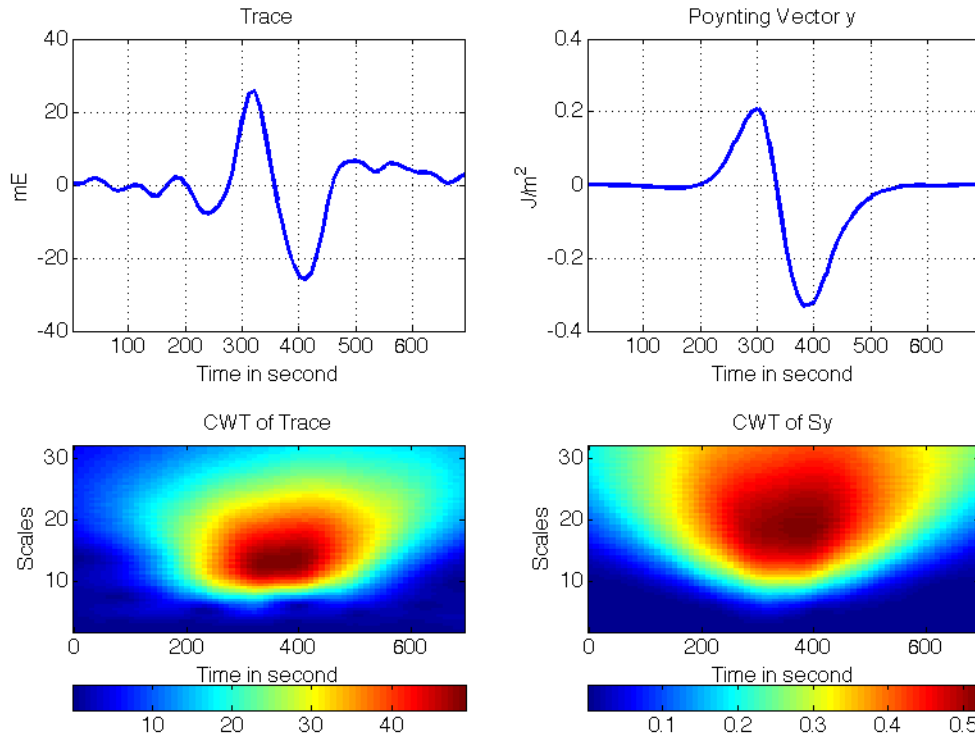


Figure 6.4: Case 1: CWT analyses of trace and cross-track Poynting vector component from 22:49:00 to 22:59:00 UTC on March 10th. Note that this example represents a case when intense ionospheric dynamics occur and the signal variation in both series is highly coherent with slight differences in the frequency content.

Based on our analyses of over 400 tracks, we can conclude that the system of the ionospheric dynamics and the corresponding disturbances observed in the gradients is not a linear process. Therefore, the behaviour of the input-output relationship observed in different tracks is different and varies substantially. In this chapter, we include another case to show a different structure observed in the time series.

In Case 2 displayed in Figure 6.5, we investigate the trace and cross-track Poynting vector measurements from 22:39:00 to 22:50:00 UTC on April 2nd, 2011 when we observe different signatures compared to Case 1. The CWT analyses confirms that the features occur within similar frequency bandwidths. We observe slightly different signatures, but the main features are kept in the signal variation with a possible phase shift between the trace and cross-track Poynting vector component. It is worth mentioning here that the auroral zone in North America is between the latitudes around  $60^\circ$  and  $72^\circ\text{N}$ . This kind of analysis shows clearly whether any physical phenomena (e.g., ionospheric currents) occurring over this region may have an effect on the GOCE measurements. Moreover, we do not expect to see any specific signal or similar signal features in every track, but we expect coherency in terms of the variations in time domain.

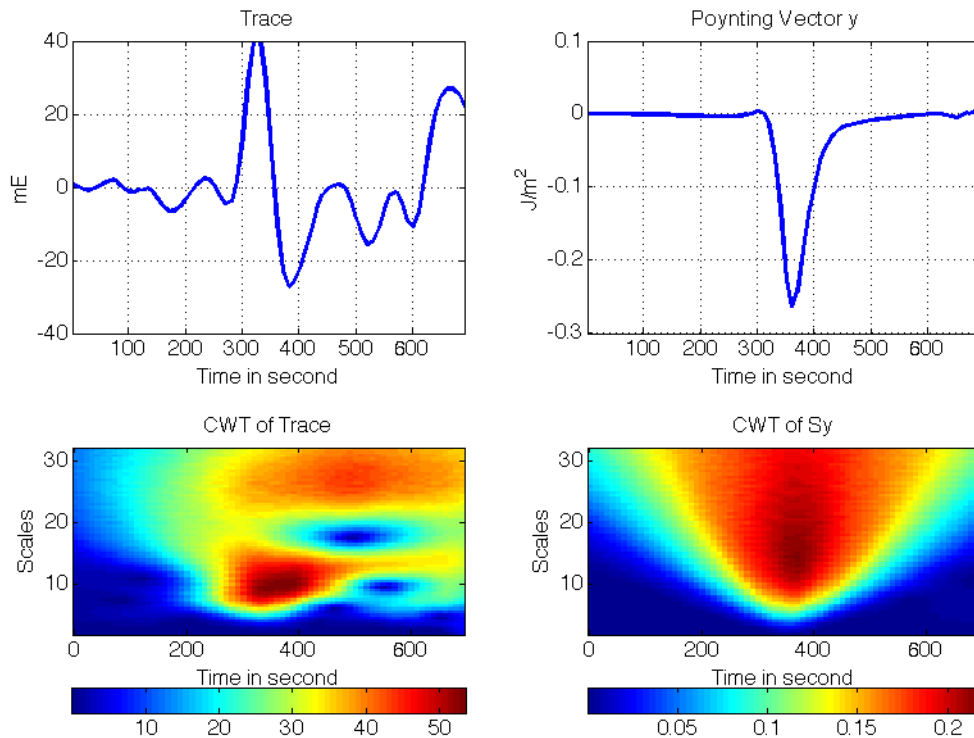


Figure 6.5: Case 2: CWT analyses of trace and cross-track Poynting vector component from 22:39:00 to 22:50:00 UTC on April 2nd, 2011. Note that the similarities of the peaks and differences measured in the frequency content between the trace and Poynting vector series.

In summary, the CWT analyses help us confirm that the GGT trace shows different signatures depending on the input ionospheric dynamics. Accordingly, we can safely expect that the variations in the GGT signal will vary in different cases and show different characteristics in time and frequency domain. Moreover, this indicates that our dynamic system is not a pure linear system and may depend on the amplitude and frequency content of the input signal which further will be discussed in the next chapter. In the following sections, we include phase and coherency analyses.

### 6.1.2 Cross Wavelet Analysis

In order to further understand the input (Poynting vector)-output (Trace) mechanism, Cross-Wavelet and Wavelet Coherence analyses of the signals are performed. Moreover, the phase delay between the input and output series is investigated.

The wavelet cross spectrum of two equally sampled time series,  $x$  and  $y$  is:

$$W_{xy}f(a, k) = S(W_x^* f(a, k)W_y(a, k)), \quad (6.3)$$

where  $W_x(a, k)$  and  $W_y(a, k)$  correspond to the CWT of the  $x$  and  $y$  at scales  $a$  and position  $k$ , respectively. The superscript  $*$  denotes complex conjugate and  $S$  indicates the smoothing operator in time and scale. The smoothing operator is expressed as :

$$S(W) = S_{scale}(S_{time}(W_n(s))), \quad (6.4)$$

where  $S_{scale}$  represents the smoothing along the wavelet scale axis and  $S_{time}$  is the smoothing in time<sup>1</sup>.

### 6.1.3 Cross Coherence Analysis

The wavelet coherence of two time series is different from the cross-spectrum and returns the magnitude squared wavelet coherence which represents the correlation between the input and output signals in time-

---

<sup>1</sup>Naturally, the smoothing operator is designed in a way so that it has a similar footprint as the wavelet used. For the Morlet wavelet, a suitable smoothing operator is presented in Torrence and Webster [1998] as:

$$S_{time}(W)|_s = (W_n(s) * c_1^{-t^2/2s^2})|_s, S_{time}(W)|_s = (W_n(s) * c_2\Pi(0.6s))|_s, \quad (6.5)$$

where  $c_1$  and  $c_2$  are normalization constants and  $\Pi$  is the rectangle function [Grinsted et al., 2004].

frequency domain as:

$$C = \frac{|S(W_x^*(a, k)W_y(a, k))|^2}{S(|W_x(a, k)|^2)S(|W_y(a, k)|^2)}, \quad (6.6)$$

where the magnitude of the wavelet coherence corresponds to local correlation coefficient between the two series in time-scale domain.

This coherence is similar to the traditional correlation coefficient and very useful for analyzing non-stationary signals. We investigate the two examples presented in Figures 6.4 and 6.5. The coherency coefficients presented in Figures 6.6 and 6.7 show that in both cases, the GGT trace and Poynting vector component are highly correlated and the local correlation coefficient is above 0.8 for the frequency intervals of our interest along the track. The high correlation coefficient along the entire track is due to the smoothness of the series.

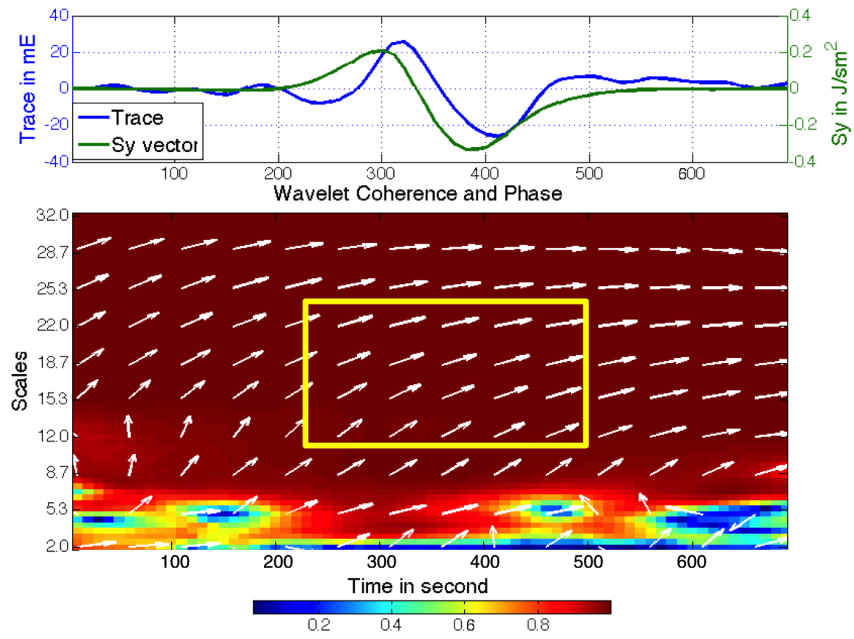


Figure 6.6: Coherency analyses of the trace and cross-track Poynting vector component measured from 22:49:00 to 22:59:00 UTC on March 10th, 2011. The arrows superimposed indicate the phase angle between the two time series. Note the phase angle about  $22^\circ$  within the scales of 8-16 indicated by the rectangle.

The arrows superimposed on the wavelet coherence figures (Figures 6.6 and 6.7), represent the local phase delay between the series and exhibit different characteristics. The standard trigonometric circle is used for reading the phases. The arrows rotating from east to north and gradually towards west indicate an increasing phase angle between the two series. For example, in Case 1, within the scales of 8-16, the phase indicates a delay angle about  $22^\circ$  between the trace and  $S_y$  vector, whereas in the higher frequencies the signals seem in phase. In the second example, the phase delay is  $45^\circ$ - $90^\circ$  which means that the Poynting vector leads the trace by  $45^\circ$ - $90^\circ$  in almost all scales. The two examples show that the delay is not consistent through all ascending tracks and it differs based on the input signal.

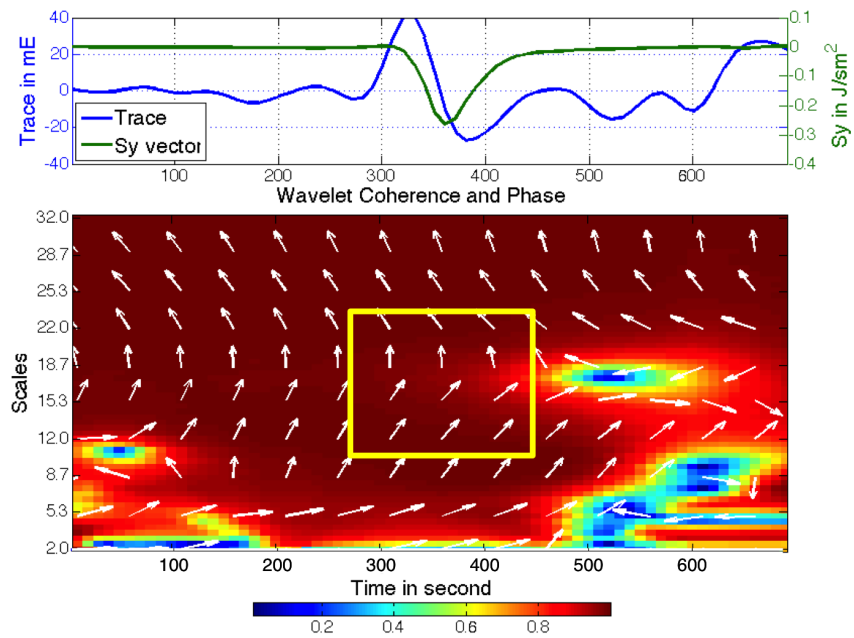


Figure 6.7: Coherency analyses of the trace and cross-track Poynting vector component measured from 22:39:00 to 22:50:00 UTC on April 2nd, 2011. The arrows superimposed indicate the phase angle between the two time series. Note the phase delay is between  $45^\circ$  and  $90^\circ$  which means that the Poynting vector leads the trace by  $45^\circ$ - $90^\circ$  in almost all the scales.

The complexity of the phase delay may be due to the complications involved in the space environment and the response of the system as well as imperfect observations and methodologies used in our analyses. The timescale for thermospheric winds to respond to ionospheric flows is tens of minutes [Walterscheid et al., 1985], during which time ionospheric current systems, which respond relatively quickly to magnetosphere and solar wind inputs, can change drastically. Therefore, thermospheric winds are the integrated result of the

time history of ionospheric plasma flows. Moreover, thermospheric winds and ionospheric currents should not necessarily be expected to agree precisely, even with perfect measurements. This is compounded by shortcomings in the SECS method, which uses sparse ground-based measurements, each of which represents an integral measure of electric currents distributed over hundreds of kilometres [Ince and Pagiatakis, 2016].

## 6.2 Summary

---

In this chapter, we investigated the correlation between ionospheric dynamics by means of cross-track component of Poynting flux and EGG disturbances using time-scale analysis, e.g., the Continuous Wavelet Transform, Cross Wavelet Phase and Wavelet Coherency analyses. We presented two randomly chosen examples. We showed in both examples that the disturbances observed in GOCE EGG measurements are highly correlated with the cross-track Poynting vector component. However, the aim of this chapter was not to summarize any correlation analyses between two series but point out the coherency between them. Therefore, it is important since the analyses presented in the following chapters are performed based on the high coherency between the series, namely solar activity proxy represented by the cross-track Poynting flux component and the disturbances observed in the gravitational gradients.

The intermediate conclusion of the thesis was made in this chapter via the help of the analyses performed. We have shown for the first time that the electromagnetic energy input to the satellite environment has an effect on the GOCE EGG measurements. We also showed that the relationship between ionospheric dynamics and GOCE accelerometer system is not linear and depends on the frequency content (time-scale) of the energy input and is subject to complex phase difference between the series. We mentioned that the coherency analyses shown for the two randomly chosen cases indicates different properties from case to case and is not an ideal information or adequate for modelling these discrepancies. Accordingly, in the following chapters, we are going to attempt performing impulse-response analyses and develop a data-driven model based on the outcomes of the dynamic system.

# 7

## Impulse-Response Analysis and Model Development

In this chapter, we introduce the development of the relation between the EGG disturbances observed in gravitational gradients over the geomagnetic poles and intense ionospheric dynamics in terms of Poynting vectors given in Chapter 4. We use the Poynting vector components that are derived from the EIC vectors and normalized SECS amplitudes as the input signal, which cause gravity gradient disturbances that are visible in the trace. Therefore, we introduce an input-output dynamic system and perform impulse-response analysis [Jenkins and Watts, 1968, Kanasevich, 1981] in which the input of the system is the Poynting vector component in cross-track direction and the response of the system is the disturbances that are observed in the trace of the GGT.

### 7.1 Dynamic Systems

---

In dynamic systems, the output of the system at any instant of time depends on the input sample at the same time as well as at other times. The “other time” here means any time instant other than the present time. Therefore, it can be past or future time [Jenkins and Watts, 1968, Kanasevich, 1981]. The input-output dynamic system (see Figure 7.1) approach is used in our analyses in which an input signal is introduced to a linear/non-linear dynamic system and an output signal is produced based on the response of the system (impulse-response) in a single input single output (SISO) system. The input signal is represented by  $u(t)$  and output signal is represented by  $y(t)$ , where  $t$  represents time.

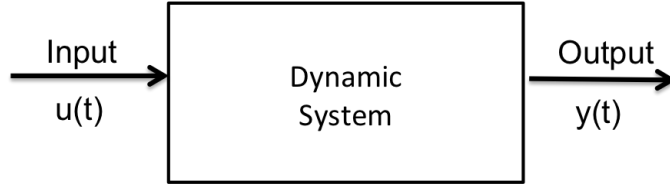


Figure 7.1: Representation of a dynamic system. The input (impulse) of the system is represented by  $u(t)$ , whereas the output (response) of the system is represented by  $y(t)$ .

The relationship between the continuous input and output signals in a linear dynamic system is expressed as:

$$y(t) = \int_{\tau=0}^{\infty} g(\tau)u(t - \tau)d\tau, \quad (7.1)$$

where  $g(\tau)$  is the impulse-response function (system) and  $\tau$  is time lag and  $u(t) = 0$  when  $t < 0$ . The transfer function of the system is

$$G(f) = \frac{Y(f)}{U(f)}, \quad (7.2)$$

where  $U(f)$  and  $Y(f)$  are the input and output signals in the frequency domain.

In our example, the very complex physics behind how the disturbances are introduced into the system is unknown and can only partly be understood based on the response analysis. Moreover, it is very difficult and even not practical to understand the entire system dynamics nor use first-principles physics based models to remove these disturbances. Accordingly, in order to remove the spurious signals (disturbances) mentioned in the first six chapters, data-driven models are examined and used in this research. Unless otherwise indicated, the information on data driven modelling presented in this chapter is taken from Lennart [1999], and Andersson et al. [1998].

## 7.2 Data-driven Modelling

---

In electronics, the system box or device (dynamic system) that manages an input signal to produce an output signal is designed based on the purpose of the dynamic system. The dynamic system can be used for control, prediction, simulation, signal processing, error detection and others. When studying the disturbances observed in GOCE EGG measurements that are the result of intense ionospheric dynamics, the possible

relationship between the input and output is not defined, or more precisely it is not known and is due to many inputs, such as instrumental errors and shortcomings of the complicated data processing. However, in such cases, it is possible that the input signal to the system (here GOCE) and output signal which represents the disturbances in GGT are measured. By using the measured input and output signals, and understanding their unknown relationship (impulse response of the dynamic system) may be possible.

The system can be defined by a black-box model, grey-box model, and user-defined model. Figure 7.2 summarizes the box-concept. The black-box concept model is used when the dynamic system is unknown and its model parameters can be adjusted based on the specific case, but not on the underlined physics. The grey-box model assumes that there are a few known physical properties of the dynamic system and a few of the parameters can be constrained based on this information. User-defined models are used for special systems when commonly used parametric models do not represent the dynamic system.

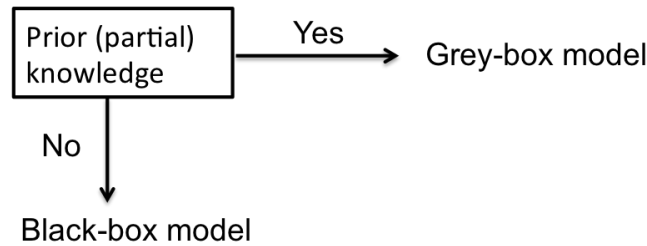


Figure 7.2: Dynamic System identification via the box-concept. The black-box concept is used when there is no prior knowledge available on the dynamic system. If there is any prior knowledge (physical properties) available, the grey-box concept, which takes into account these parameters, can be used.

Our experiment consists of input and output signals, namely the Poynting vector component in cross-track direction and the disturbances observed in trace, respectively. As given in the previous chapters, Poynting vector components are interpolated into the satellite position along the satellite track, whereas the EGG measurements are filtered into a frequency bandwidth of interest (180-300s).

As it is mentioned previously, the optimum bandwidth interval of GOCE EGG for accurate measurements is 10-200s. The reason we use another bandwidth [180-300]s here is that the similarities between the GOCE measurements and ionospheric dynamics are more dominant and highly correlated with each other over this interval. Therefore, it is the optimum interval to investigate the relation between the GOCE EGG disturbances and ionospheric dynamics.

After the preprocessing of both measurements is completed, they need to be investigated into two sepa-

rate parts, the estimation and validation data<sup>1</sup>. Estimation data are used to estimate the model parameters, whereas the validation data are used to test the validity of the model for other input series, where the output is simulated and compared with the real output measurements. Different kinds of model structures such as transfer function, state-space models, process models, and polynomial models can be tested. The loop that is used in system identification is displayed in Figure 7.3.

The model parameters are estimated based on the input and output signals of the dynamic system. Once the model structure is known/decided, estimation data are used to simulate the output (measurements) of the dynamic system. Then, the simulated output is compared with the real output of the dynamic system and based on the error minimization (best fit approach using least squares), model coefficients are calculated. Afterwards, the estimated model that is developed based on a set of these estimation data needs to be tested by another set of data, namely the evaluation data. Therefore, the quality of the model and the ability of the model to simulate the output of the dynamic system is tested.

In order to decide whether the model is acceptable for the application, each trial can be tested by using residual analyses that are summarized in Figure 7.3 where the validation data are used. Autocorrelation of the residuals and cross correlation of the residuals and input signals are examined whether they are within the confidence interval or not. Ideal cross-correlation analysis of the residuals and input signal should equal to zero. Based on the residual analyses results, the model parameters may be adjusted to represent the input-output relationship better.

Low order data-driven models are preferred since high order models can be very unstable depending on the datasets used in the estimation of the model parameters. The candidate model is tested by using residual analyses and uncertainty evaluation. The final model is developed for the intended application and refinements can be possible in the future when there are more input data available globally or the physics of the system is better known.

---

<sup>1</sup>To be consistent with the Matlab toolbox, we used “data” instead of “measurements” here. In fact, the data consists of Poynting vector and trace here.

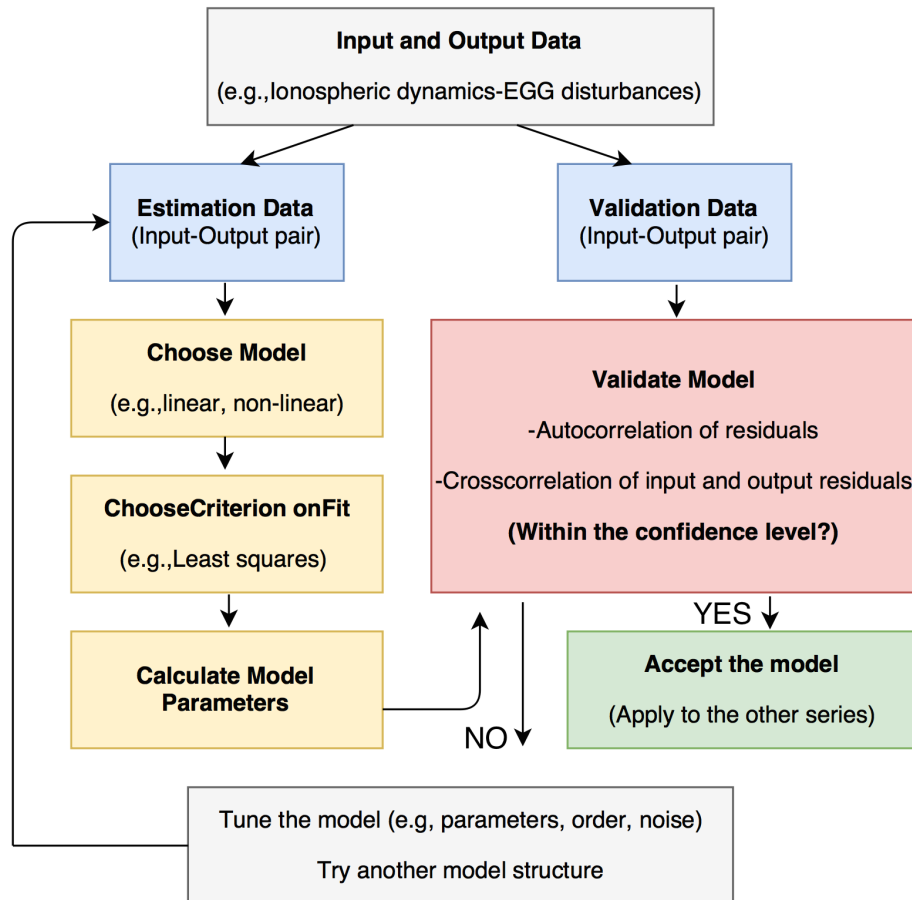


Figure 7.3: Input-output dynamic system representation for black-box model determination. Estimation data are used to estimate model parameters based on different model structures. Each model structure trial is validated by the validation data. Autocorrelation and cross correlation test applied to residuals. If the test results are within the confidence level, then the model can be accepted. If the results are not within the confidence level, the model needs to be revised by adjusting its parameters. (adopted from Lennart [1999]).

### 7.2.1 Identification of the System

The steps taken in the system identification are given in this section. The model development procedure starts by formulating the answers to the following questions:

- Do we know anything about the system a priori? Can the system be described with a Black-box or gray-box model?

As mentioned in the previous section the dynamic system of Poynting vector and GOCE EGG disturbances is not known. Therefore, the system is a black-box system. If we have a priori knowledge or physical models, we can introduce it into the dynamic system to adjust the model parameters (see Figures 7.2 and 7.3).

- Is the output a linear or non-linear function of the input?

Even though it is very possible that the system we deal with is a non-linear system, starting with a linear system is an acceptable approach.

- Do we want to describe how other external sources affect the output signal?

Other than a single input signal  $u(t)$ , there are also other external sources  $v(t)$  affecting the system output (e.g., calibration error, instrumental error, noise). In order to handle this error, we assume that it is an additional unmeasured input in modelling and they are considered as the random noise component of the system.

Figure 7.4 depicts a real system example in which we have different input sources causing the disturbances observed. The disturbances of our interest might be coming from many different sources such as ionospheric dynamics, calibration and instrumental error, or errors in data processing (e.g., calculation of angular accelerations). Based on the model example represented in Figure 7.4, all the inputs contribute to the errors observed in the GGT gradients, therefore they are measured and are input into the system.

The dynamic system that is presented in Figure 7.4 is modified and the new model is presented in Figure 7.5, where the random noise is introduced to the dynamic system. Moreover, any effects coming from other sources that contribute the disturbance observed over the polar regions are assumed as the disturbances on the system which is different from the EGG disturbances. Possible instrumental and calibration errors are assumed within the random noise level. Therefore, in this research, we can assume that the only input that contributes to the EGG disturbances is the ionospheric dynamics.

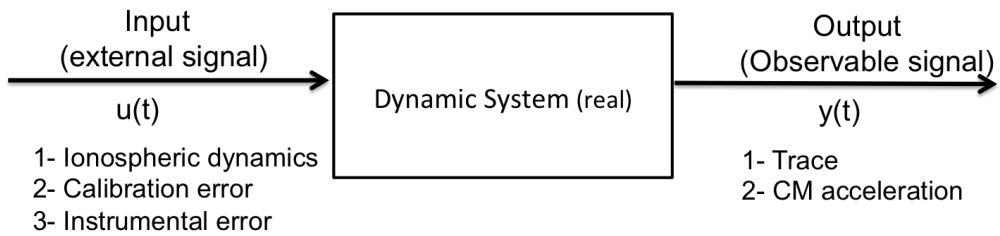


Figure 7.4: Input-output dynamic system representation. Input signal consists of different sources, such as ionospheric dynamics and errors due to calibration and instruments, as well as data processing. Output of the dynamic system is the trace and CM acceleration.

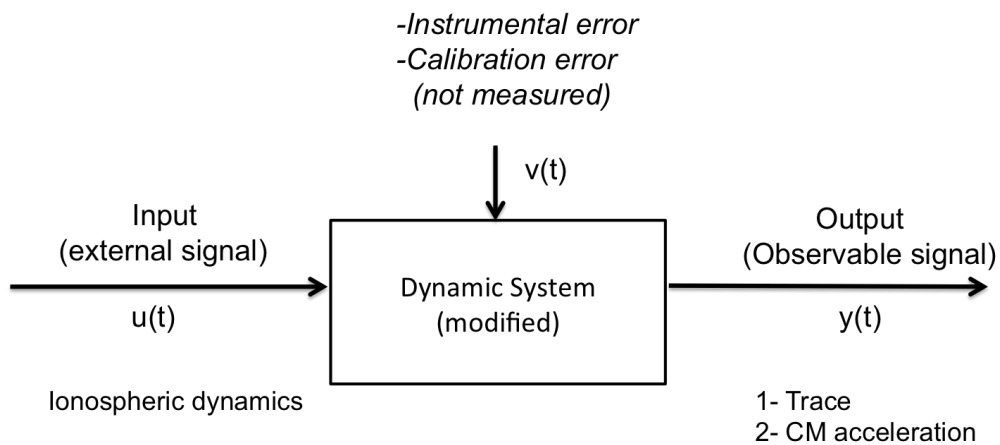


Figure 7.5: Input-output modified dynamic system representation that assumes the ionospheric dynamics as the only source for the disturbances observed in trace. The other error sources are assumed as not measured. The original  $v(t)$  concept is adopted from Lennart [1999].

## 7.2.2 Determination of the Model Structure

The System Identification Toolbox of Matlab is used in the model development. As mentioned in the previous section, the model validation is performed based on a numerical measured fitting. The percent of the output variation reproduced by the model is calculated based on error minimization via least-squares fit. In this technique, we need to make sure that there are enough measurements for the estimation as well as for the validation process. The data-driven model needs to be validated by independent datasets different from the datasets used in the model's development.

One key point of this methodology is making the decision on which model structure is most appropriate for the data. The quality of the resulting model depends crucially on the chosen model structure, i.e., linear and non-linear model structure. Since, the problem of the GOCE gradiometer disturbances is not a well-known problem nor has it been studied before, our initial solution will be based on testing many of the input-output relations. Once the appropriate model is chosen, it can be adjusted and modified to approve whether it is acceptable for the intended application, using specific criteria, such as the residual analysis.

Residual analyses are performed using the cross-correlation of the input signal and the residuals as well as the autocorrelation of the residuals themselves. If the cross-correlation and auto-correlation analyses show coefficients within the confidence level of 95% then the model can be accepted as a successful and effective model for the application. It is worth noting that the cross correlation of the input signal and the residuals ideally should be zero and the system identification is not an easy one-shot procedure but iterative.

In order to answer the questions listed in Section 7.1.1, we need to test several transfer functions (or impulse response functions). We start the procedure with understanding the model structures. The model structures can be listed as:

1. Linear parametric (transfer functions, state-space models, process models)
2. Linear non-parametric (Impulse-response, frequency-response)
3. Non-linear models

In the linear parametric model, the input is related to output in difference or differential form which can be represented in Laplace or z-transform forms. In this category, one may include a transfer function, state-space models, process models and polynomial models. The linear systems can also be represented by non-parametric linear models which are the curves representing the system properties. These models can directly be estimated from the data.

Impulse and step responses are investigated to gain first level knowledge on the system characteristics, such as stationary gain and time delay. One can draw conclusions on the system linearity, time invariance, and on the presence of external or other disturbances. A system's transient response is its output to a transient signal, such as an impulse or a step in its input. From the input and output data, the transient response is estimated via a flexible (high-order) linear model. A system's frequency response is its response to sinusoid input signal; the output of a linear system is expected to have the same frequency as the input signal with different amplitude and phase shift.

## 7.3 Development of the Model

---

The impulse response model is the expression of the relationship between the input and output of the system in terms of ratio of polynomials. The model order is equal to the order of the denominator polynomial. The roots of the denominator polynomial are called model poles and the roots of the numerator polynomial are the zeros of the model which represent also the stability of the system.

### 7.3.1 Basics of Transfer Function

A transfer function can be computed using different structures for different types of signals. For continuous signals the transfer function is expressed as:

$$Y(s) = \frac{P}{Q}U(s), \quad (7.3)$$

that is equal to

$$Y(s) = b_0 \frac{(p - z_1)(p - z_2)\dots(p - z_N)}{(p - \lambda_1)(p - \lambda_2)\dots(p - \lambda_N)}U(s), \quad (7.4)$$

where  $Y(s)$  and  $U(s)$  represent the Laplace transforms of the output and input, respectively, and  $s$  is the Laplace transform variable. The numerator and denominator polynomials,  $P$  and  $Q$ , respectively, describe the input and output in the Laplace space and  $z_1, z_2, \dots, z_N$  and  $\lambda_1, \lambda_2, \dots, \lambda_N$  correspond to zeros and poles of the system, respectively.

For discrete series, the transfer function is described as:

$$y(t) = \frac{P(q^{-1})}{Q(q^{-1})}u(t), \quad (7.5)$$

where the roots of  $P(q^{-1})$  and  $Q(q^{-1})$  are written in terms of the shift operator ( $q^{-1}$ ). The delay is introduced by  $\tau$  as:

$$y(t) = \frac{P}{Q}u(t - \tau). \quad (7.6)$$

### 7.3.2 Model Structure Selection

A time series model with no exogenous<sup>2</sup> input can be expressed by an autoregressive (AR) model as described in Lennart [1999] :

$$A(q)y(t) = e(t), \quad (7.7)$$

where  $A(q)$  is a polynomial in the shift operator  $q$ ,  $y(t)$  is the output of the system and  $e(t)$  is white noise. The AR model structure is a process model. The model outputs are only dependent on previous outputs. System inputs and errors are not introduced in the modelling.

A time series model with exogenous input displayed in Figure 7.5 can be expressed by an autoregressive exogenous (ARX) model as in and Figure 7.6. We use this model structure approach to solve this particular problem.

The model is usually depicted as:

$$A(q)y(t) = B(q)u(t) + e(t), \quad (7.8)$$

where  $q^{-1} = u(t - 1)$  is the shift operator. The polynomial coefficients are given as follows:

$$A(q) = 1 + a_1q^{-1} + \dots + a_{n_a}q^{-n_a}, \quad (7.9)$$

and

$$B(q) = b_1 + b_2q^{-1} \dots + b_{n_b}q^{-n_b+1}, \quad (7.10)$$

where  $q^{-1}u(t) = u(t - 1)$ ,  $n_a$  and  $n_b$  are orders of the polynomial  $A(q)$  and  $B(q)$ , respectively.

---

<sup>2</sup>Exogeneous: Independent inputs here.

The model input and output equation therefore is expressed as

$$y(t) + a_1y(t-1) + a_2y(t-2) + \dots + a_{n_a}y(t-n_a) = b_1 + b_2u(t-1) + \dots + b_{n_b}y(t-n_b+1) + e(t), \quad (7.11)$$

and with  $n_k$  introduced as the input-output delay expressed as fixed leading zeros of the  $B$  polynomial,

$$y(t) + a_1y(t-1) + \dots + a_{n_a}y(t-n_a) = b_1u(t-n_k) + b_2u(t-n_k-1) + \dots + b_{n_b}y(t-n_k-n_b+1) + e(t). \quad (7.12)$$

The final model can therefore be expressed as  $y(t) = \frac{B(q)}{A(q)}u(t-n_k) + e(t)$ .

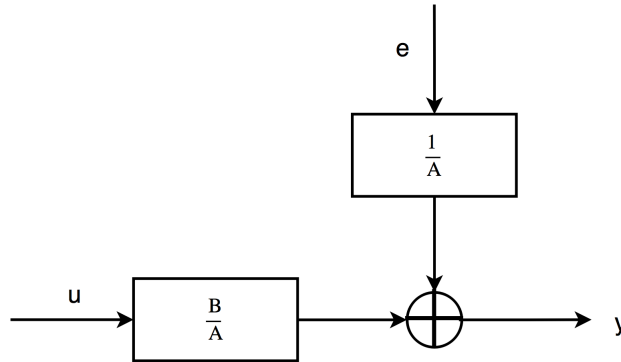


Figure 7.6: ARX Model Structure. The basic input, output, and error configuration is depicted.  $B$  and  $A$  are polynomials in the delay operator. The white noise is represented by  $e$ .

## 7.4 Model estimation

---

We approach the modelling of the disturbances from two different perspectives. The initial step is to choose an input and output signal pair that represent the general characteristics of the system. We compute a few candidate transfer functions based on the definition of a simple transfer function and ARX model. From there on:

1. We can evaluate the computed transfer function by using other input and output pairs and perform residual analyses and examine whether the computed candidate function represents the system for all tracks of our interest.

or

2. We can use the same structure of the candidate transfer functions (same number of zeros, poles, and delay) but compute new coefficients of the polynomials, therefore different amplitude responses for each track dynamically.

In this research, we use the first approach, in which we compute a transfer function and use it for all the tracks. The choice of the input signal should be performed carefully. The sampling interval of the signal should not create any aliasing effects. Moreover, the duration (length) of the signal needs to be long enough to estimate the parameters reliably. However, in this research we are only able to use the data over the vicinity of terrestrial magnetometer observatories; therefore, the signal length varies between 300 and 900 seconds with a sampling interval of 10 seconds.

Since the equivalent currents are developed as a result of modelling and upward continuation of terrestrial magnetic field disturbance measurements, the input signal, namely the Poynting vector is already naturally a low pass filtered series. The output signal, namely the GGT trace is filtered to the bandwidth of 180-300 seconds, which is not exactly the measurement bandwidth of the gradiometer (10-200s) in this particular case. According to Andersson et al. [1998], the amplitude of the signal should be chosen as large as possible which helps achieve a good signal-to-noise ratio. Also, the amplitude needs to be kept in the range that the linearity assumption for the model holds. Moreover, the data need to be de-trended and any outliers should be removed in advance.

The delay in the response of the system indicates the delay in the response to start growing. Therefore, the response is not usually immediate but with delay. Based on the response analyses we may be able to decide about the degree of the model and time delay. Our preliminary investigations show that the response

slope does not change immediately but with a delay and a different structure in time. The model can be assumed as at least second or higher order. Also, looking at the epoch that the response dies out gives us information on the behaviour of the system, and how long the effect of the input lasts in the output signal.

Two model structures with different zeros and order are tested based on the input and output series along a satellite track: a step response and frequency response analyses and the model simulated values are presented in this section. The input and output of the system for one of the tracks are shown in Figure 7.7. As explained above, a segment of the series, in which the signal-to-noise ratio is high, is extracted to develop the model. The original series along the satellite track are shown in black, whereas the segment used in modelling is shown in red. By using the extracted red segment, three transfer functions and three ARX models of different zeros and poles are tested.

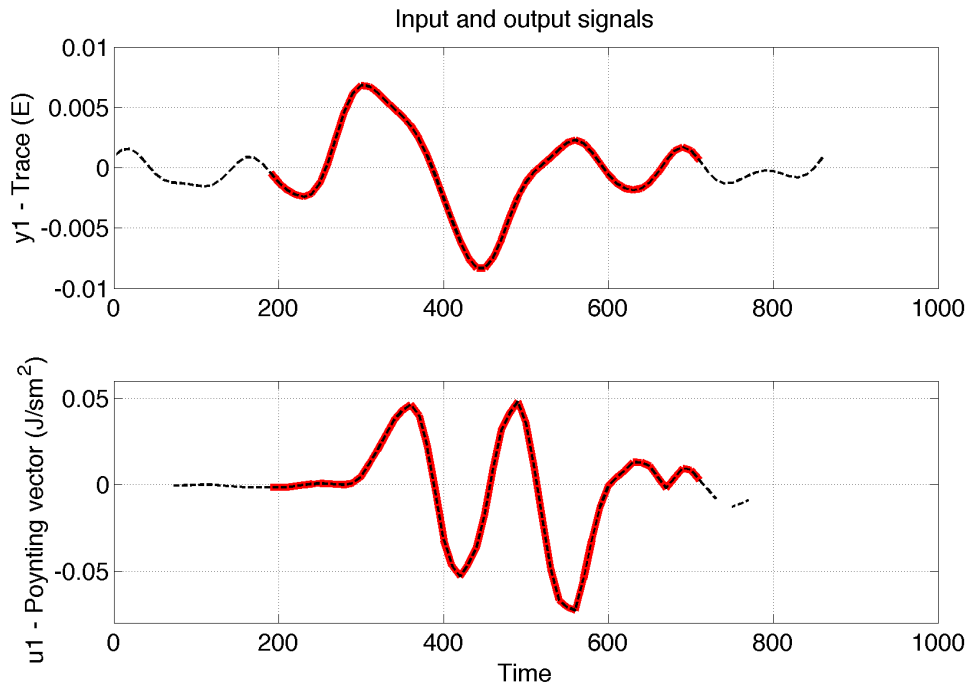


Figure 7.7: Example of input and output series along an ascending track. The black colour shows all the measurements along the track, whereas the red colour represents the segment that is used in the model development due to high signal to noise ratio. The extraction of the segment is performed manually.

The two different structures are as follows: 1) The basic transfer function that is computed based on continuous input and output signals. Therefore, the signals are assumed continuous. 2) The ARX model that is computed based on discrete input and output signals. It is worth noting that the ARX approach takes into account the noise information. The model characteristics and coefficients are given in Tables 7.1 and 7.2 where Var indicates variable and the coefficients are unit-less.

Table 7.1: List of transfer functions and numerical values for the coefficients that are used in the simulations.

Model	Var	num	den	noise variance
tf21	s	[0.0015, 1.4903 $10^{-5}$ ]	[1, 0.0040, 5.9273 $10^{-4}$ ]	3.0235 $10^{-5}$
tf31	s	[5.5596 $10^{-5}$ , -4.451 $10^{-7}$ ]	[1, 0.0372, 9.5582 $10^{-4}$ , 1.9985 $10^{-5}$ ]	1.6842 $10^{-5}$
tf32	s	[6.7139 $10^{-4}$ , 5.7394 $10^{-5}$ , 1.9667 $10^{-9}$ ]	1, 0.0394, 9.2553 $10^{-4}$ , 2.1286 $10^{-5}$ ]	1.5490 $10^{-5}$

Table 7.2: List of arx models and numerical values for the coefficients that are used in the simulations.

Model	Var	a [ $a_0, a_1 \dots$ ]	b [ $b_0, b_1 \dots$ ]	Noise variance
arx221	$z^{-1}$	[1, -1.9291, 0.09987]	[0, 0.0130, -0.0136]	6.4393 $10^{-6}$
arx321	$z^{-1}$	[1, -2.8868, 2.8612, -0.9726]	[0, -8.4636 $10^{-4}$ , 1.3265 $10^{-4}$ ]	3.1542 $10^{-6}$
arx625	$z^{-1}$	[1, -5.3605, 12.4649, -16.1037, 12.1945, -5.1287, 0.9351]	[0, 0, 0, 0, 0, -4.5760 $10^{-5}$ , 7.7830 $10^{-5}$ ]	4.5956 $10^{-6}$

The step response of the two different model structures with different number of zeros and poles are displayed in Figure 7.8. The black line represents a transfer function of 2 poles and 1 zero, the red line represents a transfer function of 3 poles and 2 zeros, whereas the green line represents a transfer function of 3 poles and 1 zero. The poles relate to the output and the zeros relate to the input signal (see Equation 7.12 coefficients  $a_1$  to  $a_n$  represent the poles, whereas  $b_1$  to  $b_m$  represent the zeros of the system.). The three transfer functions show similar transition behaviour, except the time that the responses die out. The response of the lower order transfer functions last longer.

The ARX model step responses are shown in the right panel of Figure 7.8. The models are named as "arxnanbnk" (e.g., arx321 where na=3, nb=2, and nk =  $\delta$  =1). Similar to the continuous signal transfer functions (e.g., tf21, cf. 7.8 left panel), the lower degree polynomial ARX model also experiences longer response period until the effect of the input signal on the output signal dies out. The parameters of the three transfer functions ( $tf_{nm}$ ,  $n$  poles and  $m$  zeros) and three arx models are given in Tables 7.1 and 7.2.

The frequency responses of these models are depicted in Figure 7.9. The simulations from the transfer functions and ARX polynomial functions are displayed in Figures 7.10 and 7.11, respectively. It is seen in

Figure 7.10 that the higher zeros and poles computed transfer function tf32's approximation to the original trace (69.27%) along the track is better than the lower degree zeros and poles transfer functions tf31 and tf21 (67.60% and 55.63%, respectively). However, this does not mean that the higher order zeros and degrees always provide better approximation. We experience that very high orders can also cause very unstable behaviour of the system, so that it does not fit any better than simple transfer functions nor is it applicable to other input and output signal pairs.

The ARX model simulations that take into account the unmeasured disturbances, such as noise, are shown in Figure 7.11. It is seen that the higher order polynomials provide better approximations (64.53%) compared to the lower ones (40.76% and 40.28%). The arx625 representing na=6 number of poles, nb=2, number of zeros and nk=5 the delay or the number of samples (5 samples x 10 seconds = 50 seconds delay) before the input affects the systems' output, it provides the best approximation among the three models. This also confirms that the any output at any epoch is dependent on the previous few (na=6 in this example) points' input signals. Therefore, in this research a weighted computation is also considered for the noise information.

A very good way of checking whether the model is good for the application intended is to look at the residuals (see Figures 7.12 and 7.13). Residuals represent the difference between the real output series and the estimated values. It is expected that the cross-correlation of the input series and residuals be independent from each other. Moreover, the auto-correlation of the residuals should be within a computed confidence level calculated based on the estimated uncertainty of the model parameters.

Figures 7.12 and 7.13 show the analyses of the residuals computed from the three transfer functions and three ARX functions given above. Autocorrelation analysis of the residuals presented in the upper panel of Figure 7.12, shows that there are higher values exceeding the confidence interval for the samples close to zero. This indicates that the model is not good enough for this application and estimation on the noise component is not adequate. Therefore, a simple transfer function needs to be supported by a noise estimation model which is included in the ARX model. The ARX model, (arx625; green coloured) shows improved results as presented in the upper panel of Figure 7.13. Therefore, it is confirmed that the final transfer function between the Poynting vector and trace needs to take into account the noise component. The other components of the evaluation of the model is the cross-correlation analysis between the input and the residuals. It is observed that the cross-correlation analyses of both models are within the confidence interval. This indicates that the models are good enough to be applied in this application. The final model and corrected series are given in the next chapter.

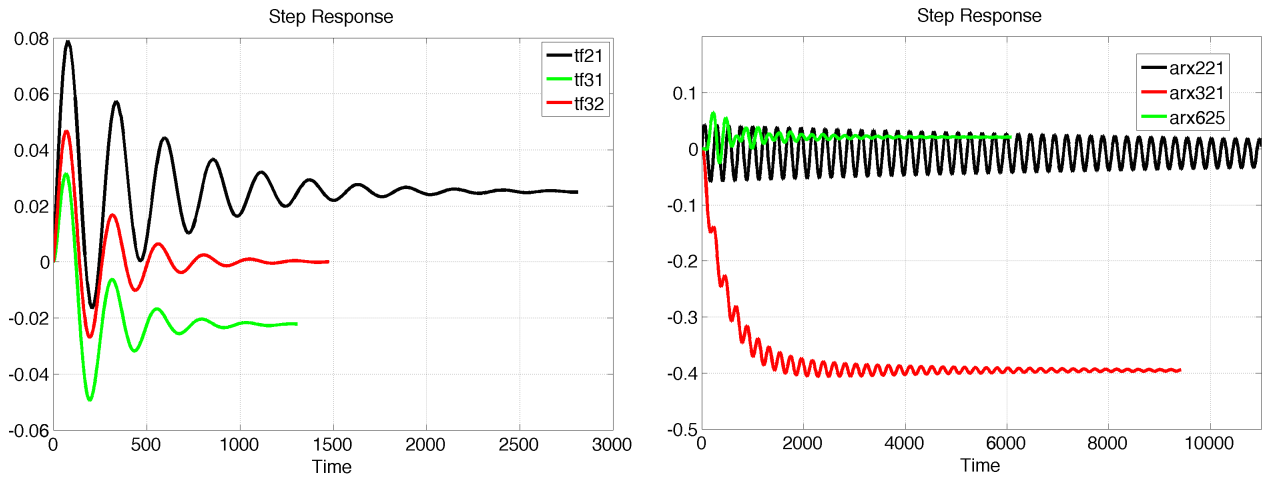


Figure 7.8: Step response of the transfer functions. The left panel shows the transfer functions computed based on continuous input and output signal assumption. The right panel shows the transfer functions that are computed based on ARX model structure.

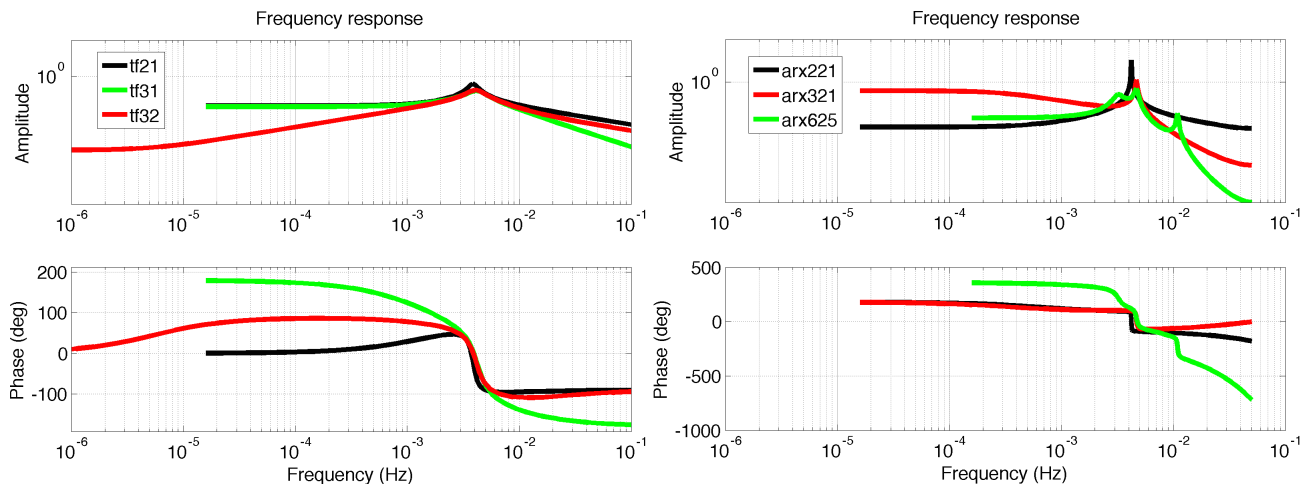


Figure 7.9: Frequency response of the transfer functions. The left panel shows the frequency response of the system based on continuous input and output signal assumption. The right panel shows the frequency response of the transfer functions that are computed based on ARX model structure.

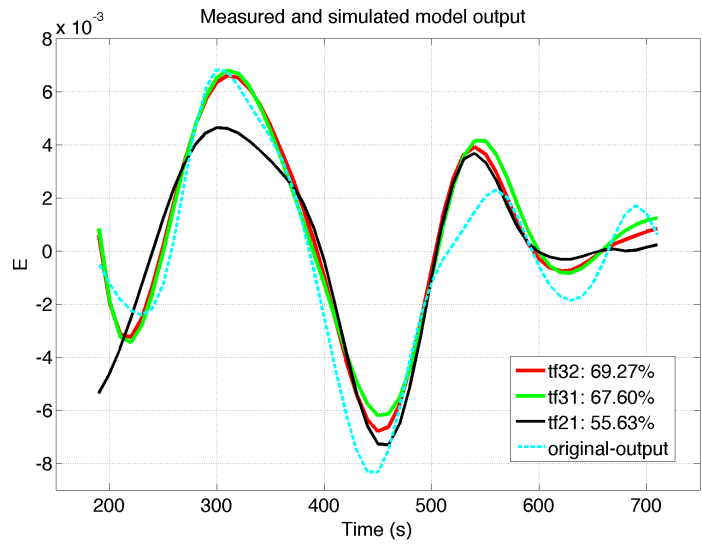


Figure 7.10: Trace measured along an ascending track over North America and simulated output values computed based on the continuous transfer functions ( $tf_{21}$ ,  $tf_{31}$ ,  $tf_{32}$ ). The cyan colour depicts the original signal, whereas the black line shows the simulated output via  $tf_{21}$ , and green line and red line shows the estimated outputs of  $tf_{31}$  and  $tf_{32}$ , respectively.

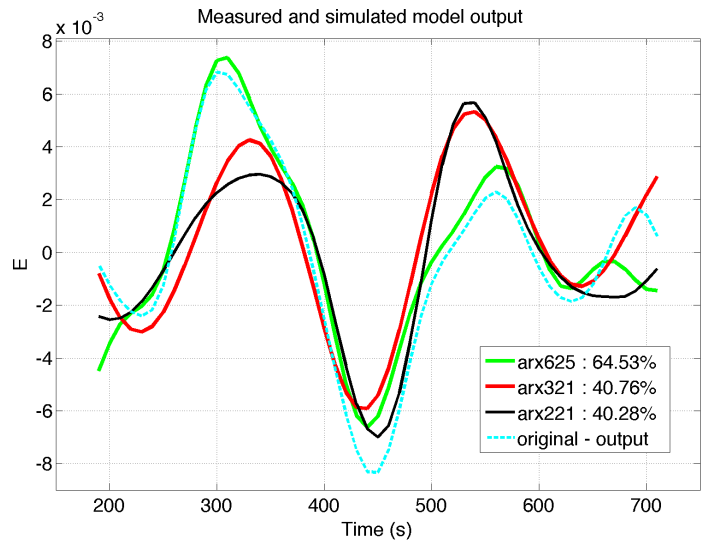


Figure 7.11: Trace measured along an ascending track over North America and simulated output values computed based on the ARX polynomial functions ( $arx_{221}$ ,  $arx_{321}$ ,  $arx_{625}$ ). The cyan colour depicts the original signal, whereas the black line shows the simulated output via  $arx_{221}$ , and green line and red line shows the estimated outputs of  $arx_{625}$  and  $arx_{321}$ , respectively.

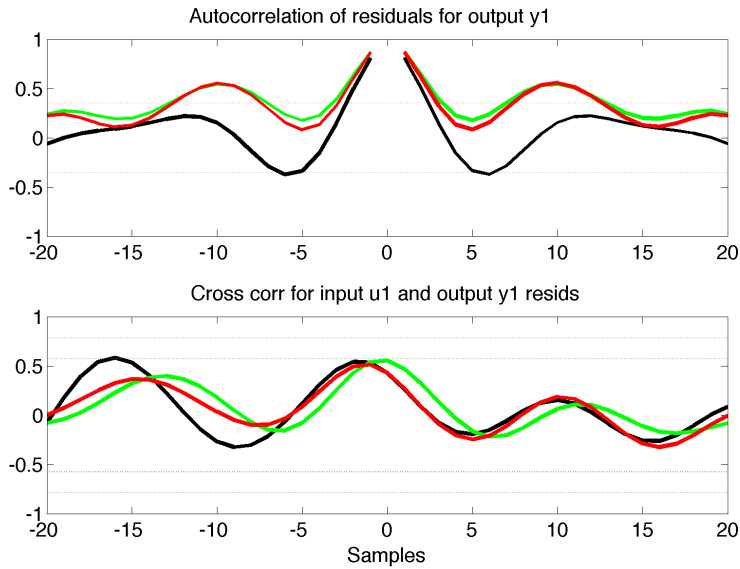


Figure 7.12: Autocorrelation of the residuals are displayed in the upper panel. Higher values exceeding the confidence intervals are observed over the samples close to zero which indicates that the model is not good enough for this application and estimation of the noise components is not adequate. Cross-correlation results between the input and the residuals which are within the confidence interval are shown in the lower panel. The green colour represents  $tf_{31}$ , whereas the red and black colours represent  $tf_{32}$  and  $tf_{21}$ , respectively.

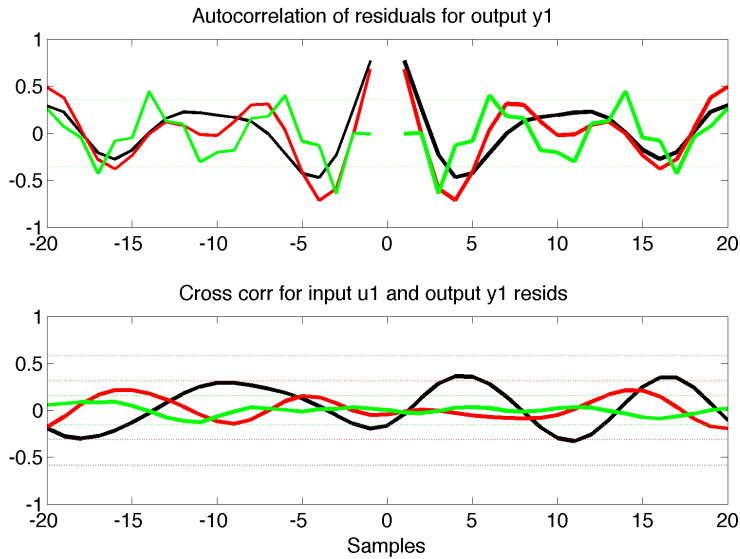


Figure 7.13: Autocorrelation of the residuals are displayed in the upper panel. Higher values exceeding the confidence intervals are observed over the samples close to zero for lower polynomial models, whereas they are reduced in a higher order model  $arx625$ . Cross-correlation results between the input and the residuals which are within the confidence interval are shown in the lower panel. The green colour represents the  $arx625$ , whereas the black and red colour represent the  $arx221$  and  $arx321$ , respectively.

## 7.5 Summary

---

In this chapter, we introduced a dynamic system of real geophysical time series and we developed the relationship between them based on the measured input and output signals. In our case, the Poynting vector component in the cross track direction is designated as the input to the dynamic system, whereas the trace of the GGT represented the output (response) of the system. The relationship between them is investigated in terms of simple impulse response functions and noise model. We performed our analyses based on the hypothesis that the ionospheric dynamics are the only cause of the EGG disturbances. This hypothesis holds since we do not have any better information to improve the model nor can we provide any physical constraints, which may be the subject of future research.

We showed that the simple continuous signal impulse response functions are now enough for modelling purposes and they need to be supported by noise models. We suggested that the arx models explain better the relationship between the input and output series. This approach is very important since it is not very common that the system identification is applied to real geophysical signals and succeed. Therefore, our methodology is unique and new to the application area and can be improved if any physical constraints can be retrieved. Understanding the system this way helps save bad data and make them useful for further analyses.

# 8

## Modelling the Measurement Errors

### 8.1 Characteristics of the disturbances

---

In this chapter, by using the two different kinds of transfer functions that were developed in the previous chapter, we predict the disturbances (measurement errors) measured in the trace. Different Poynting vector components in the cross-track direction are introduced into the system as input signals. Output signals are predicted and compared with the trace that is derived from the filtered diagonal GGT components. Moreover, these predicted values are subtracted from the filtered series and the residuals represent the corrected trace.

In this section, we take a closer look at the signatures observed in the trace and present the corrected trace in the following sections. Eliminating the disturbances from the trace does not improve the quality of the gradients but helps us understand the cause of the disturbances and investigate the effects on the gradients in detail and apply the corrections to the responsible gradient, probably after further investigations.

The upper panel of Figure 8.1 shows the original trace that is obtained from the summation of the calibrated diagonal GGT components during the three days from March 9 to 11, 2011 when high  $Kp$  values are observed. The original trace has a linear trend as seen during the period of the three days which is related to the instrumental drift. Moreover, it shows continuous periodic variability which is due to the orbital and semi-orbital periodicities.

The GGT components during the same time interval are filtered into the gradiometer measurement bandwidth (10-200s) and summation of the filtered GGT components are displayed as trace filtered with respect to GPS Time (time tag of the EGG measurements) in the lower panel of Figure 8.1. Very high and low frequency components are filtered out and EGG measurements are expected to be of high accuracy within

this interval. Moreover, the trace is expected to be within the instrumental noise level  $\sim 11\text{mE}$ . As mentioned in the previous chapters, the trace shows much higher noise level at particular epochs and locations.

The orbital periodicity of GOCE is about 5400 seconds ( $\sim 90$  minutes) and there are 16 to 17 orbits per day (cf., 3.1). Moreover, besides these peaks of particular periodicity<sup>1</sup> for each semi-orbit, there are other components which increase the noise level and make the trace larger. In the previous chapter, we already confirmed that these noisy segments correspond to the periods of intense ionospheric dynamics when there is increasing solar activity during which large variations are observed in the measurements collected by ACE and WIND as well as terrestrial observatories.

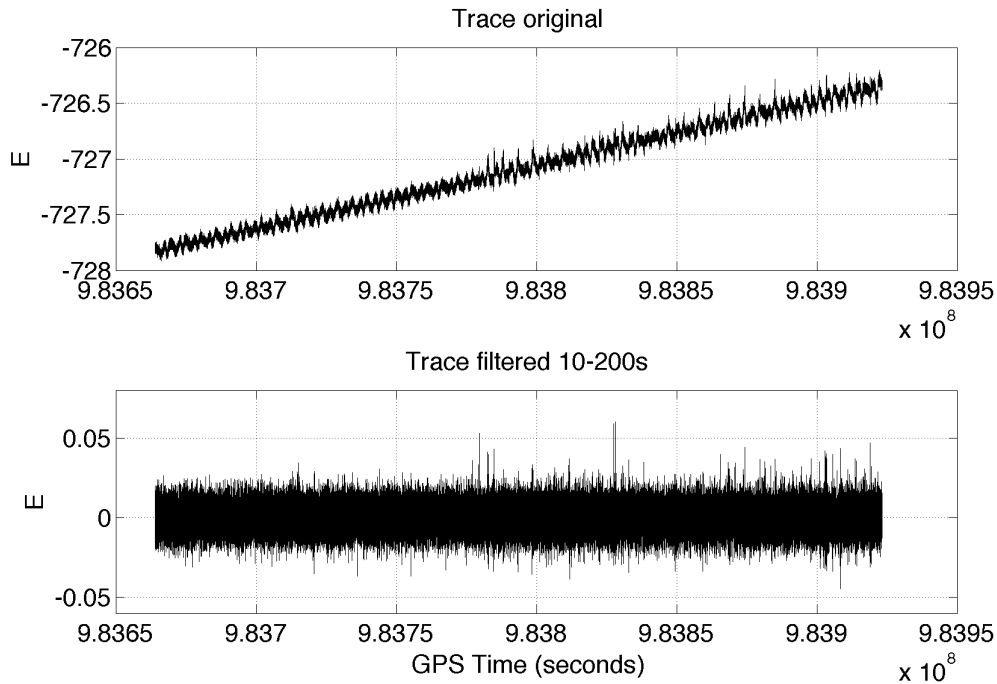


Figure 8.1: Original trace and trace obtained from filtered series are displayed for the period of March 9-11, 2011. The original trace is the summation of the calibrated diagonal gravity gradients whereas the filtered trace is the summation of the filtered diagonal gravity gradients measured by GOCE EGG. The original trace shows a linear trend which is related to the instrumental drift.

In this section, we are moving to the analyses of the frequency bandwidth of 180-300s<sup>2</sup>. The GGT diagonal components are further filtered into the frequency bandwidth in which we observe the largest similarities with the Poynting vector components. The signature of the disturbances is not unique and shows

<sup>1</sup>After spectral analysis was performed in Chapter 3.

<sup>2</sup>Note that the instrument measurement bandwidth is 10-200s, whereas now we are looking into the frequency bandwidth of 180-300s.

variability from case to case. Therefore, it cannot be predicted based on its known properties. The period of the disturbances may also show differences depending on the satellite environment.

## 8.2 Characteristics of CM accelerations and GGT components

---

To start with, we show CM accelerations measured in the three orthogonal directions by 3 orthogonally mounted accelerometer pairs. The CM accelerations measured along-track, cross-track and radial directions are displayed in Figure 8.2. The geographical distributions of the CM accelerations are given in Figures 3.4, 3.5, and 3.6 in Chapter 3. In this chapter, before we present the effect of space weather on the GGT trace in spatial domain, we more closely look into selected tracks and also we study the Poynting vector and its effect on the EGG measurements.

Figure 8.2 presents the CM accelerations measured in the three directions along a random satellite track. As displayed in the figure, the cross-track direction which is shown by red solid line experiences much larger variations than the other two directions. However, the variation in the radial direction shown by green colour also seems to be affected by ionospheric dynamics which has not been mentioned in the literature.

The GGT diagonal components and trace of the same track<sup>3</sup> are displayed in Figure 8.3. The  $V_{yy}$  component is shown by red solid line whereas  $V_{xx}$  and  $V_{zz}$  components are shown by blue and green dashed lines. The summation of the three diagonal components (trace) is displayed by the black line which experiences the disturbances around the regions between latitudes  $58^\circ$  and  $70^\circ$  N. A closer look at the trace shows a larger disturbance coinciding with the large variations of  $V_{yy}$  component.

The CM accelerations are scaled in order to examine the CM, Poynting vector, and  $V_{yy}$  visually together. CM accelerations measured in cross-track (CM\_25y) and radial directions (CM\_36Z), Poynting vector (Poyn\_y) component in cross-track direction,  $V_{yy}$  component and trace along the track are shown in Figure 8.4. It is seen that the two CM accelerations measured in two different directions show different signatures along the satellite track. However, even though the signatures are different, the variations in both signals occur within the same time interval. On the other hand, the larger variation that is observed in the cross-track CM components corresponds to the positive-to-negative variation in cross-track Poynting vector component in time domain. Especially, the CM acceleration in radial direction follows a similar signature to the Poynting vector with a time delay. Within the same time interval,  $V_{yy}$  component also shows a larger variation that corresponds to the disturbances observed in trace. All these indicate that the intense ionospheric dynamics are measured by the accelerometers in all directions.

---

<sup>3</sup>Starting at 21:12 UTC, on March 31 2011.

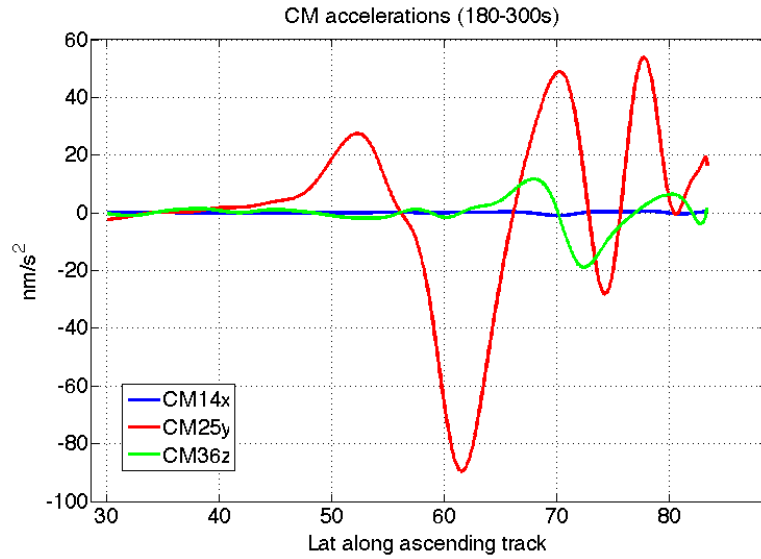


Figure 8.2: CM accelerations filtered into the frequency band of [180-300]s. The cross-track CM acceleration shows larger variations compared to the other two directions. Moreover, CM measurements in the radial direction show considerable variation which may enhance the effect of the external sources on the EGG measurements.

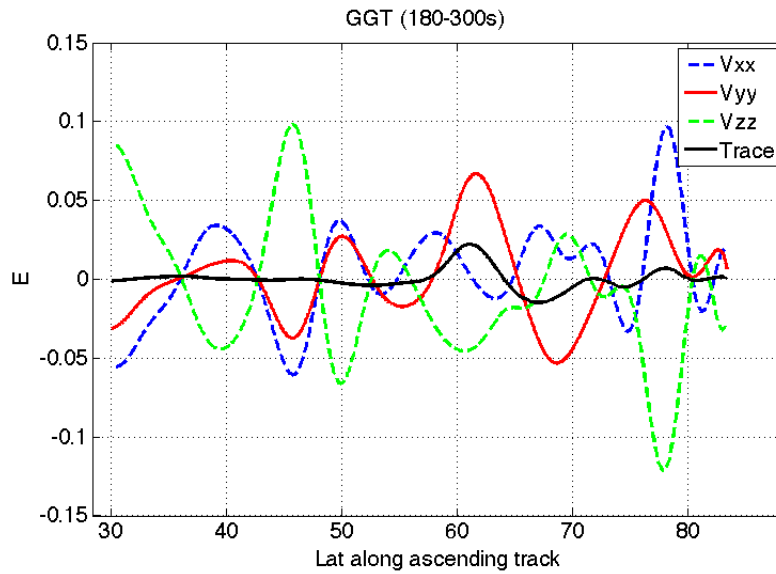


Figure 8.3: Filtered GGT components and trace. The  $V_{yy}$  component and trace are shown in red and black solid lines, respectively, whereas  $V_{xx}$  and  $V_{zz}$  components are shown by blue and green dashed lines. Note that the larger variations in trace coincide with the larger variations of  $V_{yy}$ .

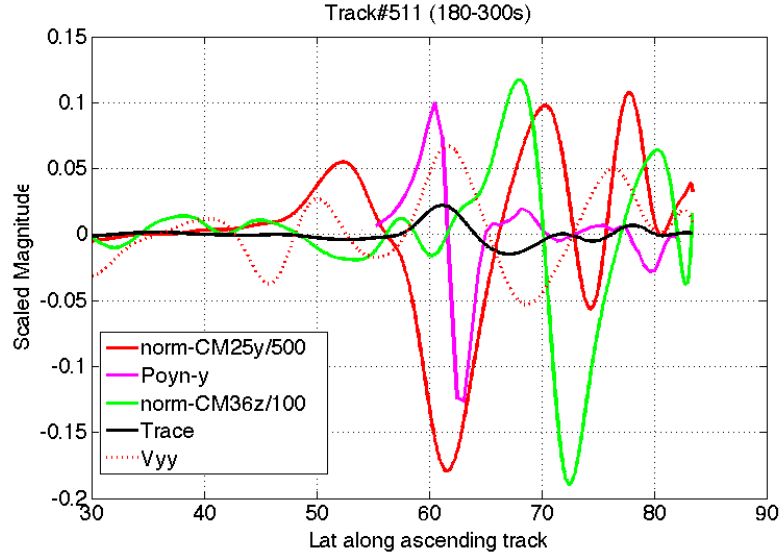


Figure 8.4: The scaled cross-track CM accelerations and Poynting vector component, scaled radial CM accelerations, trace and cross-track gradient are shown. Note the time interval when the Poynting vector component varies from positive to negative, and the trace shows higher noise level.

### 8.3 Investigations of other tracks

---

Even though understanding the nature of these spurious signals is not straightforward, there are many cases in which the trace hints the coherency between the signatures in the accelerometer measurements and the external effects over auroral ovals that last for a few hours. The auroral ovals are known to be the regions where intense dynamics exist. Subsequently, we investigate five successive tracks shown in Figure 8.5 for further analyses.

The trace of the five tracks (cf., Figure 8.5) that are affected from the ionospheric dynamics are depicted in Figure 8.6. In these examples, the trace is obtained from the diagonal GGT components that are filtered into the bandwidth interval of [180-300] seconds. The five tracks that are displayed with different colours show similar behaviour between the latitudes  $60^\circ$  and  $80^\circ$  North. As the track shifts from east to west, the signatures also vary slightly in spatial domain. For example, the track starting from 19:42 UTC as shown in blue presents the variation starting from latitude  $62^\circ$  North which returns to its normal behaviour over latitude  $82^\circ$  North. The next track shown in green over a different region starting at 21:12 UTC experiences slightly different effects from the previous track. The following tracks show similar signatures again with shift in the position.

A closer examination of these five tracks from latitude  $52^\circ$  to  $72^\circ$  is presented in Figure 8.7. The blue line representing the trace along the satellite track starting from 19:42 UTC shows a variation of reaching over 40 mE magnitude. The subsequent tracks indicate similar shape signatures of smaller magnitudes (20-30 mE) plus a shift in the position of the signature's location. The peaks correspond to similar latitudes (between  $65^\circ$  and  $72^\circ$  North) in the geographical coordinate system, and same latitudes in geomagnetic coordinates system. Therefore, this indicates that the disturbances occur due to the effects that are related to the geomagnetic field.

The five corresponding Poynting vectors (input signal to the system) along the track are shown in Figure 8.8 using the same colour code as in Figure 8.6. The blue line represents a track over Greenland and has the cross track Poynting vector component computed over a very limited area (see Figure 8.5). Therefore, the Poynting vector is only available at high latitudes and does not provide any considerable contribution to our analysis. The next track that is shown in red passes over the Labrador Sea and Davis Strait. Even though there are no actual geomagnetic measurements performed over the oceans, the geomagnetic field disturbance measurements that are taken on land are used to generate the grid values in these regions and therefore available for our comparison purposes. The red line shows a considerable variation, decreases to negative magnitudes at about latitude  $55^\circ$  North which corresponds to the region where we observe disturbance in trace as shown in Figure 8.6.

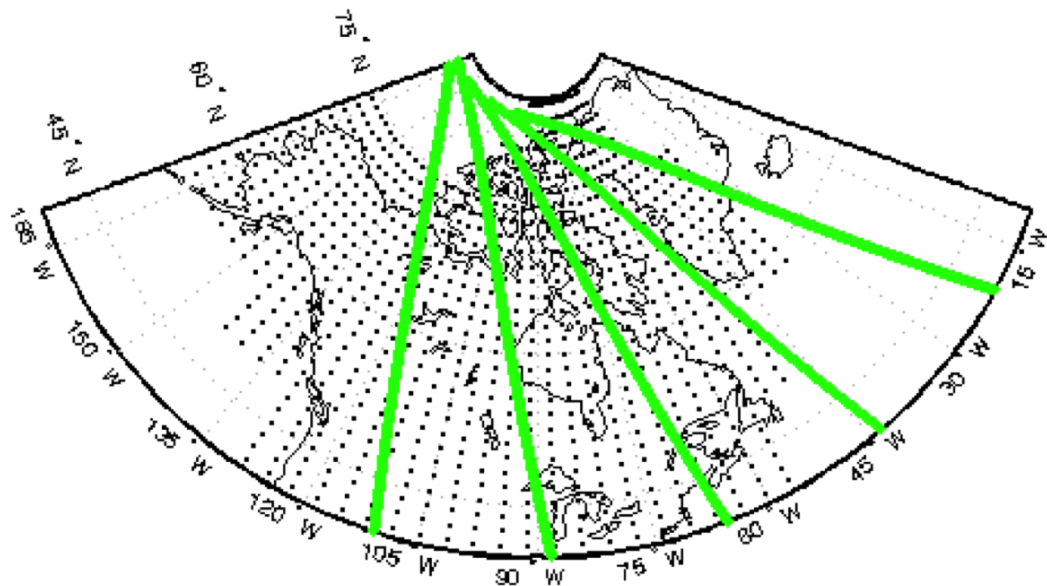


Figure 8.5: Five subsequent tracks investigated are shown. Note that the corrections will be effective over the grid area only.

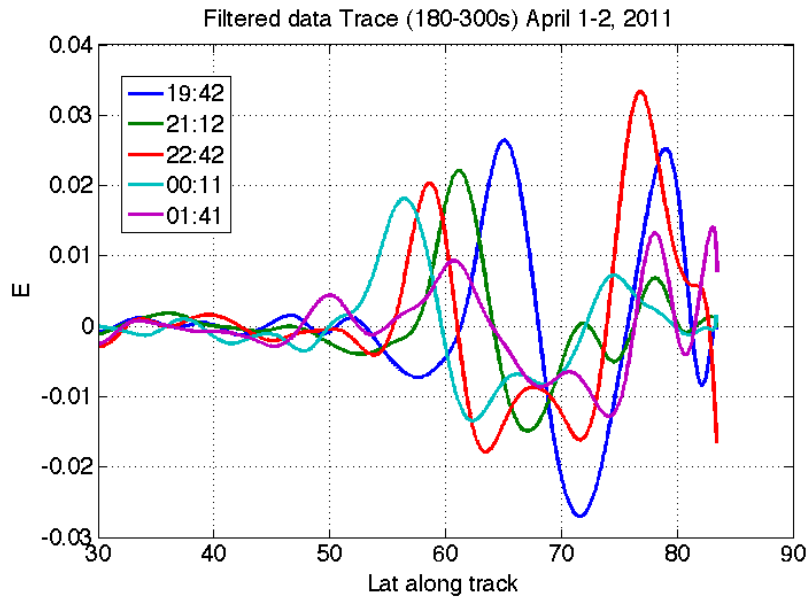


Figure 8.6: The five tracks investigated: The blue track that passes over Greenland shows a signature of the disturbance starting from latitude  $60^\circ$  North. The following tracks are 15 degrees apart to the West from the previous track and experience similar signatures over similar regions with slight phase differences.

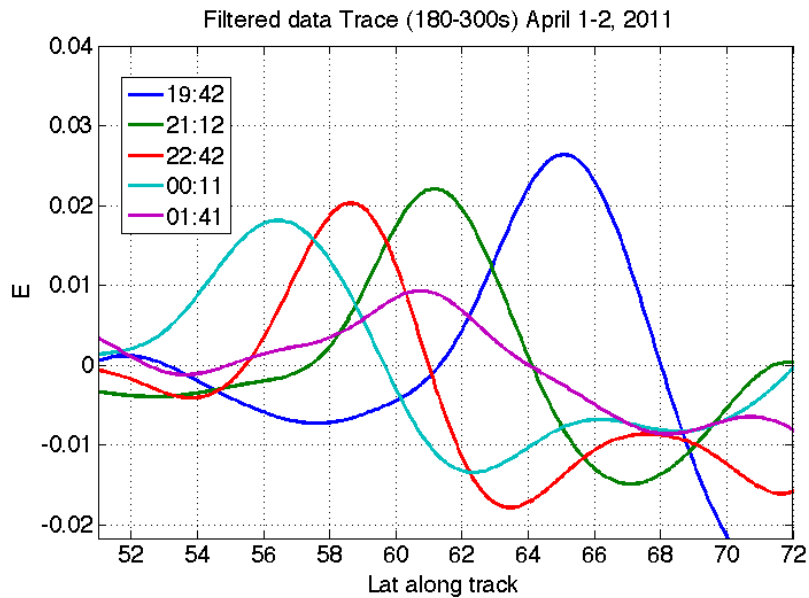


Figure 8.7: A closer look at the five tracks. Note the similar characteristics of the signatures shifting with the shifting tracks in space domain.

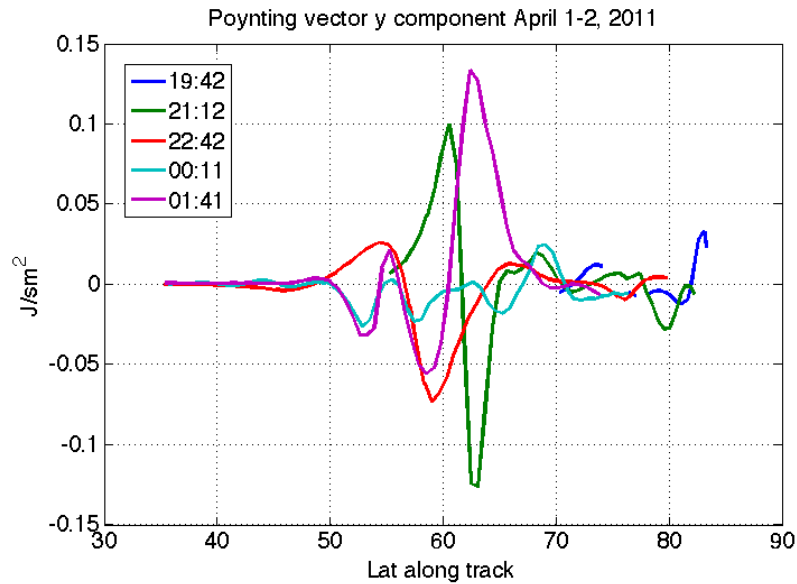


Figure 8.8: The blue track crosses over Greenland; therefore, it is only available for a short period of time since the SEC grid extension does not reach to the North Atlantic Ocean and it is limited over Greenland. The subsequent tracks correspond to observations of electromagnetic energy flow over Canada and show remarkable variations over latitudes between 50° and 70° North.

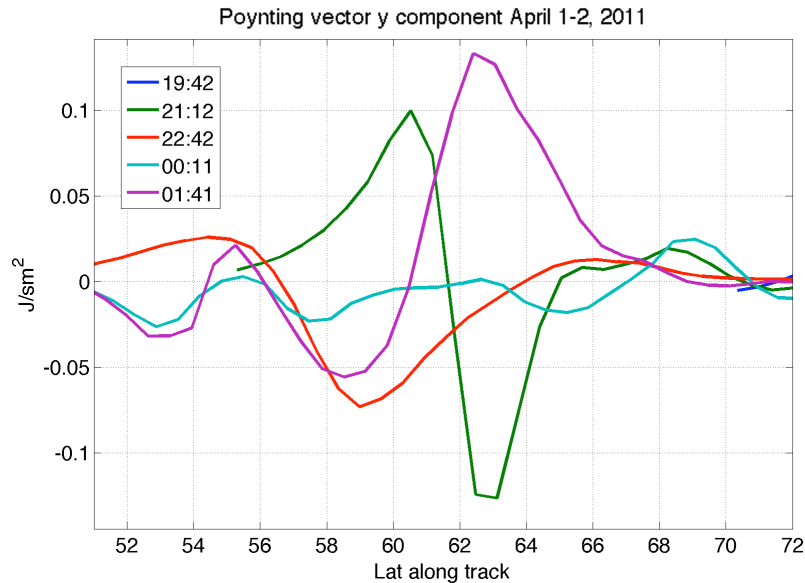


Figure 8.9: A closer look at the five tracks. Note the positive-to-negative variations between the latitudes 56° and 66° North.

In the following section we show how these disturbances can be reduced after modelling using the response method. The presented results are original and of a great importance. This discovery of the causality between the disturbances measured by EGG and Poynting flux of the electromagnetic energy will lead to improvements in the quality of the GOCE EGG products and expand the use of GOCE EGG measurements in other disciplines related to space physics.

## 8.4 Modelling the disturbances

---

In this section, we apply the impulse-response functions that were presented in the previous chapter to our original series and model the disturbances observed in the trace and accordingly in the gravitational gradients. We present a few cases with different signatures that exemplify the CM accelerations, gradients, and Poynting vector. Moreover, we apply the model to reduce the disturbances and explain how this method can be optimized to apply to the current GOCE data processing methodology and probably provide input to ionospheric modelling.

The impulse-response function is applied to the regions where Poynting vector components are available; therefore, the model will only be applicable over Canada and western Greenland. This procedure is automated and the output signal is predicted by using different Poynting vector values as input. It should be noted that it is a dynamic system and the trace will not be corrected if the Poynting vector is not available. Therefore, not all the large disturbances can be modelled and removed from the trace.

The arx625 model we introduced in the previous chapter is depicted in Figure 8.10 using real input and output signals with respect to the latitude along the track. The input and output series are represented by  $u(t)$  and  $y(t)$  and the model description is given under the figure. The full red circle in the output signal shows the epoch at which the model predictions are performed. The previous open circles indicate that the corresponding measurements taken at output epochs are considered in the model computations. The full red circle in the input signal indicates the epoch of the input signal that is used in the computations which corresponds to the epoch of model calculation by a delay of 5 sample points (50 seconds). Moreover, the previous points marked in the input signal by red open circles indicate that there are effects also contributing with much smaller weights from the measurements collected at the previous epochs to the output signal (response of the system).

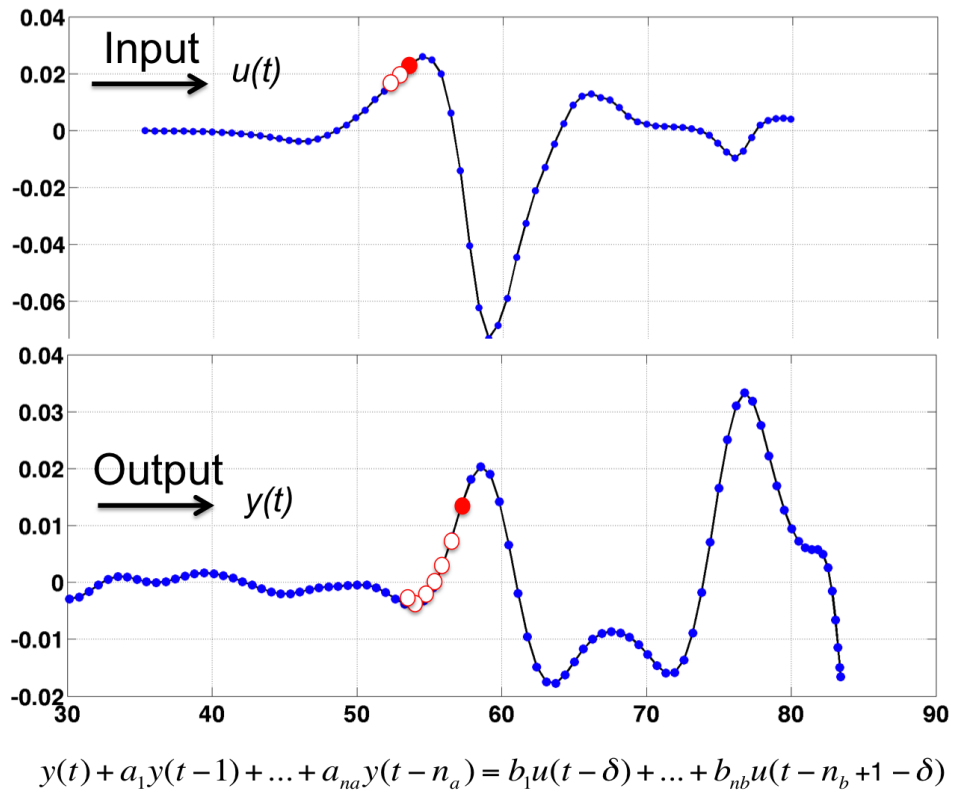


Figure 8.10: The graphical representation of the arx625 model. Note the 50 seconds of delay between the red full circles filled in the input and output signals which indicates the delay ( $\delta = nk$ ) of the system response.

The five tracks shown in Figure 8.7 are corrected based on this approach and presented in Figure 8.11. Except the blue line, the trace in the other four tracks now show much less variability. The disturbance observed in trace starting at 19:42 UTC is not removed since the track was positioned over the ocean and partly over Greenland; therefore, the Poynting vector components do not exist at the epochs corresponding to disturbed series. It also confirms that the corrections are only available at the regions where the Poynting vector is available.

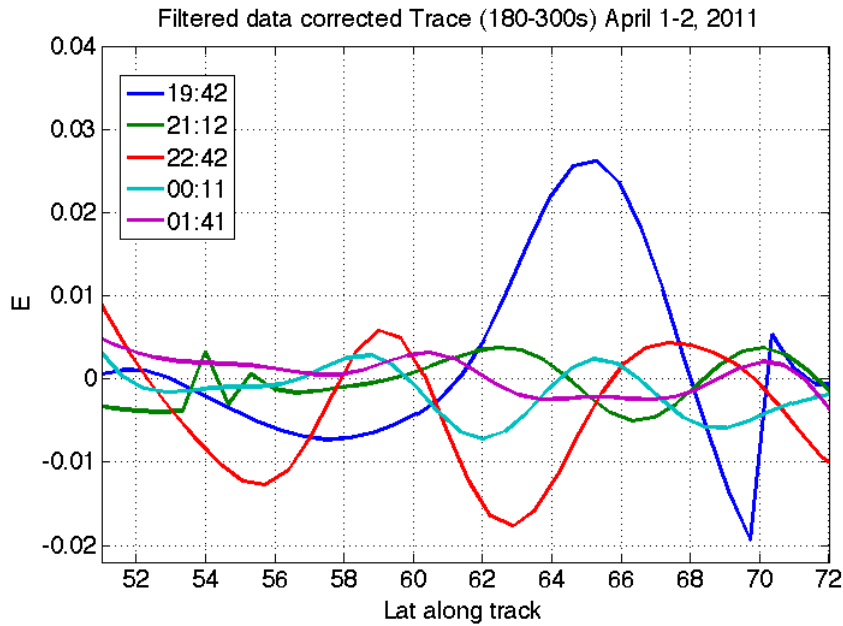


Figure 8.11: A closer look at the five subsequent tracks over a geomagnetically active period. Now the trace is corrected (except the blue track) and within the noise level of the instrument.

The trace that is obtained from the filtered diagonal gradients is now downsampled to 10 s intervals and displayed in Figure 8.12. The signature over the auroral oval is distinguishable which was presented previously in Chapter 2. Even though the signatures are spread over high latitudes, since the Poynting vector is only available over Canada and Greenland, we focus applying the corrections in these regions only. The corrected trace over the North Pole is shown in Figure 8.13 for the same time period, March-April, 2011. The reduced signatures over Hudson Bay in Canada and western Greenland is very distinguishable and within the noise level of the instrument. Therefore, we can say that the technique we use here is successful but limited by the availability of the Poynting vector.

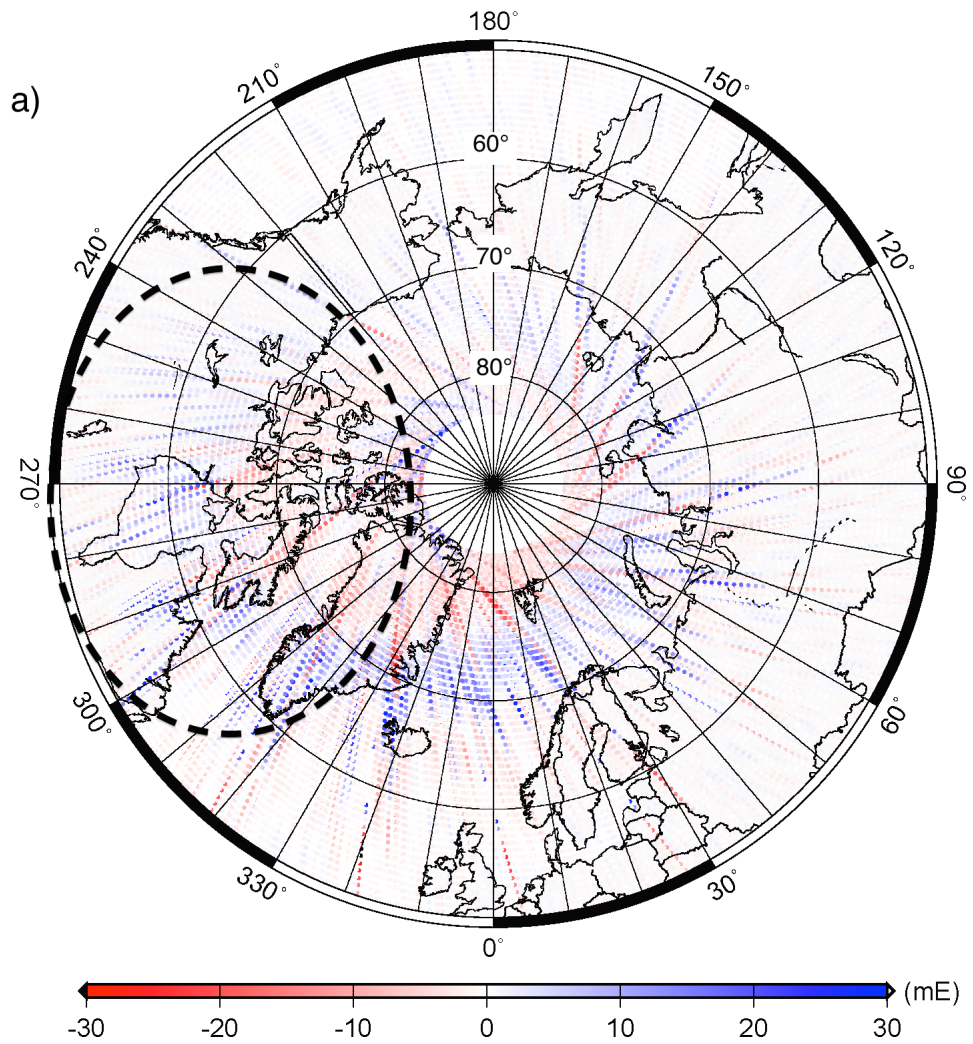


Figure 8.12: Trace obtained from filtered diagonal gravitational gradients is downsampled in 10 second interval during March-April, 2011. Note the strong signatures over high latitudes and auroral oval.

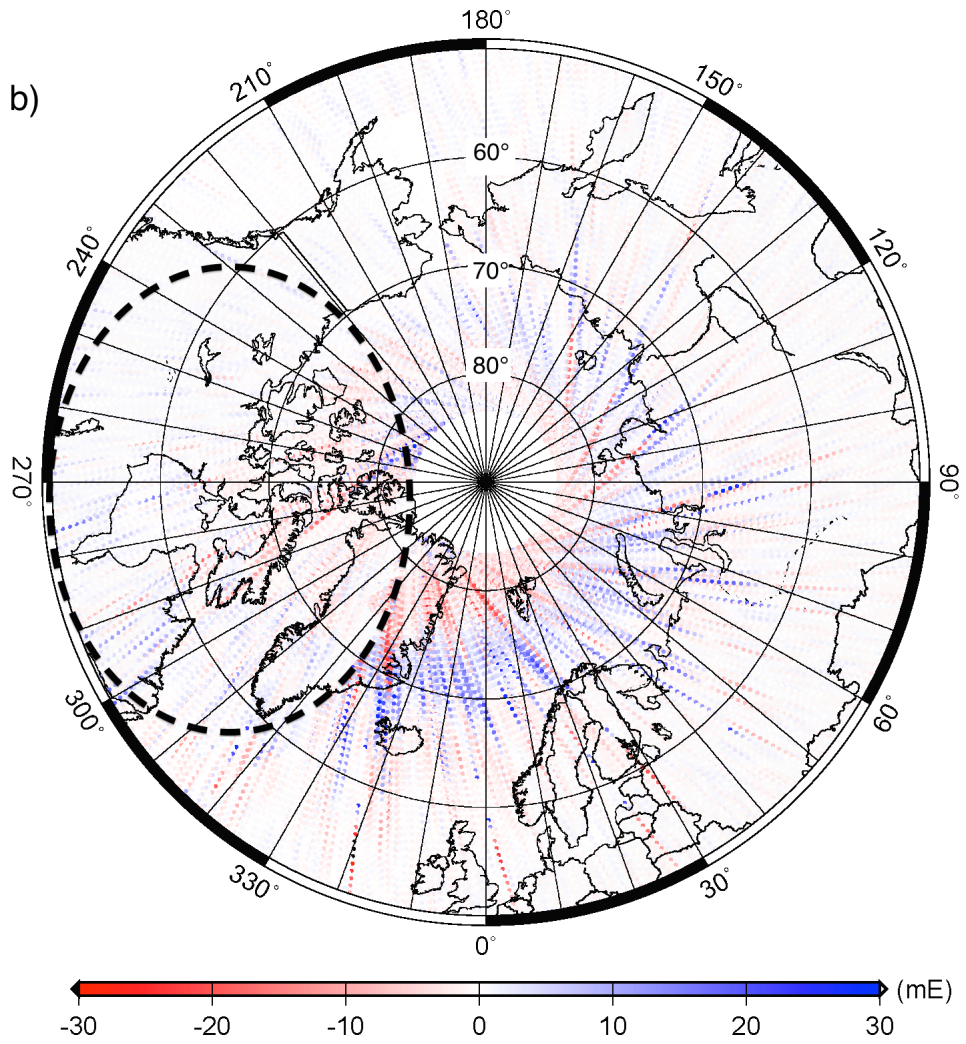


Figure 8.13: Corrected trace obtained by using model arx625 during March-April, 2011 . Note the improvement over Canada and western Greenland.

The statistics of the original filtered trace and corrected trace are given in Tables 8.1 and 8.2 for 954 tracks during March-April, 2011 and the five tracks presented in Figure 8.7, respectively. The maximum and minimum values, mean values and the standard deviations are presented for different latitude intervals over the high latitudes. The standard deviation is computed for each track (954 in total and 5 for the tracks shown in the example) and the average value is given in the tables. The statistics of the corrected series are given in parenthesis.

The 6 different latitude intervals are namely  $30-87^\circ$ ,  $50-85^\circ$ ,  $50-60^\circ$ ,  $50-70^\circ$ ,  $60-70^\circ$ , and  $60-85^\circ$  and the statistics are calculated for ascending tracks only. It is also worth noting that the statistics of 954 tracks do not only represent the statistics of disturbed tracks, but also the ones that are within the noise level of the instrument. However, the 5 tracks we look into are all noisy tracks and their statistics should be able to represent the improvement of the corrections better.

Table 8.2 shows the statistics of the 5 disturbed tracks for the 6 latitude intervals. It is found that the largest disturbances occur over the latitude interval  $60-85^\circ$ . It is critical that the higher altitudes show higher standard deviations which also indicates the larger dynamics in these regions. We found that 20 to 30 % improvement has been accomplished after the corrections applied. It is worth mentioning that the latitude interval  $50^\circ$  to  $70^\circ$  show the largest improvement. This improvement is probably due to the availability of the input data (Poynting vector) over this interval.

To the best of our knowledge, this is the first time in gravity field missions history that external datasets have been used to understand and improve the quality of the gravity measurements. We have shown very clearly that the disturbances of GOCE gravitational gradients are due to ionospheric dynamics and they can be eliminated via data-driven modelling. This research is unique also from the perspective of the method (model) applied. To the best of our knowledge there are only a few examples of impulse-response method application in geophysical applications including space weather and geodesy since there are many complexities which cause the models to be very unstable.

Table 8.1: Statistics of 954 ascending tracks before and after corrections based on arx625 transfer function. See the values in parenthesis for the statistics of corrected series. The values are given in miliEotvos unit.

Trace	30-87°	50-85°	50-60°	50-70°	60-70°	60-85°
Max	45.5 (47.4)	45.5 (47.4)	0.1963 (0.0013)	45.42 (47.42)	45.52 (47.42)	45.52 (47.42)
Min	-117.22 (-104.59)	-117.22 (-104.59)	-33.4 (-78.3)	-117.22 (-104.59)	-117.22 (-104.59)	-117.22 (-104.59)
Mean	$9.2909 \cdot 10^{-2}$ ( $1.0377 \cdot 10^{-1}$ )	$-1.6270 \cdot 10^{-1}$ ( $-1.7050 \cdot 10^{-1}$ )	$-1.4243 \cdot 10^{-2}$ ( $-1.0938 \cdot 10^{-1}$ )	$-2.2244 \cdot 10^{-2}$ ( $-1.7735 \cdot 10^{-2}$ )	$-8.8027 \cdot 10^{-3}$ ( $-1.2111 \cdot 10^{-1}$ )	$-2.2623 \cdot 10^{-1}$ ( $-1.8457 \cdot 10^{-1}$ )
Std	<b>2.7</b> <b>(2.3)</b>	<b>3.2</b> <b>(2.6)</b>	<b>1.5</b> <b>(1.4)</b>	<b>2.7</b> <b>(2.2)</b>	<b>3.1</b> <b>(2.5)</b>	<b>3.6</b> <b>(2.9)</b>

Table 8.2: Statistics of the 5 ascending tracks before and after corrections based on arx625 transfer function. See the values in parenthesis for the statistics of corrected series. The values are given in miliEotvos unit.

Trace	30-87	50-85	50-60	50-70	60-70	60-85
Max	33.1 (24.5)	33.1 (24.5)	20.6 (12.2)	26.2 (19.4)	26.2 (19.4)	33.1 (24.5)
Min	-27.1 (-18.1)	-27.1 (-18.1)	-11.7 (-9.0)	-26.2 (-17.9)	-26.2 (-17.9)	-27.1 (-18.1)
Mean	$2.3794 \cdot 10^{-1}$ ( $7.3170 \cdot 10^{-2}$ )	$5.3016 \cdot 10^{-1}$ ( $4.5390 \cdot 10^{-1}$ )	$0.2300 \cdot 10^{-1}$ ( $0.1900 \cdot 10^{-1}$ )	$-6.7964 \cdot 10^{-1}$ ( $-2.1347 \cdot 10^{-1}$ )	$-0.3800 \cdot 10^{-1}$ ( $-0.2600 \cdot 10^{-1}$ )	$-1.7251 \cdot 10^{-1}$ ( $-1.9879 \cdot 10^{-1}$ )
Std	<b>8.4</b> <b>(6.7)</b>	<b>10.2</b> <b>(7.5)</b>	<b>6.3</b> <b>(4.5)</b>	<b>9.9</b> <b>(6.8)</b>	<b>9.0</b> <b>(6.5)</b>	<b>11.0</b> <b>(8.1)</b>

## 8.5 Summary

---

In this chapter, we presented our results that include the improved trace measurements. The models developed in the previous chapters were used to predict the disturbances which occur due to intense ionospheric dynamics only and remove them from the original trace measurements. Therefore, the residual trace after the correction is within the noise level of the instrument. We presented our results both in time and spatial domains and pointed out the improvement in the trace statistically.

We mentioned the drawback of this approach is that it can only be applied to the regions where the input signal (Poynting vector) is available, but we also achieved for the first time in the GOCE literature to show the possible ways of reducing the disturbances and improve the gradients that are measured. We indicated that the results can be improved with the availability of higher resolution Poynting flux in time and spatial domains as well as with the contribution of the datasets from the Scandinavian countries and Russia.

It is worth reminding that the analyses presented in this Chapter are convincing examples of causality analyses that support the coherency analyses given in Chapter 6. It is possible that there may be other causalities between the EGG measurement errors and ionospheric dynamics. We have clearly shown one of the causalities based on the hypothesis that the ionospheric dynamics are the single cause of the disturbance observed in the gravitational gradients.

## Conclusions and Recommendations for Future Research

### 9.1 Conclusions

---

In this research, we investigated the disturbances observed in GOCE gravitational gradients by examining the trace of the Gravitational Gradient Tensor during a 2-month period of intense ionospheric dynamics. We identified the specific conditions in the satellite environment that cause the disturbances at particular times and geographical positions. We demonstrated that the disturbances over the geomagnetic poles are due to intense ionospheric dynamics. The satellite environment is expected to be affected from these intense variations (e.g., ionospheric currents) which leak into the gravitational gradients due to different reasons, e.g., shortcomings of the current in-flight calibration procedure of GOCE mission. We corrected the disturbances by using external datasets and data-driven modelling techniques. There are limitations due to the availability of the external datasets and the complex relationship between the GGT disturbances and the external datasets which can be improved in the future. Also, the current methodology applied here can be improved and recommendations are also given in this section.

First of all, we identified how large the spurious signals are and whether they occurred at specific epochs and at particular locations. The measurements from March-April, 2011 were investigated in time, spatial and frequency domains and their characteristics were studied in detail. We decided that a more rigorous examination was needed to identify the sources of the disturbances and the relationship between the disturbances and their sources. We investigated the 2-month data along the ascending and descending satellite tracks within different frequency bands. We found that the disturbances show different characteristics in the ascending and descending tracks, where the disturbances are much larger in magnitude and spread over a larger area in the North Pole along the ascending tracks.

Based on the Laplace condition, the GGT trace can be used to test the quality of the gravitational gradients. Hence, as a rule of thumb, the GGT trace was computed and used to examine the sources of the disturbances further by performing correlation analyses between the trace and the external datasets using Wavelet Coherency Analysis. External datasets consisted of horizontal equivalent ionospheric currents (EICS), vertical currents (SECS) and the Poynting flux that was computed from EICS and SECS. This is extremely vital since the space physics and parameters that are used to monitor the space weather were introduced to a topic of physical geodesy. Therefore, transdisciplinary investigations are performed. To the best of our knowledge, for the first time in satellite gravity and space physics literature, it is shown that the electromagnetic energy input into the satellite environment is measured by the accelerometers and has an effect on the quality of the GOCE gravitational gradients.

Our research included the dependence of the EGG disturbances on the orientation and strength of the Interplanetary Magnetic Field components, the motion between the ions and neutral gases as well as on the field aligned current signatures driven by neutral wind and ion drift. We were particularly interested in the vertical currents that enter into the ionosphere and drift away from the ionosphere which differentiates zonal regions (negative-positive magnitude) in the polar regions that are similar to the ones shown in the trace and CM plots. The above investigations were published in the Journal of Geodesy [Ince and Pagiatakis, 2015] and presented in numerous international conferences and workshops.

We identified particular cases when the disturbances occurred and showed clearly that the cause of the disturbances were intense ionospheric dynamics, which may or may not occur during geomagnetically active periods. Our analyses demonstrated for the first time that intense dynamics in the satellite environment degraded the quality of the GOCE EGG gravity measurements and consequently the GOCE products. Previous studies have not provided any explicit explanation on the cause(s) of these disturbances but speculated that they could be related to cross-wind effects in the thermosphere. However, the forces that generate the neutral winds have not been given explicitly in the current literature. Therefore, we discovered that the disturbances present in the GGT components were due to ionospheric dynamics and we suggested using external datasets to find and assess their causality relation. Our research proposed the development of a correction model over North America and Greenland due to the limited availability of SECS data in the region.

We showed that the accelerometer measurements can possibly be used in ionospheric modelling in the future. Previous studies showed that GOCE accelerations could be used in the evaluation of thermospheric wind models. In this dissertation, we showed for the first time that it is possible to retrieve from the gradiometer measurements more information, such as intense dynamics of the ionosphere, which also can cause the excitation of the thermospheric winds. Our results were published in Journal of Geodesy.

For sake of completeness, we also looked into other GOCE measurements, such as the angular accelerations, which also experience similar disturbances. Our analyses on the angular accelerations confirmed that the entire satellite body was affected from these external sources and it was not due to instrumental artifacts. The disturbances were clearly presented using the comparisons of the  $V_{yy}$  that were measured by GOCE EGG and the  $V_{yy}$  calculated from GRACE-only or from combined models of satellite and terrestrial data. We noted that the disturbances show different characteristics based on the frequency interval we looked at, which means that the disturbances have frequency dependent characteristics.

We extended our investigations with the use of the Canadian Ionosphere and Atmosphere Model (CIAM) to simulate electric field and neutral winds during quiet and stormy periods, based on  $Kp$  index, F10.7 solar flux and Canadian SuperDARN measurements. The simulations clearly showed the differences in the ionospheric conditions in terms of electric field strength and neutral winds. Hence, we showed that the electrical potential drop (potential difference between the maxima and minima) increases during stormy periods over the poles, which implies that the GOCE measurements are affected by intense ionospheric condition. Many of the results were planned to be presented in the COSPAR meeting (30 July - 7 August, 2016 in Istanbul that has been cancelled) and presented in the 1st Joint Commission 2 and IGFS Meeting International Symposium on Gravity, Geoid and Height Systems in Thessaloniki, 30 July - 7 August in Istanbul.

Lastly, we developed the relationship between the ionospheric dynamics and the disturbances measured by GOCE EGG. By using this relationship, we presented the dynamic system and (data-driven) model that predicts these disturbances over the regions where we have information on the ionospheric currents. We showed for the first time in GOCE literature that these disturbances can be modelled by using external data and GOCE products currently available can still be improved. These results will be published in Geophysical Research Letters.

## 9.2 Recommendations for Future Research

---

We performed our analyses in North America and Greenland. Since the input data of our system were limited to the terrestrial observatories over these regions, we could not correct the EGG measurements over other regions. By the help of similar proxies (e.g., Poynting flux) over Russia and Scandinavia, more complete analyses can be performed. Moreover, local observations are also required in the South Pole to understand the similar disturbances in the South geomagnetic pole that are smaller in magnitude and spread over a

smaller area. Hence, in order to extend the area of improved gradients, the EICS and SECS amplitudes over other regions also need to be included in our investigations.

GOCE models so far disregard the measurements over these regions and augment the measurements set from other models, such as GRACE. With any contribution to the quality of the data in these regions, detection of higher resolution time-variable signals could be possible by the GOCE gradients. Recent publications [Herceg et al., 2014, Bouman et al., 2014] indicated that GOCE data could be more sensitive to temporary variations of the ice and mass changes by using longer time series. Specifically, Bouman et al. [2014] mentioned that these spurious signals degraded GOCE's ability to estimate the reconciled ice mass balance in Greenland. By further improving the GOCE data processing, detecting and monitoring the time-variable Greenland gravity field may be improved, which is also crucial for sea level variation studies. Moreover, ocean currents and water surface speeds derived from the GOCE gradient measurements [Knudsen et al., 2011] could be improved in terms of the spatial resolution, which also makes this research important.

Deng et al. [2011] showed that a sudden enhancement of ion convection in the thermosphere causes Joule heating to increase due to the increase of the difference between ion drift and neutral wind. Joule heating is dominant in the energy transport process from the magnetosphere to ionosphere/thermosphere. Moreover, Deng et al. [2011] mentioned that the thermospheric response at CHAMP and GRACE altitudes would be affected by the high altitude energy variation and also by the vertical wave propagation due to energy input at lower altitudes (below 150 km). In the same paper, it has been mentioned that energy deposition at different altitudes forms very different thermospheric dynamics. Therefore, our analysis could be improved by using the ionospheric currents at the satellite altitude.

Even though GOCE was a geodetic mission, very useful information on space weather has been obtained [Bruinsma et al., 2014, Doornbos et al., 2013] and can further be improved when combined with other datasets (e.g. ESA's Cluster II). GOCE data were recently used to retrieve and validate thermospheric air density and wind models [Bruinsma et al., 2014] and exceeded their proposed and expected aims. GOCE-derived horizontal thermospheric wind and density profiles have already been used in many recent solar physics and thermosphere-ionosphere-magnetosphere coupling studies [Doornbos et al., 2013, Drob et al., 2015, Lu et al., 2014]. GOCE accelerometer measurements could further be used to:

- (a) understand the relation between  $\mathbf{S} = \mathbf{E} \times \delta\mathbf{B}$  Poynting vector and neutral winds as well as their dynamics in vertical direction;
- (b) evaluate the equivalent currents derived from terrestrial observations; and
- (c) help estimate the currents (e.g. EICS and SECS) where no magnetometer measurements exist

.  
Our analyses on the transfer functions are promising, not only for understanding the GOCE disturbances, but also be useful for the ionosphere/magnetosphere coupling models. Even though there are many effects that pose a fundamental limit to the degree to which accelerometers can be used to deduce ionospheric flows and currents, the use of gradiometer data together with other datasets could help estimate the ionospheric currents from a very low Earth orbiter satellite in an inverse manner, support the magnetosphere-ionosphere coupling studies and improve the developed space weather models during storm periods, all of which expand the application areas of GOCE measurements.

## References

- Amm, O., 1997: Ionospheric elementary current systems in spherical coordinates and their application. *Journal of geomagnetism and geoelectricity*, **49**(7), 947–955.
- Amm, O., M. Engebretson, T. Hughes, L. Newitt, A. Viljanen, and J. Watermann, 2002: A traveling convection vortex event study: Instantaneous ionospheric equivalent currents, estimation of field-aligned currents, and the role of induced currents. *Journal of Geophysical Research: Space Physics*, **107**(A11).
- Amm, O., and A. Viljanen, 1999: Ionospheric disturbance magnetic field continuation from the ground to the ionosphere using spherical elementary current systems. *Earth, Planets and Space*, **51**(6), 431–440.
- Andersson, L., U. Jönsson, K. H. Johansson, and J. Bengtsson, 1998: A manual for system identification. *Laboratory Exercises in System Identification. KF Sigma i Lund AB. Department of Automatic Control, Lund Institute of Technology, Box, 118*.
- Atkinson, G., 1970: Auroral arcs: Result of the interaction of a dynamic magnetosphere with the ionosphere. *Journal of Geophysical Research*, **75**(25), 4746–4755.
- Benveniste, J., and R. Floberghagen, 2015: Summary and recommendations from the fifth international user workshop. *ESA Special Publication*, volume 728, 26.
- Bouman, J., J. Ebbing, S. Meekes, R. A. Fattah, M. Fuchs, S. Gradmann, R. Haagmans, V. Lieb, M. Schmidt, D. Dettmering, et al., 2015: Goce gravity gradient data for lithospheric modeling. *International Journal of Applied Earth Observation and Geoinformation*, **35**, 16–30.
- Bouman, J., S. Fiorot, M. Fuchs, T. Gruber, E. Schrama, C. Tscherning, M. Veicherts, and P. Visser, 2011: Goce gravitational gradients along the orbit. *Journal of Geodesy*, **85**(11), 791–805.
- Bouman, J., M. Fuchs, E. Ivins, W. Wal, E. Schrama, P. Visser, and M. Horwath, 2014: Antarctic outlet glacier mass change resolved at basin scale from satellite gravity gradiometry. *Geophysical Research Letters*, **41**(16), 5919–5926.
- Bouman, J., R. Koop, C. C. Tscherning, and P. Visser, 2004: Calibration of goce sgg data using high–low sst, terrestrial gravity data and global gravity field models. *Journal of Geodesy*, **78**(1-2), 124–137.

- Bouman, J., S. Rispens, T. Gruber, R. Koop, E. Schrama, P. Visser, C. C. Tscherning, and M. Veicherts, 2009: Preprocessing of gravity gradients at the goce high-level processing facility. *Journal of Geodesy*, **83**(7), 659–678.
- Bruinsma, S., E. Doornbos, and B. Bowman, 2014: Validation of goce densities and evaluation of thermosphere models. *Advances in Space Research*, **54**(4), 576–585.
- Campbell, W. H., 2003: *Introduction to geomagnetic fields*. Cambridge University Press.
- Cesare, C., and G. Catastini, 2005: Gradiometer on-orbit calibration procedure analysis. technical note to esa. Technical report, GO-TN-AI-0069.
- Cesare, S., 2002: Performance requirements and budgets for the gradiometric mission. technical note. Technical report, GOC-TN-AI-0027, Alenia Spazio, Turin, Italy.
- Cowley, S., 2000: Magnetosphere-ionosphere interactions: A tutorial review. *Magnetospheric current systems* 91–106.
- Cravens, T. E., 2004: *Physics of solar system plasmas*. Cambridge University Press.
- Deng, Y., T. J. Fuller-Rowell, R. A. Akmaev, and A. J. Ridley, 2011: Impact of the altitudinal joule heating distribution on the thermosphere. *Journal of Geophysical Research: Space Physics (1978–2012)*, **116**(A5).
- Doornbos, E., S. Bruinsma, B. Fritsche, P. Visser, J. Van Den IJssel, J. T. Encarnacao, and M. Kern, 2013: Air density and wind retrieval using goce data. *ESA Special Publication*, volume 722, 7.
- Drinkwater, M. R., R. Haagmans, D. Muzi, A. Popescu, R. Floberghagen, M. Kern, and M. Fehringer, 2006: The goce gravity mission: Esas first core earth explorer. *Proceedings of the 3rd international GOCE user workshop*, European Space Agency Noordwijk, The Netherlands, 6–8.
- Drob, D. P., J. T. Emmert, J. W. Meriwether, J. J. Makela, E. Doornbos, M. Conde, G. Hernandez, J. Noto, K. A. Zawdie, S. E. McDonald, et al., 2015: An update to the horizontal wind model (hwm): The quiet time thermosphere. *Earth and Space Science*, **2**(7), 301–319.
- ESA, S. C., 2006: Goce l1b products user handbook. Technical report, The European GOCE Gravity Consortium EGG-GOCE-GSEG-EOPG-TN-06-0137.
- Fehringer, M., G. Andre, D. Lamarre, and D. Maesli, 2008: A jewel in esa’s crown. *ESA bulletin*, (133), 14–23.

- Floberghagen, R., M. Fehringer, D. Lamarre, D. Muzi, B. Frommknecht, C. Steiger, J. Piñeiro, and A. Da Costa, 2011: Mission design, operation and exploitation of the gravity field and steady-state ocean circulation explorer mission. *Journal of Geodesy*, **85**(11), 749–758.
- Fomichev, V., W. Ward, S. Beagley, C. McLandress, J. McConnell, N. McFarlane, and T. Shepherd, 2002: Extended canadian middle atmosphere model: Zonal-mean climatology and physical parameterizations. *Journal of Geophysical Research: Atmospheres*, **107**(D10).
- Frommknecht, B., D. Lamarre, M. Meloni, A. Bigazzi, and R. Floberghagen, 2011: Goce level 1b data processing. *Journal of Geodesy*, **85**(11), 759–775.
- Fuchs, M. J., J. Bouman, T. Broerse, P. Visser, and B. Vermeersen, 2013: Observing coseismic gravity change from the japan tohoku-oki 2011 earthquake with goce gravity gradiometry. *Journal of Geophysical Research: Solid Earth*, **118**(10), 5712–5721.
- Fukushima, N., 1976: Generalized theorem for no ground magnetic effect of vertical currents connected with pedersen currents in the uniform-conductivity ionosphere. *Report of Ionosphere and Space Research in Japan*, **30**(1), 35–40.
- Gjerloev, J., R. Hoffman, J. Sigwarth, and L. Frank, 2007: Statistical description of the bulge-type auroral substorm in the far ultraviolet. *Journal of Geophysical Research: Space Physics*, **112**(A7).
- Gottlieb, D., and C.-W. Shu, 1997: On the gibbs phenomenon and its resolution. *SIAM review*, **39**(4), 644–668.
- Grinsted, A., J. C. Moore, and S. Jevrejeva, 2004: Application of the cross wavelet transform and wavelet coherence to geophysical time series. *Nonlinear processes in geophysics*, **11**(5/6), 561–566.
- Hapgood, M., 1992: Space physics coordinate transformations: A user guide. *Planetary and Space Science*, **40**(5), 711–717.
- Heppner, J. P., 1973: High latitude electric fields and the modulations related to interplanetary magnetic field parameters. *Radio Science*, **8**(11), 933–948.
- Herceg, M., C. C. Tscherning, and J. Levinsen, 2014: Sensitivity of goce gradients on greenland mass variation and changes in ice topography. *Journal of Geodetic Science*, **4**(1).
- Hofmann-Wellenhof, B., and H. Moritz, 2006: *Physical geodesy*. Springer Science & Business Media.

- Ince, E. S., and S. D. Pagiatakis, 2015: Effects of the magnetic field on the goce level 1b gradiometer data over magnetic poles. *ESA Special Publication*, volume 728, 29.
- Ince, E. S., and S. D. Pagiatakis, 2016: Effects of space weather on goce electrostatic gravity gradiometer measurements. *Journal of Geodesy*, **90**(12), 1389–1403.
- Jenkins, G. M., and D. G. Watts, 1968: *Spectral analysis*. Holden-day.
- Jevrejeva, S., A. Grinsted, J. Moore, and S. Holgate, 2006: Nonlinear trends and multiyear cycles in sea level records. *Journal of Geophysical Research: Oceans*, **111**(C9).
- Kamide, Y., and A. Brekke, 1993: Altitude variations of ionospheric currents at auroral latitudes. *Geophysical research letters*, **20**(4), 309–312.
- Kamide, Y., and A. C.-L. Chian, 2007: *Handbook of the solar-terrestrial environment*. Springer Science & Business Media.
- Kamide, Y., A. Richmond, and S. Matsushita, 1981: Estimation of ionospheric electric fields, ionospheric currents, and field-aligned currents from ground magnetic records. *Journal of Geophysical Research: Space Physics*, **86**(A2), 801–813.
- Kanasewich, E. R., 1981: *Time sequence analysis in geophysics*. University of Alberta.
- Kelley, M. C., 2009: *The Earth's Ionosphere: Plasma Physics & Electrodynamics*, volume 96. Academic press.
- King, J., and N. Papitashvili, 2005: Solar wind spatial scales in and comparisons of hourly wind and ace plasma and magnetic field data. *Journal of Geophysical Research: Space Physics (1978–2012)*, **110**(A2).
- Kivelson, M. G., and C. T. Russell, 1995: *Introduction to space physics*. Cambridge university press.
- Knudsen, P., R. Bingham, O. Andersen, and M.-H. Rio, 2011: A global mean dynamic topography and ocean circulation estimation using a preliminary goce gravity model. *Journal of Geodesy*, **85**(11), 861–879.
- Knyazeva, M., A. Namgaladze, and O. Martynenko, 2012: Mathematical modeling of nighttime enhanced electron density regions in the earths ionospheric f2 layer and plasmasphere. *Geomagnetism and Aeronomy*, **52**(3), 368–377.
- Koop, R., J. Bouman, E. Schrama, and R. Visser, 2002: Calibration and error assessment of goce data. *Vistas for Geodesy in the New Millennium*. Springer, 167–174.

- Kumar, P., and E. Foufoula-Georgiou, 1997: Wavelet analysis for geophysical applications. *Reviews of geophysics*, **35**(4), 385–412.
- Lamarre, D., 2007: The very basic principles of the goce gradiometer in-flight calibration. *Proc. of the 3rd International GOCE User Workshop*, 91–94.
- Lennart, L., 1999: System identification: theory for the user. *PTR Prentice Hall, Upper Saddle River, NJ* 1–14.
- Lepping, R., M. Acuña, L. Burlaga, W. Farrell, J. Slavin, K. Schatten, F. Mariani, N. Ness, F. Neubauer, Y. Whang, et al., 1995: The wind magnetic field investigation. *Space Science Reviews*, **71**(1-4), 207–229.
- Lu, G., D. Baker, R. McPherron, C. Farrugia, D. Lummerzheim, J. Ruohoniemi, F. Rich, D. Evans, R. Lepping, M. Brittnacher, et al., 1998: Global energy deposition during the january 1997 magnetic cloud event. *Journal of Geophysical Research: Space Physics*, **103**(A6), 11685–11694.
- Lu, G., M. Hagan, K. Häusler, E. Doornbos, S. Bruinsma, B. Anderson, and H. Korth, 2014: Global ionospheric and thermospheric response to the 5 april 2010 geomagnetic storm: An integrated data-model investigation. *Journal of Geophysical Research: Space Physics*, **119**(12), 10–358.
- Lühr, H., S. Rentz, P. Ritter, H. Liu, and K. Häusler, 2007: Average thermospheric wind patterns over the polar regions, as observed by champ. *Annales Geophysicae*, volume 25, 1093–1101.
- Mallat, S., 1998: A wavelet tour of signal processing academic. *New York*, **16**.
- Mann, I., D. Milling, I. Rae, L. Ozeke, A. Kale, Z. Kale, K. Murphy, A. Parent, M. Usanova, D. Pahud, et al., 2008: The upgraded carisma magnetometer array in the themis era. *Space Science Reviews*, **141**(1-4), 413–451.
- Martynenko, O., V. Fomichev, K. Semeniuk, S. Beagley, W. Ward, J. McConnell, and A. Namgaladze, 2014: Physical mechanisms responsible for forming the 4-peak longitudinal structure of the 135.6 nm ionospheric emission: First results from the canadian iam. *Journal of Atmospheric and Solar-Terrestrial Physics*, **120**, 51–61.
- Mayer-Gürr, T., N. Zehentner, B. Klinger, and A. Kvas, 2014: Itsg-grace2014: a new grace gravity field release computed in graz. *Presentation at the GRACE Science Team Meeting (GSTM), Potsdam*, volume 9, 2014.
- McCarthy, D. D., and G. Petit, 2004: Iers conventions (2003). Technical report, DTIC Document.

- McPherron, R. L., C. Russell, and M. Aubry, 1973: Satellite studies of magnetospheric substorms on august 15, 1968: 9. phenomenological model for substorms. *Journal of Geophysical Research*, **78**(16), 3131–3149.
- Misiti, M., Y. Misiti, G. Oppenheim, and J. P. Michel, 1996: Wavelet toolbox: for use with matlab.
- Moore, J., A. Grinsted, and S. Jevrejeva, 2006: Is there evidence for sunspot forcing of climate at multi-year and decadal periods? *Geophysical research letters*, **33**(17).
- Namgaladze, A., M. Förster, and R. Y. Yurik, 2000: Analysis of the positive ionospheric response to a moderate geomagnetic storm using a global numerical model. *Annales Geophysicae*, volume 18, Springer, 461–477.
- Partamies, N., L. Juusola, E. Tanskanen, K. Kauristie, J. Weygand, and Y. Ogawa, 2011: Substorms during different storm phases. *Annales Geophysicae*, volume 29, Copernicus GmbH, 2031–2043.
- Pavlis, N. K., S. A. Holmes, S. C. Kenyon, and J. K. Factor, 2012: The development and evaluation of the earth gravitational model 2008 (egm2008). *Journal of Geophysical Research: Solid Earth (1978–2012)*, **117**(B4).
- Peterseim, N., A. Schlicht, C. Stummer, and W. Yi, 2011: Impact of cross winds in polar regions on goce accelerometer and gradiometer data. *Proceedings of the 4th International GOCE User Workshop*, volume 31.
- Pulkkinen, A., O. Amm, and A. Viljanen, 2003: Ionospheric equivalent current distributions determined with the method of spherical elementary current systems. *Journal of Geophysical Research: Space Physics (1978–2012)*, **108**(A2).
- Reigber, C., G. Balmino, P. Schwintzer, R. Biancale, A. Bode, J.-M. Lemoine, R. König, S. Loyer, H. Neumayer, J.-C. Marty, et al., 2002: A high-quality global gravity field model from champ gps tracking data and accelerometry (eigen-1s). *Geophysical Research Letters*, **29**(14).
- Rispens, S., and J. Bouman, 2009: Calibrating the goce accelerations with star sensor data and a global gravity field model. *Journal of Geodesy*, **83**(8), 737–749.
- Rostoker, G., 1972: Geomagnetic indices. *Reviews of Geophysics*, **10**(4), 935–950.
- Rummel, R., O. Abrikosov, and R. Van Hees, 2010: Goce high level processing facility goce level 2 product data handbook. *The European GOCE Gravity Consortium EGG-C.-2010.-77 p.*

- Rummel, R., T. Gruber, and R. Koop, 2004: High level processing facility for goce: products and processing strategy. *Proceedings of the 2nd International GOCE User Workshop, ESA-SP569*, ESA, 8–10.
- Rummel, R., W. Yi, and C. Stummer, 2011: Goce gravitational gradiometry. *Journal of Geodesy*, **85**(11), 777–790.
- Russell, C., 2000: The polar cusp. *Advances in Space Research*, **25**(7), 1413–1424.
- Schack, P., R. Pail, and A. Schlicht, 2014: Investigations into the characteristics of the goce gravity gradients during the low orbit phase abstract 5th international goce user workshop.
- Sechi, G., G. André, D. Andreis, and M. Saponara, 2006: Magnetic attitude control of the goce satellite. *Guidance, Navigation and Control Systems*, volume 606, 37.
- Seeber, G., 2003: *Satellite geodesy: foundations, methods, and applications*. Walter de Gruyter.
- Selsis, F., 2011: Neutral atmosphere. *Encyclopedia of Astrobiology*. Springer, 1112–1112.
- Siemes, C., 2012: Goce gradiometer calibration and level 1b data processing. Technical report, ESA Working Paper EWP-2384. [https://earth.esa.int/c/document\\_library/get\\_file](https://earth.esa.int/c/document_library/get_file).
- Siemes, C., R. Haagmans, M. Kern, G. Plank, and R. Floberghagen, 2012: Monitoring goce gradiometer calibration parameters using accelerometer and star sensor data: methodology and first results. *Journal of Geodesy*, **86**(8), 629–645.
- Stone, E., A. Frandsen, R. Mewaldt, E. Christian, D. Margolies, J. Ormes, and F. Snow, 1998: The advanced composition explorer. *The Advanced Composition Explorer Mission*. Springer, 1–22.
- Stummer, C., 2012: *Gradiometer data processing and analysis for the GOCE mission*. PhD thesis, Technische Universität München.
- Stummer, C., T. Fecher, and R. Pail, 2011: Alternative method for angular rate determination within the goce gradiometer processing. *Journal of Geodesy*, **85**(9), 585–596.
- Stummer, C., C. Siemes, R. Pail, B. Frommknecht, and R. Floberghagen, 2012: Upgrade of the goce level 1b gradiometer processor. *Advances in Space Research*, **49**(4), 739–752.
- Tanskanen, E., 2009: A comprehensive high-throughput analysis of substorms observed by image magnetometer network: Years 1993–2003 examined. *Journal of Geophysical Research: Space Physics*, **114**(A5).

- Tanskanen, E., A. Viljanen, T. Pulkkinen, R. Pirjola, L. Häkkinen, A. Pulkkinen, and O. Amm, 2001: At substorm onset, 40% of al comes from underground. *Journal of Geophysical Research: Space Physics*, **106**(A7), 13119–13134.
- Tapley, B. D., S. Bettadpur, J. C. Ries, P. F. Thompson, and M. M. Watkins, 2004: Grace measurements of mass variability in the earth system. *Science*, **305**(5683), 503–505.
- Torrence, C., and P. J. Webster, 1998: The annual cycle of persistence in the el niño/southern oscillation. *Quarterly Journal of the Royal Meteorological Society*, **124**(550), 1985–2004.
- Touboul, P., B. Foulon, B. Christophe, and J. Marque, 2012: Champ, grace, goce instruments and beyond. *Geodesy for Planet Earth*. Springer, 215–221.
- Troshichev, O., A. Janzhura, and P. Stauning, 2006: Unified pcn and pcs indices: Method of calculation, physical sense, and dependence on the imf azimuthal and northward components. *Journal of Geophysical Research: Space Physics (1978–2012)*, **111**(A5).
- Untiedt, J., and W. Baumjohann, 1993: Studies of polar current systems using the ims scandinavian magnetometer array. *Space Science Reviews*, **63**(3-4), 245–390.
- Van den IJssel, J., P. Visser, E. Doornbos, U. Meyer, H. Bock, and A. Jäggi, 2011: Gocce ssti l2 tracking losses and their impact on pod performance. *Proceedings of 4th International GOCE User Workshop, Munich, Germany, 31 March-1 April 2011; ESA SP-696*, European Space Agency (ESA).
- Vanhamäki, H., O. Amm, and A. Viljanen, 2003: One-dimensional upward continuation of the ground magnetic field disturbance using spherical elementary current systems. *Earth, planets and space*, **55**(10), 613–625.
- Visser, P., 2008: Exploring the possibilities for star-tracker assisted calibration of the six individual goce accelerometers. *Journal of Geodesy*, **82**(10), 591–600.
- Walterscheid, R., L. Lyons, and K. Taylor, 1985: The perturbed neutral circulation in the vicinity of a symmetric stable auroral arc. *Journal of Geophysical Research: Space Physics*, **90**(A12), 12235–12248.
- Weygand, J. M., O. Amm, A. Viljanen, V. Angelopoulos, D. Murr, M. Engebretson, H. Gleisner, and I. Mann, 2011: Application and validation of the spherical elementary currents systems technique for deriving ionospheric equivalent currents with the north american and greenland ground magnetometer arrays. *Journal of Geophysical Research: Space Physics (1978–2012)*, **116**(A3).

- Wright Jr, J., T. Lennon, R. Corell, N. Ostenso, W. Huntress Jr, J. Devine, P. Crowley, and J. Harrison, 1995: The national space weather program, strategic plan. office of the federal coordinator for meteorological services and supporting research. Technical report, Publication FCM-P30-1995 (Washington, DC).
- Yi, W., 2011: *The Earth's gravity field from GOCE*. PhD thesis, Munich: Institute of Astrometry and Physical Geodesy, Technical University Munich.
- Yi, W., R. Rummel, and T. Gruber, 2013: Gravity field contribution analysis of goce gravitational gradient components. *Studia Geophysica et Geodaetica*, **57**(2), 174–202.